THE ARCTIC *CYLINDROCYSTIS* (ZYGNEMATOPHYCEAE, STREPTOPHYTA) GREEN ALGAE ARE GENETICALLY AND MORPHOLOGICALLY DIVERSE AND EXHIBIT EFFECTIVE ACCUMULATION OF POLYPHOSPHATE[1]

Dovilė Barcytė[2] (iD)

Department of Ecology, Faculty of Science, Charles University, Viničná 7, Prague 2, CZ-128 44, Czech Republic

Jana Pilátová (iD)

Department of Experimental Plant Biology, Faculty of Science, Charles University, Viničná 5, Prague 2, CZ-128 44, Czech Republic

Peter Mojzeš (iD)

Institute of Physics, Faculty of Mathematics and Physics, Charles University, Ke Karlovu 5, Prague 2, CZ-121 16, Czech Republic

and Linda Nedbalová (iD)

Department of Ecology, Faculty of Science, Charles University, Viničná 7, Prague 2, CZ-128 44, Czech Republic

The green algal genus *Cylindrocystis* is widespread in various types of environments, including extreme habitats. However, very little is known about its diversity, especially in polar regions. In the present study, we isolated seven new *Cylindrocystis*-like strains from terrestrial and freshwater habitats in Svalbard (High Arctic). We aimed to compare the new isolates on a molecular (*rbc*L and 18S rDNA), morphological (light and confocal laser scanning microscopy), and cytological (Raman microscopy) basis. Our results demonstrated that the Arctic *Cylindrocystis* were not of a monophyletic origin and that the studied strains clustered within two clades (tentatively named the soil and freshwater/glacier clades) and four separate lineages. Morphological data (cell size, shape, and chloroplast morphology) supported the presence of several distinct taxa among the new isolates. Moreover, the results showed that the Arctic *Cylindrocystis* strains were closely related to strains originating from the temperate zone, indicating high ecological versatility and successful long-distance dispersal of the genus. Large amounts of inorganic polyphosphate (polyP) grains were detected within the chloroplasts of the cultured Arctic *Cylindrocystis* strains, suggesting effective luxury uptake of phosphorus. Additionally, various intracellular structures were identified using Raman microscopy and cytochemical and fluorescent staining. This study represents the first attempt to combine molecular, morphological, ecological, and biogeographical data for Arctic *Cylindrocystis*. Our novel cytological observations partially explain the success of *Cylindrocystis*-like microalgae in polar regions.

Streptophytic green algae, or charophytes (Streptophyta, Viridiplantae), particularly the conjugating green algae of the class Zygnematophyceae, have been demonstrated to be the closest relatives of land plants (Wodniok et al. 2011, Ruhfel et al. 2014). Increased scientific attention has therefore been paid toward the stress tolerance, adaptation, molecular diversity, and evolution of this particular algal group (Pichrtová et al. 2014a,b, 2016, 2018, Herburger et al. 2015, 2016, de Vries et al. 2016, 2018, Rippin et al. 2017, Holzinger et al. 2018). Such data help to better elucidate the colonization of terrestrial environments by streptophytic algae and the origin of all embryophytes. For example, desiccation tolerance was the key trait in the emergence of life on land, and zygnematophytes have been shown to withstand intense and prolonged periods of water shortage (Pichrtová et al. 2014a,b, Herburger et al. 2015, Rippin et al. 2017).

The Zygnematophyceae encompass morphologically diverse green algae, ranging from nonmotile unicellular or unbranched filamentous forms to small colonial forms. They are widely distributed and are found mostly in freshwater systems, including limnoterrestrial habitats such as ephemeral pools. In addition to periodic desiccation exposure, zygnematophytes can also survive low pH levels and temperatures, high visible light and UV radiation levels, and low-nutrient conditions (Hall and McCourt 2017). Since the first land plants were likely exposed to such environmental stresses

(Wodniok et al. 2011), different types of studies on streptophytes inhabiting extreme environments are an important research direction. For example, under low-temperature and high-light stress, de Vries et al. (2018) demonstrated that Zygnematophyceae exhibit many of the stress-signaling factors known from land plants (i.e., embryophyte stress signaling had evolved in their algal progenitors). Thus, little explored zygnematophytes living in challenging environmental conditions could hold the key to understanding terrestrialization and our Earth as it exists.

Polar habitats include the aforementioned physical extremes and represent some of the harshest environments on Earth. Nevertheless, the Zygnematophyceae are a successful group of organisms in both the Arctic and Antarctic. For example, zygnematophytes form abundant scum mats in hydroterrestrial environments (Pichrtová et al. 2018) and thrive on the bare ice of glaciers (Yallop et al. 2012, Lutz et al. 2018). However, despite their indisputable role as primary producers and their influence on the acceleration of ice sheet melting (Yallop et al. 2012), little is known about the diversity and ecology of polar streptophytic microalgae. This situation is due in part to limited sampling efforts, along with difficulties in cultivating cold-adapted microorganisms. One group of such enigmatic microorganisms found in polar regions is the green algal genus *Cylindrocystis*.

Cylindrocystis is a genus of saccoderm green microalgae (known as desmids) that are systematically placed in the family Mesotaeniaceae of the order Zygnematales (Zygnematophyceae). It includes ecologically versatile photosynthetic microorganisms inhabiting a wide range of environments. For example, *Cylindrocystis* are commonly found in acidic oligotrophic freshwaters of the temperate zone, especially in peat bogs (Coesel and Meesters 2007, Štěpánková et al. 2012) or subaerial habitats (Škaloud 2009). These algae are also considered typical ice specialists and have been reported from glaciers in both southern and northern hemispheres (Takeuchi and Kohshima 2004, Stibal et al. 2006, Nedbalová and Sklenář 2008, Yallop et al. 2012, Lutz et al. 2018). However, *Cylindrocystis* have also been detected in hot and dry desert crust communities (Flechtner et al. 1998, Lewis and Lewis 2005).

A number of *Cylindrocystis* species have been described based on the morphological characteristics of vegetative cells and zygospore structure (Lütkemüller 1913, Prescott et al. 1972). However, their taxonomic status remains unclear. *Cylindrocystis* (*C.*) *brebissonii*, the type species of the genus, is probably the most frequently reported taxon. Several varieties of this species have been described based on morphological peculiarities and habitat type. For example, the infraspecific epithet *cryophila* was proposed by Kol (1942) to distinguish cryophilic *C. brebissonii* thriving in ice fields and snow banks from aquatic *C. brebissonii*, whereas Flechtner et al.

(1998) established the variety *deserti* to accommodate *C. brebissonii* occurring in dry Mexican soils. Other described varieties include the epithets *minor* (now *C. gracilis*), *curvata*, *jenneri*, and *turgida*, referring to different cell dimensions and zygospore shapes of *C. brebissonii* (Prescott et al. 1972, Lenzenweger 2003).

Despite its wide distribution, *Cylindrocystis* remains a cryptic taxon requiring further examination. For example, very few studies based on molecular data have provided insights into the genetic diversity of the genus *Cylindrocystis* and shown its complex phylogenetic structure (Hall et al. 2008, Gontcharov and Melkonian 2010). The authors of these studies demonstrated that *Cylindrocystis* sensu lato represents a group of polyphyletic taxa intermixed with members of the traditional family Zygnemataceae, encompassing filamentous genera such as *Zygnema*, *Zygnemopsis*, and *Mougeotia*. In addition, there are no molecular data on cultured polar *Cylindrocystis*, and knowledge of *Cylindrocystis* morphotypes in the High Arctic is restricted mostly to the aforementioned *C. brebissonii* var. *cryophila* (Kol 1942). However, *Cylindrocystis* might not be that simple and may present hidden biodiversity. For example, Pichrtová et al. (2018) revealed extremely high molecular diversity of the Arctic *Zygnema*, which are close relatives of the genus *Cylindrocystis*. On the other hand, Ryšánek et al. (2016) demonstrated relatively low diversity of another streptophytic algal genus, *Klebsormidium* (Klebsormidiophyceae), in polar regions. Since Arctic *Cylindrocystis* have not yet been studied in detail, the establishment of cultures of these algae is a valuable approach for biodiversity studies, enabling the linkage of morphology, phylogeny, and ecology. Here, we isolated and studied seven *Cylindrocystis* strains from different cold habitats in the High Arctic (Svalbard). We used genetic (18S rDNA and *rbc*L) and morphological/cytological (light, confocal laser scanning, and Raman microscopy) attributes to compare the new isolates. We focused on the following questions: (i) How many genotypes and morphotypes do the new isolates from Svalbard represent? (ii) Do they share a monophyletic origin, or have they evolved independently? (iii) Are the identified genotypes unique to the Arctic, or have they been detected elsewhere? (iv) Finally, what observed morphological/cytological traits could make them successful in harsh Arctic habitats?

MATERIALS AND METHODS

Origin, isolation, and cultivation of strains. Seven strains with a *Cylindrocystis*-like morphology were newly isolated from soil and water samples collected in 2016 and 2018 in Spitsbergen (78° N, 16° E; Fig. S1 in the Supporting Information; Table 1). Spitsbergen is the main and the largest island of the Svalbard archipelago located in the Arctic Ocean and is characterized by a relatively mild climate compared to other regions at the same latitudes due to the warm Atlantic West Spitsbergen Current (Walczowski and Piechura 2011). The

mean temperatures vary from $-12°C$ in winter to $+5°C$ in summer, and the area receives between 200 and 400 mm of precipitation annually (Førland et al. 2011). Five samples originated from Petuniabukta located in Billefjorden, where the Czech field camp "Nostoc" is established. The bay is surrounded by the Pyramiden, Mumien, and Svenbrehøgda mountain ranges and five small valley glaciers (Ferdinandbreen, Svenbreen, Hørbyebreen, Ragnarbreen and Ebbabreen). Two samples were collected on Breinosa Mountain close to the Foxfonna Glacier located on the southern side of the Adventdalen Valley in Adventfjorden. Small quantities of the collected field material were incubated for several weeks in Bold's Basal Medium (BBM; Bischoff and Bold 1963) in CELLSTAR® 12-well plates (Greiner Bio-One, Kremsmünster, Austria). Cells of *Cylindrocystis* were isolated using a micropipette and a Nikon Diaphot 200 inverted phase-contrast microscope (Tokyo, Japan). The isolated cells were continued to be grown in multiwell plates in a Q-Cell 200 incubator (PolLab, Wilkowice, Poland) at 20°C with constant light of 20–30 μmol photons $\cdot$ m^{-2} $\cdot$ s^{-1}. For comparison, we purchased an additional strain from the Culture Collection of Algae at the University of Texas at Austin, *Cylindrocystis brebissonii* var. *deserti* UTEX B 2684, isolated from the soil surface in the Baja California Desert, Mexico. All newly established strains are housed in the working collection at the Department of Ecology, Charles University, Prague.

DNA extraction, PCR, and DNA sequencing. For total genomic DNA extraction, algal cells were disrupted using the bead-beating method with a Precellys®24 homogenizer (Bertin Instruments, Montigny-le-Bretonneux, France). The DNA was isolated using the Geneaid Plant Genomic DNA Mini Kit (New Taipei City, Taiwan). The ribulose-1,5-bisphosphate carboxylase/oxygenase large subunit (*rbc*L) was amplified with the primers RH1 and 1385R (McCourt et al. 2000). 18S ribosomal DNA (rDNA) was amplified with the primers NS1 and 18L (Hamby et al. 1988). The PCR assays were performed with the Qiagen Multiplex PCR Plus Kit (Hilden, Germany) in a total volume of 10 μL using a GenePro thermal cycler (BioER, Hangzhou, China). The PCR products were quantified in a 1% agarose gel, stained with GelRed® (Biotium Inc., Fremont, CA, USA), cleaned with ethanol and measured with a Thermo Scientific™ NanoDrop™ One UV-Vis spectrophotometer (Waltham, MA, USA). The purified PCR products were Sanger sequenced by Macrogen (Amsterdam, the Netherlands) in both directions using the same primer pairs, including the additional 18S rDNA sequencing primers 895R (Remias et al. 2012b) and 1422R (Barcytė et al. 2017). The sequencing reads were assembled and edited using the SeqAssem program (Hepperle 2004). The sequences were submitted to GenBank and are available under accession numbers MN177723 to MN177736.

Sequence alignment, model selection, and phylogenetic analyses. The BLAST algorithm (Altschul et al. 1997) was employed to search the GenBank database for sequences closely related to the newly sequenced strains. The data previously published by Gontcharov and Melkonian (2010) were also taken into account. For phylogenetic analyses, 27 chloroplast *rbc*L sequences and 24 nuclear 18S rDNA sequences were acquired. Multiple sequence alignments of the *rbc*L and 18S rDNA sequences were computed separately using the MAFFT 7.0 algorithm (Katoh et al. 2019). The alignments were checked and modified manually in the program BioEdit 7.2.5 (Hall 1999). The *rbc*L alignment comprised 34 sequences/1293 positions, and the 18S rDNA alignment comprised 31 sequences/1766 positions. We partitioned the *rbc*L data set by the three codon positions, and the best nucleotide substitution models were estimated using PartitionFinder2 (Lanfear et al. 2012) as implemented in the CIPRES Science Gateway 3.3 (Miller et al. 2010). The Bayesian information criterion (BIC) and the "greedy" heuristic algorithm, along with the option of "linked branch lengths," were employed. The outcome suggested a TIM+I model for the first codon position, TVMEF+I for the second codon position and HKY+I+G for the third codon position. Additionally, the nucleotide substitution model that best fit the 18S rDNA data set was estimated with Modeltest 3.7 (Posada and Crandall 1998) in conjunction with PAUP* 4.0 (Swofford 2003). Based on the Akaike information criterion (AIC), the MIFef model was chosen as the best-fit model for the data set. All phylogenetic analyses were conducted using maximum likelihood (ML) and Bayesian inference (BI) at the XSEDE user portal via CIPRES. The ML analysis for the partitioned *rbc*L data set was computed using Garli 2.01 (Zwickl 2006) with 100 bootstrap replicates. The ML analysis for the nonpartitioned 18S rDNA data set was performed using RAxML 8.2.10 (Stamatakis 2014) with 1,000 bootstrap replicates. The BI analyses were computed using MrBayes 3.2.6 (Ronquist et al. 2012). The set of proposed nucleotide substitution models was therefore modified accordingly (e.g., RAxML applies only GTR+I and GTR+I+G models). Two Markov chain Monte Carlo runs (MCMC) for 500,000 generations with trees sampled every 100 generations were performed in the BI. The convergence of parameters was checked with Tracer 1.7.1 (Rambaut et al. 2018). For each run, the first 25% of the sampled trees was discarded as burn-in. Bayesian posterior probabilities were used to assess the branch support of the Bayesian tree. For the visualization of the phylogenetic trees, the program FigTree 1.4.2 was used (Rambaut 2007).

Microscopy. Vegetative cells were observed and documented using 1-month-old cultures. Light microscopy was carried out using an Olympus BX43 light microscope (Tokyo, Japan). Microphotographs were taken with an Olympus DP27 digital camera. The Olympus microimaging software cellSens 1.15 was used for morphometric measurements of the strains. One hundred cells of each strain were measured for size comparisons. The length and width of the strains were graphed using Prism8 (GraphPad Software, San Diego, CA, USA).

TABLE 1. Origin of the studied Arctic *Cylindrocystis* strains.

Strain	Habitat	No. on map	Description	Coordinates
			Locality	
P2016	Soil	1	BSC in abandoned settlement Pyramiden	78°39.40741′, 016°23.83477′
P2018	Soil	2	BSC in abandoned settlement Pyramiden	78°39.40640′, 016°23.84109′
CWM	Soil	3	Wet hummock meadow in Petuniabukta	78°43.81667′, 016°26.68333′
CFN	Soil	4	Czech field station "Nostoc"	78°41.13321′, 016°27.40408′
Sven	Glacier	5	Glacier Svenbreen	78°43.59360′, 016°21.05400′
Fox6	Freshwater/glacier	6	Meltwater close to glacier Foxfonna	78°08.63810′, 016°05.59993′
Fox7	Freshwater/glacier	7	Meltwater close to glacier Foxfonna	78°08.57846′, 016°05.80122′

BSC, biological soil crust.

The 3D morphology of the chloroplasts of the *Cylindrocystis* strains was reconstructed using a Leica TCS SP8 laser scanning confocal microscope (Wetzlar, Germany) equipped with the data processing software Leica Application Suite (LAS X), with final visualization in the form of a maximum projection and an optical cross-section through the middle of the cell. A diode-pumped solid-state (DPSS) laser was used as the source of excitation at a wavelength of 561 nm with acquisition of the emission light of chlorophyll *a* and *b* fluorescence in the range of 650–750 nm.

For in situ determination of the chemical composition of intracellular structures, confocal Raman microscopy was used (Moudříková et al. 2017a,b). Algal cells harvested by centrifugation were mixed with a 1% w/v solution of low-gelling agarose ($T = 39°C$), immediately spread as a single-cell layer between a quartz slide and a coverslip and sealed with a CoverGrip sealant (Biotium Inc., Fremont, CA, USA). Agarose immobilization was used to prevent the movement of the cells during the acquisition of Raman spectra. Two-dimensional Raman maps were obtained with a WITec alpha300 RSA confocal Raman microscope (Ulm, Germany) with laser excitation at 532 nm (20 mW power at the focal plane) and an Olympus oil-immersion objective UPlanFLN 100×, NA 1.30. Using a scanning step of 200 nm in both directions and an integration time of 100 ms per cell voxel, a Raman map of *Cylindrocystis* cell size was acquired within 30–45 min. To remove the strong autofluorescence of chlorophyll obscuring the Raman spectra of photosynthetic microorganisms, wide area, low-power photobleaching of the entire cell with a defocused 532-nm laser beam was applied prior to mapping according to Moudříková et al. (2016). Raman chemical maps were constructed by multivariate decomposition of the baseline-corrected spectra into the spectra of pure chemical components using WITec Project Plus 5.1 software.

To visualize different organelles and structures, cell staining for one selected strain was also applied using cytochemical and fluorescent dyes. Toluidine blue staining was performed using a 0.005–0.01% solution at pH 7. Fluorescent staining was performed separately for each dye: DAPI (4′,6-diamidino-2-phenylindole, dilactate; Invitrogen, Carlsbad, CA, USA), for staining nucleic acids at a final concentration of 1 μg/mL with excitation/emission maxima of 358/461 nm; SYTO13 (Molecular Probes, Eugene, OR, USA), a green fluorescent nucleic acid dye, at the final concentration of 3 μM with excitation/emission maxima of 488/509 nm; MitoTracker Red CMXRos (Thermo Fischer Scientific, Waltham, MA, USA), a red fluorescent dye that stains mitochondria in live cells whose accumulation is dependent upon the membrane potential, at a final concentration of 3 μM with excitation/emission maxima of 579/599 nm; LysoTracker Green DND-26 (Invitrogen), a green fluorescent dye that stains acidic compartments in live cells, at a final concentration of 2 μM with excitation/emission maxima of 504/511 nm; DiOC5(3) (3,3′-Dipentyloxacarbocyanine iodide; Sigma-Aldrich, St. Louis, MO, USA) a green fluorescent lipophilic dye that stains the endomembrane system, at a final concentration of 5 μg · mL^{-1} with excitation/emission maxima of 484/500 nm; and Nile red (NR; Carl Roth GmbH, Karlsruhe, Germany) a yellow-fluorescent dye that stains lipid droplets and other lipophilic structures in live cells, at a final concentration of 1 μg · mL^{-1} with excitation/emission maxima of 552/636 nm. All staining was performed within a period of 10 min. Microphotography acquisition was performed using an Olympus Provis AX70 microscope equipped with a fluorescent block (U-MWU, U-MWIB, U-MWG) and a Nikon D3100 DSLR camera.

RESULTS

Phylogenetic analyses. Seven new strains with a *Cylindrocystis*-like morphology isolated from terrestrial and freshwater habitats in the High Arctic were sequenced and analyzed. The phylogenetic analyses (ML and BI) performed based on the separate *rbc*L and 18S rDNA data sets were congruent in terms of the elucidated clades, lineages, and sister relationships. Nevertheless, both tree topologies are presented to show that the *rbc*L molecular marker was more variable than 18S rDNA (Figs. 1 and 2). For example, strains P2016 and CWM differed from each other by 30 nucleotides in the *rbc*L sequences but were identical in their 18S rDNA sequences. Similarly, strains Sven and Fox6 differed by eight nucleotides in their *rbc*L sequences but had identical 18S rDNA sequences. Another reason for presenting the two phylogenetic trees is that the two *Cylindrocystis* strains (ACOI 310 and UTEX 1259) revealed by the BLAST algorithm as close relatives of the three newly sequenced strains were represented only by *rbc*L sequences (Fig. 1). Since one of our aims was to compare the new isolates with all available data, we considered it useful to analyze the two separate data sets with as many identified close relatives as possible.

The Arctic *Cylindrocystis* strains investigated in this study were split into two main clades (tentatively named the soil clade and the freshwater/glacier clade based on the habitats from which the new strains originated) and four lineages. The soil clade encompassed two well-supported lineages including the four *Cylindrocystis* isolates from Petuniabukta (Figs. 1 and 2). The first lineage of the soil clade was composed of three new strains (P2018, P2016, and CWM) and *Cylindrocystis brebissonii* var. *deserti* UTEX B 2684 isolated from the desert soil crust in Mexico. The most similar *rbc*L sequence to the UTEX strain came from strain P2018, which differed by 25 nucleotides. In contrast, when 18S rDNA sequences were compared, strains P2016 and CWM were more similar to the UTEX strain (three nucleotide difference) than the P2018 strain (seven nucleotide difference). The second lineage of the soil clade included the new CFN strain along with two isolates (M 3004 and M 3019) from unknown habitats in Germany (generally specified as freshwater; CCAC <www.ccac.uni-koeln.de>) and the desert isolate BCP-LG2-VF30 from the USA (Figs. 1 and 2). The two European strains were more similar to the polar CFN strain than the American strain. That is, strains M 3004 and M 3019 differed from the CFN strain by 33 and 35 nucleotides, respectively, in their *rbc*L sequence and by 21 nucleotides in their 18S rDNA sequence. Additionally, the desert isolate BCP-LG2-VF30 showed 46 and 30 nucleotide differences in its chloroplast and nuclear sequences, respectively, compared to the CFN strain.

The freshwater clade contained new strains isolated from the glacier ice (Sven) and meltwater (Fox6 and Fox7) close to the glacier. The Sven and Fox6 strains were much more closely related to each other than to the Fox7 strain and, thus, represented
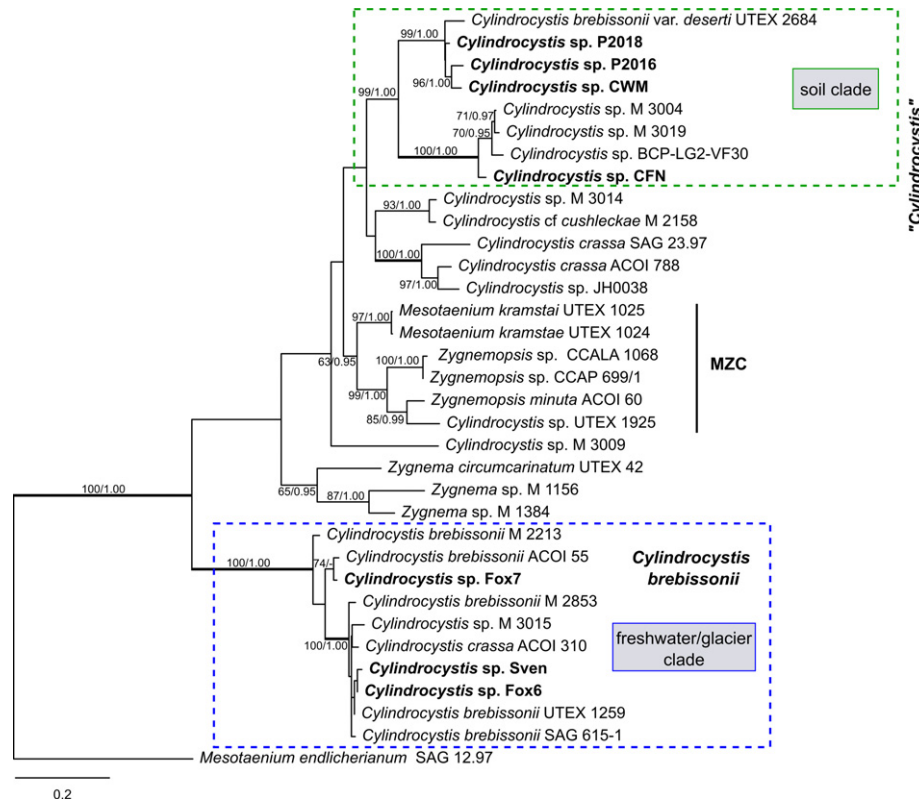
FIG. 1. Maximum-likelihood phylogenetic tree of the *rbc*L sequences. The numbers next to branches indicate statistical support (maximum-likelihood/Bayesian posterior probabilities). The "*Cylindrocystis*," MZC and *Cylindrocystis brebissonii* clades were delimited according to Gontcharov and Melkonian (2010). New sequences are in bold. [Color figure can be viewed at wileyonlinelibrary.com]
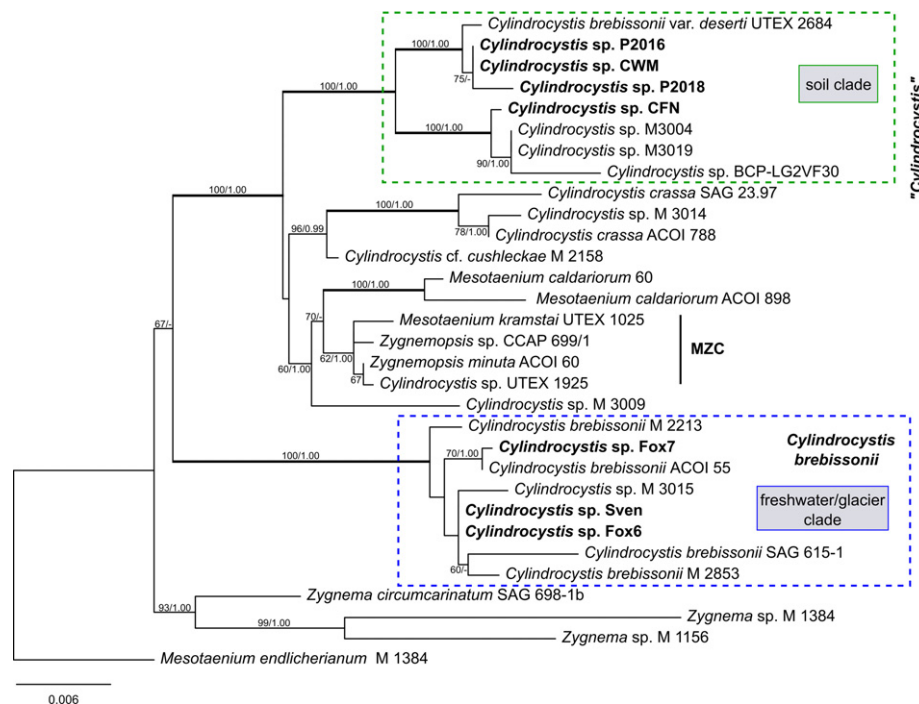

FIG. 2. Maximum-likelihood phylogenetic tree of the 18S rDNA sequences. The numbers next to branches indicate statistical support (maximum-likelihood/Bayesian posterior probabilities). The "*Cylindrocystis*," MZC and *Cylindrocystis brebissonii* clades were delimited according to Gontcharov and Melkonian (2010). New sequences are in bold. [Color figure can be viewed at wileyonlinelibrary.com]

two independent phylogenetic lineages. The closest identified relative of the Fox7 strain was the ACOI 55 strain originating from Portugal. The *rbc*L and 18S rDNA sequences of these strains differed from each other by 12 nucleotides and one nucleotide, respectively. Additionally, strains Sven and Fox6 grouped together with strain M 2853 isolated from a peat bog in Austria, M 3025 originating from Germany, ACOI 310 isolated from a pond in Portugal, UTEX 1259 of unknown origin and SAG 615-1 from England. This grouping of strains was fully statistically supported (ML/BI: 100/1.00) in the *rbc*L phylogenies (Fig. 1). However, the same data cluster (excluding two strains) did not receive any statistical support in the 18S rDNA phylogenetic trees (Fig. 2). The total number of variable sites within the aforementioned clade encompassing seven strains was 49 nucleotide positions in the *rbc*L alignment and 20 positions among the five sequences in the 18S rDNA alignment. The most similar *rbc*L sequence to strains Sven and Fox6 was the sequence of strain UTEX 1259, which differed by 11 and five nucleotides from the former strains, respectively. The 18S rDNA data comparisons revealed strain M 2853 to be the most similar to the two Arctic strains with a difference of four nucleotides.

Morphological/cytological observations. The vegetative cells of all strains investigated in this study usually had cylindrical shapes with broadly rounded ends (Fig. 3). The morphometric parameters (length and width) of the six studied strains (excluding the glacier strain Sven, which did not survive, but included the desert strain UTEX B 2684) are summarized in Figure S2 and Table S1 in the Supporting Information. The cells contained either a single chloroplast occupying most of the cell's volume or a chloroplast composed of two separating halves, which eventually detached from each other and became two separate chloroplasts (Fig. 4). Each of the chloroplast halves (or two individual chloroplasts) contained at least one round or subellipsoidal pyrenoid surrounded by starch plates (Fig. 3). Large empty holes within the chloroplast mark a pyrenoid position in the images obtained through confocal laser scanning microscopy (e.g., Fig. 4, A–C, E, G). All the studied strains exhibited a robust cell wall with a smooth surface. The nucleus was located in the cell's center. The algae reproduced by vegetative cell division, and no conjugation or zygospores were observed in the cultures.

In greater detail, the desert strain UTEX B 2684 had short broadly cylindrical or sometimes almost spherical cells (Fig. 3A). The chloroplast was plate-like with parietally undulating ridges, often composed of two or even four parts (Fig. 4A). Sometimes chloroplast thylakoids were whirled, giving them a "rosy" look. Two or even three small pyrenoids were often observed within a single part of the divided chloroplast. The two Arctic strains P2016 and P2018 also had rather short-sized to medium-sized cells, which were usually straight and often possessed a central thylakoid bridge (which we referred to as the "Charles bridge"—an allusion to the oldest bridge in Prague, dating back to 1357) joining two stellate chloroplasts (Figs. 3, B and C; 4, B and C). One end of the P2016 cells was slightly broader than the other, and the rare longer cells appeared slightly curved. The pyrenoids were rather large and round in shape. In contrast, strain CWM exhibited slimmer cells (Fig. S2B), which were often notably curved. These cells also possessed a central thylakoid extension connecting two plate-like chloroplasts with irregularly radiating ridges (Fig. 3D). CFN typically presented cylindrical straight cells, but globular cells were also occasionally present. The cells contained a plate-like chloroplast with ridges radiating in all directions and reaching the cell wall. The formation of the single delicate "Charles bridge" was also observed but was not very common (Fig. 3E). Instead, the two halves of the chloroplast were connected by several thylakoid extensions (both central and parietal). The freshwater strain Fox6 exhibited cylindrical straight cells with stellate chloroplasts (Fig. 3F). The central chloroplast cores contained a large subellipsoidal pyrenoid and exhibited additional radial lobes arranged vaguely (Fig. 3F). The glacier strain Sven showed a very similar chloroplast structure to the last strain (Fig. 3G). In contrast, strain Fox7 had a somewhat reticulate chloroplast composed of longitudinal delicate twisting ridges, and the pyrenoid, if visible, was subellipsoidal in shape. The chloroplast was rarely divided into two conspicuous parts (Figs. 3H and 4G).

As seen in the images of chlorophyll fluorescence (Fig. 4), the chloroplasts of the Arctic *Cylindrocystis* strains (especially notable in CWM; Fig. 4D) contained large numbers of nonfluorescent spherical objects distributed within the chloroplast bodies similar to grains in pomegranate. To elucidate their chemical nature, confocal Raman microscopy was used. The Raman spectra of the spectrally orthogonal (i.e., linearly independent) components that fully describe the spectral variability of the Raman maps of seven *Cylindrocystis* strains are shown in Figure 5. The spherical objects inside the chloroplasts were identified as polyphosphate (polyP) grains based on the characteristic Raman bands centered at 698 and 1165 · cm^{-1} (Fig. 5A; Moudříková et al. 2016, 2017a). The chemical map of polyP in CWM cells is a negative copy of the Raman image of chloroplasts visualized by their characteristic Raman spectrum consisting mainly of bands attributable to glycolipids and proteins (Fig. 6). Furthermore, the Raman chemical map of the chloroplasts resembles the fluorescence image of CWM chloroplasts (Fig. 4D). The same complementarity of the Raman maps of polyP and chloroplasts can be observed in other *Cylindrocystis* strains, except for UTEX B 2684 (Figs. S3–S8 in the Supporting Information).
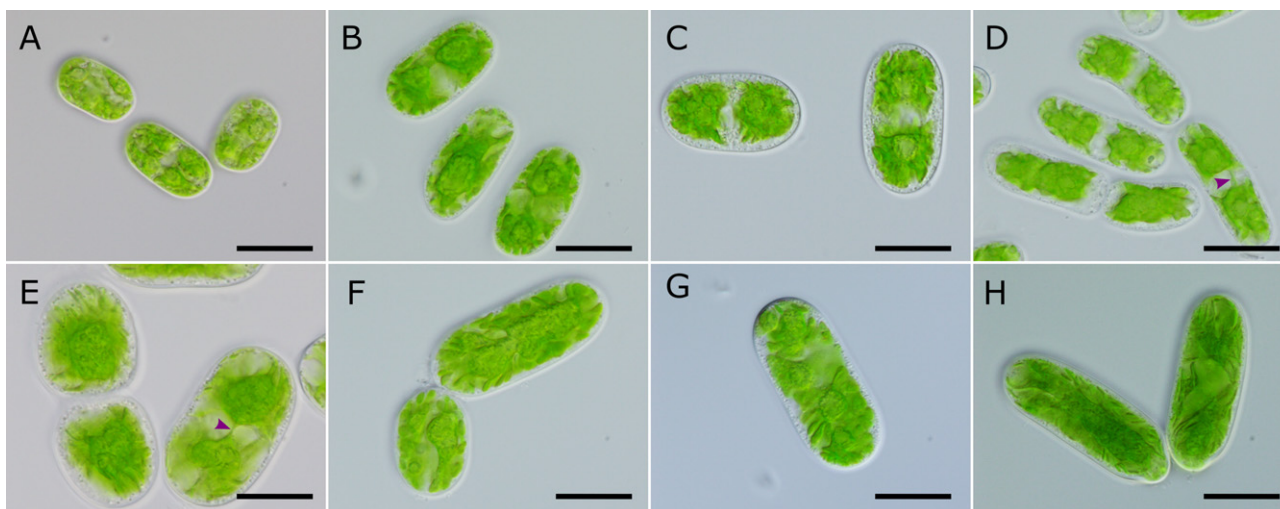
Fɪɢ. 3. Light microscopy photographs of the studied *Cylindrocystis* strains: (A) UTEX B 2684; (B) P2016; (C) P2018; (D) CWM; (E) CFN; (F) Fox6; (G) Sven; (H) Fox7. The arrowhead points to the "Charles bridge." Scale bars represent 20 μm. [Color figure can be viewed at wileyonlinelibrary.com]

According to characteristic Raman spectra, other intracellular structures can be visualized by their Raman chemical maps, for example, starch granules, lipid droplets containing triacylglycerols, cell walls containing cellulose, nuclei, or mitochondria (e.g., strain CWM, Fig. 6; for other strains, see Figs. S3–S8).

In addition to the Raman vibrational assessment of the cell content, we have also applied staining protocols (strain *Cylindrocystis* sp. CWM) using toluidine blue and various fluorescent dyes (Figs. 7 and 8). We aimed to address the nature of the small granules in the cytoplasm previously referred to Kopetzky-Rechtperg bodies (Fig. 7A) and to better co-localize the polyP grains. The application of toluidine blue allowed the visualization of numerous small cytoplasmic granules spread throughout the cell that were stained in blue (Fig. 7B). Their size and localization were compatible with the previously described structures (Fig. 7A; drawn as small black dots in the cell's periphery). The polyP grains, which otherwise appeared bluish in the bright field, were stained deep-purple color by toluidine blue (Fig. 7B), while DAPI stained them in yellow (Fig. 7C). Both staining methods showed that polyP resided within the plastids (Fig. 7, C and D).

Employing fluorescent dyes, we additionally stained nuclei (DAPI, SYTO13), mitochondria (DAPI, SYTO13, MitoTracker Red), lysosomes (Lyso-Tracker Green), lipid droplets (NR), and endomembrane systems such as the endoplasmic reticulum and Golgi apparatus (DiOC5(3); Figs. 7D and 8). We also combined fluorescent staining with cytochemical staining by toluidine blue (Fig. 8B). Our results showed that the application of the two types of stains together is not a good combination for co-localizing internal cell structures or compounds. For example, after toluidine blue treatment, mitochondria (SYTO 13 and MitoTracker Red) and lysosomes (LysoTracker Green) were not visualized at all (Fig. 8B).

DISCUSSION

Diversity. This study represents the first attempt to examine the diversity of Arctic *Cylindrocystis* using a culture-based approach. We found five different genotypes at the 18S rDNA level and seven different genotypes at the *rbc*L level among seven studied strains that morphologically resembled the genus *Cylindrocystis*. The origin of the new isolates was not monophyletic, confirming the complex phylogenetic structure of *Cylindrocystis*-like microalgae (Hall et al. 2008, Gontcharov and Melkonian 2010). The new isolates fell within the two previously identified clades: the "*Cylindrocystis*" clade and the *C. brebissonii* clade (Gontcharov and Melkonian 2010). The "*Cylindrocystis*" clade was composed of four main lineages, including the species *C. crassa* and *C. cushleckae* and numerous other strains without a species affiliation. The four Arctic isolates constituted two separate lineages within that clade (Figs. 1 and 2). The three freshwater isolates clustered within the clade of *C. brebissonii*. However, we refrained from assigning them to the single species of *C. brebissonii*, since this group of organisms likely harbors cryptic species. Overall, our phylogenetic analyses suggested that the seven new isolates could constitute at least five different taxa, which was corroborated by their different morphologies (see Discussion below). For a more detailed estimation of the genetic relationships among close relatives and especially species delineation, more variable molecular markers such as the ATP synthase beta subunit (*atpB*) or internal
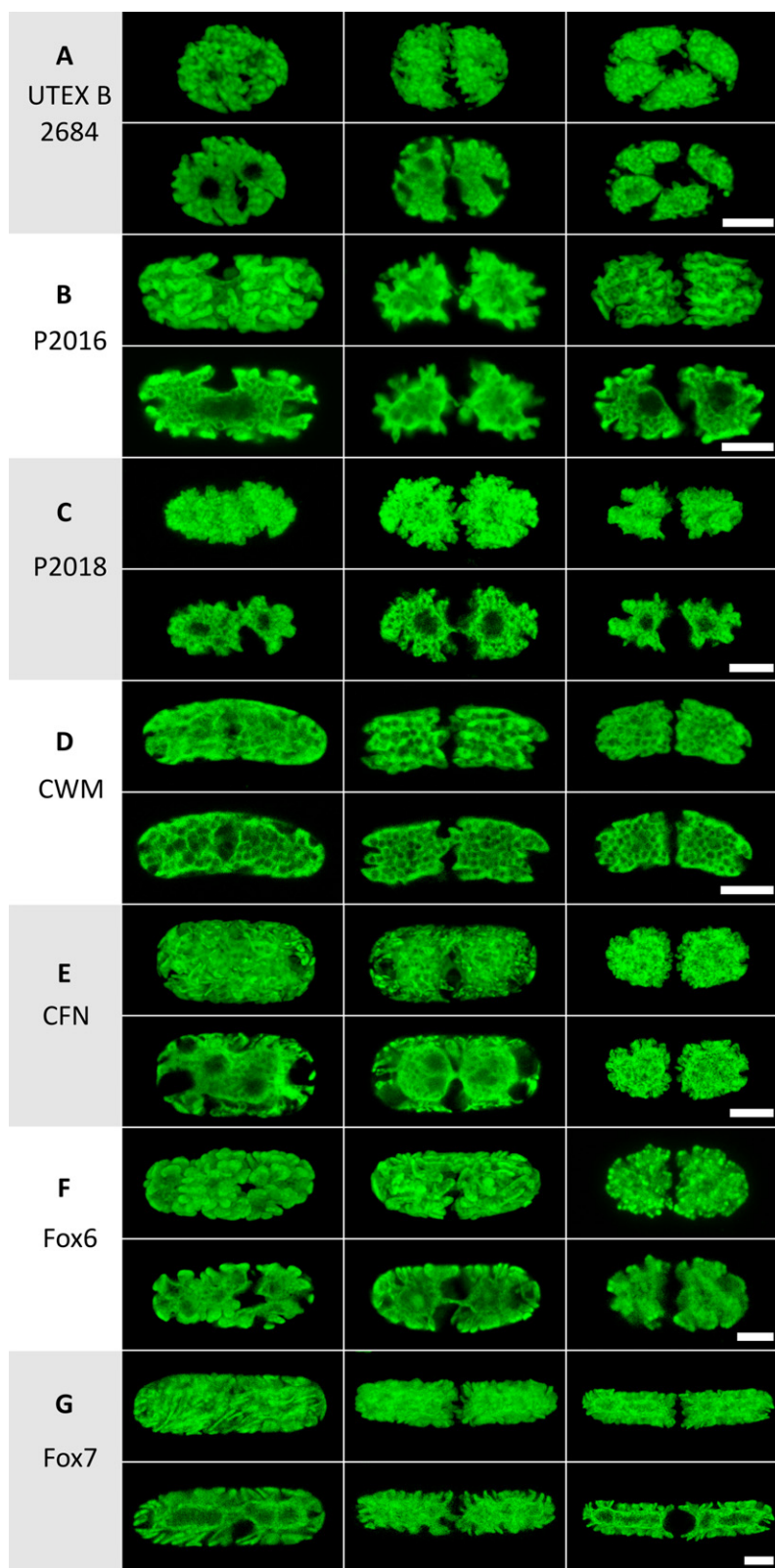
FIG. 4. Confocal laser scanning microscopy of the studied strains showing their chloroplast morphology and ontogeny (single plate, semi-divided, divided chloroplasts are shown in columns, respectively). The top row shows the maximum projection, and the bottom row shows the optical cross-section in the middle of the same cell. Scale bars represent 10 μm. [Color figure can be viewed at wileyonlinelibrary.com]
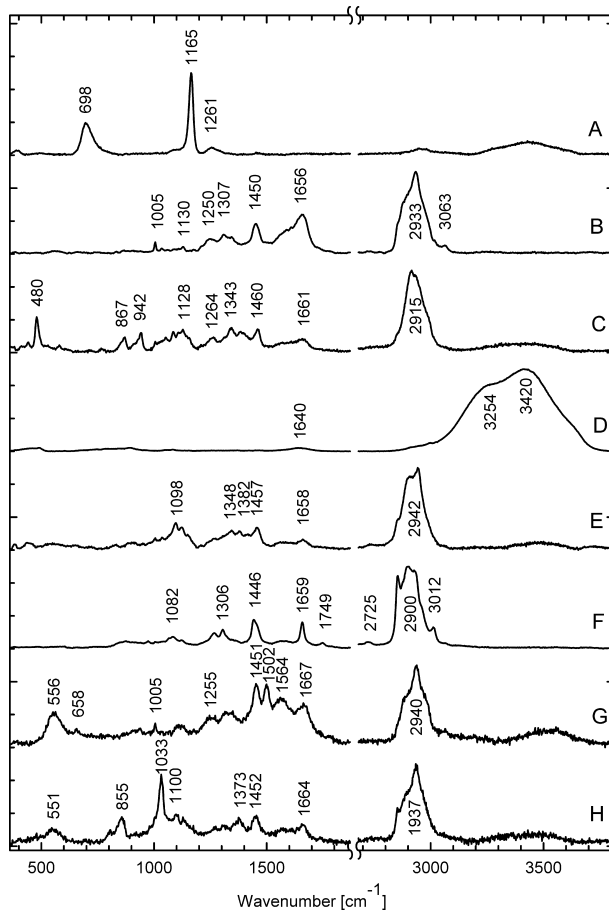
FIG. 5. Raman spectra of linearly independent spectral components fully describing the spectral variability of the Raman maps of the seven *Cylindrocystis* strains. Polyphosphate (A), chloroplasts (B), starch (C), water (D), cell wall containing cellulose (E), neutral lipids (F), nucleus (G), and mitochondria (H).

transcribed spacer 2 (ITS2) could be useful (e.g., Stancheva et al. 2013, Mikhailyuk et al. 2018).

In addition to providing the first insights into the genetic diversity of the Svalbard *Cylindrocystis*, this study revealed their morphological diversity by showing that different genotypes could be discerned by their morphological appearance. However, this might not necessarily be true for closely related or cryptic species. Using confocal laser scanning microscopy, this work also demonstrated that the chloroplast morphology of the studied strains was not stable (Fig. 4), which could potentially be an age-related trait. The strains of our defined soil clade (Figs. 1 and 2) generally had short and broadly cylindrical cells, except for the CWM strain (Fig. 3D). The strains of the freshwater/glacier clade were usually two or three times longer than they were wide (Fig. S2). The re-examined Mexican desert strain UTEX B 2684 not only had the shortest cells (Fig. S2A) but it was also the only strain that did not possess the central thylakoid extension. Additionally, the "Charles bridge" was easily visible

in the bright field observations of the Arctic strains (e.g., strains CWM and CFN; Fig. 3, D and E) or could be detected in a cross-section through the middle of the cells under confocal microscopy (e.g., strain Fox6; Fig. 4F). In addition, UTEX B 2684 occasionally contained a chloroplast composed of four equal parts (Fig. 4A), which was not observed in any other strain included in this study. Such morphological peculiarities of UTEX B 2684 support the phylogenetic results, showing its separation from the Arctic soil strains (Figs. 1 and 2).

Based on our observations, cell length and width could indeed be an important *Cylindrocystis* "species" characteristic, as considered in the past (Lütkemüller 1913, Prescott et al. 1972, Lenzenweger 2003). For example, strain CWM had the narrowest cells (Fig. S2B), which were also curved (Fig. 3D). Additionally, the CFN strain had the broadest cells (Fig. S2B). These characteristics distinguished them well from the other two closely related soil strains P2016 and P2018 (Figs. 1 and 2). The freshwater strain Fox7 had the longest cells (Fig. S2A). It also had the most delicately lobed chloroplasts (Fig. 4G). Additionally, its closest identified relative, strain Fox6, had chloroplasts with rather large blunt lobes, resembling buds (Fig. 4F). A similar type of lobe was present in the soil strain P2016 (Fig. 4B). For comparison, the 3D chloroplast morphology of Ecuadorian glacier *Cylindrocystis* (Nedbalová and Sklenář 2008) also resembles that of strain Fox6, although it presents deeper incisions.

In conclusion, our molecular and morphological data showed that the diversity of Arctic *Cylindrocystis*-like organisms is not restricted to the single species *C. brebissonii*. Our results point to a much larger number of deeply divergent phylogenetic lineages with *Cylindrocystis*-like morphology. As noted by Gontcharov and Melkonian (2010), the "*Cylindrocystis*" clade represents a new genus or even several new genera. Therefore, *Cylindrocystis* now awaits a thoughtful investigation and taxonomic reclassification, which could be a challenging task considering that conjugating green algae do not willingly reproduce sexually and form zygospores—a crucial morphological trait for recognizing taxa described in the past century—when grown in cultures. Finally, this study provides the first reference sequences of Arctic *Cylindrocystis*, which could be further used for studying eukaryotic communities in Arctic ice and soil using culture-independent approaches, such as next-generation sequencing (Lutz et al. 2018, Rippin et al. 2018). However, we predict even higher diversity of microalgae with a *Cylindrocystis*-like morphology in the High Arctic than was identified in this study.

Ecology. *Cylindrocystis brebissoni* represents one of the three main species of glacier algae. Strain Sven was isolated directly from an ice sample, whereas Fox6 and Fox7 were isolated from meltwater close to the glacier, suggesting a glacier origin of the last
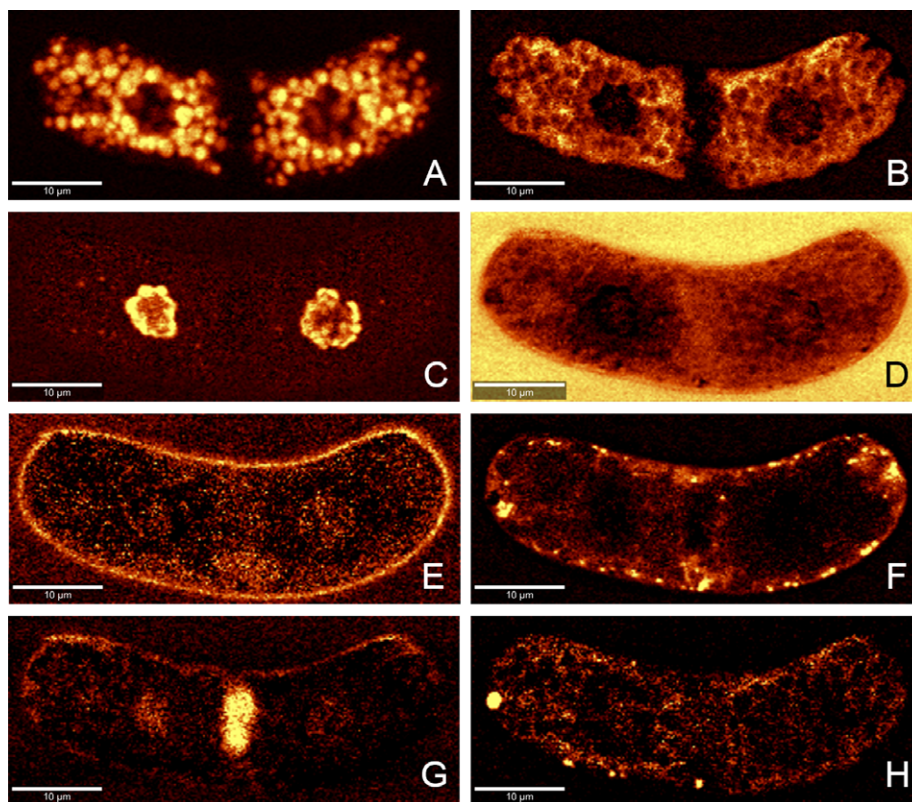
Fig. 6. Raman chemical maps of CWM cells highlighting the polyphosphate grains (A), chloroplasts (B), starch granules (C), water content (D), cell wall containing cellulose (E), lipid droplets (F), nucleus (G), and mitochondria (H). The corresponding Raman spectra are shown in Figure 5. [Color figure can be viewed at wileyonlinelibrary.com]
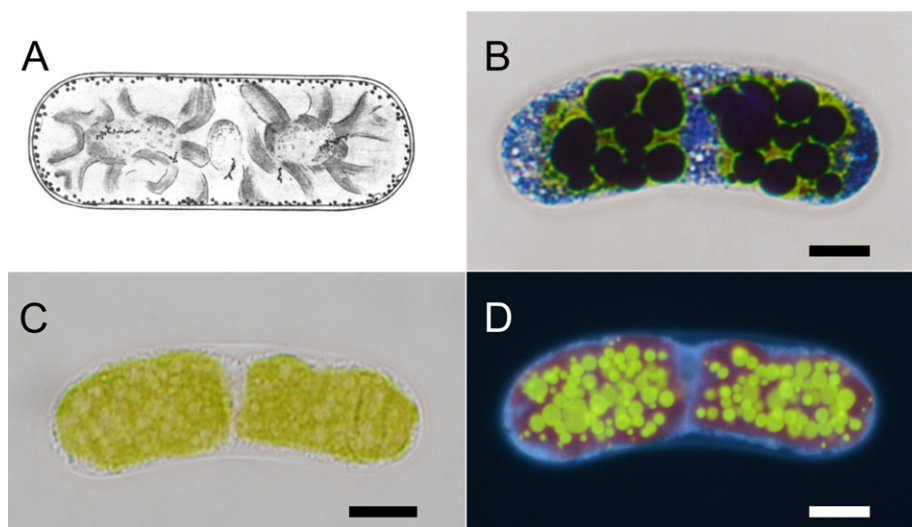

Fig. 7. Kopetzky-Rechtperg bodies depicted in a drawing, courtesy of Hirn (1953) (A); toluidine blue staining showing small structures (presumably Kopetzky-Rechtperg bodies) in the cytoplasm around the plastid, and dark polyphosphate grains inside of the plastids of *Cylindrocystis* sp. CWM (B); DAPI staining under bright-field microscopy (C) and under UV excitation (D) showing brightly shining polyP grains inside of the autofluorescent chloroplasts along with nucleus in-between the two chloroplasts and mitochondria around them. Scale bars represent 10 μm. [Color figure can be viewed at wileyonlinelibrary.com]

two strains as well. In Svalbard, *Cylindrocystis* has been previously reported from glacier surfaces (Stibal et al. 2006). Studies conducted in Greenland found *Cylindrocystis* to be either a dominant (Yallop et al. 2012) or insignificant (Lutz et al. 2018) constituent of the cryoflora based on direct cell
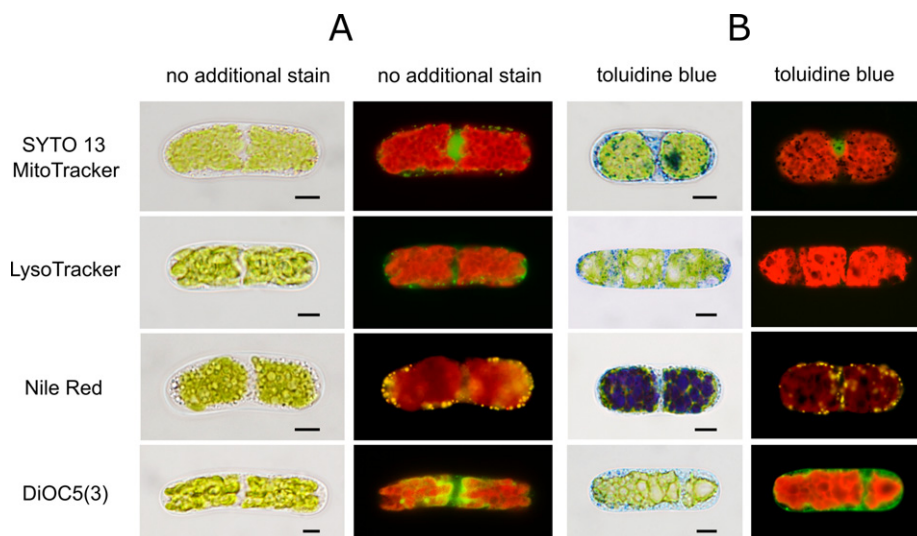
FIG. 8. Fluorescent staining (A) and effect of toluidine blue on fluorescent staining (B) in *Cylindrocystis* sp. CWM showing various organelles: chloroplasts (autofluorescence), nucleus (SYTO13), mitochondria (SYTO13 and MitoTracker), lysosomes (LysoTracker), lipid droplets (Nile red), endomembrane system (DiOC5(3)). Scale bars represent 10 μm. [Color figure can be viewed at wileyonlinelibrary.com]

counting and oligotyping, respectively. However, despite its known occurrence in cold habitats, *Cylindrocystis* is much less studied compared to its counterparts thriving on bare ice in both polar and alpine glacier ecosystems. For example, two other glacier zygnematophytes, *Mesotaenium berggrenii* and *Ancylonema nordenskiöldii,* have gained attention for their physiology and ultrastructure and the compounds that they produce (Remias et al. 2009, 2012a,b). In addition to ice, *Cylindrocystis* has been previously detected in biological soil crusts in Svalbard (Borchhardt et al. 2017). Arctic soil *Cylindrocystis* algae can easily be recognized in Arctic plain habitats because they form macroscopic gelatinous colonies, a well-known characteristic of desmids. In terrestrial habitats, such a gelatinous coating is useful for the retention of the limited water present and protection against rapid desiccation. In addition, mucilaginous gels could be important for protecting cells against high UV radiation, predation, and parasitism, as observed in Cyanobacteria (e.g., Ehling-Schulz et al. 1997). Since we found *Cylindrocystis* in the same locality (soil surface) after 2 years (2016 and 2018), local occurrence could be important in the success of this algal group in terrestrial environments, in contrast to the widespread minute coccoid trebouxiophytes (Hodač et al. 2016). Life in mucilaginous coatings could ensure a stable presence in otherwise unstable Arctic habitats. First, the cells would be less easily blown away. Second, colonies and populations could be established in microhabitats with a sufficient nutrient supply, for example, close to glaciers (Fox6 and Fox7) or wet meadows (CWM), where meltwater could carry nutrients. For example, *Cylindrocystis* has been previously found to form conspicuous jelly biomass

where a glacier stream floods the soil or shallow pools appear (Elster et al. 1997). Notably, the two isolates (P2016 and P2018) found at the same site were phylogenetically distinct from each other, which suggests that the colonies are likely composed of several similar species that we could have overlooked while isolating the strains and assuming that the colonies were composed of a single species. For example, mats of *Zygnema* or *Trentepohlia* (Chlorophyta), which are usually perceived as homogeneous, have been demonstrated to be composed of several different genotypes (Klimešová et al. 2018, Pichrtová et al. 2018).

Until now, zygnematophytes have generally been considered freshwater organisms. However, the identified Arctic soil strains were closely related to the two desert isolates (UTEX B 2684 and BCP-LG2-VF30), confirming the presence of algae with a true terrestrial nature within the Zygnematophyceae. As revealed from molecular data, the strains isolated from terrestrial and freshwater habitats were phylogenetically separated. The *Cylindrocystis brebissonii* clade includes true freshwater/glacier species, while the "*Cylindrocystis*" clade encompasses species from both freshwater and terrestrial habitats. However, to better elucidate the ecological speciation of this algal group, increased taxon sampling is necessary. Nevertheless, *Cylindrocystis* could be an excellent model organism for studying terrestrialization since freshwater, limnoterrestrial and terrestrial algae with a *Cylindrocystis*-like morphology have been described.

Distribution. Our new data confirmed that the genus *Cylindrocystis* (in its broad traditional understanding) is not highly habitat selective and that similar genotypes are widely distributed, occurring from cold polar regions to arid deserts. However,

the polar and desert isolates likely represent different species. Similar to the terrestrial genotypes, similar freshwater genotypes are also widely distributed (e.g., strains Fox7 and ACOI 55). There have thus far been no available sequences of Antarctic *Cylindrocystis* that could confirm the bipolar distribution of the identified soil and freshwater/glacier clades (Figs. 1 and 2). For example, Ryšánek et al. (2016) showed that both Arctic and Antarctic *Klebsormidium* strains fell within the same clade and comprised cosmopolitan species. Pichrtová et al. (2018) also demonstrated that polar *Zygnema* strains did not form any endemic lineages and were intermixed with strains originating from different geographic regions. The current knowledge allows us to conclude that the two discussed *Cylindrocystis* clades show at least a polar-temperate distribution and that the newly isolated Arctic strains likely originated from temperate communities. Furthermore, terrestrial genotypes might naturally be better adapted to desiccation, which is a crucial physiological trait for long-distance dispersal. On the other hand, local conditions might exert a strong influence on their diversification, resulting in more variable genotypes (e.g., soil clade; Figs. 1 and 2). Since water environments are more stable and more similar worldwide than terrestrial habitats, the same or similar freshwater genotypes are expected to be more widespread (e.g., freshwater/glacier clade; Figs. 1 and 2).

Polyphosphate. The most apparent characteristic observed in the Raman chemical maps of all *Cylindrocystis* strains (except for UTEX B 2684) was the presence of a large number of small spherical polyP grains (diameter 1–5 μm), presumably nested within the chloroplasts (Fig. 6A; Figs. S3A–S8A). Our results constitute the first direct proof of the presence of polyP in the cells of zygnematophytes.

Inorganic polyP is a linear polymer consisting of many tens or hundreds of orthophosphate residues (P_i) linked by high-energy phosphoanhydride bonds (Kornberg 1995, Kulaev et al. 2004). PolyP, known in biology from the beginning of the 20th century as volutin granules (Meyer 1904), is found in all kinds of living organisms, from bacteria, fungi, protozoa, and insects to vertebrates, including mammals, and naturally including microalgae (Kulaev et al. 2004). This still enigmatic polymer has been shown to play multiple roles in the basic metabolism of prokaryotic and eukaryotic cells, and its newly emerging functions in the microbial world have been reviewed repeatedly (Harold 1966, Albi and Serrano 2016, Jiménez et al. 2017, Xie and Jakob 2019). PolyP has been shown to serve as a reservoir of phosphorus (Harold 1966), divalent cations (Siderius et al. 1996), and energy (Kornberg et al. 1999) and to play a role in pH buffering (Pick et al. 1991), detoxification (Keasling et al. 1998), and as an antioxidative agent (Gray and Jakob 2015). PolyP was further found to be a potent protein-like chaperone that protects cells against stress-induced protein

aggregation (reviewed recently by Xie and Jakob 2019), thus potentially playing an important role in stress resistance (Gray and Jakob 2015).

Within intact cells, polyP can be visualized by histochemical staining (toluidine blue) or fluorescence labeling (DAPI), as we have demonstrated (Fig. 7, B–D). It can also be unambiguously identified and quantified in a label-free manner by Raman microscopy due to characteristic Raman bands at approximately 698 and 1165 · cm^{-1} (Fig. 5A; Moudříková et al. 2016, 2017a). The simplest explanation for the presence of polyP grains in Arctic *Cylindrocystis* may stem from their role as an effective long-term reservoir of phosphorus. The algal cells isolated from natural but nutrient-poor Arctic habitats were cultivated in relatively P_i-rich BBM medium ([P_i] ~ 1.72 mM). Consequently, the cells might accumulate a considerable amount of polyP in preparation for a phosphate shortage. Such excessive accumulation of phosphorus in the form of polyP is known as luxury uptake. Microalgae that mostly inhabit P_i-poor environments are naturally equipped to take up and store P_i whenever it becomes available (Cembella et al. 1982, 1984).

Another hypothesis explaining the presence of numerous polyP grains may be related to the function of polyP in stress resistance. The *Cylindrocystis* strains were cultivated at significantly higher temperatures compared to the temperatures from which they were isolated (20°C versus below 5°C). Therefore, it is reasonable to assume that the cells could have suffered from temperature stress. Furthermore, to keep the studied strains alive, they had to be cultivated in the small volumes with repeated reinoculation and were therefore frequently transferred to fresh medium rich in P_i. The response to this possible stress was connected with increased P_i uptake and biosynthesis of polyP, the reserves of which were stored as polyP granules in chloroplasts. This temperature stress could also explain why the desert strain UTEX 2684 did not accumulate polyP under the same cultivation conditions. However, it is clear that a more systematic study on this particular phenomenon is necessary to clarify a real reason for such excessive accumulation of polyP by Arctic *Cylindrocystis* strains.

Nevertheless, our results suggest that the exceptional ability of Arctic *Cylindrocystis* strains to accumulate polyP could be of interest for better understanding the biomolecular mechanism of luxury P_i uptake as well as the search for microalgae that are more suitable for biotechnological applications related to microalgae-based P removal, such as phosphorus uptake from nutrient-rich wastewaters and the potential application of polyP-enriched algal biomass to fertilize crop soils (Solovchenko et al. 2016).

Cytochemical and fluorescent staining. Blue-green bodies stained by toluidine blue have been previously shown to occur in the cytoplasm of genus

Cylindrocystis (Kopetzky-Rechtperg 1931, 1949) Their presence has also been demonstrated in other zygnematophyces, such as *Closterium, Cosmarium, Netrium, Zygnema, Spirogyra,* and *Mougeotia* (Höfler and Schindler 1951, Hirn 1953). The chemical composition of these mysterious bodies is attributed to pectins (due to showing similar staining to the cell wall), polyphosphate, or tannins (Kopetzky-Rechtperg 1949, Hirn 1953). However, our staining results did not support any of the aforementioned hypotheses, and Kopetzky-Rechtperg bodies (sometimes referred to simply as Kopetzky bodies) are still of an unknown nature and composition.

Toluidine blue has been used in cyto- and histochemical staining protocols for various purposes in different tissues of both plants and animals, such as achieving better contrast of the cell wall, cytoplasm, or mucilaginous sheaths. Its basic reaction highlights acidic structures, such as nucleic acids in the nucleus or mitochondria, PolyP granules, and lysosomes (Love et al. 1955, Brook 1992, Ohtomo et al. 2004, Zhang and Tung 2018). In neurons, Nissl bodies stained by toluidine blue have been shown to be rosettes of ribosomes attached to the rough endoplasmic reticulum that may be simultaneously stained by lipophilic fluorescent dyes such as DiOC (Chelvanayagam and Beazley 1997, Singhrao and Nair-Roberts 2010).

However, toluidine blue is not a very specific dye. As we have shown, it can also prevent the co-localization of various cell structures (Fig. 8B). The disappearance of the fluorescence signal in the case of mitochondrial and lysosomal staining may be explained as follows: (i) toluidine blue may stain different kinds of organelles at the same time, such as mitochondria as well as lysosomes or even Nissl bodies; and (ii) toluidine blue used as a counterstain is not fluorescent and absorbs light, it is applied at a higher concentration of several orders of magnitude than more sensitive fluorescent dyes and can therefore overlap with these dyes and obstruct their fluorescence. The phenomenon of fluorescence quenching by toluidine blue has been reported by Chelvanayagam and Beazley (1997). Nissl bodies can be expected to appear as dark spots of toluidine-blue-stained bodies directly connected to the endomembrane system stained by DiOC5(3), which was probably beyond the resolution available in this study (Fig. 8B).

In conclusion, staining with fluorescent dyes is usually more specific and sensitive than staining with toluidine blue. Toluidine blue stains diverse structures, and the identification of these structures might therefore be challenging. The application of multistaining and other methods (e.g., Raman microscopy) should be carried out for the better recognition of various cell bodies and compounds.

Albi, T. & Serrano, A. 2016. Inorganic polyphosphate in the microbial world. Emerging roles for a multifaceted biopolymer. *World J. Microbiol. Biotechnol.* 32:1–12.

Altschul, S. F., Madden, T. L., Schäffer, A. A., Zhang, J., Zhang, Z., Miller, W. & Lipman, D. J. 1997. Gapped BLAST and PSI-BLAST: a new generation of protein database search programs. *Nucleic Acids Res.* 25:3389–402.

Barcytè, D., Hodač, L. & Nedbalová, L. 2017. *Lunachloris lukesovae* gen. et sp. nov. (Trebouxiophyceae, Chlorophyta), a novel coccoid green alga isolated from soil in South Bohemia. *Czech Republic. Eur. J. Phycol.* 52:281–91.

Bischoff, H. W. & Bold, H. C. 1963. Phycological studies IV. Some soil algae from Enchanted Rock and relatedalgal species. *Univ. Texas Publ.* 6318:1–95.

Borchhardt, N., Baum, C., Mikhailyuk, T. & Karsten, U. 2017. Biological soil crusts of Arctic Svalbard – water availability as potential controlling factor for microbial biodiversity. *Front. Microbiol.* 8:1485.

Brook, A. J. 1992. *Spirotaenia alpina* (Zygnemaphyceae: Mesotaeniaceae), a saccoderm desmid new to the British Isles: Revised description and observations on cell division. *Br. Phycol. J.* 27:29–38.

Cembella, A. D., Antia, N. J. & Harrison, P. J. 1982. The utilization of inorganic and organic phosphorus-compounds as nutrients by eukaryotic microalgae: a multidisciplinary perspective: Part 1. *Crit. Rev. Microbiol.* 10:317–91.

Cembella, A. D., Antia, N. J. & Harrison, P. J. 1984. The utilization of inorganic and organic phosphorus compounds as nutrients by eukaryotic microalgae: a multidisciplinary perspective. Part 2. *Crit. Rev. Microbiol.* 11:13–81.

Chelvanayagam, D. K. & Beazley, L. D. 1997. Toluidine blue-O is a Nissl bright-field counterstain for lipophilic fluorescent tracers Di-ASP, DiI and DiO. *J. Neurosci. Methods* 72:49–55.

Coesel, P. F. M. & Meesters, K. J. 2007. *Desmids of the Lowlands.* KNNV Publishing, Zeist, The Netherlands, 351 pp.

Ehling-Schulz, M., Bilger, W. & Scherer, S. 1997. UV-B-induced synthesis of photoprotective pigments and extracellular polysaccharides in the terrestrial cyanobacterium *Nostoc commune. J. Bacteriol.* 179:1940–5.

Elster, J., Svoboda, J., Komárek, J. & Marvan, P. 1997. Algal and cyanoprocaryote communities in a glacial stream, Sverdrup Pass, 79°N, Central Ellesmere Island, Canada. *Algol. Stud.* 85:57–93.

Flechtner, V. R., Johansen, J. R. & Clark, W. H. 1998. Algal composition of microbiotic crusts from the Central Desert of Baja California, Mexico. *Great Basin Nat.* 58:295–311.

Førland, E. J., Benestad, R., Hanssen-Bauer, I., Haugen, J. E. & Skaugen, T. E. 2011. Temperature and precipitation development at Svalbard 1900–2100. *Adv. Meteorol.* https://doi.org/10.1155/2011/893790.

Gontcharov, A. A. & Melkonian, M. 2010. Molecular phylogeny and revision of the genus *Netrium* (Zygnematophyceae, Streptophyta): *Nucleotaenium* gen. nov. *J. Phycol.* 46:346–62.

Gray, M. J. & Jakob, U. 2015. Oxidative stress protection by polyphosphate – new roles for an old player. *Curr. Opin. Microbiol.* 24:1–6.

Hall, T. A. 1999. BioEdit: a user-friendly biological sequence alignment editor and analysis program for Windows 95/98/NT. *Nucleic Acids Symp. Ser.* 41:95–8.

Hall, J. D., Karol, K. G., McCourt, R. M. & Delwiche, C. F. 2008. Phylogeny of the conjugating green algae based on chloroplast and mitochondrial nucleotide sequence data. *J. Phycol.* 44: 467–77.

Hall, J. D. & McCourt, R. M. 2017. Zygnematophyta. *In* Archibald, J. M., Simpson, A. G. B. & Slamovits, C. H. [Eds.] *Handbook of the Protists.* Springer International Publishing AG, Cham, Switzerland, pp. 135–63.

Hamby, R. K., Sim, L., Issel, L. & Zimmer, E. 1988. Direct RNA sequencing: Optimization of extraction and sequencing techniques for work with higher plants. *Plant Mol. Biol. Rep.* 6:175–92.

Harold, F. M. 1966. Inorganic polyphosphates in biology: structure, metabolism, and function. *Bacteriol. Rev.* 30:772–94.

Hepperle, D. 2004. SeqAssem©. A sequence analysis tool, contig assembler and trace data visualization tool for molecular sequences. Win32-Version. Available at http://www.sequentix.de (last accessed 20 May 2019).

Herburger, K., Lewis, L. A. & Holzinger, A. 2015. Photosynthetic efficiency, desiccation tolerance and ultrastructure in two phylogenetically distinct strains of alpine *Zygnema* sp. (Zygnematophyceae, Streptophyta): role of pre-akinete formation. *Protoplasma* 252:571–89.

Herburger, K., Remias, D. & Holzinger, A. 2016. The green alga *Zygogonium ericetorum* (Zygnematophyceae, Charophyta) shows high iron and aluminium tolerance: protection mechanisms and photosynthetic performance. *FEMS Microbiol. Ecol.* 92:fiw103.

Hirn, I. 1953. Vitalfärbungsstudien an Desmidiaceen. *Flora* 140:453–73.

Hodač, L., Hallmann, C., Spitzer, K., Elster, J., Faßhauer, F., Brinkmann, N., Lepka, D., Diwan, V. & Friedl, T. 2016. Widespread green algae *Chlorella* and *Stichococcus* exhibit polar-temperate and tropical-temperate biogeography. *FEMS Microbiol. Ecol.* 92:fiw122.

Höfler, K. & Schindler, H. 1951. Vitalfärbung von Algenzellen mit Toluidinblaulösungen gestufter Wasserstoffionenkonzentration. *Protoplasma* 40:137–51.

Holzinger, A., Albert, A., Aigner, S., Uhl, J., Schmitt-Kopplin, P., Trumhová, K. & Pichrtová, M. 2018. Arctic, Antarctic, and temperate green algae *Zygnema* spp. under UV-B stress: vegetative cells perform better than pre-akinetes. *Protoplasma* 255:1239–52.

Jiménez, J., Bru, S., Ribeiro, M. P. C. & Clotet, J. 2017. Polyphosphate: popping up from oblivion. *Curr. Genet.* 63:15–8.

Katoh, K., Rozewicki, J. & Yamada, K. D. 2019. MAFFT online service: multiple sequence alignment, interactive sequence choice and visualization. *Brief. Bioinf* 20:1160–66.

Keasling, J. D., van Dien, S. J. & Pramanik, J. 1998. Engineering polyphosphate metabolism in *Escherichia coli*: Implications for bioremediation of inorganic contaminants. *Biotechnol. Bioeng.* 58:231–9.

Klimešová, M., Rindi, F. & Škaloud, P. 2018. DNA cloning demonstrates high genetic heterogenity in populations of the subaerial green alga *Trentepohlia* (Trentepohliales, Chlorophyta). *J. Phycol.* 55:224–35.

Kol, E. 1942. The snow and ice algae of Alaska. *Smithson Misc. Collect.* 101:1–36.

Kopetzky-Rechtperg, O. 1931. Die "Zersetzungskorperchen" der Desmidiaceenzelle. *Arch. Protistenk.* 75:270–83.

Kopetzky-Rechtperg, O. 1949. Zellbau und Zelleinschlüsse bei Conjugaten, besonders Desmidiales. *Protoplasma* 39:106–12.

Kornberg, A. 1995. Inorganic polyphosphate: toward making a forgotten polymer unforgettable. *J. Bacteriol.* 177:491–6.

Kornberg, A., Rao, N. N. & Ault-Riché, D. 1999. Inorganic polyphosphate: a molecule of many functions. *Annu. Rev. Biochem.* 68:89–125.

Kulaev, I. S., Vagabov, V. M. & Kulakovskaya, T. V. 2004. *The Biochemistry of Inorganic Polyphosphates.* John Wiley & Sons, Chichester, UK, 294 pp.

Lanfear, R., Calcott, B., Ho, S. Y. & Guindon, S. 2012. PartitionFinder: combined selection of partitioning schemes and substitution models for phylogenetic analyses. *Mol. Biol. Evol.* 29:1695–701.

Lenzenweger, R. 2003. *Desmidiaceenflora von Österreich.* Teil 4. J Cramer, Stuttgart, Germany.

Lewis, L. A. & Lewis, P. O. 2005. Unearthining the molecular phylodiversity of desert soil green algae (Chlorophyta). *Syst. Biol.* 54:936–47.

Love, R., Orsi, E. V. & Berry, E. E. 1955. A simple stain for mitochondria. *Proc. Soc. Exp. Biol. Med.* 88:666–9.

Lütkemüller, J. 1913. Die Gattung *Cylindrocystis* Menegh. *Verh. KK. Zool.-Bot. Ges. Wien* 63:212–30.

Lutz, S., McCutcheon, J., McQuaid, J. B. & Benning, L. G. 2018. The diversity of ice algal communities on the Greenland Ice Sheet as revealed by oligotyping. *Microb. Genom.* 4:e000159.

McCourt, R. M., Karol, K. G., Bell, J., Helm-Bychowski, K. M., Grajewska, A., Wojciechowski, M. F. & Hoshaw, R. W. 2000. Phylogeny of the conjugating green algae (Zygnematophyceae) based on *rbc*L sequences. *J. Phycol.* 36:747–58.

Meyer, A. 1904. Orientierende Untersuchungen über Verbreitung, Morphologie und Chemie des Volutins. *Bot. Zeitung* 62:113–52.

Mikhailyuk, T., Lukešová, A., Glaser, K., Holzinger, A., Obweger, S., Nyporko, S., Friedl, T. & Karsten, U. 2018. New taxa of streptophyte algae (Streptophyta) from terrestrial habitats revealed using an integrative approach. *Protist* 169:406–31.

Miller, M. A., Pfeiffer, W. & Schwartz, T. 2010. Creating the CIPRES Science Gateway for inference of large phylogenetic trees. *In Proceedings of the Gateway Computing Environments Workshop (GCE)*, New Orleans, LA, pp. 1–8.

Moudříková, Š., Mojzeš, P., Zachleder, V., Pfaff, C., Behrendt, D. & Nedbal, L. 2016. Raman and fluorescence microscopy sensing energy-transducing and energy-storing structures in microalgae. *Algal Res.* 16:224–32.

Moudříková, Š., Nedbal, L., Solovchenko, A. & Mojzeš, P. 2017b. Raman microscopy shows that nitrogen-rich cellular inclusions in microalgae are microcrystalline guanine. *Algal Res.* 23:216–22.

Moudříková, Š., Sadowsky, A., Metzger, S., Nedbal, L., Mettler-Altmann, T. & Mojzeš, P. 2017a. Quantification of polyphosphate in microalgae by Raman microscopy and by a reference enzymatic assay. *Anal. Chem.* 89:12006–13.

Nedbalová, L. & Sklenář, P. 2008. New records of snow algae from the Andes of Ecuador. *Arnaldoa* 15:17–20.

Ohtomo, R., Sekiguchi, Y., Mimura, T., Saito, M. & Ezawa, T. 2004. Quantification of polyphosphate: different sensitivities to short-chain polyphosphate using enzymatic and colorimetric methods as revealed by ion chromatography. *Anal. Biochem.* 328:139–46.

Pichrtová, M., Hájek, T. & Elster, J. 2014b. Osmotic stress and recovery in field populations of *Zygnema* sp. (Zygnematophyceae, Streptophyta) on Svalbard (High Arctic) subjected to natural desiccation. *FEMS Microbiol. Ecol.* 89:270–80.

Pichrtová, M., Hájek, T. & Elster, J. 2016. Annual development of mat-forming conjugating green algae *Zygnema* spp. in hydroterrestrial habitats in the Arctic. *Polar Biol.* 39:1653–62.

Pichrtová, M., Holzinger, A., Kulichová, J., Ryšánek, D., Šoljaková, T., Trumhová, K. & Němcová, Y. 2018. Molecular and morphological diversity of *Zygnema* and *Zygnemopsis* (Zygnematophyceae, Streptophyta) from Svalbard (High Arctic). *Eur. J. Phycol.* 53:492–508.

Pichrtová, M., Kulichová, J. & Holzinger, A. 2014a. Nitrogen limitation and slow drying induce desiccation tolerance in conjugating green algae (Zygnematophyceae, Streptophyta) from polar habitats. *PLoS ONE* 9:e113137.

Pick, U., Zeelon, O. & Weiss, M. 1991. Amine accumulation in acidic vacuoles protects the halotolerant alga *Dunaliella salina* against alkaline stress. *Plant Physiol.* 97:1226–33.

Posada, D. & Crandall, K. A. 1998. MODELTEST: testing the model of DNA substitution. *Bioinformatics* 14:817–8.

Prescott, G. W., Croasdale, H. T. & Vinyard, W. C. 1972. *North American Flora. Series II, Part 6, Desmidiales. Part I. Saccodermae, Mesotaeniaceae.* New York Botanical Garden, Bronx, NY.

Rambaut, A. 2007. Figtree, a graphical viewer of phylogenetic trees. Available at http://tree.bio.ed.ac.uk/software/figtree (last accessed 20 May 2019).

Rambaut, A., Drummond, A. J., Xie, D., Baele, G. & Suchard, M. A. 2018. Posterior summarisation in Bayesian phylogenetics using Tracer 1.7. *Syst. Biol.* 67:901–4.

Remias, D., Holzinger, A., Aigner, S. & Lütz, C. 2012a. Ecophysiology and ultrastructure of *Ancylonema nordenskiöldii* (Zygnematales, Streptophyta), causing brown ice on glaciers in Svalbard (high arctic). *Polar Biol.* 35:899–908.

Remias, D., Holzinger, A. & Lütz, C. 2009. Physiology, ultrastructure and habitat of the ice alga *Mesotaenium berggrenii* (Zygnematophyceae, Chlorophyta) from glaciers in the European Alps. *Phycologia* 48:302–12.

Remias, D., Schwaiger, S., Aigner, S., Leya, T., Stuppner, H. & Lütz, C. 2012b. Characterization of an UV- and VIS-absorbing, purpurogallin-derived secondary pigment new to algae and highly abundant in *Mesotaenium berggrenii* (Zygnematophyceae, Chlorophyta), an extremophyte living on glaciers. *FEMS Microbiol. Ecol.* 79:638–48.

Rippin, M., Becker, B. & Holzinger, A. 2017. Enhanced desiccation tolerance in mature cultures of the streptophytic green alga *Zygnema circumcarinatum* revealed by transcriptomics. *Plant Cell Physiol.* 58:2067–84.

Rippin, M., Lange, S., Sausen, N. & Becker, B. 2018. Biodiversity of biological soil crusts from the Polar Regions revealed by metabarcoding. *FEMS Microbiol. Ecol.* 94:fiy036.

Ronquist, F., Teslenko, M., van der Mark, P., Ayres, D. L., Darling, A., Höhna, S., Larget, B., Liu, L., Suchard, M. A. & Huelsenbeck, J. P. 2012. MrBayes 3.2: efficient Bayesian phylogenetic inference and model choice across a large model space. *Syst. Biol.* 61:539–42.

Ruhfel, B. R., Gitzendanner, M. A., Soltis, P. S., Soltis, D. E. & Butleigh, J. G. 2014. From algae to angiosperms-inferring the phylogeny of green plants (Viridiplantae) from 360 plastid genomes. *BMC Evol. Biol.* 14:23.

Rýšánek, D., Elster, J., Kováčik, L. & Škaloud, P. 2016. Diversity and dispersal capacities of a terrestrial genus *Klebsormidium* (Streptophyta) in polar regions. *FEMS Microbiol. Ecol.* 92: fnw039.

Siderius, M., van den Musgrave, A., Ende, H., Koerten, H., Cambier, P. & van der Meer, P. 1996. *Chlamydomonas eugametos* (Chlorophyta) stores phosphate in polyphosphate bodies together with calcium. *J. Phycol.* 32:402–9.

Singhrao, S. K. & Nair-Roberts, R. G. 2010. In situ hybridization and immunofluorescence on resin-embedded tissue to identify the components of Nissl substance. *Microsc. Res. Tech.* 73:555–9.

Škaloud, P. 2009. Species composition and diversity of aero-terrestrial algae and cyanobacteria of the Boreč Hill ventaroles. *Fottea* 9:65–80.

Solovchenko, A., Verschoor, A. M., Jablonowski, N. D. & Nedbal, L. 2016. Phosphorus from wastewater to crops: An alternative path involving microalgae. *Biotechnol. Adv.* 34:550–64.

Stamatakis, A. 2014. RaxML version 8: a tool for phylogenetic analysis and post-analysis of large phylogenies. *Bioinformatics* 30:1312–3.

Stancheva, R., Hall, J. D., McCourt, R. M. & Sheath, R. G. 2013. Identity and phylogenetic placement of *Spirogyra* species (Zygnematophyceae, Charophyta) from California streams and elsewhere. *J. Phycol.* 49:588–607.

Štěpánková, J., Hašler, P., Hladká, M. & Poulíčková, A. 2012. Diversity and ecology of desmids of peat bogs in the Jeseníky Mts: spatial distribution, remarkable finds. *Fottea* 12:111–26.

Stibal, M., Šabacká, M. & Kaštovská, K. 2006. Microbial communities on glacier surfaces in Svalbard: impact of physical and chemical properties on abundance and structure of cyanobacteria and algae. *Microb. Ecol.* 52:644–54.

Swofford, D. L. 2003. *PAUP*: Phylogenetic Analysis Using Parsimony (*and Other Methods), Version 4.* Sinauer Associates, Sunderland, MA.

Takeuchi, N. & Kohshima, S. 2004. A snow algal community on Tyndall Glacier in the Southern Patagonia Icefield, Chile. *Arct. Antarct. Alp. Res.* 36:92–9.

de Vries, J., Curtis, B. A., Gould, S. B. & Archibald, J. M. 2018. Embryophyte stress signaling evolved in the algal progenitors of land plants. *Proc. Natl. Acad. Sci. USA* E3471–80.

de Vries, J., Stanton, A., Archibald, J. M. & Gould, S. B. 2016. Streptophyte terrestrialization in light of plastid evolution. *Trends Plant Sci.* 21:467–76.

Walczowski, W. & Piechura, J. 2011. Influence of the west Spitsbergen current on the local climate. *Int. J. Climatol.* 31:1088–93.

Wodniok, S., Brinkmann, H., Glöckner, G., Heidel, A. J., Philippe, H., Melkonian, M. & Becker, B. 2011. Origin of land plants: Do conjugating green algae hold the key? *BMC Evol. Biol.* 11:104.

Xie, L. & Jakob, U. 2019. Inorganic polyphosphate, a multifunctional polyanionic protein scaffold. *J. Biol. Chem.* 294:2180–90.

Yallop, M. L., Anesio, A. M., Perkins, R. G., Cook, J., Telling, J., Fagan, D., MacFarlane, J. et al. 2012. Photophysiology and albedo-changing potential of the ice algal community on the surface of the Greenland ice sheet. *ISME J.* 6:2302–13.

Zhang, W. & Tung, C. H. 2018. Real-time visualisation of lysosome destruction using a photosensitive toluidine blue nanogel. *Chemistry* 24:2089–93.

Zwickl, D. J. 2006. Genetic algorithm approaches for the phylogenetic analysis of large biological sequence data sets under the maximum likelihood criterion. Ph.D. dissertation, The University of Texas at Austin, 125 pp.

Supporting Information

Additional Supporting Information may be found in the online version of this article at the publisher's web site:

Figure S1. Map showing the Svalbard archipelago (A) and the sampling sites in Petuniabukta (B) and Adventdalen (C).

Figure S2. Cell lengths and widths of the investigated strains (n = 100). The line within the box indicates the median, and the whiskers indicate the lowest and the highest measurements.

Figure S3. Raman chemical maps of CFN cells highlighting the polyphosphate grains (A), chloroplasts (B), starch granules (C), water content (D), cell wall containing cellulose (E), lipid droplets (F), nucleus (G), and mitochondria (H). The corresponding Raman spectra are shown in Figure 5.

Figure S4. Raman chemical maps of Fox6 cells highlighting the polyphosphate grains (A), chloroplasts (B), starch granules (C), water content (D), cell wall containing cellulose (E), lipid droplets (F), nucleus (G), and mitochondria (H). The corresponding Raman spectra are shown in Figure 5.

Figure S5. Raman chemical maps of Fox7 cells highlighting the polyphosphate grains (A), chloroplasts (B), starch granules (C), water content (D), cell wall containing cellulose (E), lipid droplets (F), nucleus (G), and mitochondria (H). The corresponding Raman spectra are shown in Figure 5.

Figure S6. Raman chemical maps of P2016 cells highlighting the polyphosphate grains (A), chloroplasts (B), starch granules (C), water content (D), cell wall containing cellulose (E), lipid droplets (F), nucleus (G), and mitochondria (H). The corresponding Raman spectra are shown in Figure 5.

Figure S7. Raman chemical maps of P2018 cells highlighting the polyphosphate grains (A), chloroplasts (B), starch granules (C), water content (D), cell wall containing cellulose (E), lipid droplets (F), nucleus (G), and mitochondria (H). The corresponding Raman spectra are shown in Figure 5.

Figure S8. Raman chemical maps of UTEX B 2684 cells highlighting the polyphosphate grains (A), chloroplasts (B), starch granules (C), water content (D), cell wall containing cellulose (E), lipid droplets (F), nucleus (G), and mitochondria (H). The corresponding Raman spectra are shown in Figure 5.
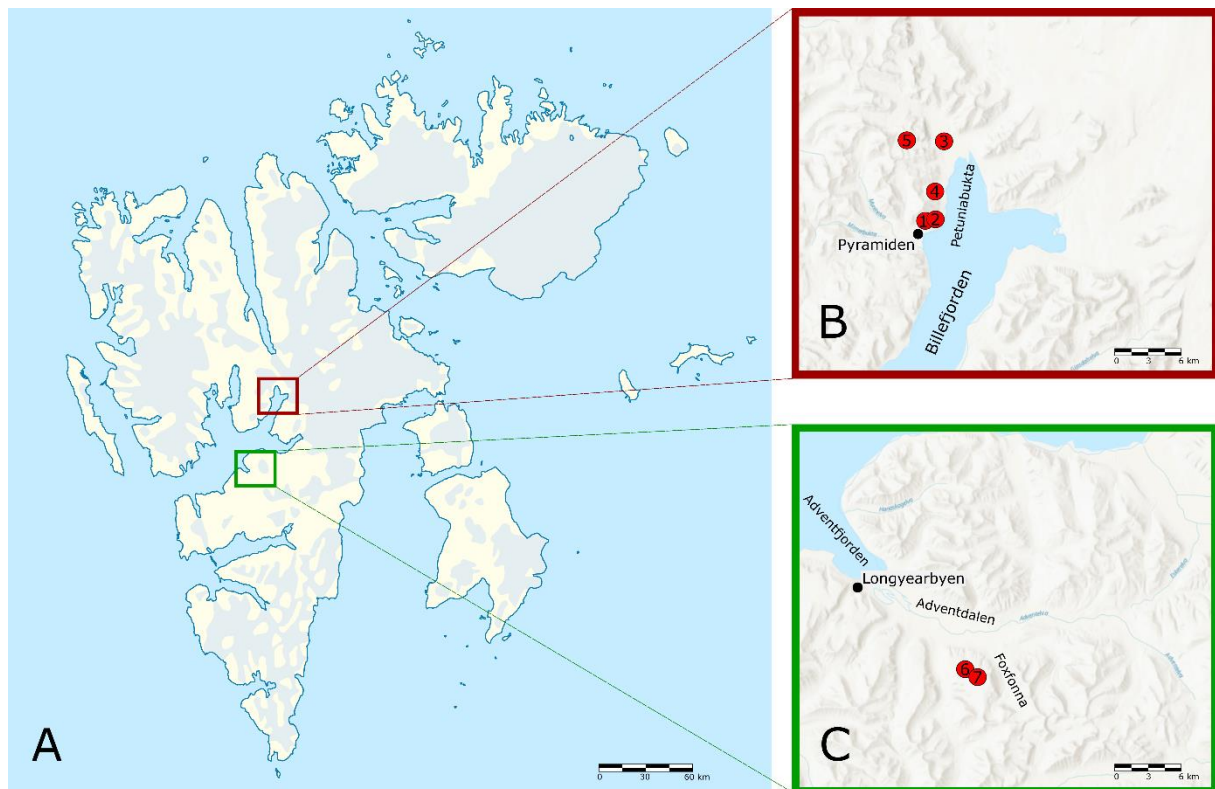
Table S1. Summary of the morphological characteristics of the studied strains.

Supplementary information

Figure S1. Map showing the Svalbard archipelago (A) and the sampling sites in Petuniabukta (B) and Adventdalen (C).

Figure S2. Cell lengths and widths of the investigated strains (n = 100). The line within the box indicates the median, and the whiskers indicate the lowest and the highest measurements.

Figure S3. Raman chemical maps of CFN cells highlighting the polyphosphate grains (A), chloroplasts (B), starch granules (C), water content (D), cell wall containing cellulose (E), lipid droplets (F), nucleus (G), and mitochondria (H). The corresponding Raman spectra are shown in Figure 5.
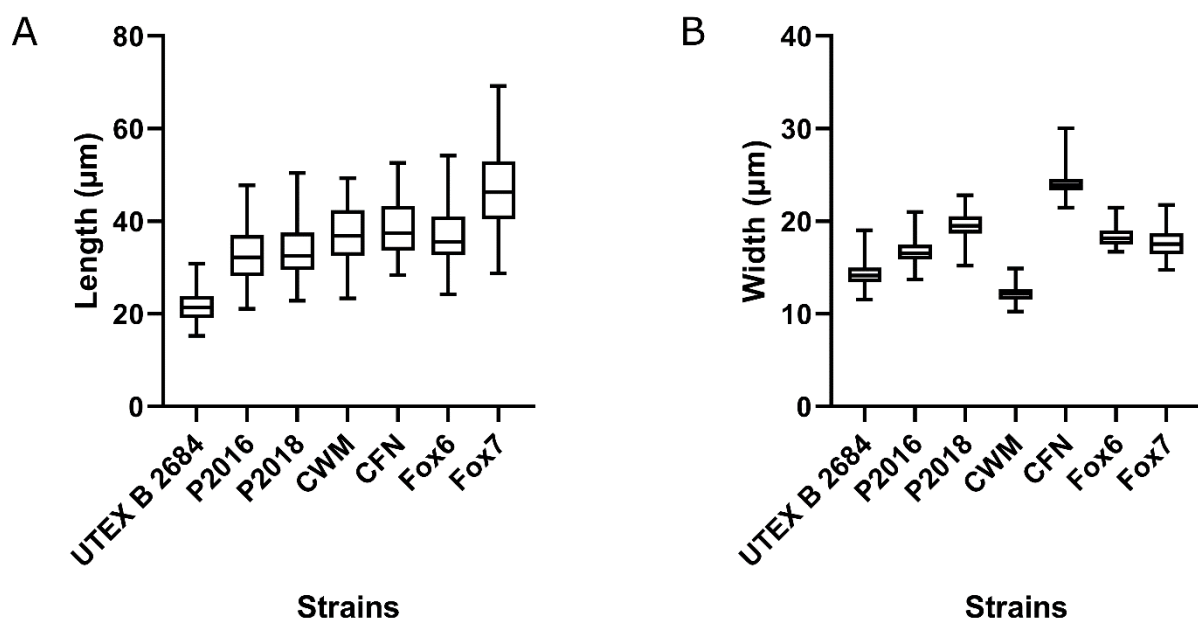

Figure S4. Raman chemical maps of Fox6 cells highlighting the polyphosphate grains (A), chloroplasts (B), starch granules (C), water content (D), cell wall containing cellulose (E), lipid droplets (F), nucleus (G), and mitochondria (H). The corresponding Raman spectra are shown in Figure 5.

Figure S5. Raman chemical maps of Fox7 cells highlighting the polyphosphate grains (A), chloroplasts (B), starch granules (C), water content (D), cell wall containing cellulose (E), lipid droplets (F), nucleus (G), and mitochondria (H). The corresponding Raman spectra are shown in Figure 5.

Figure S6. Raman chemical maps of P2016 cells highlighting the polyphosphate grains (A), chloroplasts (B), starch granules (C), water content (D), cell wall containing cellulose (E), lipid droplets (F), nucleus (G), and mitochondria (H). The corresponding Raman spectra are shown in Figure 5.
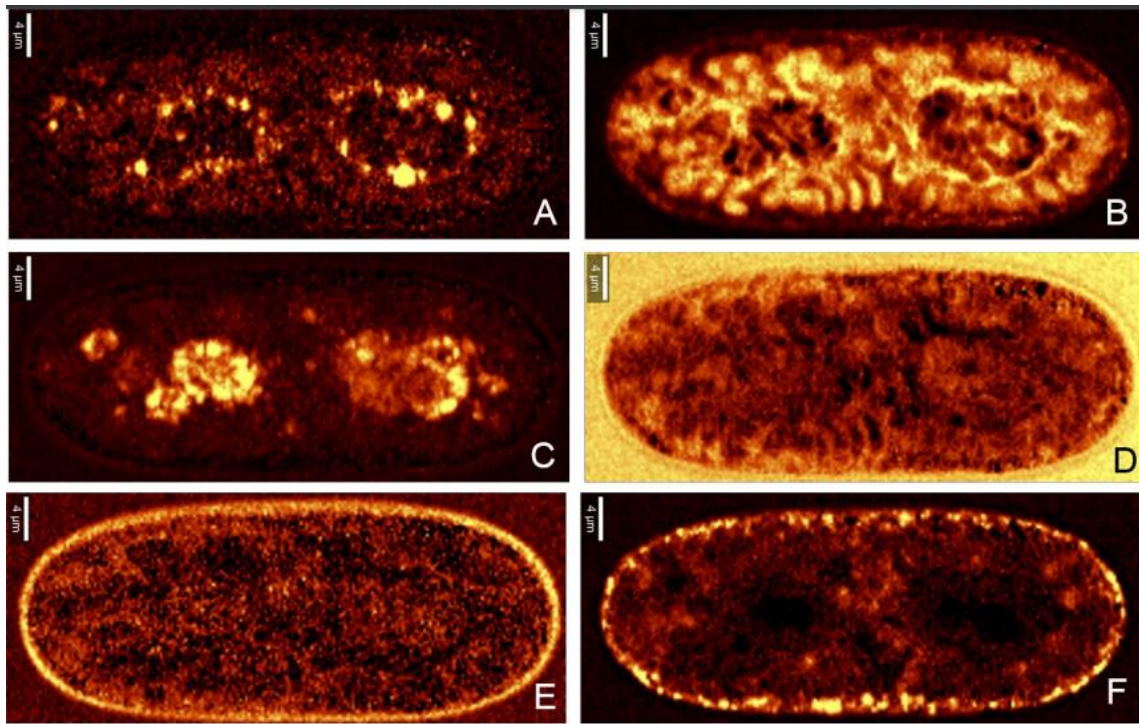
Figure S7. Raman chemical maps of P2018 cells highlighting the polyphosphate grains (A), chloroplasts (B), starch granules (C), water content (D), cell wall containing cellulose (E), lipid droplets (F), nucleus (G), and mitochondria (H). The corresponding Raman spectra are shown in Figure 5.

Figure S8. Raman chemical maps of UTEX B 2684 cells highlighting the polyphosphate grains (A), chloroplasts (B), starch granules (C), water content (D), cell wall containing cellulose (E), lipid droplets (F), nucleus (G), and mitochondria (H). The corresponding Raman spectra are shown in Figure 5.
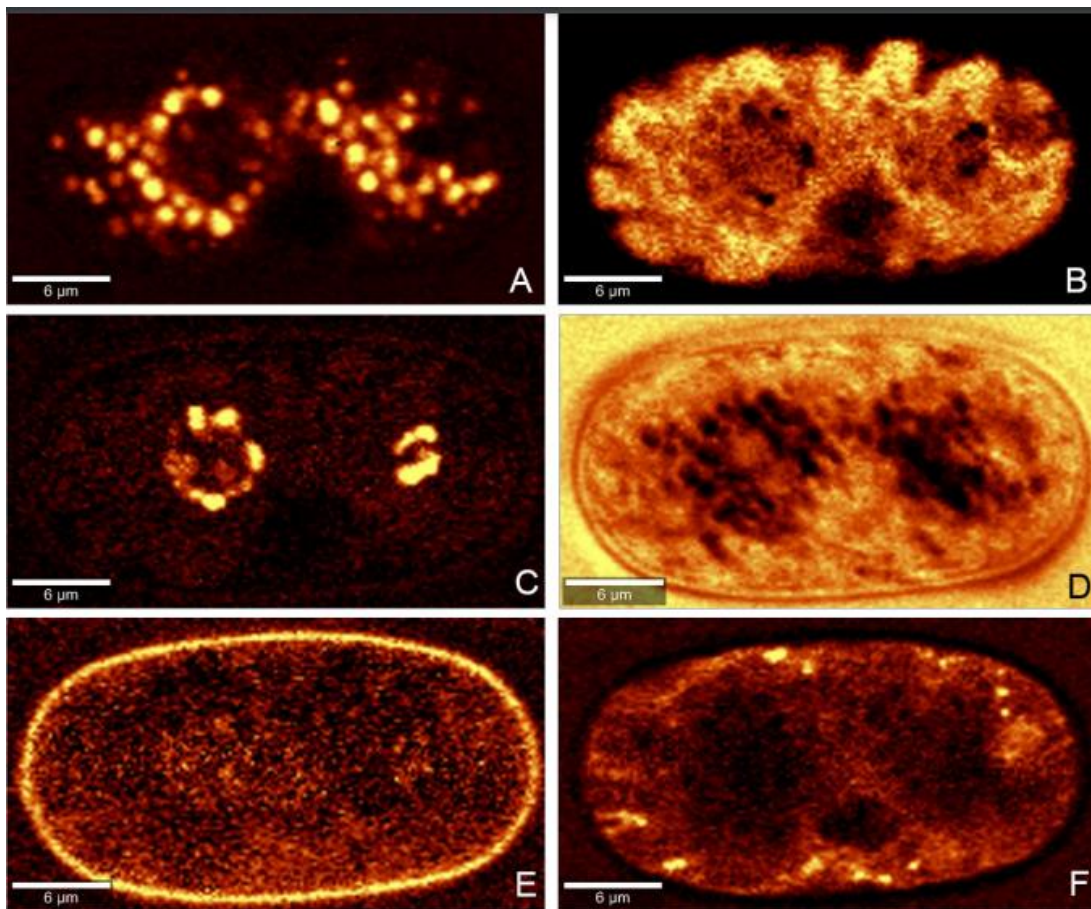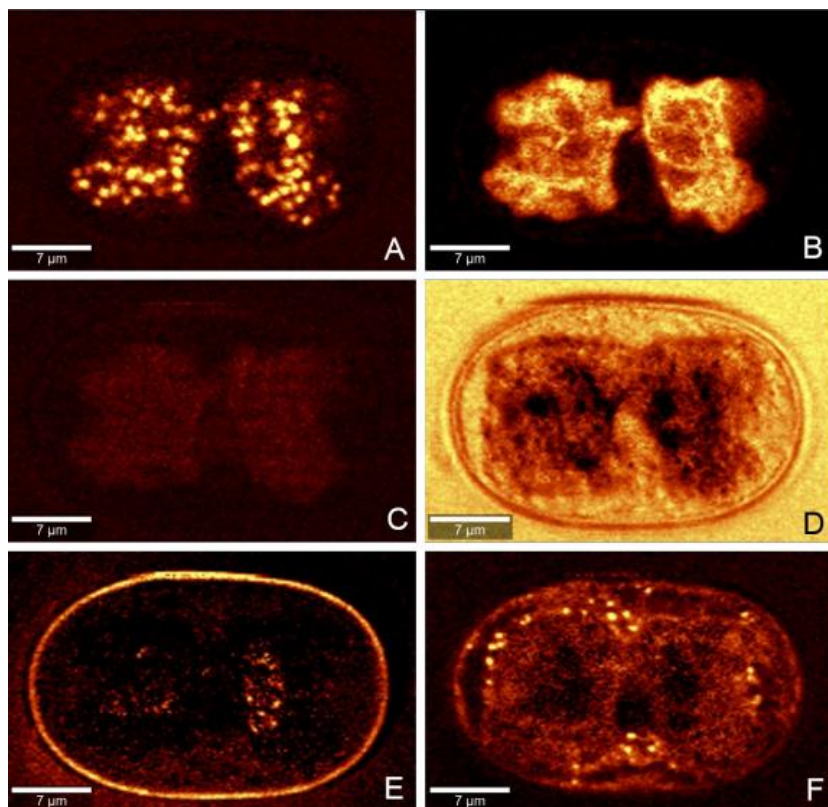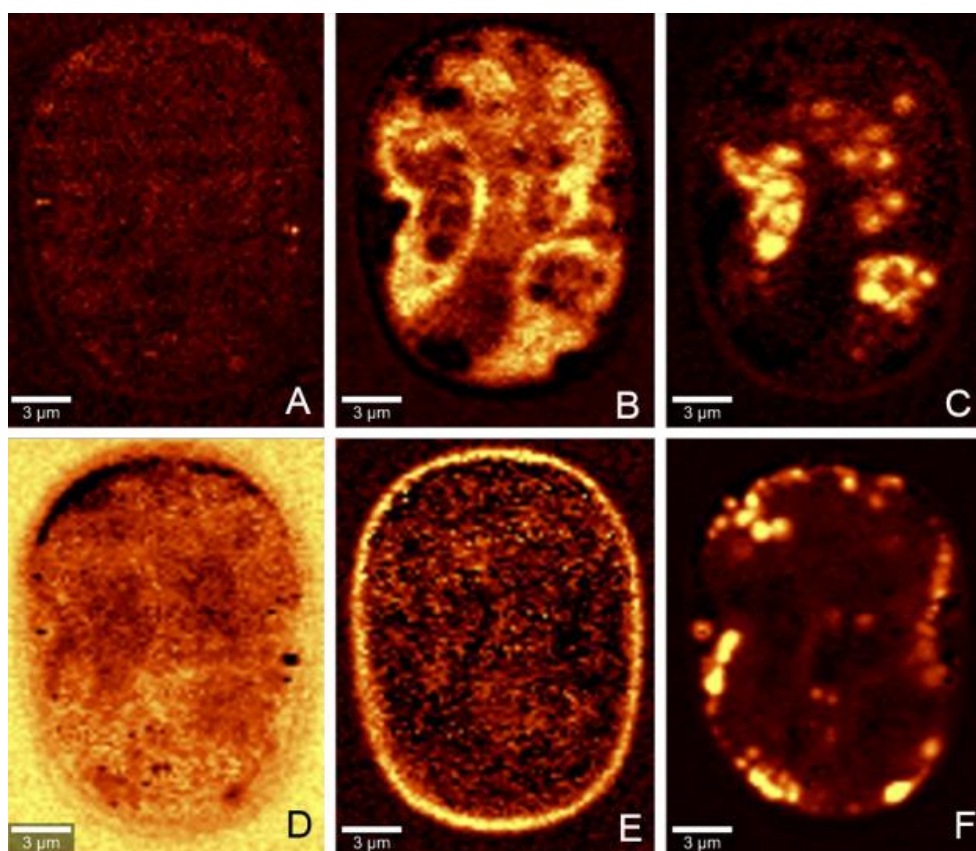
Table S1. Summary of the morphological characteristics of the studied strains.

Strain	Average dimensions		Cell	Chloroplast			Pyrenoid	PolyP detected
	Length ± SD (µm)	Width ± SD (µm)		Shape	Lobes	Thylakoid extensions (connecting 2 chloroplasts)		
UTEX B 2684	21,5 ± 3,4	14,4 ± 1,4	cylindrical straight or globular	plate-like	undulating parietal ridges	-	small round	no
P2016	32,4 ± 5,7	16,7 ± 1,3	cylindrical straight, one end often slightly broader than the other, slightly curved	stellate	blunt buds	central	round	yes
P2018	33,5 ± 5,3	19,6 ± 1,4	cylindrical straight	stellate	inclusion-like	central	round	yes
CWM	37,5 ± 6,5	12,2 ± 0,9	cylindrical curved	plate-like	irregularly radiating ridges	central	round	yes
CFN	38,4 ± 6,0	24,3 ± 1,7	cylindrical straight or globular	plate-like	radiating ridges	central and parietal	round	yes
Fox6	37,1 ± 6,1	18,3 ± 1,0	cylindrical straight	stellate	blunt buds	-	big subellipsoidal	yes
Fox7	47,2 ± 8,4	17,7 ± 1,4	cylindrical straight	reticulate	longitudinal twisting ridges	-	big subellipsoidal	yes

Guanine, a high-capacity and rapid-turnover nitrogen reserve in microalgal cells

Peter Mojzeš[a,b] [ID], Lu Gao[b,c] [ID], Tatiana Ismagulova[d] [ID], Jana Pilátová[e] [ID], Šárka Moudříková[a] [ID], Olga Gorelova[d] [ID], Alexei Solovchenko[d,f] [ID], Ladislav Nedbal[b,1] [ID], and Anya Salih[g,h]

[a]Institute of Physics, Faculty of Mathematics and Physics, Charles University, CZ-12116 Prague 2, Czech Republic; [b]Institute of Bio- and Geosciences/Plant Sciences (IBG-2), Forschungszentrum Jülich, D-52428 Jülich, Germany; [c]Faculty of Mathematics and Natural Sciences, Heinrich Heine University, D-40225 Düsseldorf, Germany; [d]Faculty of Biology, Moscow State University, Leninskie Gori 1/12, 119234, GSP-1, Moscow, Russia; [e]Department of Experimental Plant Biology, Faculty of Science, Charles University, CZ-12844 Prague 2, Czech Republic; [f]Faculty of Geography and Natural Sciences, Pskov State University, 180000 Pskov, Russia; [g]Antares Fluoresci Research, Dangar Island, NSW 1797, Australia; and [h]Confocal Bioimaging Facility, Western Sydney University, NSW 1797, Australia

Nitrogen (N) is an essential macronutrient for microalgae, influencing their productivity, composition, and growth dynamics. Despite the dramatic consequences of N starvation, many free-living and endosymbiotic microalgae thrive in N-poor and N-fluctuating environments, giving rise to questions about the existence and nature of their long-term N reserves. Our understanding of these processes requires a unequivocal identification of the N reserves in microalgal cells as well as their turnover kinetics and subcellular localization. Herein, we identified crystalline guanine as the enigmatic large-capacity and rapid-turnover N reserve of microalgae. The identification was unambiguously supported by confocal Raman, fluorescence, and analytical transmission electron microscopies as well as stable isotope labeling. We discovered that the storing capacity for crystalline guanine by the marine dinoflagellate *Amphidinium carterae* was sufficient to support N requirements for several new generations. We determined that N reserves were rapidly accumulated from guanine available in the environment as well as biosynthesized from various N-containing nutrients. Storage of exogenic N in the form of crystalline guanine was found broadly distributed across taxonomically distant groups of microalgae from diverse habitats, from freshwater and marine free-living forms to endosymbiotic microalgae of reef-building corals (*Acropora millepora*, *Euphyllia paraancora*). We propose that crystalline guanine is the elusive N depot that mitigates the negative consequences of episodic N shortage. Guanine ($C_5H_5N_5O$) may act similarly to cyanophycin ($C_{10}H_{19}N_5O_5$) granules in cyanobacteria. Considering the phytoplankton nitrogen pool size and dynamics, guanine is proposed to be an important storage form participating in the global N cycle.

nitrogen cycle | nutrient storage | phytoplankton | guanine | coral

Planktonic algae represent an essential driver of the global carbon cycle, which may be constrained by low or fluctuating nitrogen (N) availability (1–3). At another extreme, high levels of bioavailable N, often from anthropogenic sources, may result in harmful algal blooms (4) or deterioration of coral reefs (5). The highly optimized nutrient interactions with symbiotic algae are also essential for reef corals that thrive in nutrient-poor waters and paradoxically form among the most productive and diverse ecosystems. Both high and low N availability may perturb the stability of individual organisms or entire ecosystems especially when not in proportion to other biogenic elements, such as phosphorus (6).

N shortages trigger extensive changes in algal metabolism (7), including cessation of cell division, reduction of photosynthesis, and accumulation of C- and energy-rich N-free compounds. Unlike cyanobacteria, eukaryotic microalgae do not possess N-rich cyanophycin to manage N deficiency (8, 9). N-deprived microalgae mobilize intracellular inorganic N; low-molecular organic N compounds, such as polyamines, amino acids, and chlorophyll (7); and polymeric N compounds, such as proteins and nucleic acids (10). However, none of these reserves may be sufficient to bridge long periods of N starvation. Thus, a pool capable of storing large

amounts of N during periods of abundance and ensuring survival and growth of algae during deficiency remains to be identified.

Among candidate N storage pools in microalgae, crystalline inclusions were considered, although later, alternative roles, such as processing of metabolic wastes (11) and light modulation (12) were also suggested. The chemical identity of crystals from the free-living marine dinoflagellate *Gonyaulax polyedra* was proposed to be guanine (13). Other crystalline inclusions hypothesized of being guanine were also observed in symbiotic dinoflagellates of an anemone *Aiptasia* sp. (14), but their chemical nature was not experimentally confirmed (11, 14). Other earlier studies suggested the inclusions were calcium oxalate (15, 16) making the N-storage function of the inclusions unlikely. Subsequent analysis of symbiotic dinoflagellate extracts from *Aiptasia* sp. identified them as crystalline uric acid (17). This identification has since been adopted for microalgal inclusions in many recent publications (18–21).

In contrast with this proposed identity (17–21) and consistent with earlier studies (13, 14), recent direct in situ analyses identified inclusions as guanine in several marine dinoflagellates (12, 22), a freshwater chlorophyte and a eustigmatophyte (23). Guanine, similar to other purines, has the potential to serve as a large-capacity N pool, but this function has never been previously confirmed, nor was its in situ chemical identity explored in diverse algal species. Guanine is widespread and, thus, widely available in nature. It is an essential component of DNA and RNA, one of the end products of

---

Significance

Vast areas of the oceans are N limited, and how microalgae can flourish in these N-poor waters is still not known. Furthermore, mechanisms and sites of N uptake and storage have not been fully determined. We show that crystalline guanine ($C_5H_5N_5O$) is an important N storage form for phytoplankton and for symbiotic dinoflagellates of corals. The widespread occurrence of guanine reserves among taxonomically distant microalgal species suggests an early evolutionary origin of its function as N storage. Crystalline guanine appears to be a multifunctional biochemical with an important role in the N cycle that remains to be elucidated. In particular, a better knowledge of N-storage metabolism is necessary to understand the impact of eutrophication on coral-symbiont interaction.
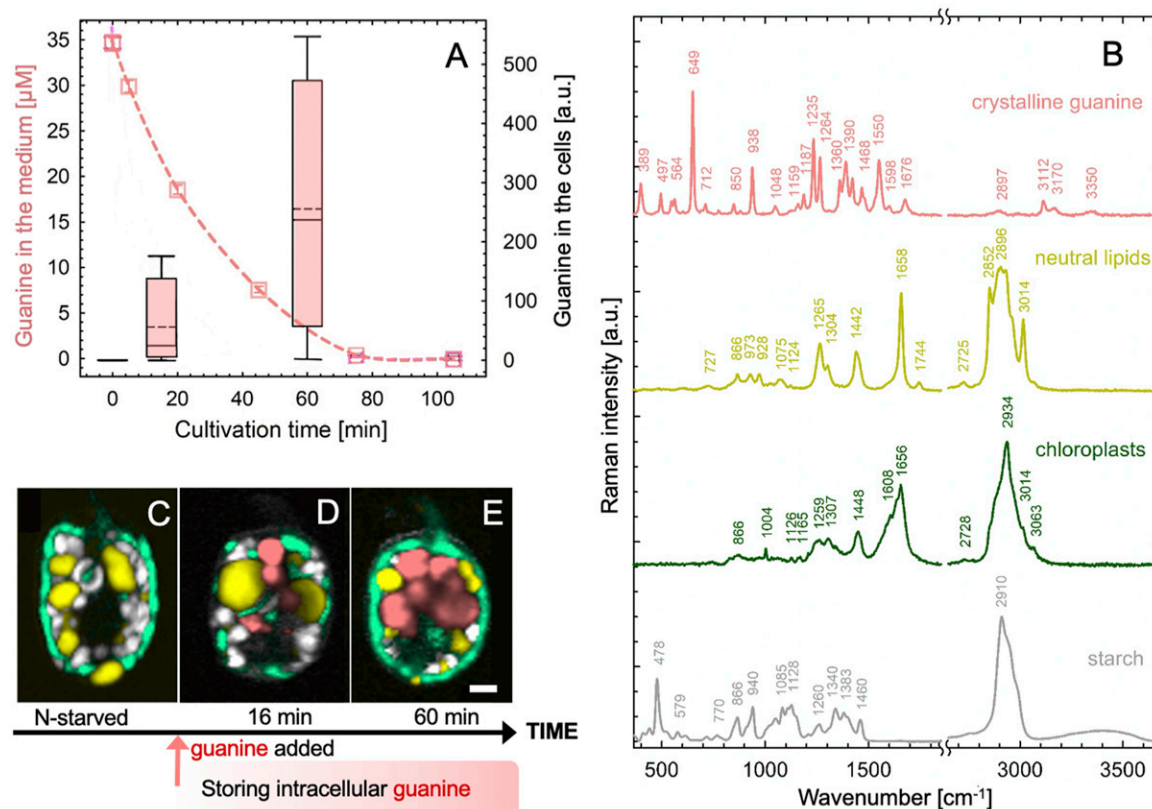
Fig. 1. Rapid uptake of guanine by N-starved *A. carterae* led to the accumulation of intracellular guanine inclusions. Cells were suspended in a saturated solution of guanine (~35 µM at 20 °C) in N-deficient f/2 medium at a density of $1.7 \pm 0.3 \times 10^5$ cells·mL^{-1}. The dashed line in *A* shows the declining concentration of guanine in the medium as measured by ultraviolet absorption (*SI Appendix*, section II.1.B). The simultaneous accumulation of guanine in the cells was assessed using Raman microscopy (*SI Appendix*, section II.1.C) and is shown in the boxplot. Raman spectra in *B* were used to generate the Raman maps in *C–E* that represent: (*C*) a typical cell after 2 wk without a N source and (*D* and *E*) cells during progressive guanine accumulation. Color legend: guanine (pink), lipids (yellow), chloroplast (green), and starch (white/gray). (Scale bar, 2 µm.) Raman maps showing separate cellular constituents in *C–E* are constructed as described in *SI Appendix*, section I.1 and presented in *SI Appendix*, Fig. S1.

nucleic acid degradation in some organisms, and utilized by some for functional purposes, such as light scattering by silvery scales of fish and bio-optical systems of many invertebrates (reviewed in ref. 24). It is widely available from decomposing fish tissues and scales, from ciliates and some phytoplankton, barnacles, and other aquatic organisms and forms part of suspended and dissolved organic N pools in the ocean. Along with other purines, guanine can serve as a N source for algae (reviewed in ref. 1). We propose that crystalline guanine and other purines (17) play a more prominent role in the N cycle than recognized to date.

To test this hypothesis, we used the unique potential of Raman microscopy and analytical transmission electron microscopy (TEM) and identified the chemical nature and the dynamics of microalgal crystal inclusions. We confirm the occurrence of crystalline guanine in free-living and symbiotic dinoflagellates and other diverse microalgal species. Our research demonstrated widespread occurrence, large N-storage capacity, and prominent dynamics of guanine in the form of crystalline inclusions in microalgae.

Results

Fast Kinetics of Uptake and Large Storage Capacity of Intracellular Guanine Inclusions in *Amphidinium carterae*. We first characterized the uptake of guanine by the widespread potentially toxic marine dinoflagellate *A. carterae*. Details of cultivation are provided in *SI Appendix*, section II.1A. Cells were kept in N-free medium (*SI Appendix*, section II.1.Aa.) for approximately 2 wk before resuspension in a saturated solution of guanine (*SI Appendix*, section II.1.Ab.). We recorded a rapid uptake rate of dissolved guanine from

the medium (dashed line, Fig. 1*A*) and its concurrent accumulation in cells (box plot, Fig. 1*A*). Dynamics and localization of guanine inclusions inside cells (in pink, Fig. 1 *C* and *D*) on the background of other cellular components was identified by the spectral signature of Raman confocal microscopy (Fig. 1*B*) (23). The rapid accumulation of the optically active guanine crystals was also documented via polarization microscopy (*SI Appendix*, section II.1.D. and Movie S1).

The dependence of uptake kinetics of dissolved guanine (Fig. 2 and *SI Appendix*, section I.2.) on cell density displayed an initial linear uptake phase (solid lines, the coefficient of determination RSQR $\geq$ 0.995) and its interpolation yielded an initial cellular uptake rate of 16 ± 4 fg (guanine)·s^{-1}·cell^{-1}, i.e., $6.3 \pm 1.5 \times 10^7$ molecules·s^{-1}·cell^{-1}.* Uptake kinetics (Fig. 2) were used to quantify intracellular guanine accumulation inside cells (*SI Appendix*, Fig. S2A) resulting in a maximum storage capacity of 143 ± 37 pg of crystalline guanine cell^{-1}, that corresponded to 68 ± 17 pg (nitrogen)·cell^{-1}. Details of these calculations are provided in *SI Appendix*, section I.2. The N pool created by starvation and refeeding was significantly larger than 17–44 pg (nitrogen)·cell^{-1} that was previously suggested to be the total N content in *A. carterae* under stationary conditions (25). Guanine storage pools may, thus, ameliorate N deficiency that occurs sporadically in a fluctuating environment.

---

*Numbers following the ± sign represent, in this work, standard deviation.
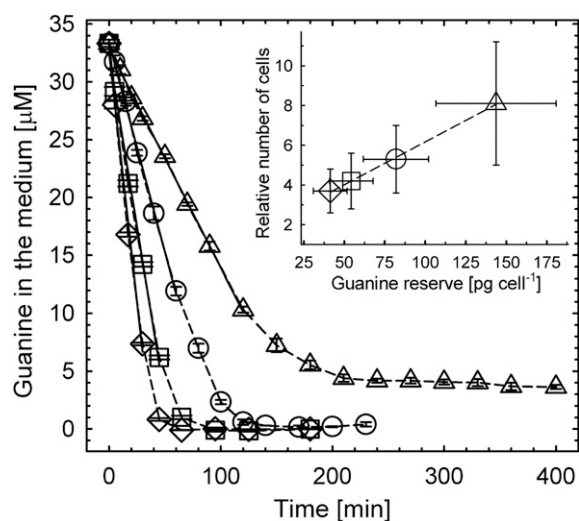
Fig. 2. Uptake of dissolved guanine from the medium by N-starved *A. carterae* and the number of generations supported by accumulated reserves (inset). The rate of guanine disappearance from the medium decreased with reduced cell density (±SD): from (122 ± 31) (◇) to (93 ± 23) (□), to (61 ± 15) (○), and to (31 ± 8) (△) × 10^3 cells·mL^{-1}. The most dilute culture (△) reduced guanine concentration in the medium from 35 to ~4 μM, revealing the maximum storage capacity of cells of 143 ± 37 (SD) pg of crystalline guanine cell^{-1}. *Inset* shows the correlation between the number of cells grown on guanine reserve and the reserve size. Details of calculations for this figure are described in *SI Appendix*, section I.2 and Fig. S2.

Cells with new guanine reserves can, after a short lag period, resume normal cell division and growth. The exponential growth phase halted only after the reserves were once again exhausted (*SI Appendix*, Fig. S2B). The number of cells that grew on these reserves was a linear function of the initially available guanine

(inset in Fig. 2). The number of cells that accumulated maximum N storage (△) increased 8.1 ± 3.1 times without N addition.

The resolution of the in situ localization of guanine crystals in *A. carterae* (Fig. 1) was increased via ultrastructural TEM imaging (Fig. 3 and *SI Appendix*, section II.1.E.) (26, 27). The solubility of guanine is known to be extremely low, and pieces of undissolved crystalline material (Fig. 3A, three white arrows) were confirmed via EDX (*SI Appendix*, section II.1.F.) to correspond to the elemental composition of a N-rich compound, likely to be guanine (Fig. 3D). *A. carterae* has a special organelle, the pusule, which is connected to the flagellar channel (28, 29). We found large globules in pusules (Fig. 3 B and C) and small crystals in vacuoles that consistently displayed typical EDX point spectra of guanine crystals (Fig. 3 E and F). Our results were inconclusive with respect to whether the guanine particles had been taken up into the pusules by phagocytosis (30) and/or via an active transport of guanine molecules dissolved in the medium from the added crystals. Guanine globules in pusules and vacuoles had irregular shapes, but the comparison of Raman spectra (Fig. 1B) with those in refs. 12, 31 confirmed that the molecules were organized in a regular anhydrous crystal structure. We hypothesized that algae may take up guanine microcrystals and, possibly, guanine-rich marine particulate fish debris via endocytosis or via the pusule (*SI Appendix*, sections I.3 and II.1.Ac and Fig. S3).

Uptake of Solid Guanine by *A. carterae* Involves Crystal Decomposition and Recrystallization. Guanine microparticles or guanine-rich debris might be taken up by dinoflagellates and directly deposited inside their cells without first dissolving or changing the original crystalline structure, similar to an engulfing mechanism proposed for algal feeding on bacteria (32). In an alternative scenario, the engulfed particles may be first dissolved within pusules or vacuoles into individual molecules. Globules of guanine may then be assembled at target intracellular locations by new crystallization (Figs. 1 and 3). Guanine crystals may also be dissolved extracellularly,
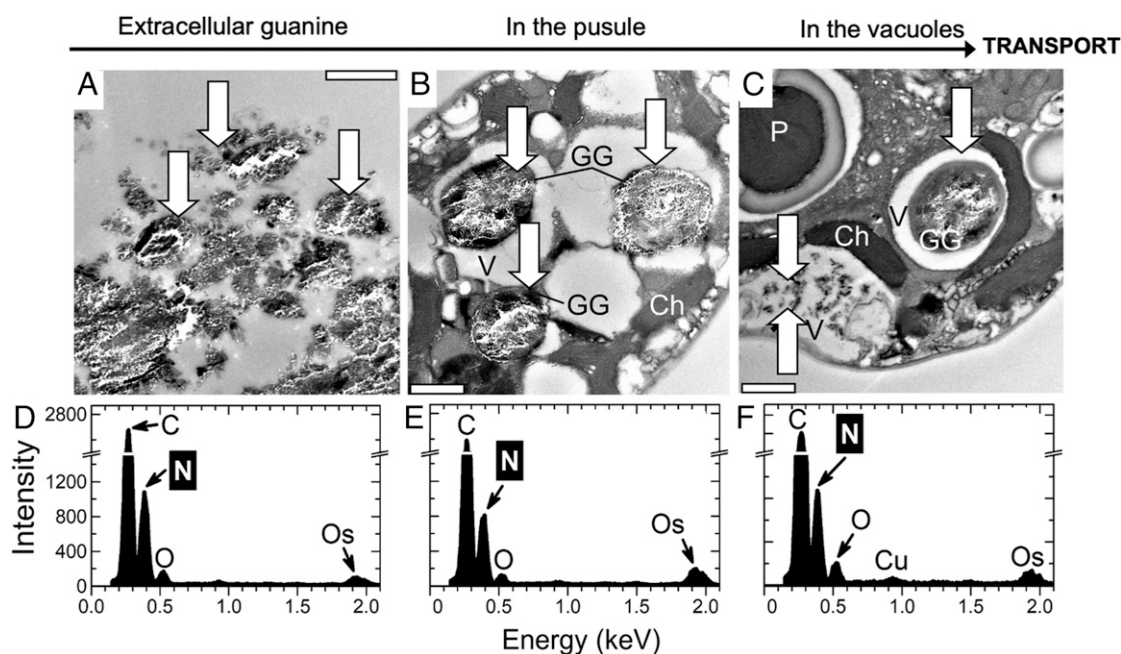
Fig. 3. TEM of semithin sections (A–C) and energy-dispersive X-ray spectroscopy (EDX) (D–F) analysis of *A. carterae* 6 h after refeeding N-starved cultures with guanine. Typical EDX point spectra of guanine crystals (D–F) indicating a high N content were obtained in the scanning TEM (STEM) mode from semithin cell sections. Arrows point to guanine particles outside (A) and inside cells (B and C). (Scale bars, 1 μm.) Ch, chloroplast; GG, globules with microcrystalline guanine; P, pyrenoid; V, vacuole.

Mojžeš et al.

subsequently taken up via active constitutive transport through their cell walls and reassembled into crystalline structures inside the cells.

Raman microscopy offers a unique opportunity to discriminate between the uptake mechanisms using the spectral contrast between fully (d_5) and partially (d_1) deuterated guanine (Fig. 4 and *SI Appendix*, sections I.3 and II.2.A and Fig. S7). The conversion of d_5-guanine to d_1-guanine requires that the molecules are directly exposed to an aqueous environment so that the four deuterium atoms bound to N can be exchanged by hydrogen from water, leaving only deuterium bound to C8 (33). Thus, if the guanine particle remained in its original crystalline form during the uptake by a cell, the N-D groups of d_5-guanine would have been protected from isotope exchange. Confirming this, a grain of guanine crystal outside of a cell (Fig. 4B) was found to remain in the d_5-guanine form (dark blue, white arrow).

The Raman spectra proved that the new reserves of intracellular guanine that appeared inside the N-starved *A. carterae* were in the d_1 form (Fig. 4, magenta). Only 30 min after the crystalline d_5-guanine was added to the cell suspension, both the d_5-guanine grain (dark blue, white arrow) outside the cell and the transformed d_1-guanine globules inside the cells (magenta) were captured simultaneously in Fig. 4 A and B. Crystalline d_1-guanine

was also found in the cells 5–12 h after feeding (Fig. 4 D and F). The large guanine globules were preferentially located at the cell center 5 h after N feeding (Fig. 4 C and D), and, subsequently, some in the form of smaller particles moved toward the cell periphery (Figs. 4 E and F and 3C).

Our analyses suggest that the guanine microcrystals were dissolved outside cells and taken up as individual molecules. Alternately, if they were engulfed as intact microcrystals, they were then dissolved intracellularly before reassembling into new crystals. In either case, the original crystalline structure was released, deuterium atoms bound to N in the d_5-form were exchanged for hydrogen from water, and the d_1-guanine molecules were reassembled into much larger inclusions in the vacuoles and/or pusules (Figs. 3 and 4).

Guanine Crystals Are Biosynthesized in *A. carterae* de Novo from Diverse Exogenic N Sources. Raman spectroscopy can also easily distinguish between ^{14}N- and ^{15}N-guanine (*SI Appendix*, sections I.3 and II.2.B and Fig. S8), thus, making it useful for determining the source of N. Feeding N-starved *A. carterae* with ^{15}N-guanine, ^{15}N-nitrate, ^{15}N-ammonium (*Top* in Fig. 5), or ^{15}N-urea (*SI Appendix*, Fig. S10) restored the culture's growth and, regardless of the N source,
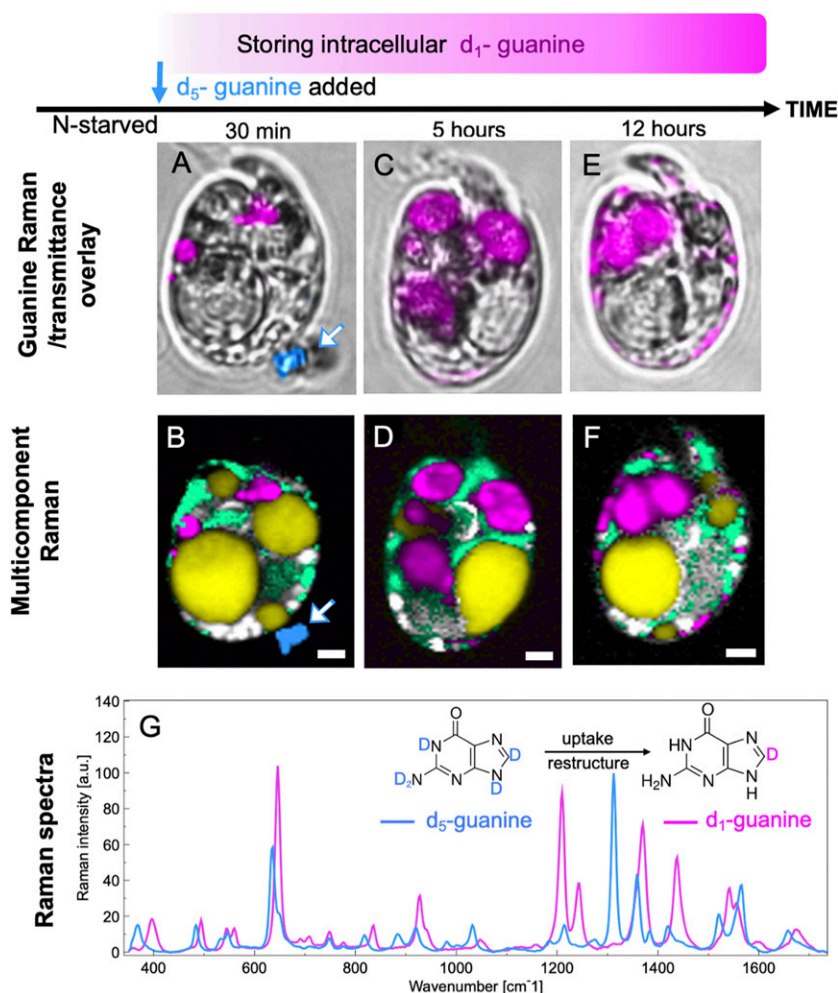
Fig. 4. Uptake of guanine includes exchange of deuterium for hydrogen atoms. Bright-field images overlaid by guanine (*A*, *C*, and *E*) and multicomponent Raman maps (*B*, *D*, and *F*) of N-starved *A. carterae* after the addition of solid crystalline fully deuterated d_5-guanine to N-depleted medium. Images collected 30 min (*A* and *B*), 5 h (*C* and *D*), and 12 h (*E* and *F*) after d_5-guanine addition. Data for d_5-guanine and partially deuterated d_1-guanine are presented in blue and magenta, respectively, in both the Raman spectrum and the images. *G* shows their respective Raman spectra. Other colors: yellow, neutral lipids; green, chloroplasts; white/gray, starch. (Scale bars [*A–F*], 2 μm.) More spectra of isotopically labeled guanine are shown in *SI Appendix*, Fig. S7. Raman maps showing separate components from data represented in *B*, *D*, and *F* are provided in *SI Appendix*, Fig. S9.

Mojžeš et al.

considerable amounts of crystalline ^{15}N-guanine appeared inside the cells during the *lag* phase that lasted ~24 h (Fig. 5, *Bottom*). On feeding *A. carterae* with nitrate, ammonium, or urea, no crystalline inclusions of other purines were observed. The accumulated or biosynthesized guanine crystals were later used to support growth until their complete disappearance in the new stationary phase. Regardless of the chemical identity of the N source, the total amount of N needed to produce a new *A. carterae* cell, estimated from the data in Fig. 5, was 14 ± 2 pg (N)·cell^{-1}. The calculation procedure was the same as in *SI Appendix*, section I.2. This amount corresponded theoretically to 30 ± 4 pg (guanine)·cell^{-1} of the presumed reserve, which was close to 23 ± 4 pg (guanine)·cell^{-1} obtained from the data presented in the graph inset in Fig. 2.

Interestingly, the intracellular guanine reserves generated by the assimilation of nitrate (middle graph in Fig. 5), ammonium, or urea were detected largely at the periphery of cells close to the chloroplasts (Fig. 6). This was in agreement with the earlier results obtained for nitrate (12). In contrast, the rapidly accumulated guanine was first located centrally in large globules (Fig. 4 *C* and *D* and *SI Appendix*, Fig. S11), which were later partially fragmented and moved to the cell periphery (Fig. 4*E*). This result obtained by Raman microscopy was confirmed with significantly higher spatial resolution by the combination of TEM and EDX methods (Figs. 3 and 6). We tentatively propose that the aforementioned differences in localization and storage dynamics indicate differences in transport and biochemical pathways following guanine biosynthesis from nitrate, ammonium, and urea compared with the direct uptake of guanine.

In Situ Chemical Identification of Inclusions in Algal Species of Diverse Taxonomical Classification and from Diverse Habitats. The chemical identity of inclusions in 14 microalgal species listed in Table 1 was examined by Raman microscopy as described in *SI Appendix*, section II.1.C. The selected species (*SI Appendix*, sections I.4. and II.3 for cultivation conditions) represent contrasting habitats, such as oligotrophic to mesotrophic marine species including both free-living (*A. carterae* and *Microchloropsis gaditana*) and coral endosymbiotic algae (*Chromera velia* and *Symbiodiniaceae*), oligotrophic to eutrophic freshwater (*Synura petersenii* and *Haematococcus pluvialis*, respectively), extremophilic/acidophilic (*Dunaliella acidophila*), terrestrial (*Lobosphaera incisa*, *Vischeria* sp., and *Klebsormidium flaccidum*), and algae from artificial anthropogenic environments (*Vacuoliviride crystalliferum* and *K. flaccidum*), their

distribution ranging from tropical/subtropical regions (*A. carterae*, *C. velia*, and *Symbiodiniaceae*) and temperate zones (*Vischeria* sp.) to the cosmopolitan species extending to the Arctic (*K. flaccidum*). Some of the tested species were established model organisms (*Chlamydomonas reinhardtii* and *Microchloropsis gaditana*), others were important production species in algal biotechnology (*M. gaditana*, *D. acidophila*, *H. pluvialis*, and *L. incisa*). The diverse phylogeny among the selected species is shown in Table 1. Spectral signatures of inclusions found in the selected algal species were compared with the spectra of multiple purines (*SI Appendix*, Fig. S4) and with calcium oxalate and calcite (*SI Appendix*, Fig. S6). Guanine inclusions were found in 13 out of 14 tested species cultivated in commonly used media (*SI Appendix*, section II.3). Only one of the tested species *K. flaccidum* was found to contain uric acid in its inclusions. This identification was completed in situ, thus, eliminating the potential artifacts caused by extraction and chemical analyses. Differences between Raman spectral signatures of guanine and uric acid are large (*SI Appendix*, Fig. S4), enabling accurate discrimination needed in light of alternatives proposed in recent literature (12, 17, 23). We cannot rule out, however, that under specific cultivation conditions, stress factors, or feeding by other organic nutrients, crystalline inclusions of other purines may not be present. Furthermore, the abundance of guanine inclusions depended not only on the availability of N nutrients (Fig. 1 *C*–*E*), but also on cultivation factors, such as CO_2 availability for *Desmodesmus quadricauda* (23) or on the cell cycle phase in *C. reinhardtii* (*SI Appendix*, section I.4 and Fig. S12). We also cannot exclude possible transformation of different purine forms with some perhaps occurring transiently or even simultaneously. Nevertheless, our experiments reliably confirm that guanine is the dominant N-storage form in the investigated microalgal species, and uric acid is found only in *K. flaccidum*, a single representative of the Streptophyta lineage. However, many more species of this lineage must be tested in the future to conclude that the Streptophyta lineage deviates from other taxonomical groups.

Coral Symbiotic Microalgae Accumulate and Store Guanine. Of particular interest in relation to guanine cell storage are the photosynthetic *Symbiodiniaceae* dinoflagellates (zooxanthellae) that live in mutualistic symbiosis with reef-building corals. The finely tuned exchange of nutrients between the coral host and the symbionts forms the foundation of healthy coral reef ecosystems (5, 21, 34, 35). However, much remains poorly understood regarding the mechanisms of nutrient uptake and storage that allow corals to
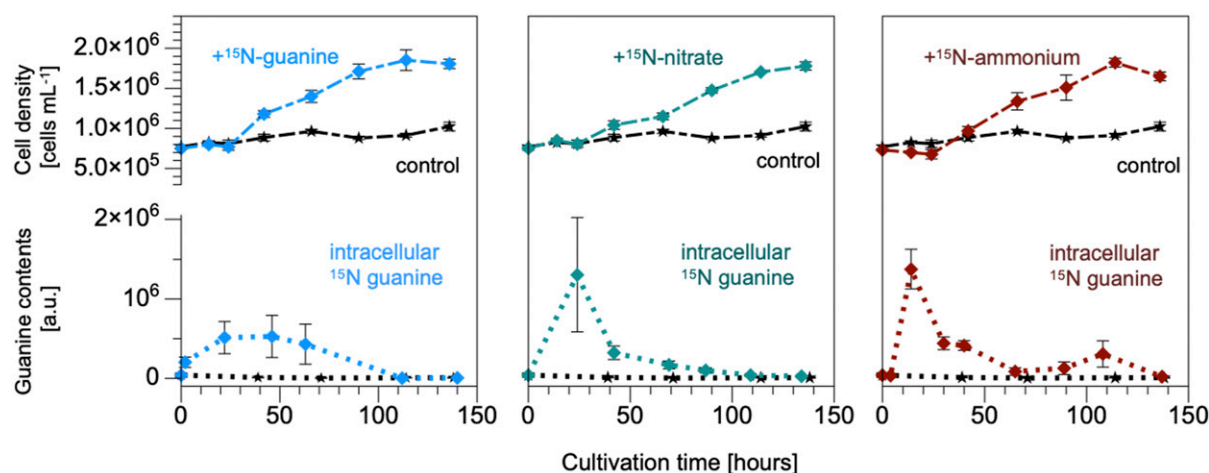
Fig. 5. N in guanine inclusions originated directly from the supplied guanine, nitrate, and ammonium. *A. carterae* cell density stagnated in controls without N feeding (black lines) and divided after addition of ^{15}N-labeled guanine, nitrate, and ammonium (all at 0.882-mM N). Intracellular crystalline guanine per cell is shown in the bottom graphs representing Raman measurements (*n* = 5–12 cells). The corresponding graph representing uptake of urea is shown in *SI Appendix*, Fig. S10.

Mojzeš et al.
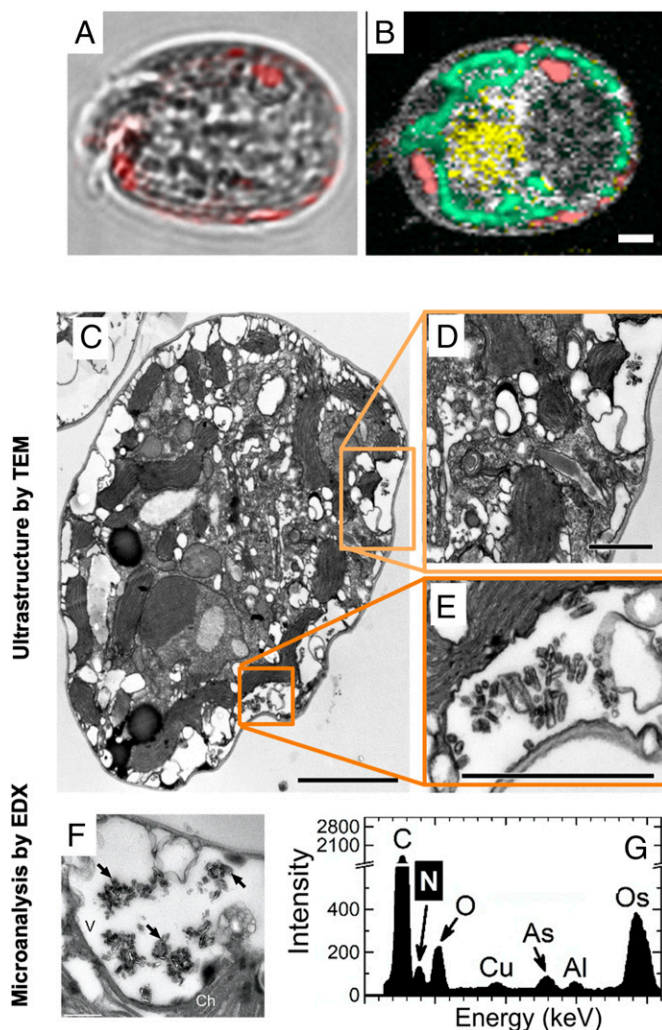
Fig. 6. Localization of guanine inclusions in *A. carterae* fed by nitrate by TEM. Bright-field images overlaid by guanine (pink) (*A*) and multicomponent Raman maps (*B*) of *A. carterae* cells 24 h after refeeding N-starved cells with nitrate. False color coding is the same as that in Fig. 1. (Scale bar, 2 μm.) TEM of ultrathin (*C–E*) as well as semithin (*F*) sections as well as EDX (*G*); (*F* and *G*) analysis of *A. carterae* cells and surrounding cells 26 h after refeeding N-starved cultures with nitrate. Typical EDX point spectra of guanine crystals (*G*) indicating high N content were obtained in the STEM mode from semithin cell sections. Arrows point to guanine crystals. (Scale bars, 2.5 [*C*], 1 [*D* and *E*], and 0.5 μm [*F*].) Ch, chloroplast; V, vacuole.

survive in the N-poor waters of tropical seas or cope with pulses of excessive nutrients due to upwelling or rainfall (5, 34, 35).

We demonstrated in this study that the numerous crystalline inclusions of endosymbiotic *Symbiodiniaceae* consist of guanine and that the external guanine is rapidly assimilated into the symbionts (Fig. 7 and *SI Appendix*, section I.5.). According to Raman microscopy (*SI Appendix*, Fig. S14), *Symbiodiniaceae* cells in the tissue of the scleractinian coral *Euphyllia paraancora* (*SI Appendix*, sections I.5 and II.4.A) exhibited similar guanine pool dynamics (Fig. 7 *A–C*) as the free-living dinoflagellate *A. carterae* (Figs. 1–4). *Symbiodiniaceae* from corals grown under optimal conditions always contained large guanine reserves (Fig. 7*A*). After 4 mo of N starvation of corals, guanine reserves were found depleted (Fig. 7*B*), the polyps shrank and became partially bleached. Upon refeeding with ^{15}N-NaNO₃, the newly synthesized ^{15}N-guanine inclusions appeared within 24 h inside *Symbiodiniaceae* cells (Fig. 7*C* and *SI Appendix*, Fig. S14).

The dynamic uptake of guanine was further confirmed in the *Symbiodiniaceae*-hosting coral *Acropora millepora*, which is widespread on the GBR, Australia, by using a combination of confocal fluorescence and reflection imaging (Fig. 7 *D–F* and *SI Appendix*, sections I.6 and II.1.C). *A. millepora* that was freshly collected from the GBR (Marine Parks Authority Permit G17/39943.1 to A.Sa., method in *SI Appendix*, section II.4.B) contained varying quantities of guanine crystals scattered peripherally among chloroplast lobes (Fig. 7*D* and *SI Appendix*, Fig. S15). Prolonged N starvation resulted in complete depletion of the guanine reserves (Fig. 7*E*). When the N-starved *Symbiodiniaceae* cells isolated from *A. millepora* were fed by a small amount of guanine powder added directly to the medium, the highly reflective guanine particles that were first visualized outside *Symbiodiniaceae* cells, began to accumulate inside cells after ~1 h (Fig. 7*F*). A similar direct uptake of guanine was observed in *Symbiodiniaceae* extracted from the zoanthid *Zoanthus* sp. (*SI Appendix*, Fig. S16, *Bottom*) and in free-living *A. carterae* (in *SI Appendix*, Fig. S16, *Top* and Movie S1).

The same dynamics of appearance and disappearance of guanine inclusions were observed for *Symbiodiniaceae* of four other cnidarian species—the anemone *Aiptasia* sp., corallimorpharian, *Rhodactis indosinensis*, leather soft coral, *Sinularia asterolobata*, and *Zoanthus* sp., cultivated in an experimental aquarium (method in *SI Appendix*, section II.4.A). This is an in situ identification of the crystalline guanine within the intact symbiotic zooxanthellae from multiple anthozoan species.

Discussion

Guanine ($C_5H_5N_5O$) holds 1.9-fold higher amounts of N per unit molecular weight than a monomer of N-storing cyanophycin ($C_{10}H_{19}N_5O_5$), known to be the long-term N reserve in cyanobacteria. The ratio is even higher when the hydration of cyanophycin is considered. As it is uncharged and almost insoluble at physiological pH, crystalline guanine is less metabolically active than various ionic N-containing compounds, enabling its accumulation in large quantities and its long-term storage inside cells without the risk of metabolic disorder. In comparison with other purines, guanine is one order of magnitude less soluble than uric acid or xanthine and two orders of magnitude less soluble than adenine or hypoxanthine. It is also more chemically stable than uric acid (1). Yet guanine can be easily mobilized from the solid state by changing pH of its aqueous environment. Although almost insoluble at neutral pH, its solubility in water increases greatly at acidic or basic pH (31). Algal metabolic activity is highly pH dependent: photosynthesis increases the pH during the day, respiration decreases it at night, and a variety of cellular pH controls alter it in response to environment and stress (36). Thus, it is possible that guanine's solubility is under cellular pH control, facilitating its transport and assimilation. In coral-algal symbiosis, pH influences the flow of N between the host and its symbionts (35) and guanine's pH solubility dependence may make it a perfect metabolic N-storage molecule. Importantly, our finding that the size of the guanine reserve in planktonic microalgae can be much higher than the N amount required for cell reproduction indicates that it is a major N pool of global importance, being proportional to the phytoplankton biomass and matching its contributions to global carbon and N cycles (2, 37).

Biogenic guanine forms a highly compact crystal structure, namely, the β-form of the anhydrous monoclinic polymorph, consisting of vertically stacked planes of hydrogen-bonded molecules (12, 38). This crystal structure explains its unique optical properties, including birefringence and an extremely high index of refraction, leading to high light scattering as recorded in our confocal reflective imaging analysis. Consequently, guanine's storage function does not exclude other possible functions, e.g., light scattering in microalgae to enhance the efficiency of photosynthesis, photoprotection from UV radiation, or the formation of photonic mirrors (12, 38).

Mojzeš et al.

Table 1. Microcrystalline purines identified by Raman microscopy in various algal strains

Species	Habitat	Phylogeny	Purine
Symbiodiniaceae	E-S	Alveolata–Dinoflagellata	Guanine
Amphidinium carterae	S	Alveolata–Dinoflagellata	Guanine
Chromera velia	S	Alveolata–Chromerida	Guanine
Microchloropsis gaditana	S	Stramenopiles–Eustigmatophyceae	Guanine
Vacuoliviridecrystalliferum	U	Stramenopiles–Eustigmatophyceae	Guanine
Vischeria sp.	T	Stramenopiles–Eustigmatophyceae	Guanine
Trachydiscus minutus	F	Stramenopiles–Eustigmatophyceae	Guanine
Synura petersenii	F	Stramenopiles–Chrysophyceae	Guanine
Lobosphaera incisa	F, T	Archaeplastida–Chlorophyta–Trebouxiophyceae	Guanine
Desmodesmus quadricauda	F	Archaeplastida–Chlorophyta–Chlorophyceae	Guanine
Chlamydomonas reinhardtii	F	Archaeplastida–Chlorophyta–Chlorophyceae	Guanine
Dunaliella acidophila	Acid	Archaeplastida–Chlorophyta–Chlorophyceae	Guanine
Haematococcus pluvialis	F	Archaeplastida–Chlorophyta–Chlorophyceae	Guanine
Klebsormidium flaccidum	T	Archaeplastida–Streptophyta–Klebsormidiophyceae	Uric acid

The screened species represent diverse habitats: Acid, acidophilic; E, endosymbiotic; F, freshwater; S, marine; T, terrestrial/aerophytic; U, unspecified. The origins of the examined species as well as cultivation approach are described in *SI Appendix*, sections I.4 and II.3.

N is limiting to phytoplankton primary productivity in many marine ecosystems and is often associated with sporadic or seasonal reintroduction from deeper waters by mixing via upwelling or storms, from organic matter remineralization and from land-based sources (1–3). N stimulates phytoplankton growth, and the connection of N metabolism to photosynthesis has long been recognized (1, 6). The ability to assimilate N from nitrate, ammonium, urea, or guanine dissolved in seawater, or, alternatively, from particulate N sources, and to rapidly sequester N as crystalline guanine for redeployment under conditions of N limitation has emerged as an important survival strategy of free-living phytoplankton algae. N storage is also a critical component of cnidarian-dinoflagellate symbiosis. Natural or anthropogenic N eutrophication is known to disrupt the N-limited state of coral symbionts, disturbing the host's control over them thereby exacerbating the damage following mass coral bleaching (5, 19). By locking excessive N in insoluble crystals and mobilizing them when required, symbiotic microalgae may effectively mitigate the negative effect of N excesses or deprivations and maintain stable nutrient stoichiometry (C:N and N:P ratios). Given the major nutritional role of the symbionts to corals and many other reef animals and the dependence of the reef ecosystem's health on efficient nutrient uptake and storage, our research addressed a critical knowledge gap regarding the mechanisms by which corals acquire and store inorganic nutrients. Such knowledge is increasingly important under escalating eutrophication and climate-induced warming of marine and freshwater ecosystems.

N storage and other diverse vital biological and biochemical functions underscore the versatility of crystalline guanine concerning symbiosis and phytoplankton dynamics. Its shared occurrence among microalgal species over the phylogenetic tree suggests the involvement of guanine in these roles early in evolution, a hypothesis consistent with the potential role of this purine close to the origins of life and its presumably prebiotic occurrence on early Earth (39). Analogous to polyphosphate, which was regarded as a molecular fossil (40) and was, subsequently, revealed to have a multitude of functions (41), the crystalline guanine can also be considered as an evolutionary old, overlooked, and forgotten multifunctional tool of nature popping up from oblivion.

Materials and Methods

Chemicals and Media. References for chemicals and protocols used for preparing cultivation media and stable isotope labeling are listed or described in detail in *SI Appendix*, section II.

Algal Strains, Corals, and Cultivation Protocols. The origins and cultivation conditions for the microalgal species in Table 1 are listed in *SI Appendix*, sections I.4. and II.3. Cnidarian species anemone, *Aiptasia* sp., corallimorpharian, *R. indosinensis*, scleractinian coral, *E. paraancora*, leather coral, *S. asterolobata*, and anthozoan *Zoanthus* sp., were purchased from a local marine aquarium shop. *A. millepora* was collected from the GBR, Australia, and studied immediately after collection or as explants cultivated in experimental aquaria. Details of the laboratory cultivation and methods to study the kinetics of guanine assimilation and turnover are provided in *SI Appendix*, sections I, II.1.A, II.3, and II.4.

Confocal Raman Microscopy. The samples for Raman measurements were prepared and treated according to the methodology described in detail elsewhere (23, 42, 43) and summarized in *SI Appendix*, section II.1.C. The inverted Raman microscope LabRam Evolution (Horiba Scientific, Longjumeau, France) and upright Raman microscope WITec alpha 300 RSA (WITec, Ulm, Germany) were used with laser excitation at 532 nm in the study. To remove interference by autofluorescence of chlorophyll, wide-area low-power photobleaching of entire cells using a defocused 532-nm laser beam was employed before mapping. No differences that would affect data interpretation were observed between measurements on the Horiba and WITec systems.

Confocal Reflection Microscopy. *Symbiodiniaceae* cells of *A. carterae* and *Zoanthus* sp. confirmed by Raman microscopy to include guanine crystals were concurrently imaged using a confocal fluorescence microscope Leica TCS SP8 (Leica Microsystems, Germany) in the reflection mode using laser excitation at 488 nm. The guanine inclusions were seen in the reflection as crystal-like highly light-scattering objects. Further details are provided in *SI Appendix*, sections I.6, II.1.C, and II.4.

Analytical Electron Microscopy. The protocol of specimen preparation for TEM is described in *SI Appendix*, section II.1.E. Ultrathin sections were cut with a LKB-8800 (LKB, Sweden) ultratome, stained with lead citrate according to the method described by Reynolds (44) and examined under a JEM-1011 (JEOL, Tokyo, Japan) electron microscope. Samples for nanoscale elemental analysis using analytical TEM with EDX were fixed, dehydrated, and embedded as above, except that sections were stained with uranyl acetate and lead citrate. Semithin sections were examined under a JEM-2100 (JEOL, Japan) electron microscope. Point EDX spectra were recorded using a JEOL bright-field STEM module and an X-Max X-ray detector system (Oxford Instruments, United Kingdom). Further details are provided in *SI Appendix*, sections II.1.E and II.1.F.

Data Availability. All study data are included in the article and supporting information.
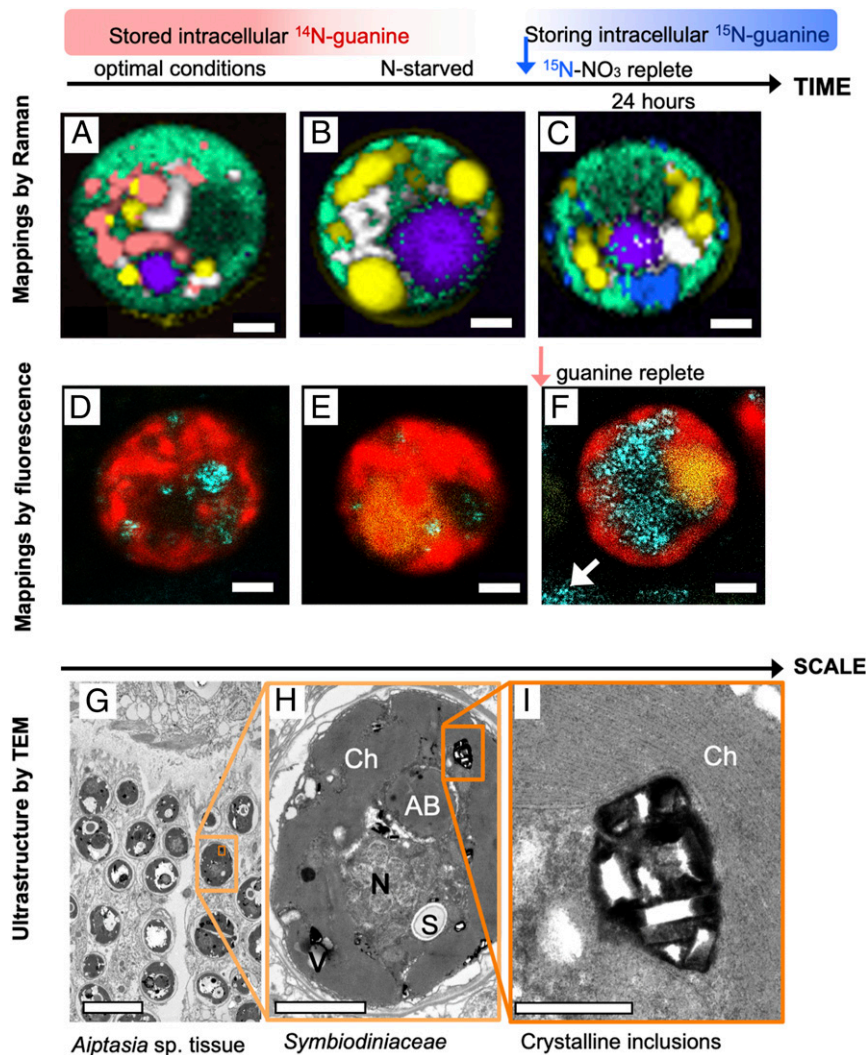
Fig. 7. Guanine in the endosymbiotic *Symbiodiniaceae* cells in corals. Raman maps of cells from tissue of the coral *E. paraancora* (*A–C*). The spectra used to construct these maps are shown in *SI Appendix*, Fig. S13. Symbionts in corals maintained under optimal nutrient conditions contained guanine crystals (*A*). Cells from corals that were kept in N-depleted seawater for 4 mo contained very few guanine crystals (*B*). Twenty-four hours after feeding the starved coral 0.3-mM ^{15}N-NaNO$_3$, cells showed large ^{15}N-guanine depots (*C*). The false color coding is the same as that in Figs. 1 and 4 with magenta added to represent accumulation bodies. (Scale bar, 2 μm.) *Symbiodiniaceae* cells isolated from the Great Barrier Reef (GBR) coral, *A. millepora* (*D–F*). Cell from freshly collected coral (*D*), N-depleted coral (*E*), and from one day after feeding with medium containing traces of undissolved guanine grains (*F*). Cyan, 488-nm laser reflection of guanine grains outside (white arrow) and inside the cells; red, chlorophyll autofluorescence at 670–700 nm; yellow, fluorescence in accumulation bodies at 500–560 nm; white arrow, remains of undissolved crystalline guanine in medium. (Scale bar, 2 μm.) Ultrastructure of *Symbiodiniaceae* cells in *Aiptasia sp.* shown at increasing magnification (*G–I*). AB, accumulation body; Ch, chloroplast; N, nucleus; S, floridean starch; V, vacuole. (Scale bars, 10 [*G*], 2 [*H*], and 0.5 μm [*I*].)

1. N. J. Antia, P. J. Harrison, L. Oliveira, The role of dissolved organic nitrogen in phytoplankton nutrition, cell biology and ecology. *Phycologia* **30**, 1–89 (1991).
2. P. G. Falkowski, Evolution of the nitrogen cycle and its influence on the biological sequestration of CO$_2$ in the ocean. *Nature* **387**, 272–275 (1997).
3. P. G. Falkowski, R. T. Barber, V. Smetacek, Biogeochemical controls and feedbacks on ocean primary production. *Science* **281**, 200–207 (1998).
4. D. M. Anderson, P. M. Glibert, J. M. Burkholder, Harmful algal blooms and eutrophication: Nutrient sources, composition, and consequences. *Estuaries* **25**, 704–726 (2002).
5. N. Rädecker, C. Pogoreutz, C. R. Voolstra, J. Wiedenmann, C. Wild, Nitrogen cycling in corals: The key to understanding holobiont functioning? *Trends Microbiol.* **23**, 490–497 (2015).
6. T. Tyrrell, The relative influences of nitrogen and phosphorus on oceanic primary production. *Nature* **400**, 525–531 (1999).
7. S. Schmollinger *et al.*, Nitrogen-sparing mechanisms in *Chlamydomonas* affect the transcriptome, the proteome, and photosynthetic metabolism. *Plant Cell* **26**, 1410–1435 (2014).
8. K. Forchhammer, R. Schwarz, Nitrogen chlorosis in unicellular cyanobacteria–A developmental program for surviving nitrogen deprivation. *Environ. Microbiol.* **21**, 1173–1184 (2019).
9. B. Watzer, K. Forchhammer, Cyanophycin synthesis optimizes nitrogen utilization in the unicellular cyanobacterium *Synechocystis* sp strain PCC 6803. *Appl. Environ. Microbiol.* **84**, e01298-18 (2018).
10. O. Baulina *et al.*, Diversity of the nitrogen starvation responses in subarctic *Desmodesmus* sp. (Chlorophyceae) strains isolated from symbioses with invertebrates. *FEMS Microbiol. Ecol.* **92**, fiw031 (2016).
11. J. Lewis, P. Burton, A study of newly excysted cells of *Gonyaulax polyedra* (Dinophyceae) by electron microscopy. *Br. Phycol. J.* **23**, 49–60 (1988).
12. A. Jantschke *et al.*, Anhydrous β-guanine crystals in a marine dinoflagellate: Structure and suggested function. *J. Struct. Biol.* **207**, 12–20 (2019).
13. R. DeSa, J. W. Hastings, The characterization of scintillons. Bioluminescent particles from the marine dinoflagellate, *Gonyaulax polyedra*. *J. Gen. Physiol.* **51**, 105–122 (1968).

14. K. B. Strychar, P. W. Sammarco, T. J. Piva, Apoptotic and necrotic stages of *Symbiodinium* (Dinophyceae) cell death activity: Bleaching of soft and scleractinian corals. *Phycologia* 43, 768–777 (2004).

15. D. L. Taylor, *In situ* studies on cytochemistry and ultrastructure of a symbiotic marine dinoflagellate. *J. Mar. Biol. Assoc. U. K.* 48, 349–366 (1968).

16. M. J. Kevin, W. T. Hall, J. J. McLaughlin, P. A. Zahl, *Symbiodinium microadriaticum* Freudenthal, a revised taxonomic description, ultrastructure. *J. Phycol.* 5, 341–350 (1969).

17. P. L. Clode, M. Saunders, G. Maker, M. Ludwig, C. A. Atkins, Uric acid deposits in symbiotic marine algae. *Plant Cell Environ.* 32, 170–177 (2009).

18. T. Krueger *et al.*, Temperature and feeding induce tissue level changes in autotrophic and heterotrophic nutrient allocation in the coral symbiosis–A NanoSIMS study. *Sci. Rep.* 8, 12710 (2018).

19. S. Rosset, J. Wiedenmann, A. J. Reed, C. D'Angelo, Phosphate deficiency promotes coral bleaching and is reflected by the ultrastructure of symbiotic dinoflagellates. *Mar. Pollut. Bull.* 118, 180–187 (2017).

20. H. Yamashita, A. Kobiyama, K. Koike, Do uric acid deposits in *zooxanthellae* function as eye-spots? *PLoS One* 4, e6303 (2009).

21. C. Kopp *et al.*, Highly dynamic cellular-level response of symbiotic coral to a sudden increase in environmental nitrogen. *MBio* 4, e00052–e13 (2013).

22. A. Jantschke, I. Pinkas, A. Schertel, L. Addadi, S. Weiner, Biomineralization pathways in calcifying dinoflagellates: Uptake, storage in MgCaP-rich bodies and formation of the shell. *Acta Biomater.* 102, 427–439 (2020).

23. Š. Moudříková, L. Nedbal, A. Solovchenko, P. Mojzeš, Raman microscopy shows that nitrogen-rich cellular inclusions in microalgae are microcrystalline guanine. *Algal Res.* 23, 216–222 (2017).

24. D. Gur, B. A. Palmer, S. Weiner, L. Addadi, Light manipulation by guanine crystals in organisms: Biogenic scatterers, mirrors, multilayer reflectors and photonic crystals. *Adv. Funct. Mater.* 27, 1603514 (2017).

25. S. Menden-Deuer, E. J. Lessard, Carbon to volume relationships for dinoflagellates, diatoms, and other protist plankton. *Limnol. Oceanogr.* 45, 569–579 (2000).

26. A. Shebanova *et al.*, Versatility of the green microalga cell vacuole function as revealed by analytical transmission electron microscopy. *Protoplasma* 254, 1323–1340 (2017).

27. T. Ismagulova, A. Shebanova, O. Gorelova, O. Baulina, A. Solovchenko, A new simple method for quantification and locating P and N reserves in microalgal cells based on energy-filtered transmission electron microscopy (EFTEM) elemental maps. *PLoS One* 13, e0208830 (2018).

28. R. E. Schmitter, The fine structure of *Gonyaulax polyedra*, a bioluminescent marine dinoflagellate. *J. Cell Sci.* 9, 147–173 (1971).

29. J. D. Dodge, Ultrastructure of dinoflagellate pusule - unique osmo-regulatory organelle. *Protoplasma* 75, 285–302 (1972).

30. R. Onuma, T. Horiguchi, Morphological transition in kleptochloroplasts after ingestion in the dinoflagellates *Amphidinium poecilochroum* and *Gymnodinium aeruginosum* (Dinophyceae). *Protist* 164, 622–642 (2013).

31. D. Gur *et al.*, Guanine crystallization in aqueous solutions enables control over crystal size and polymorphism. *Cryst. Growth Des.* 16, 4975–4980 (2016).

32. H. J. Jeong *et al.*, Heterotrophic feeding as a newly identified survival strategy of the dinoflagellate *Symbiodinium*. *Proc. Natl. Acad. Sci. U.S.A.* 109, 12604–12609 (2012).

33. J. M. Delabar, M. Majoube, Infrared and Raman-spectroscopic study of N-15 and D-substituted guanines. *Spectrochim. Acta A* 34, 129–140 (1978).

34. L. Muscatine, J. W. Porter, Reef corals: Mutualistic symbioses adapted to nutrient-poor environments. *BioSci.* 27, 454–460 (1977).

35. D. Yellowlees, T. A. V. Rees, W. Leggat, Metabolic interactions between algal symbionts and invertebrate hosts. *Plant Cell Environ.* 31, 679–694 (2008).

36. K. L. Barott, A. A. Venn, S. O. Perez, S. Tambutté, M. Tresguerres, Coral host cells acidify symbiotic algal microenvironment to promote photosynthesis. *Proc. Natl. Acad. Sci. U.S.A.* 112, 607–612 (2015).

37. P. G. Falkowski, The role of phytoplankton photosynthesis in global biogeochemical cycles. *Photosynth. Res.* 39, 235–258 (1994).

38. A. Hirsch *et al.*, "Guanigma": The revised structure of biogenic anhydrous guanine. *Chem. Mater.* 27, 8289–8297 (2015).

39. N. Kitadai, S. Maruyama, Origins of building blocks of life: A review. *Geoscience Frontiers* 9, 1117–1153 (2018).

40. A. Kornberg, N. N. Rao, D. Ault-Riché, Inorganic polyphosphate: A molecule of many functions. *Annu. Rev. Biochem.* 68, 89–125 (1999).

41. L. Xie, U. Jakob, Inorganic polyphosphate, a multifunctional polyanionic protein scaffold. *J. Biol. Chem.* 294, 2180–2190 (2019).

42. Š. Moudříková *et al.*, Raman and fluorescence microscopy sensing energy-transducing and energy-storing structures in microalgae. *Algal Res.* 16, 224–232 (2016).

43. Š. Moudříková *et al.*, Quantification of polyphosphate in microalgae by Raman microscopy and by a reference enzymatic assay. *Anal. Chem.* 89, 12006–12013 (2017).

44. E. S. Reynolds, The use of lead citrate at high pH as an electron-opaque stain in electron microscopy. *J. Cell Biol.* 17, 208–212 (1963).

PLANT BIOLOGY

BIOPHYSICS AND COMPUTATIONAL BIOLOGY

Supplementary Information for

Guanine, a high-capacity and rapid-turnover nitrogen reserve in microalgal cells

Peter Mojzeš[1,2], Lu Gao[2,3], Tatiana Ismagulova[4], Jana Pilátová[5], Šárka Moudříková[1], Olga Gorelova[4], Alexei Solovchenko[4,6], Ladislav Nedbal[2*], Anya Salih[7]

Corresponding author: Ladislav Nedbal
Email: l.nedbal@fz-juelich.de

This PDF file includes:

> Supplementary text
> Figures S1 to S16
> Table S1
> Legend for Movie S1
> SI APPENDIX References

Other supplementary materials for this manuscript include the following:

> Movie S1

I. Supplementary Information Text

I.1. Localization of guanine, lipids, chloroplasts, and starch by Raman microscopy (Fig. 1 in the main text). The images in Fig. S1 are complementary to those in Fig. 1 in the main text and show Raman maps of individual cell components in separate panels (D-O). The separate maps in Fig. S1 provide a more detailed information than the overlays in Fig. 1C–E (here repeated in Fig. S1 A-C). The method to obtain these maps is described in detail in SI APPENDIX II.1.C

I.2. Kinetics of guanine accumulation and maximum storage capacity (Figs. 2 in the main text). The mean amount of guanine accumulated per cell can be calculated from the drop in the guanine concentration in the supernatant (Fig. 2) and by normalization to cell density. We assumed that during the short uptake periods of our experimental treatments, the guanine was neither used for growth nor transformed into other chemical forms. This assumption was supported by the guanine accumulation analysis shown in Fig. 1.
Fig. S2 shows data used to calculate the guanine storage capacity of *A. carterae.* The most diluted experimental algal suspension (triangles in Figs. 2 and S2) took up only a fraction of the available guanine and by dividing this amount by the number of cells present, the resultant estimated maximal storage capacity of *A. carterae* cells was 143 ± 37 pg (guanine)$\cdot$cell^{-1}.

I.3. Raman spectra of various purines and stable-isotope-labelled guanines (Figs. 4 and 5 in the main text). *Identification.* The chemical nature of the crystalline inclusions within cells was determined by comparing their Raman spectra with Raman spectra of reference samples (SI Appendix II.1.C.). Raman spectra of several purines, including crystalline guanine and uric acid, are shown in Fig. S4. Fig. S5 presents a comparison with various forms of uric acid. Raman spectra of calcite, calcium oxalate monohydrate, and calcium oxalate dihydrate that were earlier suspected to be present in algal inclusions are shown in Fig. S6.
Deuterium-labelling. Deuterated crystalline d_1-guanine, d_4-guanine, and d_5-guanine were used as reference samples. The materials and preparation are described in SI Appendix II.2.A. Raman spectra of these isotopically-labeled deuterium-guanine forms can be easily distinguished due to their distinct spectral fingerprints (Fig. S7).
^{15}N-labelling. To distinguish the N-source of guanine biosynthesized *de novo* from the compounds constituting N-sources in the media commonly used for microalgal cultivation (*i.e.*, nitrate, ammonium, urea), and to eliminate any doubt about the origin of the endogenous guanine, isotopically labeled ^{15}N-compounds were used as the alternative N-sources. Consequently, ^{15}N-guanine newly biosynthesized from specific exogenous ^{15}N-sources was easily distinguished from the preexisting ^{14}N-guanine or from ^{14}N-guanine recycled from degraded cellular components. Spectral differences between Raman spectra of crystalline ^{14}N- and ^{15}N-guanine are highlighted in Fig. S8.

I.4. In situ chemical identification of inclusions in diverse algal species (Tab.1 in the main text). Diverse algal species listed in the table below together with their origin were tested in cultivation media and under conditions recommended for their cultivation by the source collections (Table S1) as further specified in SI Appendix II.3.

Species	Origin.	Code
Symbiodiniaceae	Isolates. *Symbiodiniaceae* cells were isolated from tissues of various cnidarian species (*Aiptasia* sp., *Euphyllia paraancora*, *Rhodactis indosinensis*, *Sinularia asterolobata*, *Zoanthus* sp.) purchased from the local marine aquarium shops. Regardless of their origin, all *Symbiodiniaceae* cells contained crystalline guanine unless their host was exposed to long-term (at least 3 months) nitrogen deficiency.	
Amphidinium carterae	**MCNA** - National Center for Marine Algae and Microbiota, Bigelow, USA	CCMP1314
Chromera velia	**MCNA** - National Center for Marine Algae and Microbiota, Bigelow, USA	CCMP2878

Microchloropsis gaditana	**NIES** - National Institute for Environmental Studies, Tsukuba, Japan	NIES-2587
Vacuoliviride crystalliferum	**NIES** - National Institute for Environmental Studies, Tsukuba, Japan	NIES-2860
Vischeria sp.	**CAUP** - Culture Collection of Algae of Charles University, Prague, Czech Republic	Q202
Trachydiscus minutus	**CCALA** - Culture Collection of Autotrophic Organisms of the Institute of Botany of the Czech Academy of Science, Třeboň, Czech Republic	838
Synura petersenii	**CAUP** - Culture Collection of Algae of Charles University, Prague, Czech Republic	Q13
Lobosphaera incisa	**CAUP** - Culture Collection of Algae of Charles University, Prague, Czech Republic	H4301
Desmodesmus quadricauda	**CCALA** - Culture Collection of Autotrophic Organisms of the Institute of Botany of the Czech Academy of Science, Třeboň, Czech Republic	463
Chlamydomonas reinhardtii	**CRC** - Chlamydomonas Resource Center, University of Minnesota, St. Paul, USA	CC-1690
Dunaliella acidophila	**CAUP** - Culture Collection of Algae of Charles University, Prague, Czech Republic	G301
Haematococcus pluvialis	**CAUP** - Culture Collection of Algae of Charles University, Prague, Czech Republic	G1002
Klebsormidium flaccidum	**NIES** - National Institute for Environmental Studies, Tsukuba, Japan	NIES-2285

I.5 Detection of guanine in symbiotic dinoflagellates in intact corals and in extracted algae (Fig. 7 in the main text). Following the enrichment of the artificial seawater (prepared from Reef Crystals sea salt, Aquarium Systems, Sarrebourg, France) in aquaria by 0.3 mM ^{15}N-NaNO$_3$ as a sole source of N, the newly synthesized ^{15}N-guanine crystals re-appeared within 24 hours inside endosymbionts of *Euphylia paraancora* as was documented by the respective Raman spectra (SI Appendix II.1.C.) that precisely distinguished between ^{14}N- and ^{15}N-guanine (Fig. 6C, Fig. S14C). To the best of our knowledge, this is the first *in situ* identification of crystalline guanine within the intact symbiotic zooxanthellae directly in tissues of several anthozoan species.
Symbiodiniaceae within *cnidarians* obtained from a commercial marine store and maintained under optimal nutrient conditions contained a considerable amount of guanine crystals (Fig. 7A, Fig. S14). When whole organisms (*e.g,*, *Euphyllia paraancora*) were subjected for four months to N-starvation under N-depleted conditions (combined nitrate, nitrite and ammonium concentration < 1 µM) with only autotrophic feeding, their symbiotic algae lost all guanine reserves, while the coral polyps showed a pronounced reduction in size and became pale (*i.e*., bleached). N limitation is known to cause an increased accumulation of lipid bodies and floridean starch granules (1, 2), as well as the reduction of chloroplast volume in symbiotic dinoflagellates (Fig. 6B, Fig. S14B).
We also explored the presence of guanine in symbiotic dinoflagellates of *Acropora millepora*, a common coral species from the Great Barrier Reef (Australia), in colonies freshly collected from the reef (Heron Island, GBR) and in their explants, prepared from colony fragments, maintained in small closed system seawater aquaria. Symbionts were analyzed either *in situ,* in the host tissue, or as extracted cells cultivated in natural seawater (Fig. 7 D-F). The crystalline guanine inclusions were identified in both types of samples characterized by confocal Raman microscopy and correlated with the highly reflective properties of guanine visualized by confocal reflection microscopy (Figs. S15, and S16). Similar to observations of the free-living *A. carterae* and to symbiotic dinoflagellates from the store aquaria kept corals, the crystals of guanine were observed in very large quantities inside the guanine-fed *Symbiodiniaceae* of *A. millepora*, were almost absent in the N-starved samples and were present in low to moderate amounts in the extracted symbionts of corals freshly collected from the reef (Fig. S15).

I.6 Confocal fluorescence and reflection imaging. Confocal fluorescence microscopy is far more widely available in biological laboratories than Raman microscopy. Confocal imaging is fast,

with high-throughput, and confocal reflection images can be acquired along with the confocal fluorescent ones. Since Raman microscopy enables the precise *in situ* identification of the chemical nature of crystalline inclusions, we first tested the validity of (SI Appendix II.1.C) of the confocal reflection microscopy to image and quantify crystalline inclusions by corresponding measurement of the same samples by Raman imaging. By being more reflective/light scattering than other cell components, we showed that crystalline inclusions such as guanine can be easily visualized in reflection mode using a confocal fluorescence microscope. Thus, the inclusions in *Symbiodiniaceae* cells were first identified by Raman microscopy as guanine crystals and immediately after, cells from the same algal extracts were imaged by the confocal fluorescence microscope Leica TCS SP8 (Leica Microsystems, Germany) in reflection mode. Guanine accumulations were seen as crystal-like, highly light-scattering inclusions. All other organelles, e.g., the nucleus, the pyrenoid, the lipid droplets, the chloroplasts, and the accumulation bodies did not produce a reflection signal (Figs. S15 and S16).

Importantly, the reflection imaging technique enabled the visualization of crystalline deposits much faster than by Raman microscopy, however, this technique could not differentiate between crystalline guanine and other light scattering crystalline inclusions, *e.g.*, calcite, calcium oxalate or uric acid. A combination of both techniques would therefore be desirable for rapid, high-throughput studies.

II. Supplementary Information: Materials and Methods

All chemicals were used for the preparation of media, the stable-isotope labeled ^{15}N-NaNO$_3$, ^{15}N-KNO$_3$, urea-^{15}N$_2$, ND$_4$OD, and DCl, as well as the crystalline nucleobases (adenine, guanine, xanthine, hypoxanthine and uric acid) were purchased from Sigma-Aldrich (St. Louis, MO, USA), unless other supplier was specified.

II.1. Uptake kinetics of dissolved guanine and intracellular guanine inclusions of A. carterae (Figs. 1- 3 in the main text).

II.1.A. Cultivation of A. carterae

The marine dinoflagellate *Amphidinium carterae* was obtained from the National Center for Marine Algae and Microbiota (NCMAS, CCMP1314), Bigelow, USA. First, 1 L culture was grown in the closed photobioreactor FMT150 (PSI, Drasov, Czech Republic) in a full f/2 medium (composition shown below in II.1.Aa). The suspension was sparged by 0.2 L·min^{-1} filtered ambient air passed through a humidifier. The cultivation regime was 12 h light / 12 h dark illumination. The irradiance was 40 µmol (photons)·m^{-2}·s^{-1} generated by blue- and red-light emitting diodes. The temperature of the suspension was kept constant at 20 °C. Minor losses of medium volume due to evaporation were replenished with distilled water. The culture growth was monitored spectrophotometrically and checked by cell counting.

N-starvation. A stationary culture grown with nitrate was harvested by centrifugation (2000 ×g, 3 min), washed by and suspended in N-deficient f/2 medium (composition in II.1.Aa.) and filtered through sintered glass filter (P100, Schott-Duran, Germany) to remove clumps of cells.

The culture remained largely synchronous and was N-starved for approximately one week. The suspension was split into equal 20 mL batches, transferred to 100 mL flasks (Schott-Duran), and placed on an orbital shaker in the growth chamber 350H (Sanyo, Osaka, Japan) at T= 20°C, illumination 40 µmol (photons) m^{-2} s^{-1}. The cells were maintained in this N-free environment for additional five days to degrade all remaining guanine crystals. The absence of crystalline guanine was checked by Raman microscopy (SI Appendix II.1.C.) and by polarization microscopy (II.1.D.).

II.1.Aa. ASW f/2 medium with and without N-source

The f/2 medium was prepared from artificial seawater (ASW) according to (3) and its N-deficient variant contained: 400 mM NaCl, 10 mM KCl, 9 mM CaCl$_2$·2H$_2$O, 20 mM MgCl$_2$·6H$_2$O, 20 mM MgSO$_4$·7H$_2$O and 1.85 mM KBr, 3.62 × 10^{-5} M NaH$_2$PO$_4$·H$_2$O, 1.06 × 10^{-4} M Na$_2$SiO$_3$·9H$_2$O, 1.17 × 10^{-5} M FeCl$_3$·6H$_2$O, 1.17 × 10^{-5} M Na$_2$EDTA·2H$_2$O, 3.93 × 10^{-8} M CuSO$_4$·5H$_2$O, 2.60 × 10^{-8} M Na$_2$MoO$_4$·2H$_2$O, 7.65 × 10^{-8} M ZnSO$_4$·7H$_2$O, 4.20 × 10^{-8} M CoCl$_2$·6H$_2$O and 9.10 × 10^{-7} M MnCl$_2$·4H$_2$O. The final concentrations of vitamins added into the autoclaved ASW f/2 from the stock solution were 2.96 × 10^{-7} M thiamine HCl (vitamin B1), 2.05 × 10^{-9} M biotin (vitamin H) and 3.69 × 10^{-10} M cyanocobalamin (vitamin B12).

The full ASW f/2 medium used for cultures grown on nitrate as a sole source of N was prepared from the N-deficient f/2 by adding 0.882 mM NaNO$_3$. The media were stored in amber glass bottles at 20 °C and used for no more than 30 days after preparation.

II.1.Ab. Medium with saturated guanine as a sole N-source
The saturated solution (~35 □M, (4)) of neutral guanine without visible solid particles was obtained by dissolving a slightly excessive amount of solid guanine in N-deficient f/2 at 60°C (stirred for 30 min) that was cooled to 20°C and filtered through a 0.22 µm Millipore membrane filter (Merck, Kenilworth, NJ, USA). The f/2 medium saturated with dissolved guanine was stored in amber glass bottles at 20 °C and used for no more than 5 days after preparation.

II.1.Ac. Feeding N-starved A. carterae by ground fish scales
The f/2 medium enriched by fish scales was prepared by leaching 100 mg of ground dry fish scales (rainbow trout, Atlantic salmon) in 100 mL of the N-deficient f/2 medium (SI Appendix II.1.Aa.) at 25°C for 24 hours. The remaining large pieces of fish scales were removed in the form of precipitate.

II.1.B. Determination of soluble guanine by UV-absorption spectrophotometer
The dissolved guanine concentration in f/2 medium was determined spectrophotometrically using the absorption spectrophotometer Specord 250 (Analytik Jena, Jena, Germany) and its published extinction coefficient value (5). Standard spectroscopic quartz cuvettes (Hellma Analytics, Jena, Germany) with optical lengths of 10, 50 and 100 mm were used depending on the measured concentrations. Spectra between 210 – 400 nm were recorded to avoid artifacts that can occur with single wavelength measurements. For each measurement, aliquots of 5, 10, or 20 mL were centrifuged (14000 ×g, 1 min) and the supernatant was filtered through the 0.22 µm Millipore membrane filter (Merck, Kenilworth, NJ, USA) to remove suspended nanoparticles. We used N-deficient f/2 medium as a blank reference.

II.1.C. Confocal Raman and confocal fluorescence - reflection microscopies
Sample preparation. The specimens for all Raman measurements were prepared and treated according to the methodology described in detail elsewhere (6-8). The algal cells were harvested by centrifugation (2000 ×g, 10 – 30 s) of 1 – 2 mL of cell culture and excess medium was discarded. Each cell pellet and a small amount of remaining medium were mixed with an approximately equal volume of 2% w/v solution of low-gelling agarose (T = 30 – 40°C) in the respective medium. The agarose solution was used to prevent movement of cells during measurements and was prepared using the low melting/gelling agarose (melting T=65°C, gelling T=28°C) purchased from Carl Roth (Karlsruhe, Germany). Several microliters of the suspension were spread as a thin layer between a quartz slide and a quartz coverslip; wet edges were dried with blotting paper and sealed with a CoverGrip sealant (Biotium, Fremont, CA, USA).
To remove the autofluorescence of chlorophyll that obscured the Raman spectra, a wide-area low-power photobleaching of the entire cell by a defocused 532 nm laser beam was applied prior to the mapping, as described previously (6). The mean guanine content per cell was quantified by Raman microscopy by measuring 5 – 12 randomly selected cells for each time point.
For confocal analysis the symbiotic algae were extracted from *Zoanthus* sp and *A. millepora* by excising and abrading tissues with a brush into filtered seawater (FSW). They were first cleaned of debris by passing through a fine nylon mesh and were further cleaned by repeated centrifugation and resuspension of the pelleted algae in FSW. A drop of microalgal suspension (A. *carterae, Zoanthus sp, A. millepora)* was placed on a glass slide under a glass coverslip for confocal analysis and for each, several slides were analysed with a total of 28-34 cells analysed from each culture or organism, and per treatment for *A. millepora.*
Raman microscopy. The quantitative dynamic studies of guanine biosynthesis and uptake by N-starved *A. carterae* were carried out using an inverted Raman microscope LabRam Evolution (Horiba Scientific, Longjumeau, France) with 532 nm laser excitation (10 mW power at the focal plane) and using the water-immersion objective Plan Apo VC 60×, NA 1.20 (Nikon, Minato, Japan). The spectrograph was equipped with a 150 gr/mm grating providing spectral resolution of 9 cm^{-1}. Raman mapping was conducted with 500 nm steps in both directions, and with two accumulations, each of 0.3 s integration time at each voxel. The apparatus was controlled by a

LabSpec 6 software (Horiba Scientific, Longjumeau, France). Further details of the apparatus were described elsewhere (6). After the format conversion, spectra were treated and analyzed by a home-made GNU Octave software (9) as described previously (8).

All other Raman measurements were conducted using an upright Raman microscope WITec alpha 300 RSA (WITec, Ulm, Germany) with a 532 nm laser excitation (20 mW power at the focal plane), an oil-immersion objective UPlanFLN 100×, NA 1.30 (Olympus, Shinjuku, Japan) and the spectrograph providing spectral resolution of 6 cm^{-1}. Scanning step in x- and y-direction was 200 nm, with an integration time of 0.1 s per voxel. Further details on the apparatus can be found in (8).

The acquired Raman spectra were treated, and the Raman chemical maps constructed by multivariate decomposition of the baseline-corrected spectra into the spectra of pure chemical components by using WITec Project Plus 5.1 software (WITec, Ulm, Germany). No differences that could affect data interpretation were observed between the results obtained with Horiba and with WITec Raman microscopes.

Confocal microscopy. For each analysis, we used Leica TCS SP5 or Leica TCS SP8 (Leica Microsystems, Heidelberg, Germany) inverted microscopes. Fluorescence imaging was by 63x water immersion objective (Plan-Apo, 1.2 NA) at excitation by Argon laser 488nm line and capturing the emission bands at 500 – 560 nm for organelles as the accumulation body and at 670-700nm for chlorophyll in two photomultiplier tubes (PMTs). Reflection from guanine was simultaneously imaged by excitation at 488nm, with the third PMT detection range centered on the laser line at 485-489nm to capture scattered wavelengths from crystals. Images were taken at approximately mid-depth into each cell at 512x512 pixel resolution.

II.1.D. Polarization microscopy

To acquire images and videos in polarized light, a polarizing accessory of the upright Raman microscope WITec alpha 300 RSA (WITec, Ulm, Germany) was used. The videos visualizing the fast formation of crystalline guanine within *A. carterae* cells were taken by WITec Project Plus 5.1 software (WITec, Ulm, Germany).

The N-starved *A. carterae* cells were immobilized between a glass slide and a glass coverslip by low-melting agarose (SI Appendix II.1.C) of approximately 100 ꙍm thickness, without sealing the coverslip edges. Several drops of guanine-enriched f/2 medium (II.1.Ab.) were placed at the coverslip edges and the microalgae located near the edges were monitored through the crossed polarizes. As the dissolved guanine diffused towards the nearby algae, its uptake was confirmed by a considerable amount of crystalline guanine appearing inside them. The rapid accumulation was visualized by the strong light depolarization by newly formed crystals as early as within 14 minutes after the guanine solution was added (Movie S1).

II.1.E. Ultrastructural transmission electron microscopy (TEM)

The microalgae for TEM were fixed in 2% v/v glutaraldehyde solution in culture medium at room temperature for 0.5 h and then post-fixed for 4 h in 1% (w/v) OsO$_4$ in the 0.1 M sodium cacodylate buffer. The samples, after dehydration through graded ethanol series including anhydrous ethanol saturated with uranyl acetate, were embedded in araldite. Ultrathin sections were made with an LKB-8800 (LKB, Sweden) ultratome, mounted to the formvar-coated TEM grids, stained with lead citrate according to Reynolds (10) and examined under JEM-1011 (JEOL, Tokyo, Japan) microscope.

II.1.F. Energy-dispersive X-ray spectroscopy (EDX)

The samples for nanoscale elemental analysis in analytical TEM using EDX were fixed, dehydrated and embedded in araldite as described above, excepting the staining with uranyl acetate and lead citrate. Semi-thin sections were examined under JEM-2100 (JEOL, Japan) microscope equipped with a LaB$_6$ gun at the accelerating voltage 200 kV. Point EDX spectra were recorded using JEOL bright-field scanning TEM (STEM) module and X-Max X-ray detector system (Oxford Instruments, UK). The energy range of recorded spectra was 0–10 keV with a resolution of 10 eV per channel. At least ten cells per specimen were analyzed. Spectra were processed with INKA software (Oxford Instruments, UK) and presented in a range 0.1-4 keV.

II.2. Combining isotopic-labelling with Raman microscopy (Fig.4 and 5 in the main text).

II.2.A. Deuterated guanine for uptake solid guanine experiments (Fig. 4 in the main text).

Heavy water (D_2O, 99.9%) used in the experiments was purchased from Silantes (München, Germany). Deuterated d_1-guanine (8)D, d_4-guanine (1,2,2,9)D and d_5-guanine (1,2,2,8,9)D were prepared from crystalline guanine (Sigma-Aldrich) according to the procedure described in (11). The isotopic purity of d_1-, d_4-, and d_5-guanine was checked by Raman microscopy (SI Appendix II.1.C.) and compared with the corresponding spectra reported in (11).

The base media and studied organisms were the same as described above in relation to Figs. 1-3. The methodological approach is described in the main text, and in further detail in SI Appendix. II.1.A for cultivation and SI Appendix II.1.C. for Raman measurements.

II.2.B. ^{15}N-sources for cell growths and guanine dynamics (Fig. 5 in the main text).

For *de novo* biosynthesis experiments, various ^{15}N-labeled compounds constituting N-sources in the media commonly used for microalgae cultivation were tested. The stable-isotope labeled ^{15}N-$NaNO_3$, ^{15}N-KNO_3 and urea-$^{15}N_2$ were purchased from Sigma-Aldrich (St. Louis, MO, USA). The ^{15}N-NH_4Cl was acquired from Silantes (München, Germany). The stable-isotope fully-labeled crystalline ^{15}N-guanine was prepared from commercially available guanosine-$^{15}N_5$ 5′-monophosphate, sodium salt, (Sigma-Aldrich) by acid hydrolysis of the N-glycosidic bond (12) and subsequent neutralization by NaOH. The precipitated neutral $^{15}N_5$-guanine (^{15}N-guanine) was washed by deionized water and dried. The isotopic purity was checked by Raman microscopy (SI Appendix II.1.C.) and compared with the corresponding spectrum reported in (11). The spectral differences between ^{15}N- and ^{14}N-guanine are shown in Fig. S8. The frequency downshifts by 5 – 20 cm^{-1} caused by the heavier ^{15}N atoms largely exceeded the experimental error ($< \pm 1$ cm^{-1}) and enabled a straightforward and an unambiguous identification of the respective species.

The media and the organisms used for the biosynthesis and uptake experiments were as described above in relation to Figs. 1-3. The 20 mL batches (in triplicate) of the N-starved *A. carterae* cells (II.1.A.) were supplemented with various ^{15}N-sources.

To provide the same amounts of N atoms regardless of the N-source, we added either ^{15}N-nitrate to the final concentration of 0.882 mM corresponding to the full f/2 medium (54.69 mg·L^{-1}), or 0.882 mM ^{15}N-ammonium (15.91 mg·L^{-1}), or 0.441mM ^{15}N-urea (26.48 mg·L^{-1}) or 0.1764 mM ^{15}N-guanine as the sole N sources. Nitrate, ammonium and urea were added in the form of 1000-fold concentrated solution. Guanine was added as a solid powder (0.53 mg per 20 mL cell suspension) because of its limited solubility.

The cell density and average cell size were measured in triplicate by the Coulter counter Multisizer 3 (Beckman Coulter, Brea, CA, USA) with a 100 µm aperture or by using Bürker counting chamber (n=9).

The mean guanine content per cell was quantified by Raman microscopy measuring 5–12 randomly selected cells for each time point.

In other methodological aspects, our approach is further described in detail in the main text, in SI Appendix II.1.A for cultivation and SI Appendix II.1.C. for Raman measurements.

II.3. Source and maintenance of free-living microalgae (Tab. 1 in the main text).

The free-living marine algal species were cultivated in a full ASW f/2 medium prepared from N-deficient f/2 (SI Appendix II.1.Aa.) enriched by 8.82 × 10^{-4} M $NaNO_3$ as a sole source of N (3). The freshwater microalgae were cultivated in the Bold's Basal Medium (BBM) (13), ½SŠ medium (14), BG-11 medium (15) or media recommended by the supplier of the algal strain. None of the media used for basic screening was enriched with guanine or other purines.

II.4. Source and maintenance of symbiotic microalgae (Fig. 7 in the main text).

II.4.A. Symbiodiniaceae from aquaria-kept anthozoans (Fig. 7 A–C in the main text).

Various cnidarian species, *e.g.*, anemone *Aiptasia* sp., corallimorpharian *Rhodactis indosinensis*, scleractinian coral *Euphyllia paraancora*, leather coral *Sinularia asterolobata*, and *Zoanthus* sp. were obtained from a marine aquarium store.

They were maintained in small experimental aquaria (8 L, closed circulation of filtered water, 25 °C, 12h/12h light/dark cycle, 100 µmol(photons)·m^{-2}·s^{-1} illumination by white- and blue-light emitting diodes) under controlled nutrient conditions in the artificial marine water prepared from

the Reef Crystals sea salt (Aquarium Systems, Sarrebourg, France) according to the manufacturer's instructions and supplemented with trace elements by a weekly dosage of commercially available solutions Coral Colours (Red Sea, Eilat, Israel).

Commercially available colorimetric Profi Test kits (Salifert, the Netherlands) were used to test and maintain the pH, carbonate hardness/alkalinity, concentrations of nitrate, nitrite, ammonia, and phosphate according to the manufacturer's instructions. The resultant color changes were quantified by the absorption spectrophotometer Specord 250 (Analytik Jena, Germany) and *via* calibration based on the concentration series of the respective compounds.

The chemical nature of the crystalline inclusions of anthozoan endosymbionts were first analysed immediately after acquisition, and subsequently, at regular intervals, by excising a small piece of soft tissue, positioning it between glass microscope slide and coverslip, and immediately analyzing by Raman microscopy (SI Appendix II.1.C.).

II.4.B. Symbiodiniaceae from reef collected coral Acropora millepora (Fig. 7 D–F *in the main text).*
Replicate explants from four *A. millepora* colonies were starved in N-depleted artificial seawater in experimental aquaria for 4 weeks. Dinoflagellate symbionts were extracted by repeated centrifugation and filtering, cultured in nutrient depleted media for additional 4 days, analyzed by confocal reflection microscopy and compared to cells one day later following the addition of crystalline guanine to the artificial seawater and to symbionts extracted from three *A. millepora* that were used for analysis immediately after reef collection and transportation to the laboratory.

III. Supplementary Information: Results
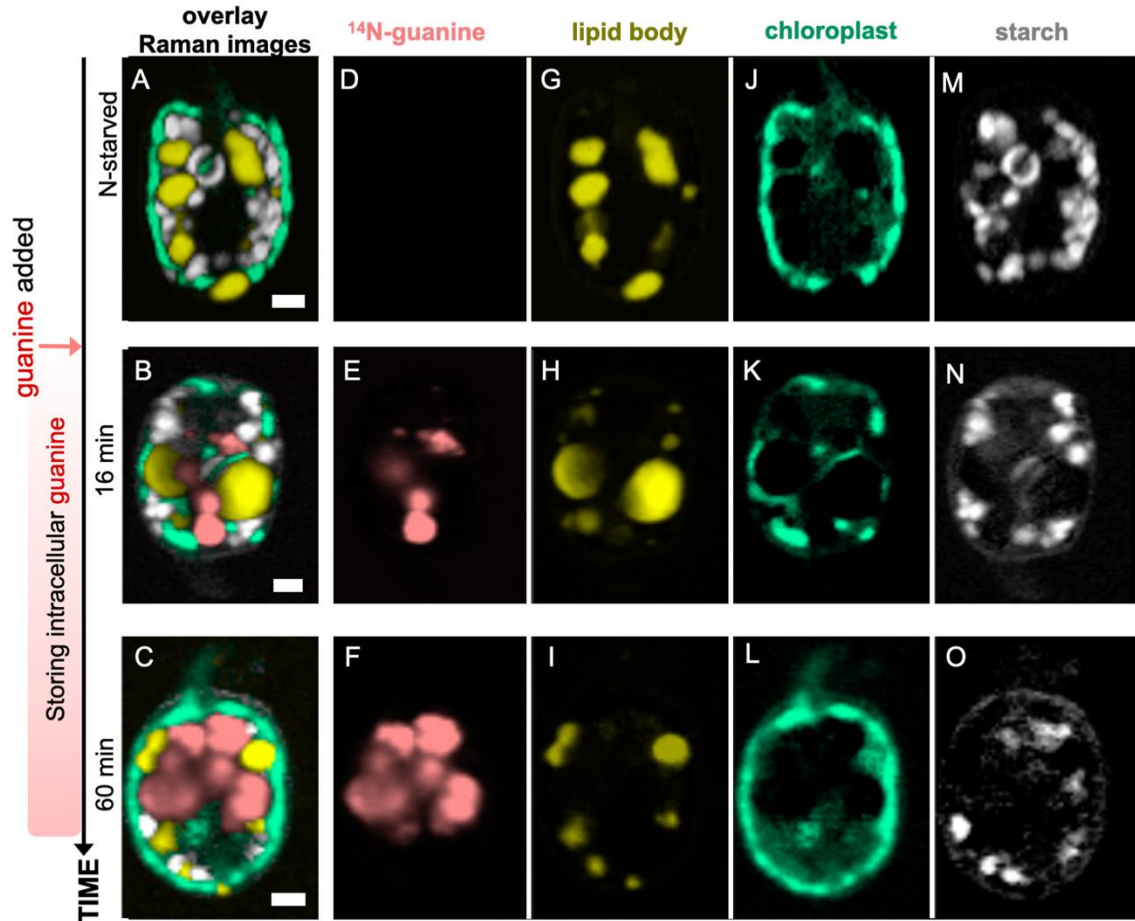
Fig. S1 (complementing Figs. 1C–E). Rapid uptake of guanine by N-starved *A. carterae* led to accumulation of intracellular guanine inclusions. The combined Raman maps (A–C) represent typical cells after two weeks of N-starvation (first row) and cells during progressive guanine accumulation (second and third rows). Intracellular distribution of crystalline guanine (D–F), neutral lipids (G–I), chloroplasts (J–L) and floridean starch (M–O) are shown in separate panels for clarity. The corresponding Raman spectra are shown in Fig. 1B. Scale bar: 2 μm.
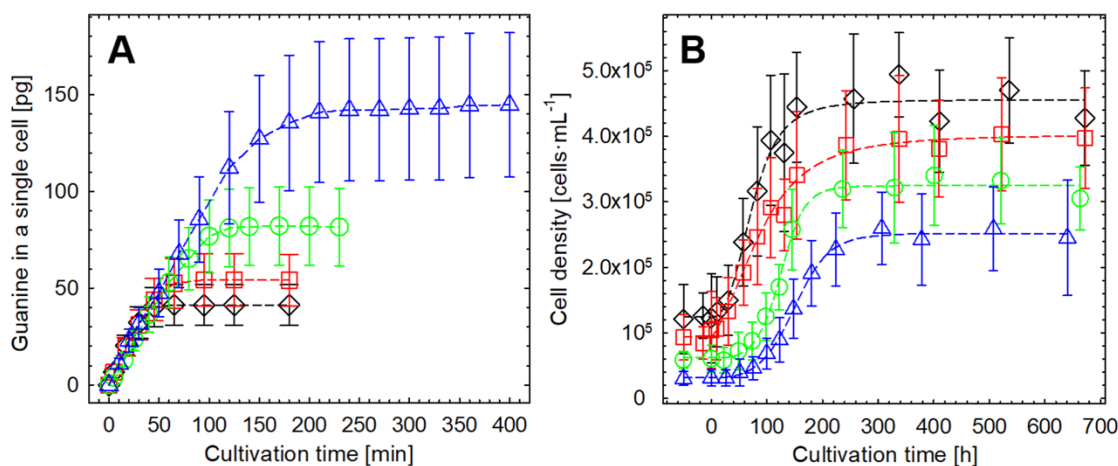
Fig. S2 (complementing Fig. 2). Rapid uptake of guanine by N-starved *A. carterae* and subsequent growth of the culture at the expense of accumulated stocks. (A) Accumulation of guanine reserves inside cells estimated from the uptake kinetics shown in Fig. 2. The cell densities were $(12.2 \pm 3.1^*) \times 10^4$ cells·mL^{-1} ($\diamond$), $(9.3 \pm 2.3) \times 10^4$ cells·mL^{-1} ($\square$), $(6.1 \pm 1.5) \times 10^4$ cells·mL^{-1} ($\bigcirc$), and $(3.1 \pm 0.8) \times 10^4$ cells·mL^{-1} ($\triangle$). The cells of the most diluted culture ($\triangle$) did not take all of the dissolved guanine from the medium, thus indicating that their maximum storage capacity was 143 ± 37 pg of crystalline guanine.

(B) Growth of cell cultures influenced by guanine reserves generated by the rapid uptake shown in **A**. Cultures were cultivated under identical conditions until they reached a new stationary phase. Their growth was monitored by cell counting (Bürker counting chamber; 2 replicates, 18 readouts). From the initial cell densities $(12.2 \pm 3.1) \times 10^4$ cells·mL^{-1} ($\diamond$), $(9.3 \pm 2.3) \times 10^4$ cells·mL^{-1} ($\square$), $(6.1 \pm 1.5) \times 10^4$ cells·mL^{-1} ($\bigcirc$), and $(3.1 \pm 0.8) \times 10^4$ cells·mL^{-1} ($\triangle$), the final cell densities increased by 3.7 ± 1.1, 4.2 ± 1.4, 5.3 ± 1.7 and 8.1 ± 3.1 times, respectively. The growths were fitted to five-parameter logistic function (RSQR ≥ 0.985).

*a number that follows the ± sign is a standard deviation (SD) in this work.
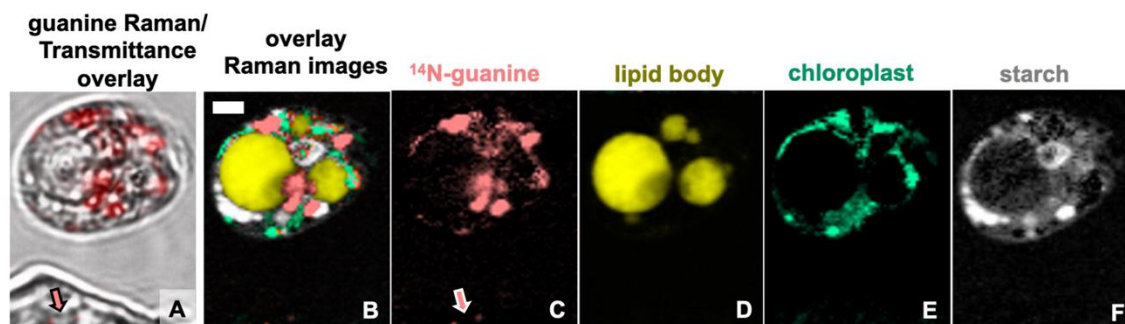
Fig. S3. N-starved *A. carterae* fed by ground fish scales. Bright field image (A) overlaid by guanine Raman map which is shown separately in panel C. Multicomponent Raman chemical map (B). Individual Raman maps of crystalline guanine (C), neutral lipids (D), chloroplasts (E) and floridean starch (F).

Outside the cell, a piece of fish scale containing a small amount of guanine is indicated by the pink arrows in (A) and (C). The cell was mapped 60 min after leachate from the fish scales was added. Raman mapping was conducted in dozens of replicates; a representative cell is shown. Scale bar: 2 μm.

The f/2 medium enriched with leachate from fish scales was prepared by maintaining 100 mg of ground dry fish scales (rainbow trout, Atlantic salmon) in 100 mL of the N-deficient f/2 medium at 25°C for 24 hours. The N-starved cells were transferred to the leachate cleaned free of coarse pieces of sediments. The presence of guanine was confirmed by Raman microscopy of 5 or more of randomly selected cells.
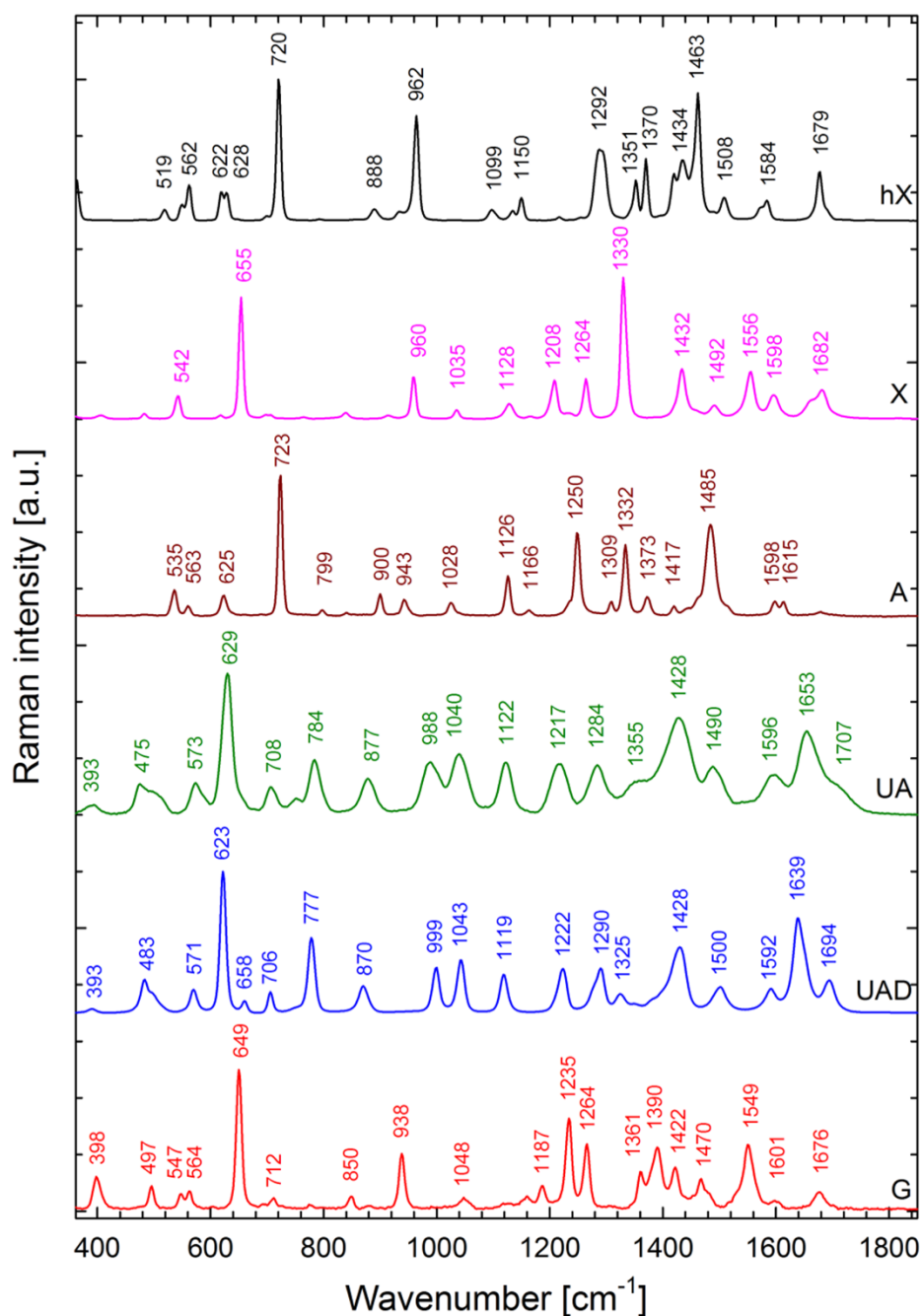
Fig. S4. Comparison of Raman spectra of crystalline anhydrous guanine (G) and crystalline forms structurally related purine bases (adenine – A; xanthine – X; hypoxanthine – hX; uric acid – UA, UAD). The spectrum UA shows uric acid detected in microalgae (*e.g.*, *Klebsormidium flaccidum*) and UAD shows the most similar spectrum of a single crystal of uric acid dihydrate for a specific crystal orientation. Uric acid present in some microalgae species could not be easily identified by means of the reference spectrum of polycrystalline anhydrous uric acid (see Fig. S5 for details). For the sake of clarity, only the range of characteristic vibrations (360 – 1850 cm^{-1}) is shown.
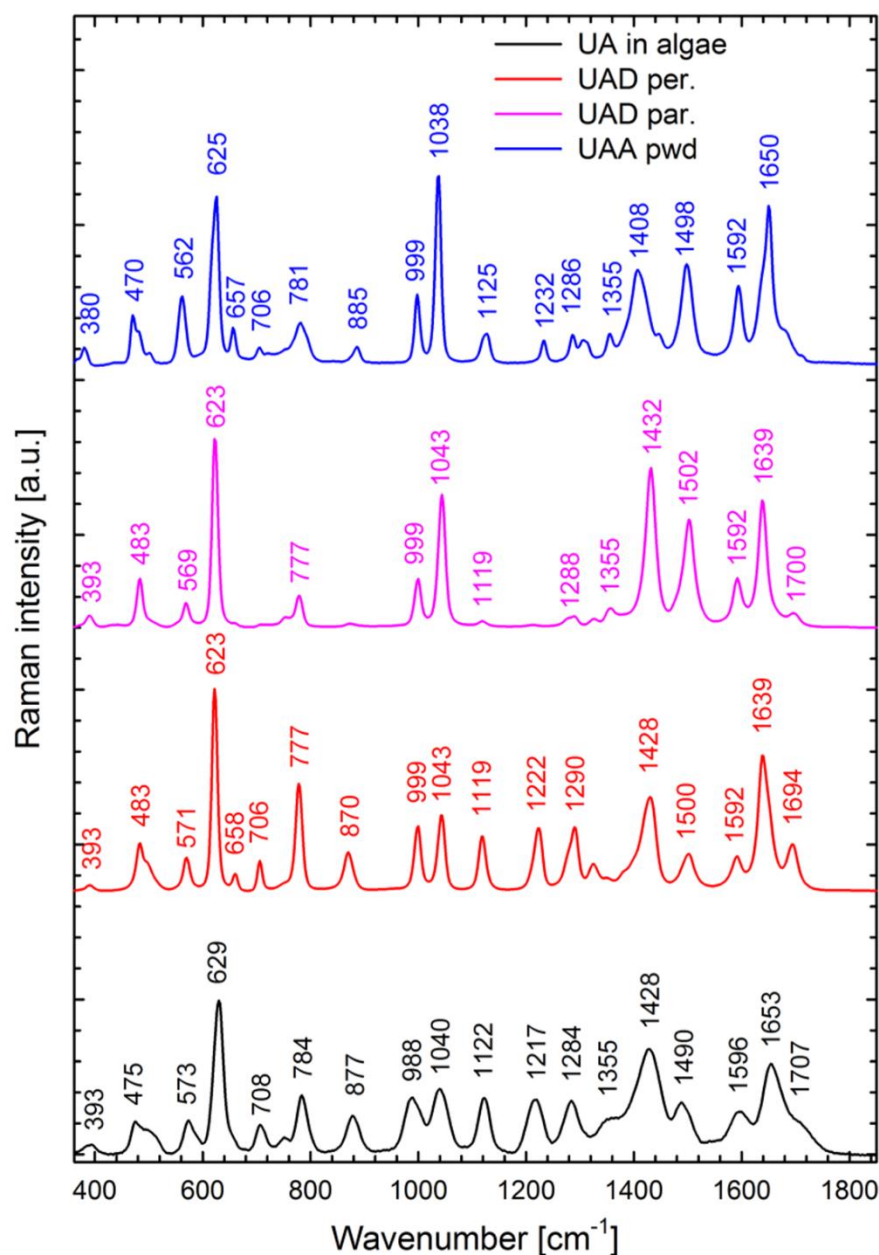
Fig. S5. Comparison of Raman spectra of different crystalline forms of uric acid. Uric acid was commercially available as an anhydrous polycrystalline powder (UAA pwd, blue line) from which it can be recrystallized under specific conditions to anhydrous or dihydrate single crystals (16). Unlike the polycrystalline UAA powder, the relative intensities of the Raman bands of single crystals were sensitive to the orientation of their flat plate faces with respect to the electric vector of the excitation beam, as was evidenced by the spectra of dihydrate uric acid single crystal oriented parallelly (UAD par, magenta line) and perpendicularly (UAD per, red line). Raman spectra of uric acid detected in microalgae (UA in algae, black line) were most similar to the spectrum of UAD per., nevertheless, Raman bands were broader, indicating a less strict crystal packing of the molecules.
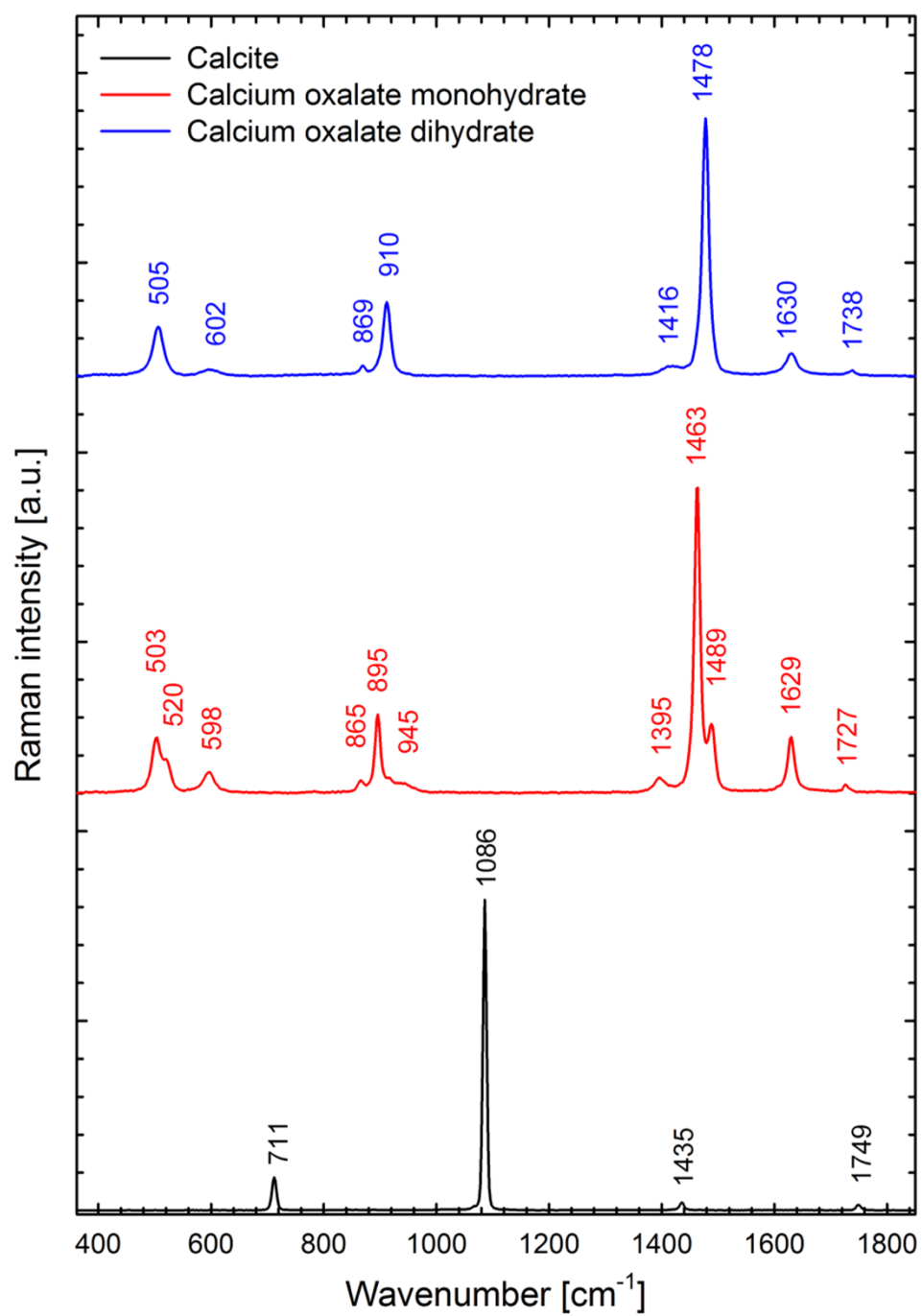
Fig. S6. Raman spectra of calcite, calcium oxalate monohydrate, and calcium oxalate dihydrate.
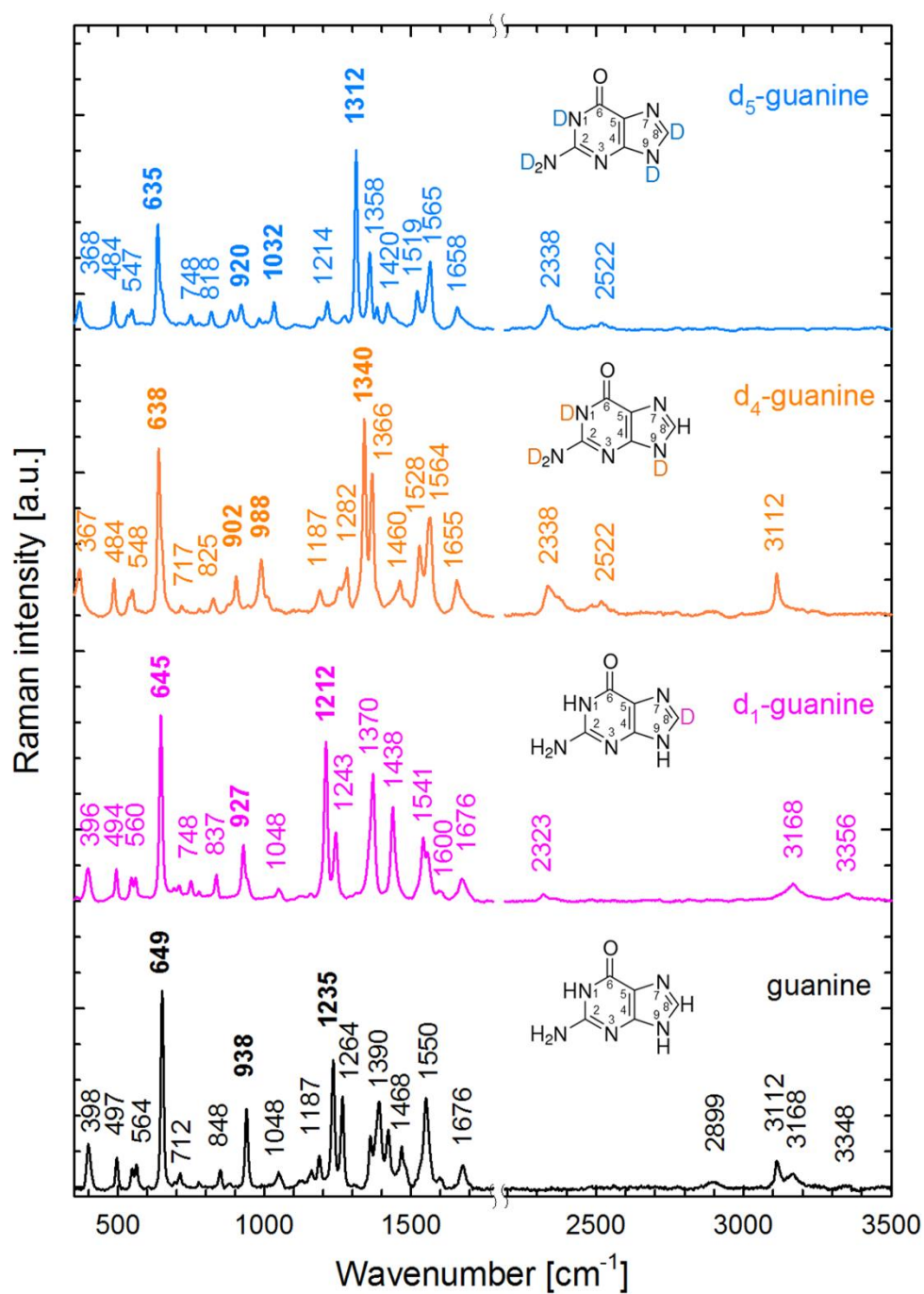
Fig. S7 (complementing Fig. 4). Raman spectra of normal guanine and its deuterium-labeled derivatives.

15
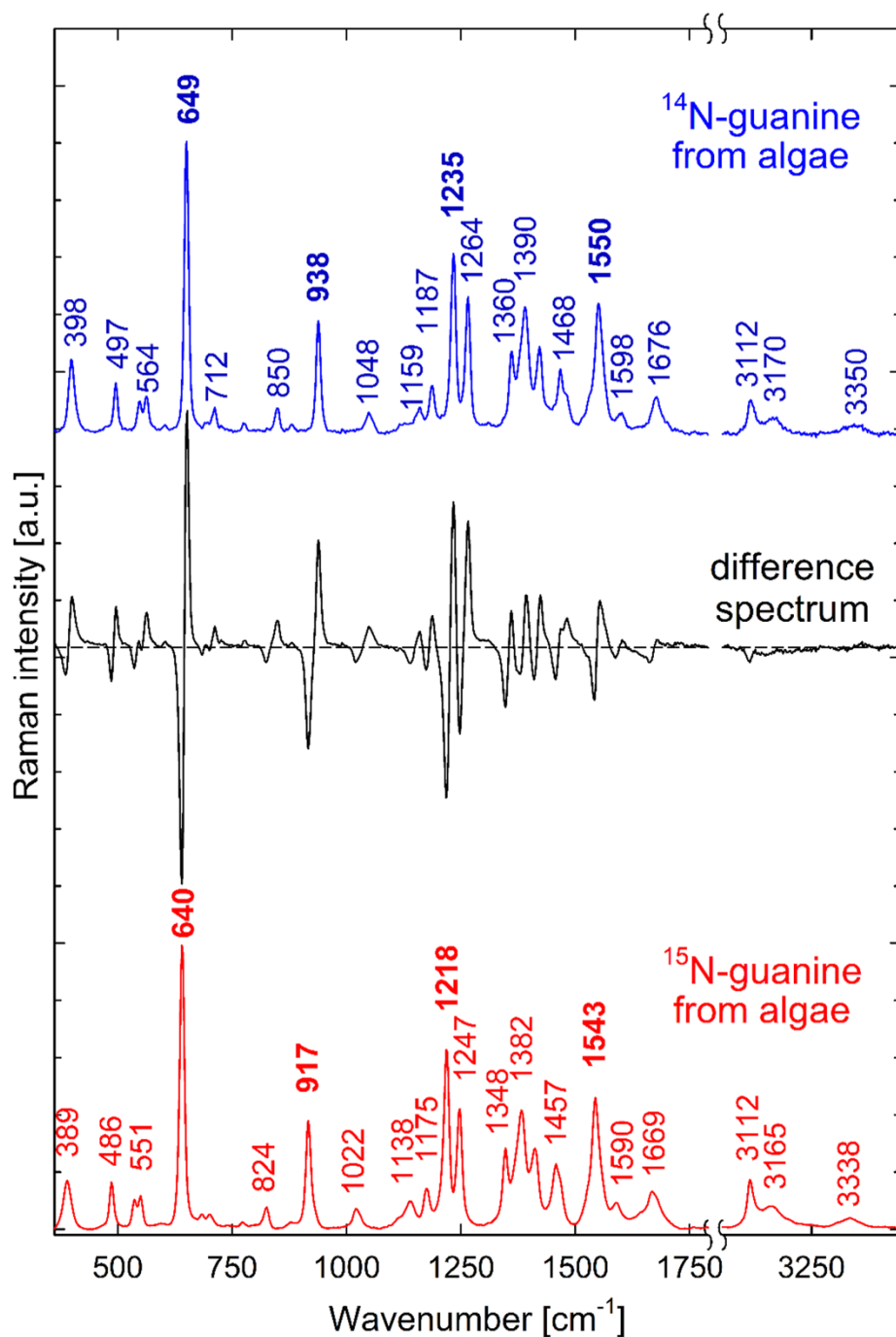
Fig. S8 (complementing Fig. 7). Direct comparison of Raman spectra of crystalline [14]N- and ^{15}N-guanine. To highlight the specific isotopic frequency shifts between both isotopic guanine species, the difference spectrum is shown for clarity. The differences in wavenumbers of individual bands of the [14]N- and ^{15}N-guanine were found sufficiently large for a reliable discrimination by Raman spectroscopy. In fact, the shifts were as large as 5–20 cm^{-1}, while the spectral resolution of our Raman spectrometer was better than ± 1 cm^{-1}.
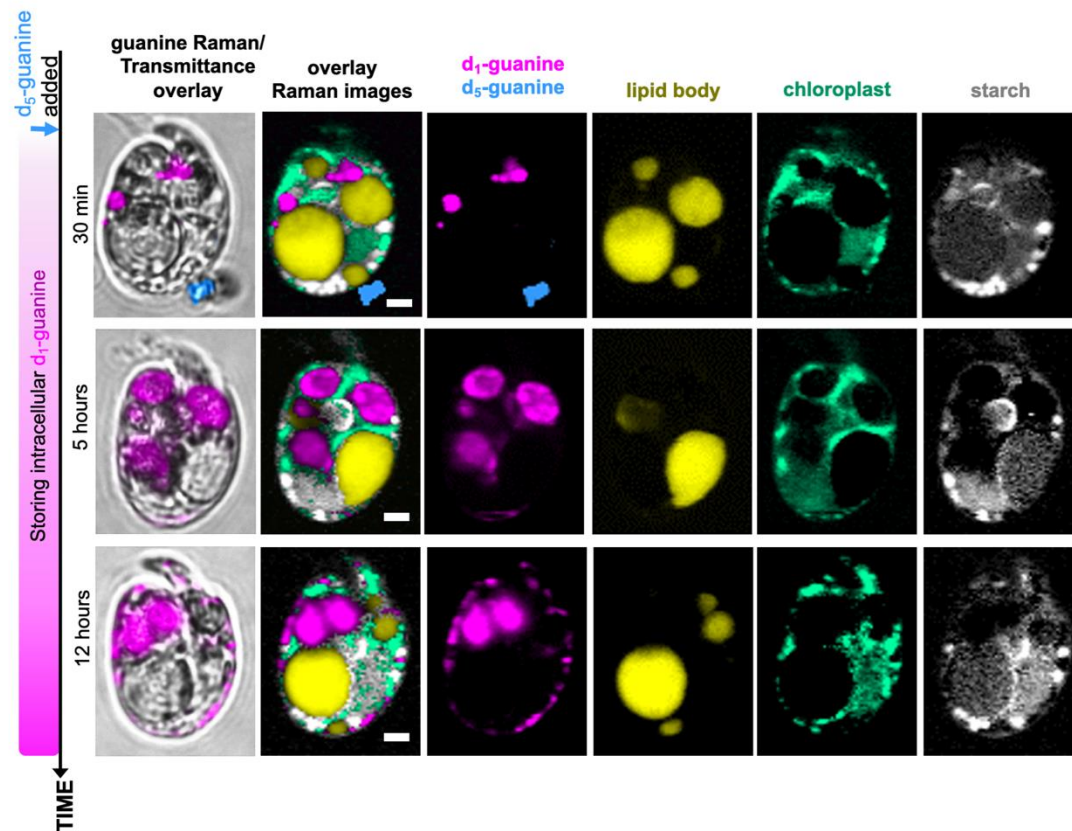
Fig. S9 (complementing Fig. 4). Uptake of guanine includes the exchange of deuterium for hydrogen atoms. Bright field images overlaid by guanine Raman maps (A, B, C), multicomponent Raman maps (D, E, F) and Raman maps of the most important components (G–R) of the N-starved *A. carterae* after the addition of solid crystalline d_5-guanine into N-depleted medium. Images collected 30 min, 5 hours and 12 hours after d_5-guanine addition. Raman maps of d_5- and d_1-guanine (G–I) are represented in blue and magenta, respectively, both in the corresponding Raman spectrum (Fig. S7) and in the images. Other colors: yellow – neutral lipids, green – chloroplasts, gray – floridean starch. Scale bars (D–F): 2 μm.
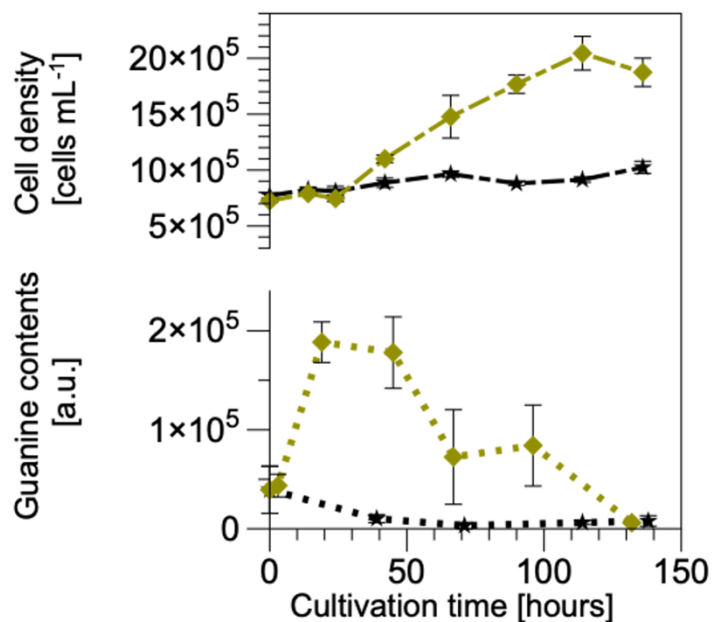
Fig. S10 (complementing Fig. 5). Nitrogen in ^{15}N-guanine inclusions originated directly from the supplied ^{15}N-labelled urea. *A. carterae* cell density stagnated in the control samples without N-feeding (black line, upper graph) and resumed growth after the addition of ^{15}N-labelled urea at concentration of 0.882 mM (N) (yellow line, upper graph). The corresponding intracellular crystalline guanine contents per cell are shown in the bottom graph representing Raman measurements of 5–12 cells.
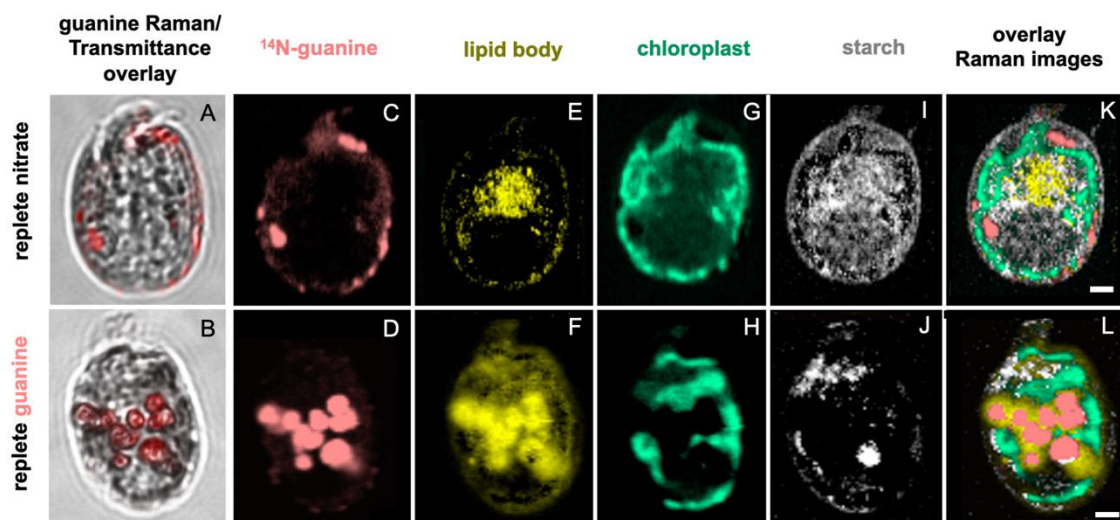
Fig. S11 (complementing Fig. 6). Localization of guanine inclusions in *A. carterae* fed by nitrate (top row) or guanine (bottom row) after 24 hours. Bright field images overlaid by guanine Raman maps (A, B). Separate Raman maps of guanine (C, D), neutral lipids (E, F), chloroplast (G, H), and floridean starch (I, J). Combined multicomponent Raman chemical map (K, L). Scale bar: 2 µm.
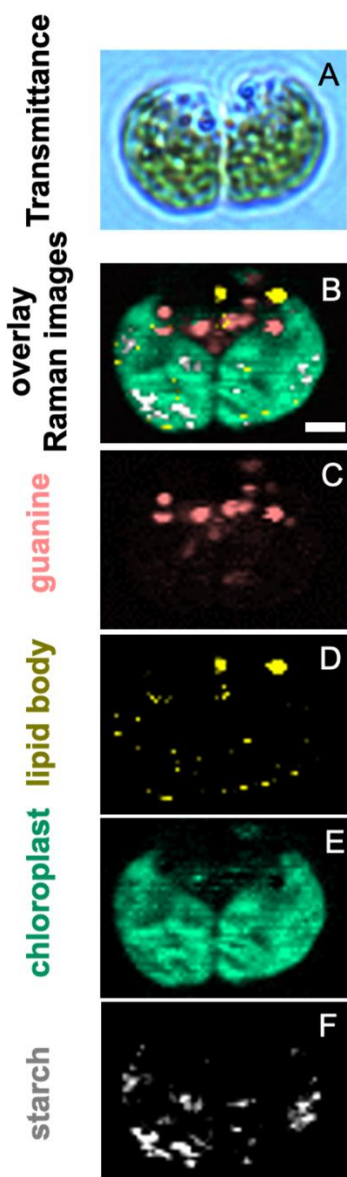
Fig. S12. Crystalline guanine inclusions in the dividing *Chlamydomonas reinhardtii*. Bright field image (A), multicomponent Raman chemical map (B), separate Raman map of guanine (C), neutral lipids (D), chloroplasts (E), and starch (F). Scale bar: 2 μm.
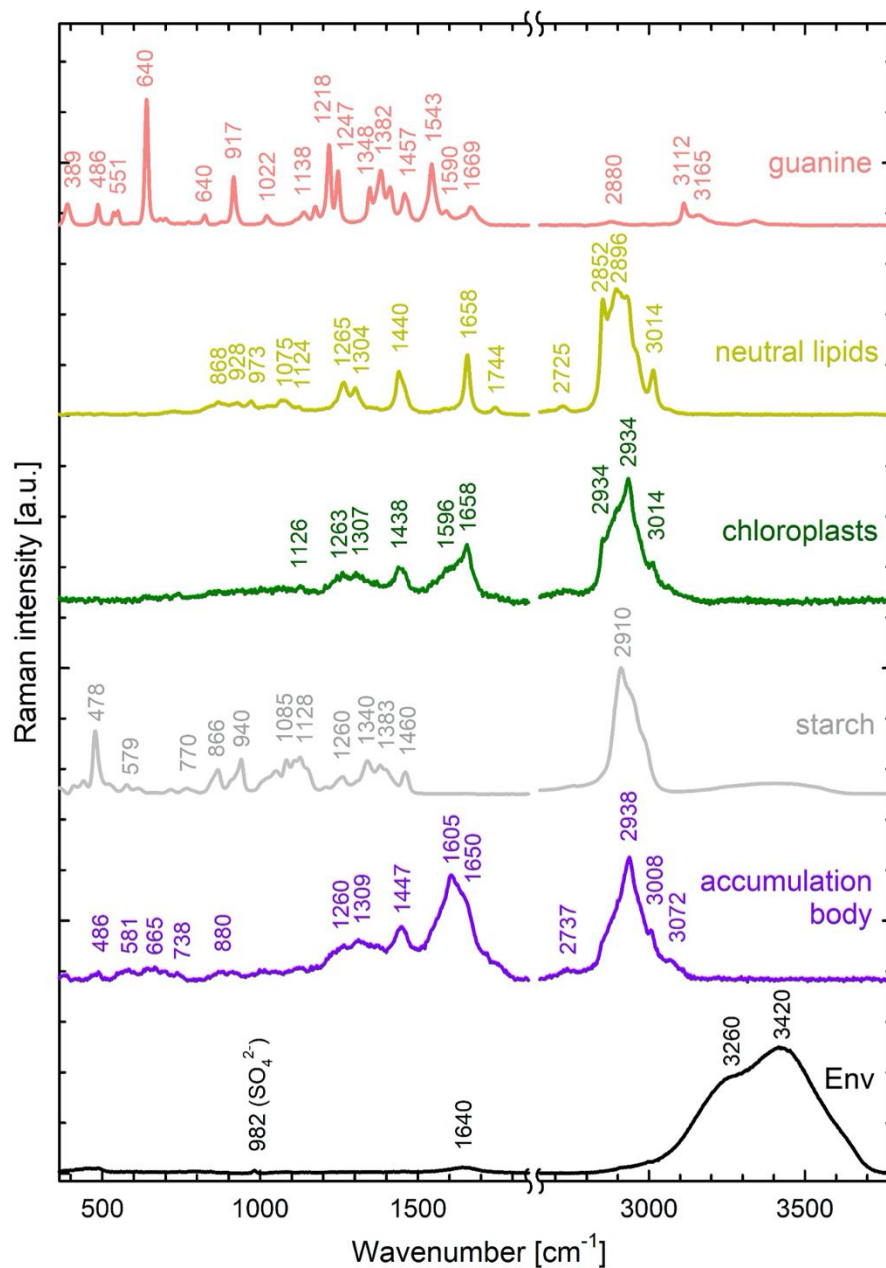
Fig. S13 (complementing Fig. 7). Raman spectra of pure components identified in *Symbiodiniaceae* **cells re-fed with ^{15}N-NaNO$_3$.** The full–range Raman spectra of crystalline ^{15}N-guanine, neutral lipids, chloroplasts, floridean starch, accumulation body, and seawater surrounding the cell were used for multivariate decomposition of Raman maps of *Symbiodiniaceae* cells and construction of chemical maps shown in Fig. 7.

21
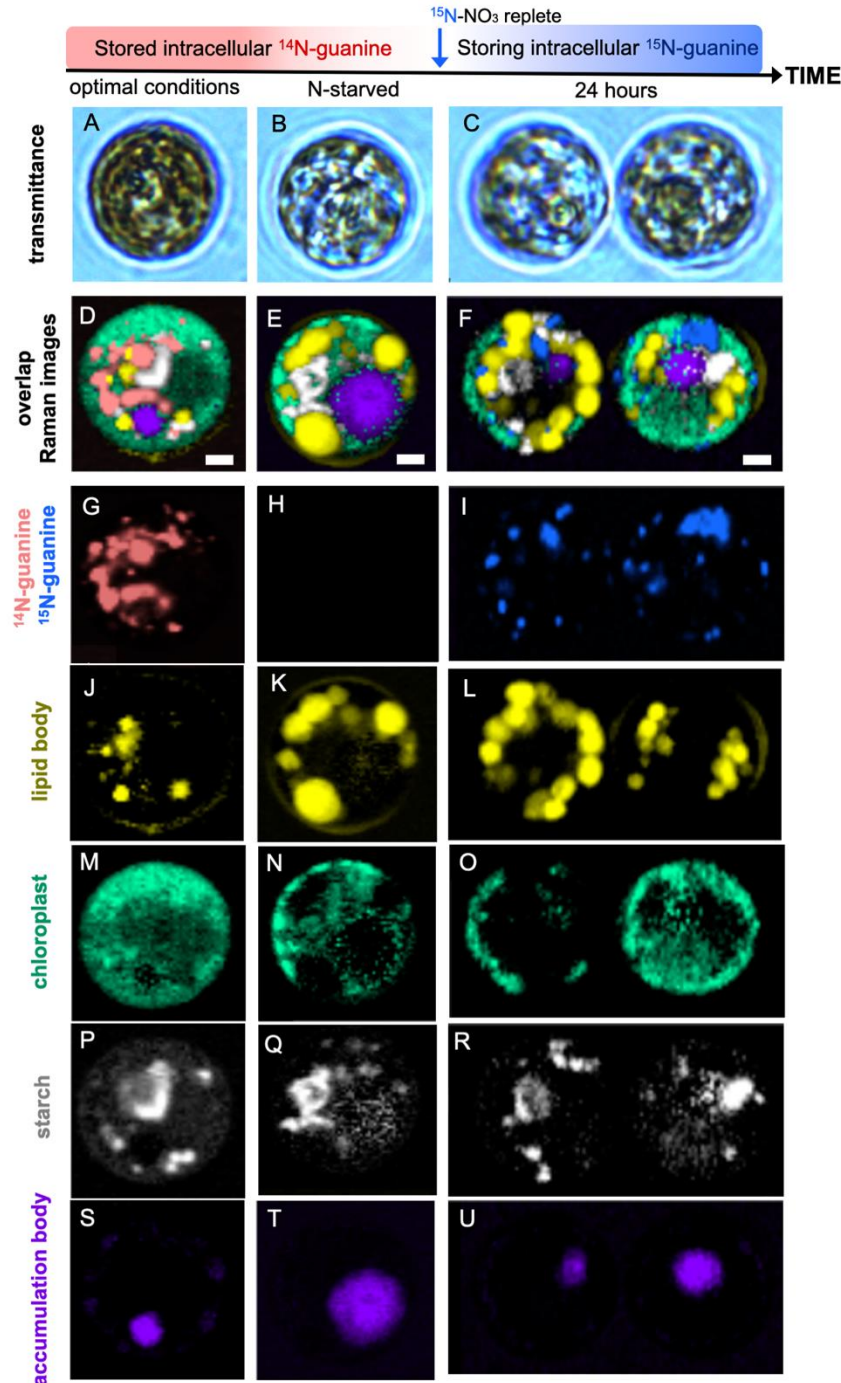
Fig. S14 (complementing Fig. 7). Raman chemical maps of *Symbiodiniaceae* cells extracted from the tissue of the coral *Euphylia paraancora*. *Algae* from corals cultivated under optimal nutrient conditions in an aquarium shop contained guanine crystals (D, G). After four-month cultivation of the entire holobiont in N-depleted seawater, they lost their guanine reserves (E, H). When corals were transferred into seawater enriched by 0.3 mM ^{15}N-NaNO$_3$, newly synthesized ^{15}N-guanine crystals appeared within 24 h (F, I) in algae as documented by the highly specific Raman spectra clearly distinguishing between ^{14}N- and ^{15}N-guanine (Fig. S8). Raman mapping was replicated (n=12 or more cells) and conducted on three holobiont replicates; representative cells are shown. Scale bar: 2 μm.
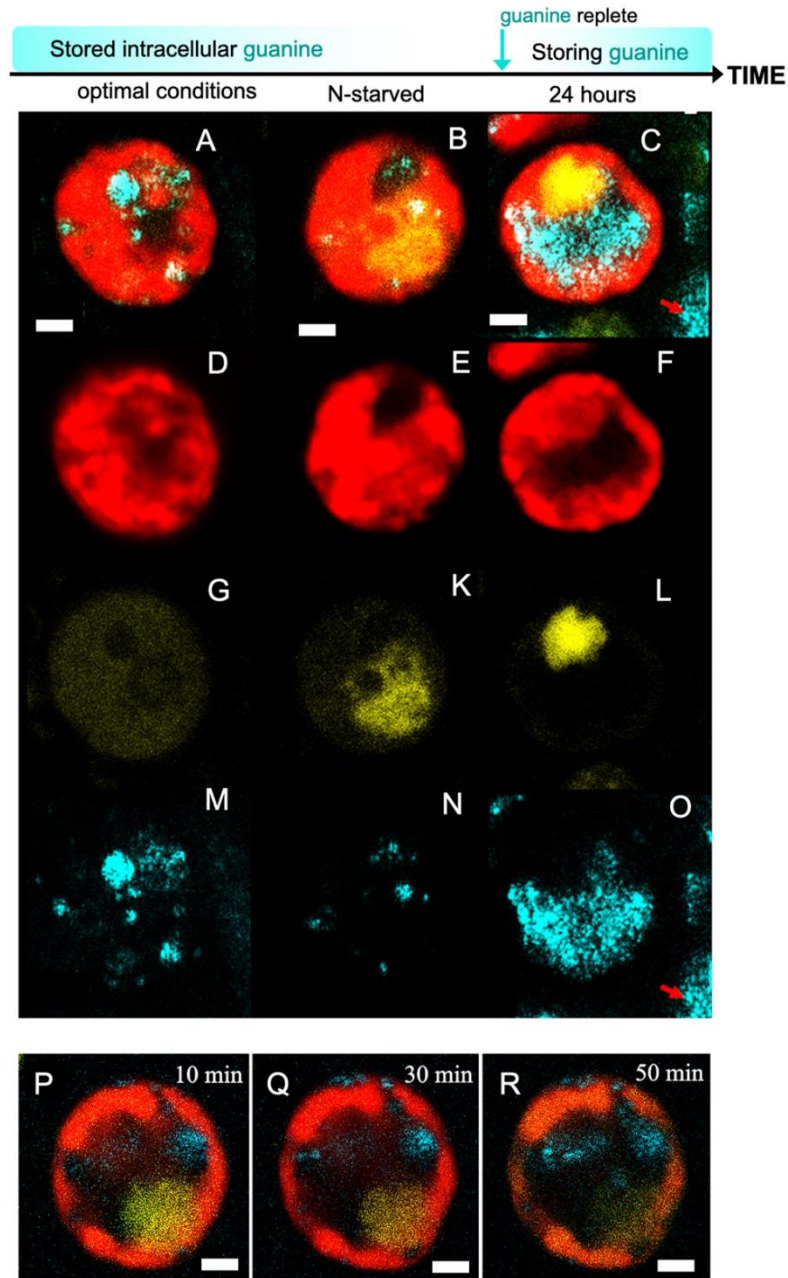
Fig. S15 (complementing Fig. 7). Confocal fluorescence and reflectance images of *Symbiodiniaceae* cells extracted from the coral *A. millepora*. Combined images (A–C), chlorophyll fluorescence 670 – 700 nm (D–F), fluorescence at 500 – 560 nm assigned predominantly to accumulation body (G–L), and 488 nm reflection of guanine microcrystals (M–O) of cells extracted from freshly reef collected corals (left column), from N-depleted corals (middle column) and from the N-depleted symbionts 24 h after the supplementation by guanine powder (right column). Combined images (P–R) illustrate the time evolution of the uptake showing the same cell 10 min (P), 30 min (Q) and 50 min (R) after the addition of guanine. Gradual bleaching of the fluorescence is visible due to laser scanning. Red arrow in images C and O indicate undissolved crystalline guanine outside the cell. Scale bar: 2 µm.
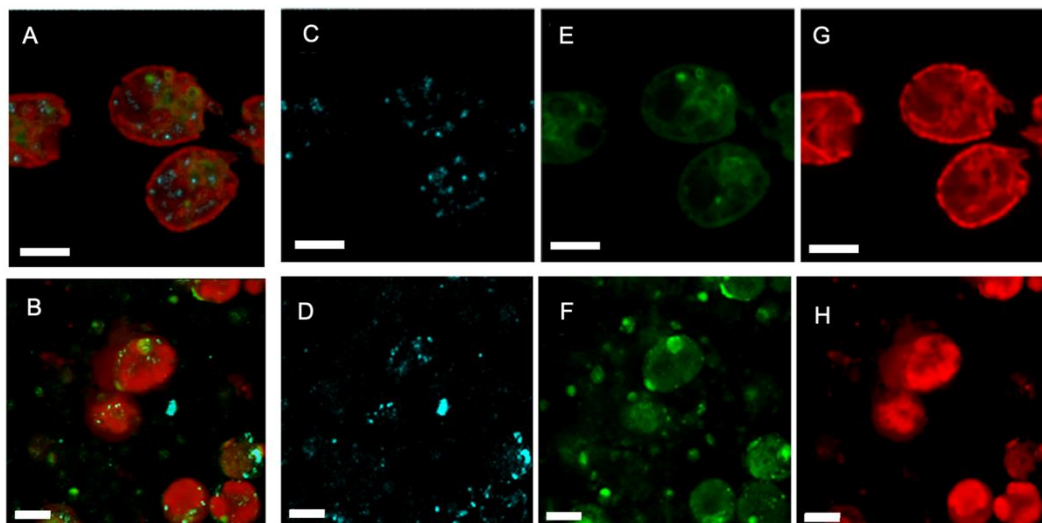
Fig. S16. (complementing Fig. 7D-F and Fig. S15). Confocal images of _A. carterae_ and _Symbiodiniaceae_ cells after N feeding. Confocal images of free-living _A. carterae_ cells (A, C, E, G) and _Symbiodiniaceae_ cells (B, D, F, H) extracted from reef _Zoanthus_ sp. and fed with guanine powder highlighting the crystalline inclusions in a reflection mode of 488 nm laser line (C, D); fluorescence emission at 500 – 560 nm from accumulation bodies and other organelles (E, F); fluorescence emissions of chlorophyll from chloroplasts 670 – 700 nm (G, H); and overlaid combined image (A, B). The presence of crystalline guanine within cells from the same batch was confirmed by Raman microscopy. Scale bar: 5 µm.

Movie S1 (separate file, complementing Fig. 1) shows a sequence captured in real time by polarization microscopy. The cover figure shows bright field (A, C) and polarization images (B, D) of an N-starved *A. carterae* cell before (A, B) and 14 minutes after feeding with dissolved guanine (C, D). The video will start upon clicking the cover figure.

SI Appendix References

1. S. Rosset, C. D'Angelo, J. Wiedenmann, Ultrastructural Biomarkers in Symbiotic Algae Reflect the Availability of Dissolved Inorganic Nutrients and Particulate Food to the Reef Coral Holobiont. *Frontiers in Marine Science* **2**, 103 (2015).
2. S. Rosset, J. Wiedenmann, A. J. Reed, C. D'Angelo, Phosphate deficiency promotes coral bleaching and is reflected by the ultrastructure of symbiotic dinoflagellates. *Marine Pollution Bulletin* **118**, 180-187 (2017).
3. R. R. L. Guillard (1975) Culture of phytoplankton for feeding marine invertebrates. in *Culture of Marine Invertebrate Animals*, eds W. L. Smith, M. H. Chanley (Plenum Press, New York, USA), pp 26-60.
4. S. H. Yalkowsky, Y. He, P. Jain, *Handbook of Aqueous Solubility Data* (CRC Press, New York, U.S.A., ed. Second, 2010).
5. D. B. Dunn, R. H. Hall, "Purines, Pyrimidines, Nucleosides, and Nucleotides: Physical Constants and Spectral Properties" in Handbook of Biochemistry and Molecular Biology. (CRC Press, 2018), 10.1201/b21846-50 chap. Purines, Pyrimidines, Nucleosides, and Nucleotides: Physical Constants and Spectral Properties.
6. Š. Moudříková *et al.*, Raman and fluorescence microscopy sensing energy-transducing and energy-storing structures in microalgae. *Algal Research* **16**, 224-232 (2016).
7. Š. Moudříková, L. Nedbal, A. Solovchenko, P. Mojzeš, Raman microscopy shows that nitrogen-rich cellular inclusions in microalgae are microcrystalline guanine. *Algal Research* **23**, 216-222 (2017).
8. Š. Moudříková *et al.*, Quantification of polyphosphate in microalgae by Raman microscopy and by a reference enzymatic assay. *Analytical Chemistry* **89**, 12006-12013 (2017).
9. J. W. Eaton, D. Bateman, S. Hauberg, R. Wehbring (2015) GNU Octave version 4.0.0 manual: a high-level interactive language for numerical computations. (CreateSpace Independent Publishing Platform).
10. E. S. Reynolds, The use of lead citrate at high pH as an electron-opaque stain in electron microscopy. *Journal of Cell Biology* **17**, 208-212 (1963).
11. J. M. Delabar, M. Majoube, Infrared and Raman-spectroscopic study of N-15 and D-substituted guanines. *Spectrochimica Acta Part a-Molecular and Biomolecular Spectroscopy* **34**, 129-140 (1978).
12. H. Ishikawa, Hydrolysis of nucleotides by acid. *The Journal of Biochemistry* **22**, 385-395 (1935).
13. H. W. Bischoff, H. C. Bold, *Some soil algae from Enchanted Rock and related algal species*, Phycological studies (University of Texas Publication, Austin, Texas, 1963), vol. IV.
14. V. Zachleder, I. Šetlík, Effect of irradiance on the course of RNA-synthesis in the cell cycle of *Scenedesmus quadricauda*. *Biol Plantarum* **24**, 341-353 (1982).
15. R. Rippka, J. Deruelles, J. B. Waterbury, M. Herdman, R. Y. Stanier, Generic assignments, strain histories and properties of pure cultures of cyanobacteria. *Journal of General Microbiology* **111**, 1-61 (1979).
16. F. Liu, D. E. Hooks, N. Li, N. A. Mara, J. A. Swift, Mechanical properties of anhydrous and hydrated uric acid crystals. *Chem. Mat.* **30**, 3798-3805 (2018).

BRIEF COMMUNICATION

Check for updates

Revisiting biocrystallization: purine crystalline inclusions are widespread in eukaryotes

Jana Pilátová [ID]1,2,3✉, Tomáš Pánek[4], Miroslav Oborník[3,5], Ivan Čepička[4] and Peter Mojzeš [ID]2

Despite the widespread occurrence of intracellular crystalline inclusions in unicellular eukaryotes, scant attention has been paid to their composition, functions, and evolutionary origins. Using Raman microscopy, we examined >200 species from all major eukaryotic supergroups. We detected cellular crystalline inclusions in 77% species out of which 80% is composed of purines, such as anhydrous guanine (62%), guanine monohydrate (2%), uric acid (12%) and xanthine (4%). Our findings shifts the paradigm assuming predominance of calcite and oxalates. Purine crystals emerge in microorganisms in all habitats, e.g., in freshwater algae, endosymbionts of reef-building corals, deadly parasites, anaerobes in termite guts, or slime molds. Hence, purine biocrystallization is a general and ancestral eukaryotic process likely present in the last eukaryotic common ancestor (LECA) and here we propose two proteins omnipresent in eukaryotes that are likely in charge of their metabolism: hypoxanthine-guanine phosphoribosyl transferase and equilibrative nucleoside transporter. Purine crystalline inclusions are multifunctional structures representing high-capacity and rapid-turnover reserves of nitrogen and optically active elements, e.g., used in light sensing. Thus, we anticipate our work to be a starting point for further studies spanning from cell biology to global ecology, with potential applications in biotechnologies, bio-optics, or in human medicine.

Crystalline inclusions, conspicuous in many unicellular eukaryotes (protists), have attracted the attention of scientists since the emergence of microscopy. After Charles Darwin documented the crystal-like particles in flagellates [1], Haeckel coined the term "biocrystal" for calcite ($CaCO_3$), celestite ($SrSO_4$), silica (SiO_2), and oxalate in protists [2]. Biocrystals or biogenically originated crystalline inclusions of either organic or inorganic chemical nature, are typically formed inside vacuoles and grow into shells and scales on cell surfaces, e.g., calcite scales of coccolithophores that take part in the global carbon cycle [3]. On the other hand, rarely reported purine inclusions of guanine, xanthine, hypoxanthine, or uric acid are often overlooked [4–8]. The recent resurgence of research on purine inclusions has shown rapid uptake kinetics of different nitrogen compounds that are converted into massive guanine nitrogen stores with sufficient capacity, in some cases, to support three consecutive cell cycles [8]. As a fundamental biogenic element, nitrogen represents a great share of biotic elemental stoichiometry, from cellular to global scales, impacting Earth's climate [9]. Biocrystalized guanine polarizes and reflects light in many animals, e.g., fish with the opalescent guanine crystals in the iridocytes of their scales resembling glittery camouflage, or as an adaptation for vision in scallops, deep-sea fishes, and arthropods that exhibit guanine-reflective retinal tapeta in their eyes [10–12] with analogous functions in alveolates [5, 13, 14].

Using Raman microscopy, we have screened all major eukaryotic groups, >200 species, most of them for the first time, searching for birefringent (light-polarizing) crystalline inclusions (for Raman spectra, see Figs. S1–S5). They are wobbling by Brownian motion inside vacuoles (Movies S1–S8). We detected common biocrystals in accordance with previously described crystalline inclusions, such as calcite, oxalate, celestite, and baryte [3], together with other birefringent structures (i.e., starch, chrysolaminarin, strontianite, and newly observed crystals of sterols and carotenoids). However, apart from these, we found a surprisingly broad occurrence of purines (>80% of examined species containing crystals), particularly crystalline anhydrous guanine (62%), uric acid (12%), xanthine (4%) and guanine monohydrate (2%), (Fig. 1; Table S1; Supplementary Text). We found anhydrous guanine crystals as dominant type in model and biotechnologically important species. It commonly occurs in cosmopolitan marine and freshwater algae—including bloom-causing dinoflagellates, in the endosymbionts of corals—crucial for the maintenance of entire coral reef ecosystems, in unicellular parasites of warm-blooded animals and in cellulose-digesting anaerobic symbionts of termites, or in slime molds. Additionally, we found uric acid in cryptophytes, diatoms, zygnematophytes, and klebsormidiophytes. We identified xanthine crystals in Amoebozoa and in biotechnologically important microalgae (e.g., *Chlorella* and *Isochrysis*). We also discovered pure guanine

[1]Department of Experimental Plant Biology, Faculty of Science, Charles University, Prague 2, Czech Republic. [2]Institute of Physics, Faculty of Mathematics and Physics, Charles University, Prague 2, Czech Republic. [3]Institute of Parasitology, Czech Academy of Sciences, České Budějovice, Czech Republic. [4]Department of Zoology, Faculty of Science, Charles University, Prague 2, Czech Republic. [5]Department of Molecular Biology and Genetics, Faculty of Science, University of South Bohemia, České Budějovice, Czech Republic. ✉email: jana.pilatova@natur.cuni.cz
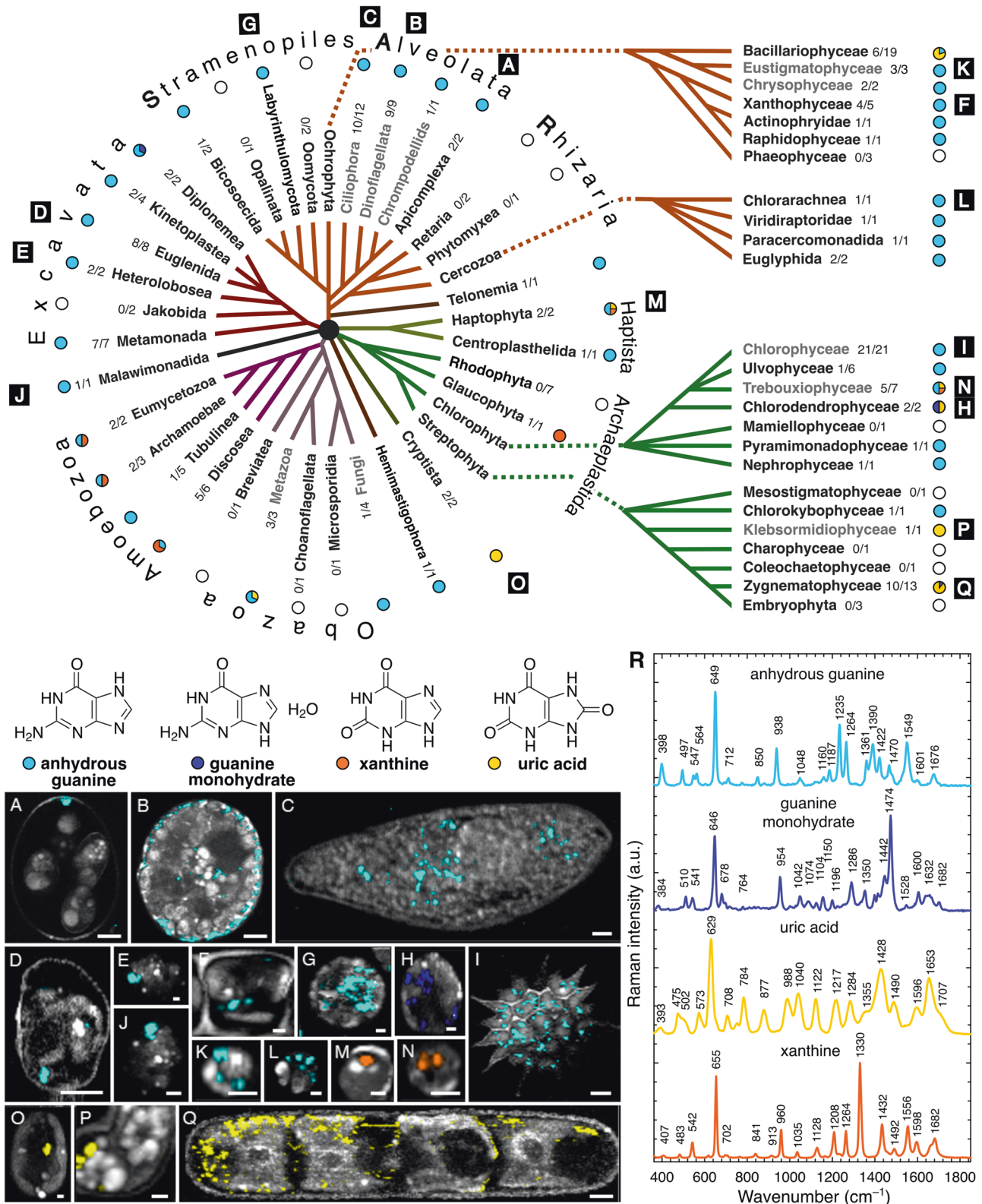
Fig. 1 Distribution of purine inclusions identified by Raman microscopy in the eukaryotic tree of life. The occurrence of anhydrous guanine (cyan), guanine monohydrate (violet), uric acid (yellow) and xanthine (orange) are illustrated in the evolutionary scheme as pie charts and in Raman maps (**A**–**Q**) together with the Raman spectra (**R**). Ratio of species positively tested for purine inclusions out of the total number of screened samples are expressed for each taxonomic category. Lineages highlighted in gray possess purine inclusions already reported elsewhere. **A** *Eimeria maxima*, (**B**) *Glenodinium foliaceum*, (**C**) *Paramecium* sp., (**D**) *Eutreptiella gymnastica*, (**E**) *Naegleria gruberi*, (**F**) *Tribonema aequale*, (**G**) *Schizochytrium* sp., (**H**) *Tetraselmis subcordiformis*, (**I**) *Pediastrum duplex*, (**J**) *Gefionella okellyi*, (**K**) *Nannochloropsis oculata*, (**L**) *Bigelowiella natans*, (**M**) *Isochrysis* sp., (**N**) *Chlorella vulgaris*, (**O**) *Cryptomonas* sp., (**P**) *Klebsormidium flaccidum*, (**Q**) *Penium margaritaceum*. Scale bars: 5 μm (**A**–**D**, **I**, **Q**), 1 μm (**E**–**H**).
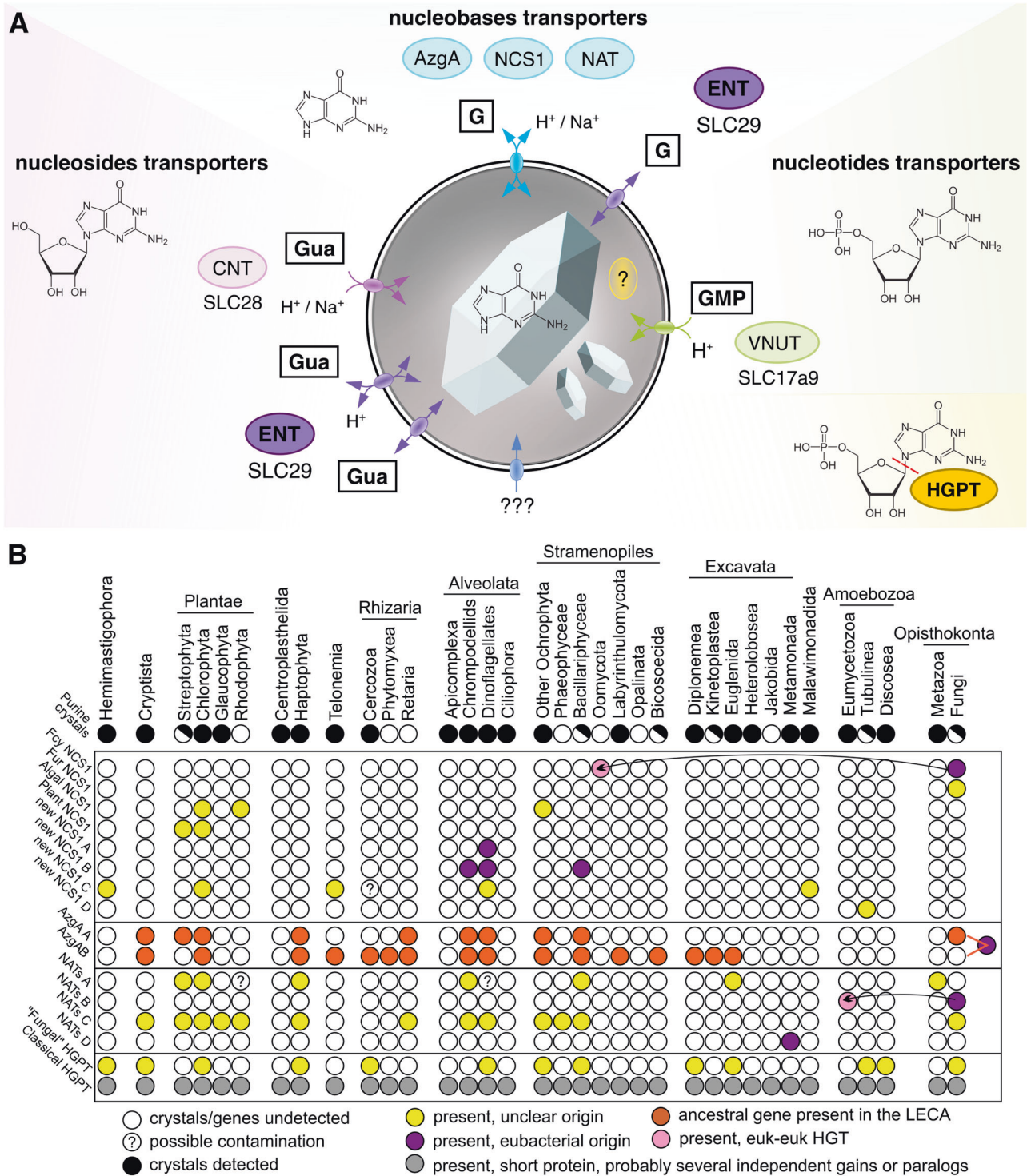
Fig. 2 Proposed scheme of guanine inclusions metabolism with emphasis on the transporters potentially involved. A Examples of analyzed protein families of nucleobases, nucleosides and nucleotides transporters: CNT concentrative nucleoside transporter, ENT equilibrative nucleoside transporter, NAT nucleobase-ascrobate transporter, NCS1 nucleobase-cation symporter 1, SLC solute carrier family, VNUT vesicular nucleotide transporter. Metabolic enzyme HGPT hypoxanthine-guanine phosphoribosyl transferase is located in the cytoplasm and possibly inside of the crystal containing vesicles (? in yellow). ENT and HGPT protein families show possibly general distribution among eukaryotes (Fig. S8, Table S3). There may be more unkown tranporters and enzymes or crystallization nuclei involved (???). B Summary table of phylogenetic distribution of the purine transporters in relation to the purine crystals occurrence in tested phylogenetic lines: NCS1, NAT, AzgA, and the metabolic enzyme of salvage pathway—HGPT. There are notions on horizontal gene transfer (HGT) in two cases. In the case of AzgA we anticipate a possible origin in last eukaryotic common ancestor (LECA).

monohydrate in marine diplonemids or its admixture to uric acid in green algae. Particular triggers for purine inclusion formation are unknown, but they are often produced after transfer to fresh growth media, media containing surplus sources of nitrogen, and under stress conditions [4, 6]. The lack of purine inclusions in some strains (Table S1) does not exclude the ability to form biocrystals because the induction of crystal formation may occur only under specific conditions. As previously reported, purine crystals may act as nitrogen storage for microalgae in which they are formed in a type of luxury uptake resulting in net removal of nitrogen from the medium [8].

Our results suggest that purine crystals might have been present in the last eukaryotic common ancestor (LECA), becoming the first type of biocrystals in eukaryotes contingent on the emergence of cell compartmentalization in early eukaryotes. We employed comparative transcriptomics and genomics to identify candidate proteins of ancient pathways responsible for purine crystal formation (PCF). Firstly, we proved the key enzyme of the salvage pathway—hypoxanthine-guanine phosphoribosyl transferase (HGPT) to be omnipresent among eukaryotes (Fig. 2, Fig. S8)—it might be responsible for purine release from its derivatives during PCF or its reusage after crystal degradation. Then, we focused on the transporters of nucleobases (i.e., purines), nucleosides and nucleotides that must be delivered to the vesicles where crystals are formed (Fig. 2). Despite the purine transporters were considered omnipresent among eukaryotes [15], our exhaustive homolog search and subsequent phylogenetic analyses challenged the ubiquity of the three of them (Supplementary Text). Nucleobase-cation symporter 1 exists in several paralogs in eukaryotes, at least three of them emerged by relatively recent horizontal gene transfer from eubacteria (Figs. S8, S9). Nucleobase-ascorbate transporter emerged independently four times in eukaryotes (Fig. S10). Only the AzgA could be possibly present in the LECA (Fig. 2, Fig. S11), although distribution of both its eukaryotic paralogs is rather limited. Finally, the solo-purine transporters are absent in some of the purine crystal-forming groups (Heterolobosea, Ciliophora, and Apicomplexa) indicating that they do not participate in PCF.

The exact distribution, function, and localization of nucleotide transporters (e.g., vesicular nucleotides transporter) cannot be reliably predicted in silico without further biochemical studies [16]. Our analyses of nucleoside transporters showed that the concentrative nucleoside transporters (CNT) occur only infrequently (Table S2). However, the equilibrative nucleoside transporters (ENT) are omnipresent in eukaryotes (Table S3) becoming the most promising target for further studies on nucleotide/nucleoside/nucleobase transporters involved in PCF. Members of the ENT family are specific for nucleosides and nucleobases, operating in a bidirectional mode or as cation symporters, with different localization in the plasma membrane or in intracellular vesicles [17]. The metabolism and transport of nucleobases, nucleosides and nucleotides is essential for all organisms and hence transporters involved in PCF may play multiple roles in the cell and are retained even when the lineage has lost the ability to form purine crystals. Thus, extensive biochemical and proteomic studies have to be employed to answer this question in future.

Due to low-solubility and high-capacity, purine inclusions might have emerged as an adaptation to nitrogen detoxification, protection against exposure to high levels of ammonia or nitrates, utilizing vacuoles as a versatile sequestration space. Simultaneously, as nitrogen-rich storage, they became a competitive advantage during nitrogen fluctuations. Currently, the nitrogen-rich microbes might be of use in biofertilizers. The value of algae-based food supplements may be limited by the medical issues associated with regular intake of purines, e.g., hyperuricemia manifesting as gouty arthritis [18]. Conversely, unicellular model organisms can help to understand the biocrystallization in the

gouty joints yielding in its potential treatment, which is currently missing [18]. The exceptional optical activity of purine crystals can be exploited in bio-optics [10]. In conclusion, purine biocrystallization is a general and an ancestral eukaryotic process operating by an as-yet-unknown mechanism bringing enough material for future studies spanning from cell biology to global ecology.

DATA AVAILABILITY
All data generated or analysed during this study are included in this published article and its Supplementary Information files.

REFERENCES
1. Darwin C. Journal of Researches Into the Geology and Natural History of the Varoius Countries Visited by HMS Beagle, Under the Command of Captain Fitzroy from 1832 to 1836 by Charles Darwin. Colburn, London; 1840.
2. Haeckel E. Kristallseelen: Studien über das anorganische Leben. Leipzig: Alfred Kröner Verlag; 1917.
3. Raven JA, Knoll AH. Non-skeletal biomineralization by eukaryotes: matters of moment and gravity. Geomicrobiol J. 2010;27:572–84.
4. Creutz CE, Mohanty S, Defalco T, Kretsinger RH. Purine composition of crystalline cytoplasmic inclusions of *Paramecium tetraurelia*. Protist. 2002;153:39–45.
5. Jantschke A, Pinkas I, Hirsch A, Elad N, Schertel A, Addadi L, et al. Anhydrous β-guanine crystals in a marine dinoflagellate: Structure and suggested function. J Struct Biol. 2019;207:12–20.
6. Moudříková Š, Nedbal L, Solovchenko A, Mojžeš P. Raman microscopy shows that nitrogen-rich cellular inclusions in microalgae are microcrystalline guanine. Algal Res. 2017;23:216–22.
7. Roush AH. Crystallization of purines in the vacuole of *Candida utilis*. Nature. 1961;190:449.
8. Mojžeš P, Gao L, Ismagulova T, Pilátová J, Moudříková Š, Gorelová O, et al. Guanine, a high-capacity and rapid-turnover nitrogen reserve in microalgal cells. Proc Natl Acad Sci. 2020;117:32722–30.
9. Sterner RW, Elser JJ. Ecological stoichiometry: the biology of elements from molecules to the biosphere. Encyclopedia of Ecology, Five-Volume Set. Princeton, New Jersey, USA: Princeton University Press; 2002.
10. Tadepalli S, Slocik JM, Gupta MK, Naik RR, Singamaneni S. Bio-optics and bio-inspired optical materials. Chem Rev. 2017;117:12705–63.
11. Palmer BA, Taylor GJ, Brumfeld V, Gur D, Shemesh M, Elad N, et al. The image-forming mirror in the eye of the scallop. Science. 2017;358:1172–5.
12. Wagner A, Wen Q, Pinsk N, Palmer BA. Functional molecular crystals in biology. Isr J Chem. 2021;61:668–78.
13. Kuhlmann HW, Bräucker R, Schepers AG. Phototaxis in *Porpostoma notatum*, a marine scuticociliate with a composed crystalline organelle. Eur J Protistol. 1997;33:295–304.
14. Yamashita H, Kobiyama A, Koike K. Do uric acid deposits in zooxanthellae function as eye-spots? PLoS ONE. 2009;4:1–9.
15. Kourkoulou A, Pittis AA, Diallinas G. Evolution of substrate specificity in the nucleobase-ascorbate transporter (NAT) protein family. Micro Cell. 2018;5:280–92.
16. Sawada K, Echigo N, Juge N, Miyaji T, Otsuka M, Omote H, et al. Identification of a vesicular nucleotide transporter. Proc Natl Acad Sci USA. 2008;105:5683–6.
17. Boswell-Casteel RC, Hays FA. Equilibrative nucleoside transporters—a review. Nucleosides Nucleotides Nucleic Acids. 2017;36:7–30.
18. Bove M, Cicero AFG, Veronesi M, Borghi C. An evidence-based review on urate-lowering treatments: implications for optimal treatment of chronic hyperuricemia. Vasc Health Risk Manag. 2017;13:23–8.

ACKNOWLEDGEMENTS

AUTHOR CONTRIBUTIONS

FUNDING

COMPETING INTERESTS

The authors declare no competing interests.

ADDITIONAL INFORMATION

Supplementary information The online version contains supplementary material available at https://doi.org/10.1038/s41396-022-01264-1.

Correspondence and requests for materials should be addressed to Jana Pilátová.

Reprints and permission information is available at http://www.nature.com/reprints

Publisher's note Springer Nature remains neutral with regard to jurisdictional claims in published maps and institutional affiliations.

SUPPLEMENTARY MATERIALS

SUPPLEMENTARY METHODS

1.1 Biological material – cell cultures and environmental samples

To assess the composition of various birefringent cell inclusions among microscopic eukaryotes, we screened species from environmental samples, cell cultures obtained from various culture collections, and strains from private collections that were kindly donated by our collaborators (listed in Table S1 and acknowledgements). The cultivation conditions for each of the tested species are shown in Table S1. Environmental samples were assessed within one week after collection. Cell cultures were observed after transfer to fresh media on the same day and/or during five consecutive days until the purine inclusions were observed. In some cases (marked with "*" in Table S1), we transferred the cells to media containing dissolved guanine (approximately 30 µM final concentration), in order to facilitate the formation of crystalline inclusions.

1.2 Polarization microscopy

We used polarization microscopy to screen organisms for intracellular crystalline inclusions. Initially, polarization microscopy was performed separately, using an Olympus AX 70 Provis microscope (Olympus, Japan) or confocal microscope (Leica TCS SP8; Leica, Germany) equipped with a digital camera (Leica MC170 HD; Leica, Germany). After installing the polarization filters directly on the Raman microscope (WITec alpha300 RSA, WITec, Germany), photomicrographs and videos were taken immediately before Raman measurements. Short videos were taken using the default settings (25 fps using the Leica TCS SP8 or 20 fps using the WITec alpha300 RSA). Videos were processed using Vegas Pro 14.0 software (MAGIX, Germany).

1.3 Raman microscopy

Measurements and data-processing were performed as described elsewhere [1–3]. The advantages and possible drawbacks of this method have recently been discussed [4]. In brief, Raman map scanning of 203 species comprising more than 3 000 measurements of whole cells, and/or single spectra of crystalline inclusions of mobile cells, or cells with fast-moving cytoplasm, was done using a confocal Raman microscope (WITec alpha300 RSA) equipped with the following

objectives: 20× EC Epiplan, NA = 0.4 (Zeiss, Germany), 50× EC Epiplan-Neofluar, NA = 0.55 (Zeiss, Germany), 60× water-immersion UPlanSApo, NA 1.2 (Olympus, Japan), 100× oil-immersion UPlanFLN, NA 1.3 (Olympus, Japan). A 532 nm laser with a power of approximately 20 mW at the focal plane was used.

For Raman map scanning, cell cultures were used as follows: 1 ml of culture was centrifuged at 2000 g for 1 min, when necessary for fast-moving flagellates, immobilization was accomplished by mixing 5 µl of the cell pellet with 5 µl of 1% low-temperature-melting agarose spread under a 20 mm diameter, 0.18mm-thick quartz coverslip sealed with CoverGrip (Biotium, USA). In cases of environmental samples, where assessment of cell movement is crucial for reliable identification of species (mostly Amoebozoa and Excavata), immobilization was not used, and data acquisition was performed *via* Raman single-spectrum mode with an integration time of 0.5 s and 20 accumulations using one of the following objectives: 50× EC Epiplan- Neofluar, 60× UPlanSApo, and 100× UPlanFLN. Raman map measurements were performed with a scanning step of 200 nm in the both directions, voxel size 1 µm^3 and an integration time of 0.07 s per voxel with either the 60× UPlanSApo or 100× UPlanFLN objectives. On average, we measured 3–10 cells of each strain from each cell culture. In case of environmental samples, we measured at least one cell. Standards of pure chemical substances were measured in water suspension. To prepare the matching references for biogenic crystals of uric acid, guanine monohydrate, xanthine, and their mixtures, the substances were dissolved in an aqueous solution (4 %) of dimethylamine (DMA) and dried on the quartz slide to allow recrystallization.

Data was analyzed using WITec Project FIVE Plus v5.1 software (WITec, Germany) to implement the following steps: cosmic ray removal, background subtraction, cropping of the spectral edges affected by detector margins, spectral unmixing with the true component analysis tool, and averaging of the mean spectrum, summarizing multiple measurements in order to optimize the signal-to-noise ratio for each single spectrum of the crystalline inclusions.

1.4 Phylogenetic analyses

In an attempt to evaluate the role of nucleobase-cation symporter 1 (NCS1), nucleobase-ascorbate transporter (NAT), AzgA, and hypoxanthine-guanine phosphoribosyl transferase (HGPT) in purine crystal biocrystallization, we tested their phylogenetic distribution and the robustness of the phylogenetic placements using methods of molecular phylogenetics. We performed an extensive set of searches of eukaryotic and prokaryotic sequence databases. Using several representative sequences of each gene as queries, we performed a BLASTp search against 87 high-quality, well-annotated eukaryotic and prokaryotic genomes and transcriptomes. To

exclude the possibility that absence of NCS1, NAT, and AzgA gene in predicted proteomes from Heterolobosea, Ciliophora, and Apicomplexa is caused by suboptimal protein prediction, we also checked the presence of their homologs (using TBLASTN search) in contigs from eight nucleotide genome assemblies representing the three groups. While HGPT homologs were easy to detect, TBLASTN did not detect any purine transporter genes. Thus, we can be confident that the absence of these genes in genomic data is not artificial. Datasets containing original sequences and their manually curated homologs, identified by BLASTp search, were included into initial datasets and aligned by MAFFT version 7. These alignments were used as inputs to build Hidden Markov Models for a final sensitive homolog search by HMMER3 software [5] to identify candidate proteins from 742 eukaryotic genomes and transcriptomes included in the EukProt database of genome-scale predicted proteins across the diversity of eukaryotes [6]. To avoid bias introduced by contaminations or erroneous protein predictions in the EukProt database, we performed a preliminary set of Maximum-Likelihood phylogenetic analyses using IQ-TREE multicore version 1.6.10 [7] under LG4X model. Between every round, we manually inspected each tree to identify possible eukaryotic and prokaryotic contaminations. Suspicious sequences were used as queries against the NCBI database of non-redundant proteins (nr) and best blast hits were added to the dataset. Final gene datasets, free of contaminant sequences and in-paralogs (recent gene duplications that resulted in several homologs with almost identical sequence), were aligned by MAFFT [8]. Alignments were manually edited in BioEdit [9], phylogenetic trees were constructed by the maximum likelihood method using RAxML [10], with LG+GAMMA+F model selected by Modelgenerator [11], and 200 nonparametric bootstrap analyses. Trimmed datasets of AzgA, NCS1, NCS2, NATs, and HGPRT protein families are stored on an online depository server, which will be accessible upon full article publication: https://figshare.com/s/ec36ff8263c1114d547a.

For assessing the distribution of equilibrative nucleoside transporter or solute carrier 29 (ENT, SLC29) and concentrative nucleoside transporter (CNT, SLC28), we used seed-sequences according to the references [12] as initial datasets aligned by MAFFT version 7. These alignments were used as inputs to build a profile HMM followed by an HMM search against 57 sequences of genomes using HMMER3 software [5].

Data and materials availability: All data is available in the main text or the supplementary materials.

SUPPLEMENTARY TEXT

Results

Here we provide a detailed description of the results presented in Fig. 1 and Table S1. We examined representatives of all currently recognized eukaryotic supergroups [13, 14] for the presence and composition of various biocrystals. Out of the 205 observed samples, 80 % contained light-polarizing structures (Movie 1–8) that we further identified to be different inclusions, among which 95 % happened to be crystalline inclusions with 80% proportion of purines. In total, crystalline inclusions were found in 77 % of measured cell cultures or environmental samples that were equally proportional in the dataset. With the focus on purine inclusions, we found anhydrous guanine, guanine monohydrate, uric acid and xanthine. To the best of our knowledge, this is the first report on the occurrence of pure crystalline guanine monohydrate in any microorganism. Apart from purine inclusions being formed by pure substances (Fig. S1), we also found four species forming mixed crystals consisting of various proportions of guanine monohydrate, uric acid and/or xanthine (Fig. S2).

Guanine inclusions (Movie S1) were ubiquitous within the **SAR** clade (Stramenopiles, Alveolata, Rhizaria). In **Alveolata,** we confirmed, for the first time, that the morphologically prominent "polar granules" in unsporulated oocysts of the parasitic apicomplexan *Eimeria maxima* consist of guanine. Furthermore, we proved that inclusions in all observed alveolates, including parasitic apicomplexans (*Eimeria maxima*, *Psychodiella sergenti*), photoparasitic chromerids, and very diversified and ecologically important dinoflagellates and ciliates consist exclusively of guanine. Among dinoflagellates, our sampling included clades with species having plastids derived from diatoms (*Glenodinium foliaceum*) and also those having complex plastids of rhodophyte origin. Moreover, we also included the bloom- or red-tide-causing species *Heterocapsa triquetra* and a fresh isolate of Symbiodiniaceae from the soft coral *Capnella imbricata*.

Compared to Alveolata, in **Stramenopiles** the situation is more complex. Guanine crystals predominate in most species, such as predatory actinophryids, bicosoecids, phototrophic and heterotrophic chrysophytes (*Synura hibernica*, *Spumella* sp., respectively), biotechnologically promising eustigmatophytes (*Nannochloropsis oculata, Eustigmatos* cf. *polyphem*), labyrinthulomycetes (*Schizochytrium* sp.), raphidophytes (*Gonyostomum* sp.), and xanthophytes (*Botrydiopsis intercedens*, *Tribonema aequale*, *Xanthonema* sp.). In contrast, diatoms have a lower prevalence of crystalline inclusions than other stramenopiles and exhibit production of uric acid crystals, for example freshwater species of *Encyonema*, *Fragilaria*, *Navicula*, and *Pleurosigma*. Guanine crystals were detected in only a single marine/brackish diatom species (Naviculaceae gen. sp., *Seminavis*-like). Diatoms are known for a very complex nitrogen metabolism employing a urea cycle comparable to the one in animals [15]. Crystalline inclusions

were not detected in the parasitic *Blastocystis* (Opalinata) or in Oomycota. Guanine crystals predominated in the sampled **Rhizaria** (*i.e.,* Cercozoa). In Gromiida and in Retaria (Foraminifera, Acantharea, Polycystinea) we suspected the previously described structures called "stercomata" [16] to be crystals of purines, calcite or celestite (strontium sulfate). For now, we did not prove any of those with certainty due to low sampling of only three species of formalin-fixed cells of Acantharea and Foraminifera.

The more intricate crystals of **Haptista** may contain a mixture of both purines (Movie S2). Among haptophytes, *Emiliania huxleyi*, a model organism with ecological importance, possesses guanine crystals, whereas the biotechnologically important *Isochrysis* sp. has xanthine crystals. In both cases, organisms were cultured in guanine-supplemented medium (Table 1). Centroplasthelida from freshwater habitats (*Rhaphidiophrys* sp.) possessed numerous guanine crystals. **Telonemida** (*Telonema* sp.) contained guanine inclusions when cultured in guanine-supplemented medium. Within **Cryptista (***Chroomonas* sp., *Cryptomonas* sp.) we showed that the highly refractile and taxonomically important Maupas body[17] consists of uric acid.

In **Archaeplastida** (Movie S3), guanine crystals were present in glaucophytes but were not detected in any of the nine sampled rhodophyte species. Guanine inclusions are consistently distributed throughout the UTC clade (Ulvophyceae, Chlorophyceae, and Trebouxiophyceae) except for the biotechnologically significant species, *Chlorella vulgaris*, which possess xanthine, and *Dictyosphaerium* sp. which contains uric acid crystals. The arctic species *Chloromonas arctica* possesses guanine crystals. Interestingly, *Chlamydomonas* in culture or environmental samples possesses guanine crystals in different life stages from flagellate to palmelloid. Xanthine is also present in the crystals of chlorodendrophytes, including another biotechnologically exploited species, *Tetraselmis subcordiformis*, whereas other marine chlorophyte counterparts contain guanine crystals (*e.g. Nephroselmis* sp.). The smallest free-living eukaryote, with the size of bacteria, *Ostreococcus tauri* (Mamiellophyceae), did not show any crystalline inclusions even though they may contain starch as a storage polysaccharide. It is also possible that our methods had insufficient resolution to detect crystalline inclusions in these tiny cells. In stark contrast to Chlorophyta, the Streptophyta, notably including land plants (Embryophyta) together with the related microalgae, Zygnematophyceae and Klebsormidiophyceae, contain uric acid inclusions. In the case of *Mesotaenium caldariorum*, the predominant uric acid includes admixtures of crystalline guanine monohydrate. However, other examined streptophytes such as *Chlorokybus atmophyticus* (Chlorokybophyceae) form guanine crystals. We detected no crystalline inclusions in *Mesostigma viride* (Mesostigmatophyceae). In Embryophyta, Coleochaetophyceae, and Zygnematophyceae we observed calcium oxalate inclusions instead of purine crystals.

Intriguingly, the transition of crystal composition from purines in green algae to calcium oxalate in land plants may be metabolically bridged through purine degradation [18, 19]. We also see a similar trend in Fungi, with yeasts possessing purine crystals, filamentous fungi producing calcium oxalate [20, 21], and some marine seaweeds (Phaeophyceae) lacking crystals altogether. Hence, loss of the capacity to form purine crystals may correlate with the development of multicellularity that the necessity to store nitrogen is replaced by transfer of soluble metabolites through the multicellular body [22].

Crystalline inclusions of varied chemical composition, primarily guanine and xanthine, occur commonly in **Amoebozoa** (Movie S4). Xanthine crystals, uncommon in other eukaryotes, are present in freshwater and marine *Mayorella* sp., in the facultatively parasitic model organism, *Acanthamoeba castellanii*, in the anaerobic model species *Mastigamoeba balamuthi*, and a model terrestrial slime mold, *Physarum polycephalum*. By contrast, guanine was present in a fresh isolate of another slime mold, *Fuligo septica*, a different species of Archamoebae (*Mastigella eilhardi*), and in species of the common genera *Thecamoeba*, *Vannella*, and *Difflugia*.

We showed by Raman microscopy that, in **Opisthokonta,** uric acid, rather than guanine, is a common excretory product of nitrogen metabolism (*e.g.* in nematodes). Interestingly, we noticed guanine microcrystals inside swarming acoelomate gastrotrichs (Platyzoa) in a sample from a peat bog (Movie S5). Using Raman microscopy, we also confirmed that guanine crystals serve as a refractile layer on fish scales. In Fungi (Holomycota) we found crystalline guanine in *Candida albicans*, which has been tested for uptake of different purine compounds previously [23]. However, we did not find any crystalline inclusions in *Saccharomyces cerevisiae*. We observed no crystalline inclusions in either intracellular parasites belonging to Microsporidia or in the free-living halophilic Choanoflagellata. We did not detect crystalline inclusions in the **Breviatea**, close relatives of opisthokonts.

In **Excavata** (Movie S6), the crystalline inclusions, present in all studied lineages, were exclusively composed of guanine, including: both heterotrophic (*Entosiphon* sp., *Rhabdomonas* sp.) and photosynthetic euglenids, freshwater and marine euglenids (*Euglena* sp*., Eutreptiella gymnastica,* respectively), in free-living kinetoplastids (but not in the parasites, such as trypanosomatids), in deep-sea diplonemids (*Namystinia karyoxenos, Rhynchopus* sp.), aerotolerant heteroloboseans (*Naegleria gruberi*), and strictly anaerobic metamonad symbionts of termites (*e.g. Macrotrichomonoides* sp. isolated from *Neotermes cubanus*). In the diplonemid, *Flectonema* sp., guanine monohydrate was detected in the form of pure crystals, probably monocrystals, as their Raman spectra exhibit similar variability of relative intensities when excited by polarized light to that of synthetically prepared monocrystals.

We found guanine crystals in *Gefionella okellyi*, from the phylogenetically distinct clade of **Malawimonadida**. Among the **CRuMs** group (Collodictyonida, Rigifilida, and Mantamonadida), we tested mantamonads but found no crystalline inclusions inside their cells, even after exposing them to guanine-enriched culture medium. Lastly, crystalline guanine was found in *Hemimastix kukwesjijk*, the only representative sampled from **Hemimastigophora**, a separate, deep-branching lineage, recently described as a new eukaryotic supergroup (Movie S7).

In addition to the predominant purine crystalline inclusions (80 %), there are also other types. Surprisingly, calcite (calcium carbonate – $CaCO_3$) was present in diatoms, thus, it is another independent observation of calcification in diatoms following the previous report in [24]. However, diatoms are mostly known for their frustules formed by amorphous silica (silicon dioxide – SiO_2, opal) [25]. Calcification (Fig. S3, Tab. S1) occurred in the seaweeds tested, including rhodophytes, ulvophytes and phaeophytes, indicating that this process occurs very commonly in marine environments [26]. Similarly, calcified shells of foramiferans and the calcite scales on the cell surface of the haptophytic coccolithophore *Emiliania huxleyi* also strongly polarized light [27]. Massive calcite incrustations occurred on surface of filamentous algae, *e.g. Oedogonium* sp., that has been previously described as crystal jewels in other freshwater filamentous algae [28]. We confirmed the mixture of calcium and strontium carbonates ($(Ca,Sr)CO_3$) in the green alga *Tetraselmis*, previously reported elsewhere to be amorphous, using different methodology [29].

Crystalline sulfates occurred in various species but only rarely (Fig. S4). Similarly, in the light-polarizing armor of Acantharea, we confirmed the presence of celestite (strontium sulfate – $SrSO_4$) [30, 31]. Interestingly, we found baryte (barium sulfate – $BaSO_4$) in three species of zygnematophytes (*Closterium peracerosum-strigosum-littorale* complex, *Cosmarium* sp., and *Spirogyra* sp.), for two of which it has been previously reported [32, 33]. In laboratory cultures and environmental isolates of *Saccamoeba* sp. we found an unprecedently complex spectrum corresponding to numerous crystalline inclusions lacking light-polarization features. The dominating peak at 998 cm^{-1} (Fig. S4, Tab. S1) resembles either a signal of sulfates or aromatic compounds. The rest of the spectrum also shows lipid-like organic matter; thus, the crystals may be formed by a complex mixture of lipids and sulfates.

Calcium oxalate monohydrate ($CaC_2O_4 \cdot H_2O$) crystals were restricted to closely related streptophytic algae and land plants: Coleochaetophyceae, Zygnematophyceae (*Cylindrocystis* sp.), and Embryophyta (*e.g.* plant models *Physcomitrella patens*, *Nicotiana tabacum*) together with calcium oxalate dihydrate ($CaC_2O_4 \cdot 2H_2O$) commonly found in Embryophyta (Fig. S5, Tab.

S1). In the Embryophyta, deposition of calcium oxalate is already known to occur under stress conditions [34].

Unexpected light-polarizing lipophilic inclusions unreported until now, occurred in some of examined samples. Compared to carotene crystals observed in the model plant *Arabidopsis thaliana* [35], we found possibly similar structures in aerophytic ulvophytes (*Trentepohlia* sp., *Scotinosphaera gibberosa*) and freshwater cyanobacteria (*Oscillatoria* sp.), comprising a mixture of carotenoids and lipids containing sterols and fatty acids (Fig. S6, Table S1, Movie S8). Similarly, in the green parasitic alga, *Phyllosiphon arisari* and a symbiont of lichens, *Symbiochloris tschermakiae*, their light-polarizing lipophilic crystals were a complex mixture of lipids, with a high proportion of unsaturated fatty acids in the former, and saturated fatty acids in the latter. Faintly light-polarizing lipophilic structures in amoebozoans (*Entamoeba histolytica*) resembled those mentioned above or contained a surplus of sterol compounds (*Acanthamoeba castellanii* and *Mastigamoeba balamuthi*). Some of them may be of a crystalline nature but this requires further evidence. All lipophilic light-polarizing structures tended to melt under prolonged illumination by a focused laser beam (ca 20 mW power) during the Raman measurements.

Refractile structures such as storage polysaccharides, *i.e.,* starch or chrysolaminarin [36, 37], or aerotopes, air-filled vesicles with a reflective interface inside the cells of cyanobacteria [38], might be confused with birefringent crystals. High-intensity light-polarization also occurs in the thick cellulose cell walls of ulvophytes, zygnematophytes, rhodophytes, glaucophytes and others, a phenomenon best-studied in plants [39], or in starch, a storage polysaccharide of Archaeplastida and in chrysolaminarin, storage polysaccharide of SAR (Fig. S7, Table S1).

Comments on Raman spectra analysis

In some protists, a monohydrate of guanine in crystalline form was detected (Figs. S1 and S2). To the best of our knowledge, this is the first report confirming the occurrence of crystalline guanine monohydrate in any microorganism. To date, only a β-polymorph of crystalline anhydrous guanine was detected in various organisms, including some microalgae and protists [3, 40, 41]. In *Flectonema* sp., guanine monohydrate was detected in the form of pure crystals (Fig. S1), probably monocrystals. We observed a few inclusions formed by purine mixtures, which has also been reported from *Paramecium* [41, 42]. In the case of *Mesotaenium caldariorum*, crystalline guanine monohydrate seems to be only a minor admixture in the more abundant uric acid (Fig. S2), however its presence was demonstrated by spectral similarity with synthetically prepared samples containing both uric acid and guanine monohydrate. The inverse proportion of the two

compounds has been found in *Tetraselmis subcordiformis*. *Isochrysis* sp. and *Chroomonas* sp. exhibited crystalline mixtures of xanthine and guanine monohydrate.

Comments on phylogenetic analyses

Hypoxanthine-guanine phosphoribosyl transferase (HGPT) (Fig. S8), omnipresent in eukaryotes, can also be found in Eubacteria, Archaea and, surprisingly enough, we detected HGPT homologs also in Nucleocytoviricota genomes. Because it is a relatively short and divergent protein, we were unable to resolve its detailed phylogeny. Based on previously introduced nomenclature [43], we distinguished a clade of "fungal HGPT" which is very divergent from the other "classical HGPTs". However, we were able to find homologs of "fungal HGPT" in virtually all eukaryotic supergroups.

The nucleobase cation symporter-1 (NCS1) family (Fig. S9) of secondary active transport proteins includes proteins from prokaryotes and several lineages of eukaryotes. We recovered NCS1 eukaryotic paralogs – fungal Fcy type, fungal Fur type, algal type, and plant type as previously described [44]. Besides, we also identified four as-yet-unknown eukaryotic paralogs that we marked as NCS1 A–D. Distribution of NCS1 in eukaryotes is extremely patchy as summarized on Fig. 2. We conclude that NCS1 transporter has been acquired by eukaryotes several times independently. Fungal Fcy type is present in various Fungi (Ascomycetes, Basidiomycetes, Gonapodya). Some Fungi even contain several distant paralogs of this gene (e.g. *Aspergillus* and *Candida*). Interestingly, homologs from Oomycota form a clade within fungal sequences, branching sister to *Aspergillus* sequences with full statistical support. Thus, our analysis strongly indicates lateral transfer of this gene from Fungi (supergroup Obazoa) to Oomycota (supergroup SAR). We identified fungal Fcy type of NCS1 transporter also in Ktedonobacteria (Chloroflexi) and two groups of Proteobacteria (Betaproteobacteria and Gammaproteobacteria). Bacterial homologs of fungal Fcy form a clade branching within fungal sequences but, in this case, with relatively low bootstrap support. Besides, the whole clade of fungal Fcy sequences shows strong affinity to eubacterial permeases including those from Gammaproteobacteria and Betaproteobacteria, so in this case, lateral transfer of Fcy from Fungi to Eubacteria is less convincing. We also identified an ecological relationship between eukaryotes that possess fungal Fcy gene, all of which are adapted to extract nutrients from plants. The Fur type of NCS1 is present exclusively in Basidiomycetes and Ascomycetes (Fungi). The source organism for Fur type is unclear. The algal type of NCS1 is present in *Nannochloropsis* (SAR), Rhodophyta, and Chlorophyta (Archaeplastida). It also has an uncertain origin. Plant type NCS1 was detected in Chlorophyta and Streptophyta (closely related lineages of the supergroup

Archaeplastida). Surprisingly, this gene is also present in Rhodelphidia, another deep-branching lineage of the supergroup Archaeplastida. The gene has unclear origin, although it shows affinity to Proteobacteria with low statistical support.

We also identified four novel clades of eukaryotic NCS1 transporters. One of them is present only in dinoflagellates and shows a close relationship to cytosine permease from Actinobacteria (with full bootstrap support); another is in *Chromera*, diatoms, and dinoflagellates; it shows affinity to Bacteroidetes and Planctomycetes with full bootstrap support. The other clade contains homologs from choanoflagellates, Hemimastigophora, telonemids, dinoflagellates, Chlorophyta, and malawimonadids. The phylogenetic position of *Incisomonas marina* (Stramenopiles) within choanoflagellates is probably due to contamination, also most likely in the case of *Paulinella* (Rhizaria) within Chlorophyta. Finally, two sequences from unrelated amoebozoans (*Filamoeba* and *Vermamoeba*) form a robust clade with no affinity to any other group, forming another eukaryotic NCS1 clade.

Nucleobase-Ascorbate Transporter (NAT) protein family (Fig. S10) is an extensively studied group of proteins. All bacterial NATs are H^+ symporters highly specific for either uracil or xanthine or uric acid. The fungal and plant members are H^+ symporters specific either for xanthine-uric acid, or for adenine-guanine-hypoxanthine-uracil. In contrast to the microbial and plant proteins, most functionally characterized mammalian NATs are highly specific for L-ascorbate/Na^+. However, the rSNBT1 NAT transporter from a rat is specific for nucleobases [45]. Our analysis convincingly shows that NAT proteins were introduced to eukaryotes at least four times independently (NAT A–D) and have their closest homologs in eubacteria, NAT B and D with high statistical support. Metazoan and plant NATs both belong to the NAT A clade that is, together with NAT C, the most widespread NAT gene in eukaryotes. In contrast, NAT B is present only in Fungi and dictyostelids; NAD D is unique for *Tritrichomonas* and it was established by horizontal gene transfer from Firmicutes (it is encoded on tritrichomonas-like genomic contig, so it is not contamination). Interestingly, some well-supported eukaryotic clades are not congruent with eukaryotic phylogeny confounding interpretation of the descent of this protein family. In some cases, it might be explained by eukaryote-to-eukaryote horizontal gene transfers (*e.g.,* from fungi to dictyostelids in NAT B).

The **AzgA** gene encodes a **hypoxanthine-adenine-guanine transporter** (Fig. S11) that is present in all main groups of eukaryotes except supergroup Amoebozoa, and it is also missing in metazoans. Our analysis convincingly shows that eukaryotic AzgA has a single origin in eukaryotes and has been probably present in two paralogs in the last eukaryotic common ancestor. We

named those paralogs AzgA A and B. Besides, the analysis indicates a series of gene duplications during evolution of certain groups as seen in Chlorophyta and Dinoflagellata.

References

1. Moudříková Š, Nedbal L, Solovchenko A, Mojzeš P. Raman microscopy shows that nitrogen-rich cellular inclusions in microalgae are microcrystalline guanine. *Algal Res* 2017; **23**: 216–222.

2. Barcytė D, Pilátová J, Mojzeš P, Nedbalová L. The arctic *Cylindrocystis* (Zygnematophyceae, Streptophyta) green algae are genetically and morphologically diverse and exhibit effective accumulation of polyphosphate. *J Phycol* 2020; **56**: 217–232.

3. Mojzeš P, Gao L, Ismagulova T, Pilátová J, Moudříková Š, Gorelová O, et al. Guanine, a high-capacity and rapid-turnover nitrogen reserve in microalgal cells. *Proc Natl Acad Sci* 2020; **117**: 32722–32730.

4. Moudříková Š, Ivanov IN, Vítová M, Nedbal L, Zachleder V, Mojzeš P, et al. Comparing biochemical and Raman microscopy analyses of starch, lipids, polyphosphate, and guanine pools during the cell cycle of *Desmodesmus quadricauda*. *Cells* 2021; **10**: 1–21.

5. Eddy SR. A probabilistic model of local sequence alignment that simplifies statistical significance estimation. *PLoS Comput Biol* 2008; **4**: 1–14.

6. Richter DJ, Berney C, Strassert JFH, Burki F, de Vargas C. EukProt: A database of genome-scale predicted proteins across the diversity of eukaryotic life. *bioRxiv* 2020; 1–11.

7. Hoang DT, Chernomor O, Von Haeseler A, Minh BQ, Vinh LS. UFBoot2: Improving the ultrafast bootstrap approximation. *Mol Biol Evol* 2018; **35**: 518–522.

8. Katoh K, Standley DM. MAFFT multiple sequence alignment software version 7: Improvements in performance and usability. *Mol Biol Evol* 2013; **30**: 772–780.

9. Hall T. BioEdit: a user-friendly biological sequence alignment editor and analysis program for Windows 95/98/NT. *Nucleic Acids Symp Ser* 1999; **41**: 95–98.

10. Stamatakis A. RAxML version 8: A tool for phylogenetic analysis and post-analysis of large phylogenies. *Bioinformatics* 2014; **30**: 1312–1313.

11. Keane TM, Creevey CJ, Pentony MM, Naughton TJ, McInerney JO. Assessment of methods for amino acid matrix selection and their use on empirical data shows that ad hoc assumptions for choice of matrix are not justified. *BMC Evol Biol* 2006; **6**: 1–17.

12. Young JD, Yao SYM, Baldwin JM, Cass CE, Baldwin SA. The human concentrative and equilibrative nucleoside transporter families, SLC28 and SLC29. *Mol Aspects Med* 2013; **34**: 529–547.

13. Adl SM, Bass D, Lane CE, Lukeš J, Schoch CL, Smirnov A, et al. Revisions to the classification, nomenclature, and diversity of eukaryotes. *J Eukaryot Microbiol* 2019; **66**: 4–119.

14. Archibald JM, Simpson AGB, Slamovits CH, Margulis L, Melkonian M, Chapman DJ, et al. Handbook of the Protists, 2nd ed. *Handbook of the Protists* . 2017. Springer International Publishing, Switzerland.

15. Smith SR, Dupont CL, McCarthy JK, Broddrick JT, Oborník M, Horák A, et al. Evolution and regulation of nitrogen flux through compartmentalized metabolic networks in a marine diatom. *Nat Commun* 2019; **10**: 1–14.

16. Hedley RH, Bertaud WS. Electron-microscopic observations of *Gromia oviformis* (Sarcodina). *J Protozool* 1962; **9**: 79–87.

17. Hoef-Emden K, Melkonian M. Revision of the genus *Cryptomonas* (Cryptophyceae): A

combination of molecular phylogeny and morphology provides insights into a long-hidden dimorphism. *Protist* 2003; **154**: 371–409.

18. Brychkova G, Fluhr R, Sagi M. Formation of xanthine and the use of purine metabolites as a nitrogen source in *Arabidopsis* plants. *Plant Signal Behav* 2008; **3**: 999–1001.

19. Yu L, Jiang J, Zhang C, Jiang L, Ye N, Lu Y, et al. Glyoxylate rather than ascorbate is an efficient precursor for oxalate biosynthesis in rice. *J Exp Bot* 2010; **61**: 1625–1634.

20. Roush AH. Crystallization of purines in the vacuole of *Candida utilis*. *Nature* 1961; **190**: 449.

21. Gadd GM, Bahri-Esfahani J, Li Q, Rhee YJ, Wei Z, Fomina M, et al. Oxalate production by fungi: Significance in geomycology, biodeterioration and bioremediation. *Fungal Biol Rev* 2014; **28**: 36–55.

22. Winter G, Todd CD, Trovato M, Forlani G, Funck D. Physiological implications of arginine metabolism in plants. *Front Plant Sci* 2015; **6**: 1–14.

23. Roush AH, Questiaux LM, Domnas AJ. The active transport and metabolism of purines in the yeast, *Candida utilis*. *J Cell Comp Physiol* 1959; **54**: 275–286.

24. Ehrlich H, Motylenko M, Sundareshwar P V, Ereskovsky A, Zgłobicka I, Noga T, et al. Multiphase biomineralization: enigmatic invasive siliceous diatoms produce crystalline calcite. *Adv Funct Mater* 2016; **26**: 2503–2510.

25. Romann J, Valmalette JC, Chauton MS, Tranell G, Einarsrud MA, Vadstein O. Wavelength and orientation dependent capture of light by diatom frustule nanostructures. *Sci Rep* 2015; **5**: 1–6.

26. Lipej L, Orlando-Bonaca M, Mavrič B. Biogenic formations in the Slovenian sea. 2016.

27. Weiner S, Addadi L. Crystallization pathways in biomineralization. *Annu Rev Mater Res* 2011; **41**: 21–40.

28. Lenzenweger R. Algen mit Kristallschmuck. *Mikrokosmos* 2002; **91**: 280.

29. Martignier A, Filella M, Pollok K, Melkonian M, Bensimon M, Barja F, et al. Marine and freshwater micropearls: Biomineralization producing strontium-rich amorphous calcium carbonate inclusions is widespread in the genus *Tetraselmis* (Chlorophyta). *Biogeosciences* 2018; **15**: 6591–6605.

30. Odum HT. Notes on the strontium content of sea water, celestite Radiolaria, and strontianite snail shells. *Science* 1951; **114**: 211–213.

31. Bütschli O. Über die chemische Natur der Skelettsubstanz der Acantharia. *Zool Anz* 1906; **30**: 784–789.

32. Brook AJ, Fotheringham A, Bradly J, Jenkins A. Barium accumulation by desmids of the genus *Closterium* (Zygnemaphyceae). *Br Phycol J* 1980; **15**: 261–264.

33. Kreger DR, Boeré H. Some observations on barium sulphate in *Spirogyra*. *Acta Bot Neerl* 1969; **18**: 143–151.

34. Nakata PA. Plant calcium oxalate crystal formation, function, and its impact on human health. *Front Biol (Beijing)* 2012; **7**: 254–266.

35. Maass D, Arango J, Wüst F, Beyer P, Welsch R. Carotenoid crystal formation in *Arabidopsis* and carrot roots caused by increased phytoene synthase protein levels. *PLoS One* 2009; **4**: 1–12.

36. Xiao H, Wang S, Xu W, Yin Y, Xu D, Zhang L, et al. The study on starch granules by using darkfield and polarized light microscopy. *J Food Compos Anal* 2020; **92**: 1–7.

37. Kreger DR, van der Veer J. Paramylon in a Chrysophyte. *Acta Bot Neerl* 1970; **19**: 401–402.

38. Li J, Liao R, Tao Y, Zhuo Z, Liu Z, Deng H, et al. Probing the cyanobacterial *Microcystis* gas vesicles after static pressure treatment: A potential in situ rapid method. *Sensors* 2020; **20**: 1–17.

39. Abraham Y, Elbaum R. Quantification of microfibril angle in secondary cell walls at subcellular resolution by means of polarized light microscopy. *New Phytol* 2013; **197**: 1012–1019.

40. Jantschke A, Pinkas I, Hirsch A, Elad N, Schertel A, Addadi L, et al. Anhydrous β-guanine crystals in a marine dinoflagellate: Structure and suggested function. *J Struct Biol* 2019; **207**: 12–20.

41. Creutz CE, Mohanty S, Defalco T, Kretsinger RH. Purine composition of crystalline cytoplasmic inclusions of *Paramecium tetraurelia*. *Protist* 2002; **153**: 39–45.

42. Pinsk N, Wagner A, Cohen L, Smalley CJH, Hughes CE, Zhang G, et al. Biogenic guanine crystals are solid solutions of guanine and other purine metabolites. *J Am Chem Soc* 2022; **144**: 5180–5189.

43. Liu X, Qian W, Liu X, Qin H, Wang D. Molecular and functional analysis of hypoxanthine-guanine phosphoribosyltransferase from *Arabidopsis thaliana*. *New Phytol* 2007; **175**: 448–461.

44. Patching SG. Recent developments in nucleobase cation symporter-1 (NCS1) family transport proteins from bacteria, archaea, fungi and plants. *J Biosci* 2018; **43**: 797–815.

45. Kourkoulou A, Pittis AA, Diallinas G. Evolution of substrate specificity in the nucleobase-ascorbate transporter (NAT) protein family. *Microb Cell* 2018; **5**: 280–292.

46. Prokopchuk G, Tashyreva D, Yabuki A, Horák A, Masařová P, Lukeš J. Morphological, ultrastructural, motility and evolutionary characterization of two new Hemistasiidae species. *Protist* 2019; **170**: 259–282.

47. Bischoff HW, Bold HC. Phycological Studies IV. Some Soil Algae from Enchanted Rock and Related Algal Species. 1963. University of Texas Publication No. 6318.

48. Votýpka J, Kostygov AY, Kraeva N, Grybchuk-Ieremenko A, Tesařová M, Grybchuk D, et al. *Kentomonas* gen. n., a new genus of endosymbiont-containing trypanosomatids of Strigomonadinae subfam. n. *Protist* 2014; **165**: 825–838.

49. Andersen RA, Morton SL, Sexton JP. Provasoli Guillard National Center for Culture of Marine Phytoplankton 1997 – list of strains. *J Phycol* 1997; **33**: 1–75.

50. Guillard RRL. Culture of phytoplankton for feeding marine invertebrates. *Culture of marine invertebrate animals*. 1975. Plenum Press, New York, pp 29–60.

51. Park JS. Effects of different ion compositions on growth of obligately halophilic protozoan *Halocafeteria seosinensis*. *Extremophiles* 2012; **16**: 161–164.

52. Bertani G. Studies on lysogenesis. I. The mode of phage liberation by lysogenic Escherichia coli. *J Bacteriol* 1951; **62**: 293–300.

53. Fulton C. Axenic cultivation of *Naegleria gruberi*. Requirement for methionine. *Exp Cell Res* 1974; **88**: 365–370.

54. Samson RA, Hoekstra ES, Oorschot CAN Van. Introduction to food-borne fungi. 1981. Centraalbureau voor Schimmelcultures, Baarn et Delft, the Netherlands.

55. Murashige T, Skoog F. A revised medium for rapid growth and bio assays with tobacco

tissue cultures. *Physiol Plant* 1962; **15**: 474–497.

56. Neff RJ, Neff RH. Induction of synchronous division in amoebae. *Synchrony in Cell Division and Growth*. 1964. Wiley Interscience, New York, pp 213–246.

57. Burgess LW, Liddell CM, Summerell BA. Laboratory manual for fusarium research: incorporating a key and descriptions of common species found in Australasia, 2nd ed. 1988. The University of Sydney, Sydney, Australia.

58. Chávez LA, Balamuth W, Gong T. A light and electron microscopical study of a new, polymorphic free-living amoeba, *Phreatamoeba balamuthi* n. g., n. sp. *J Protozool* 1986; **33**: 397–404.

59. Diamond LS. Establishment of various trichomonads of animals and man in axenic cultures. *J Parasitol* 1957; **43**: 488–490.
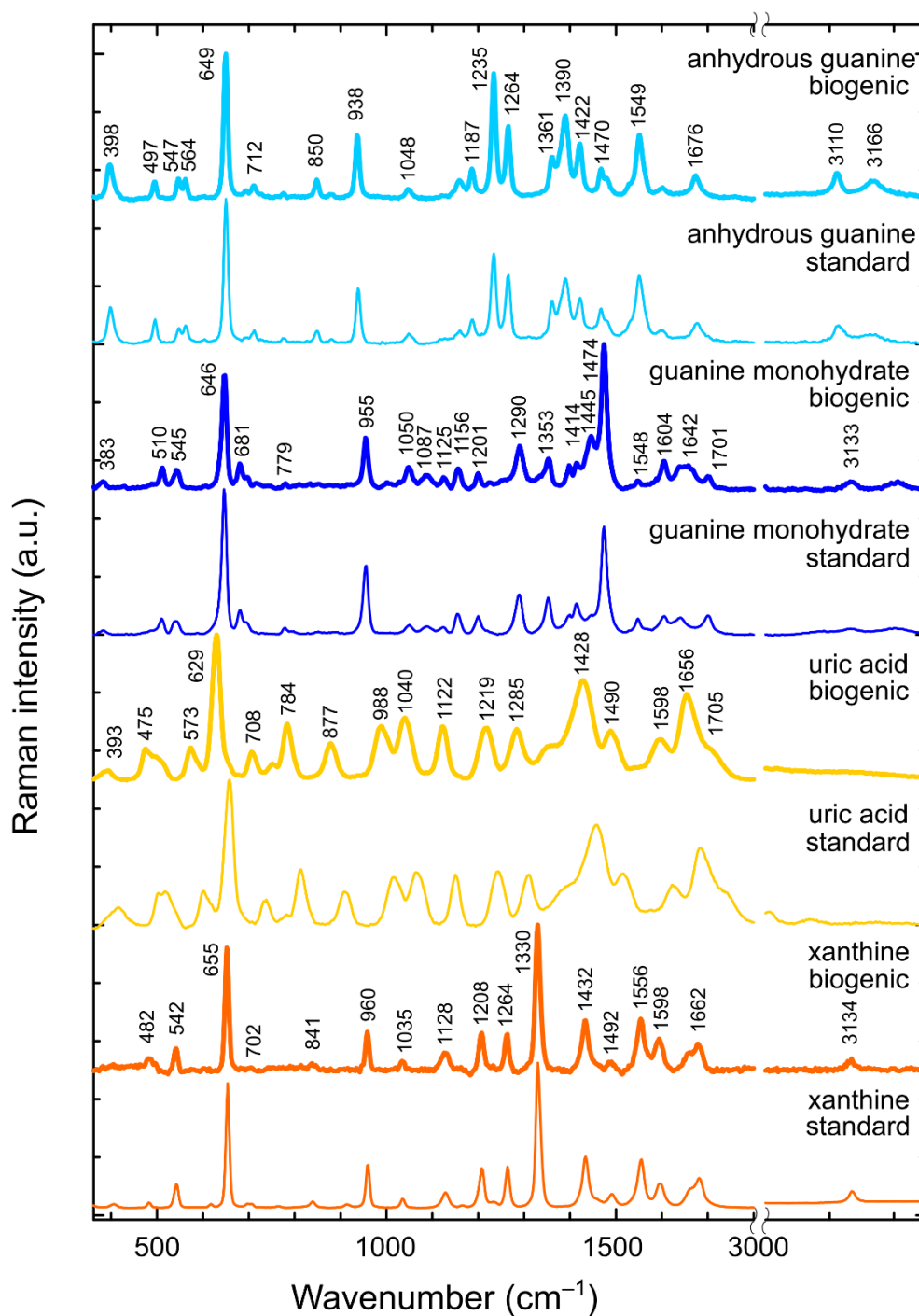
Fig. S1.

Representative Raman spectra of biogenic purine crystalline inclusions measured in biological species followed by their respective standards of pure chemical compounds. Biogenic crystals have been spectrally extracted directly from measured species. Standards of anhydrous guanine and xanthine have been measured as suspension of pure compounds in water, guanine monohydrate and uric acid has been recrystallized from 4% dimethylamine water solution.
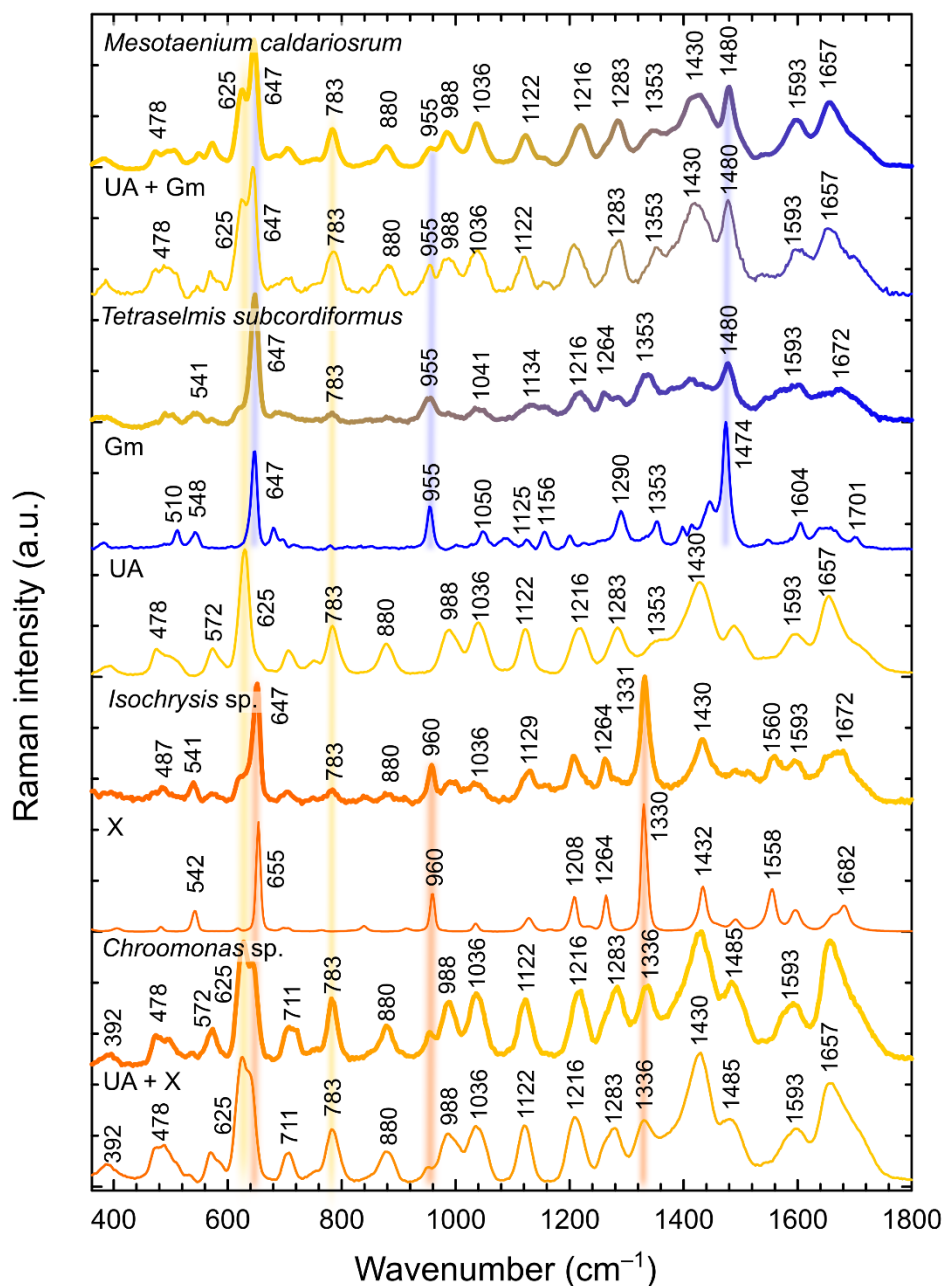
Fig. S2.

Representative Raman spectra of biogenic purine inclusions forming mixtures of uric acid (UA) and guanine monohydrate (Gm) in different proportions with a dominance of the former in the case of *Mesotaenium caldariorum*, or the latter in *Tetraselmis subcordiformis*. Xanthine (X) dominates the crystals with uric acid admixtures found in *Isochrysis* sp., whereas *Chroomonas* sp. has higher proportions of uric acid over xanthine. The reference spectra of pure substances are shown along with those of mixtures of "UA + Gm" and "UA + X" recrystallized from 4% dimethylamine solution, as Raman spectra of purine mixtures exhibit some spectral shifts and changes in relative intensities compared to the pure substances.
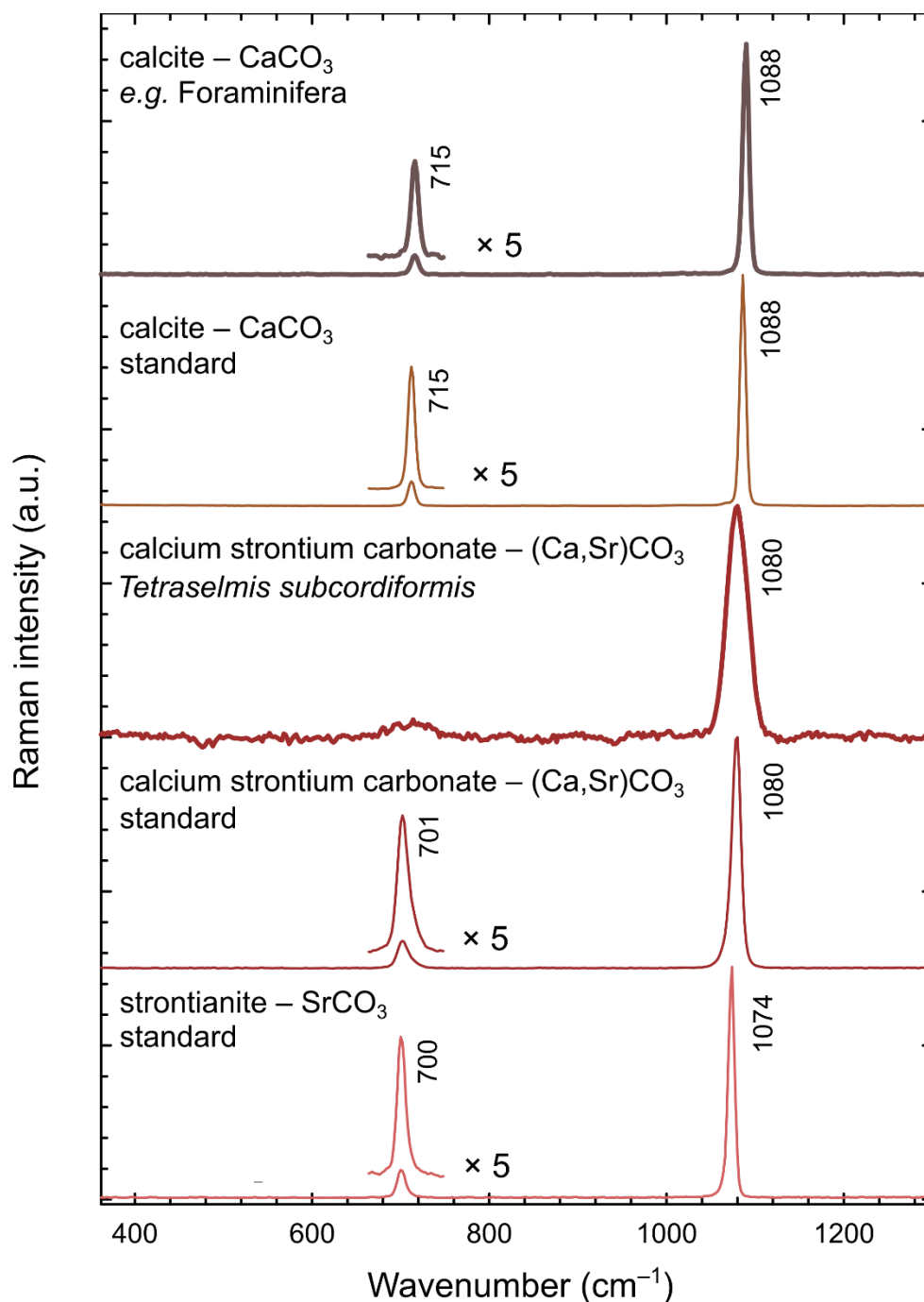
Fig. S3.

Representative Raman spectra of carbonate minerals observed in inspected species, all of them strongly polarize light: calcite or calcium carbonate ($CaCO_3$) found in various diatoms, Foraminifera, multicellular Rhodophytes and seaweed with respective standard and the mixture of calcium and strontium carbonates (($Ca,Sr)CO_3$) found in *Tetraselmis* sp. with respective standards of pure chemical substances.
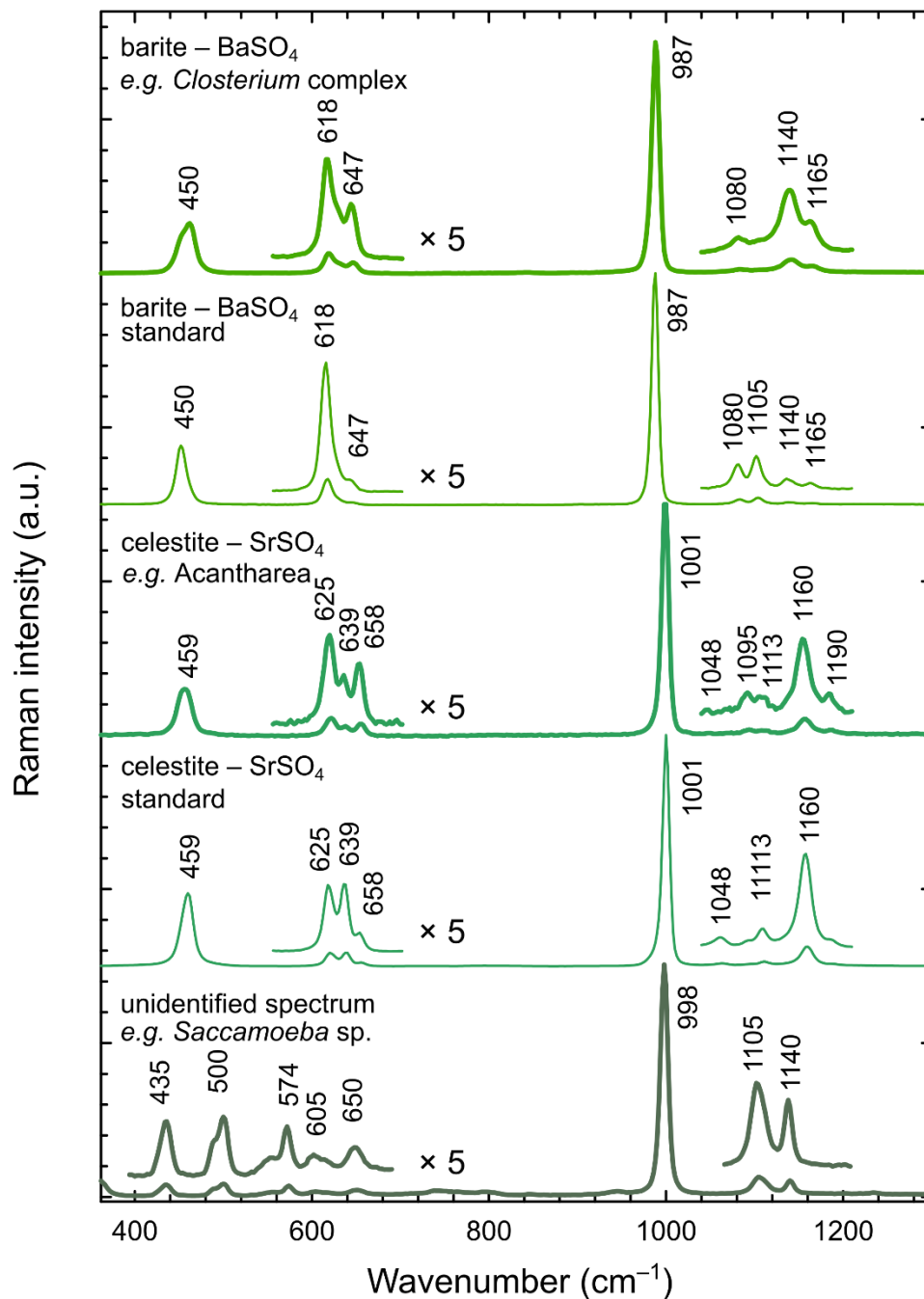
Fig. S4.

Representative Raman spectra of sulfate minerals observed in inspected species followed by respective standards of pure chemical substances, all of them faintly polarize light: baryte ($BaSO_4$) found in *Closterium peracerosum-strigosum-littorale* complex, *Cosmarium* sp., *Spirogyra* sp., celestite ($SrSO_4$) found in skeletons of Acantharea, and unidentified spectra of sulfate resembling minerals mixed with lipophilic organic matter found in *Saccamoeba* sp. Raman spectra of sulfates show variability in dependence of crystal orientation and minor admixtures of other salts.
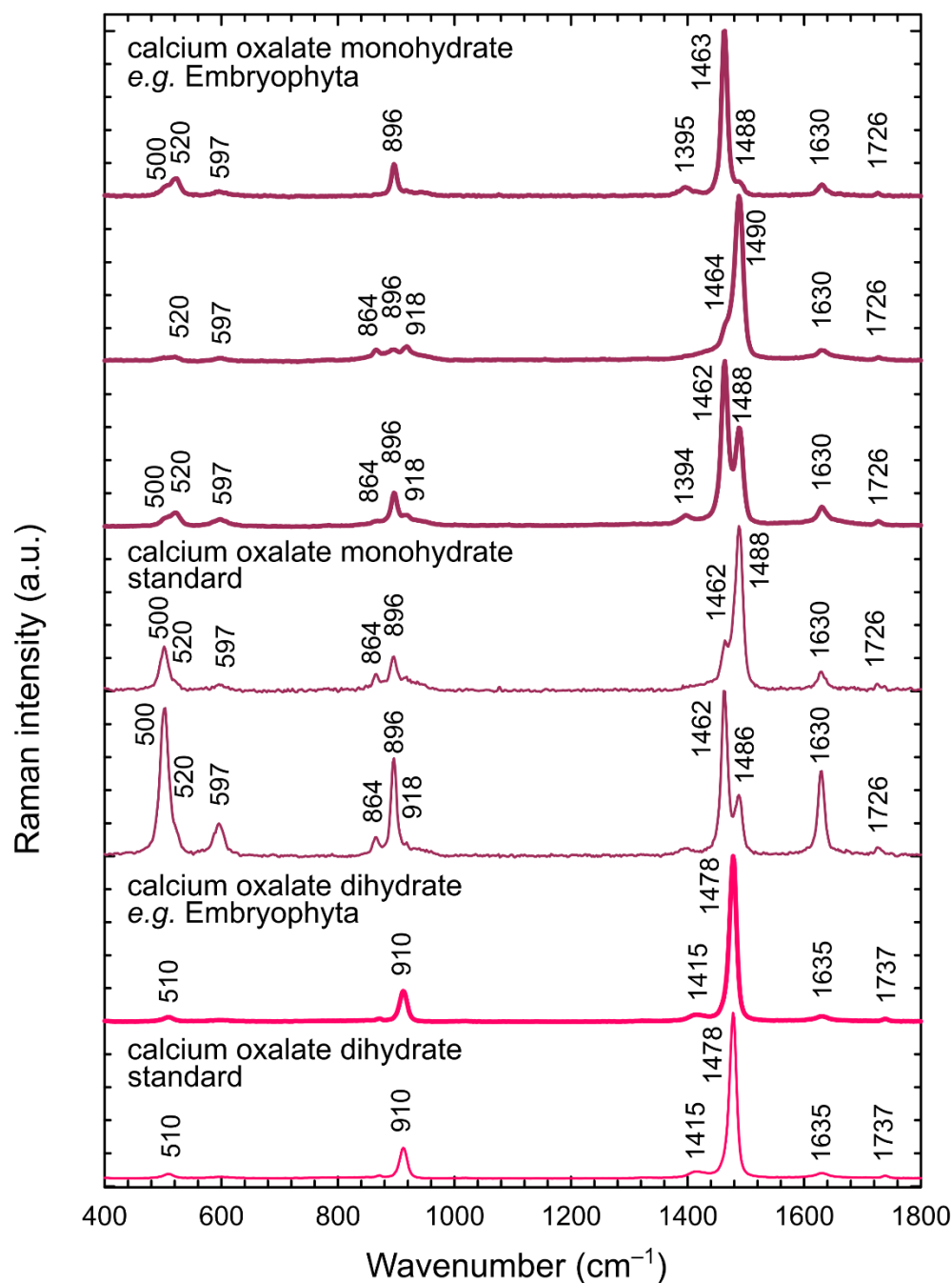
Fig. S5.

Representative Raman spectra of organic crystals polarizing light observed in inspected species followed by respective standards of pure chemical substances. The crystals of calcium oxalate monohydrate strongly polarize Raman signal – the major peaks interchange their relative intensities according to the crystal orientation with respect of polarization plane of the excitation beam. It was found in Coleochaetophyceae, Zygnematophyceae, Embryophyta. The calcium oxalate dihydrate was found in Embryophyta.
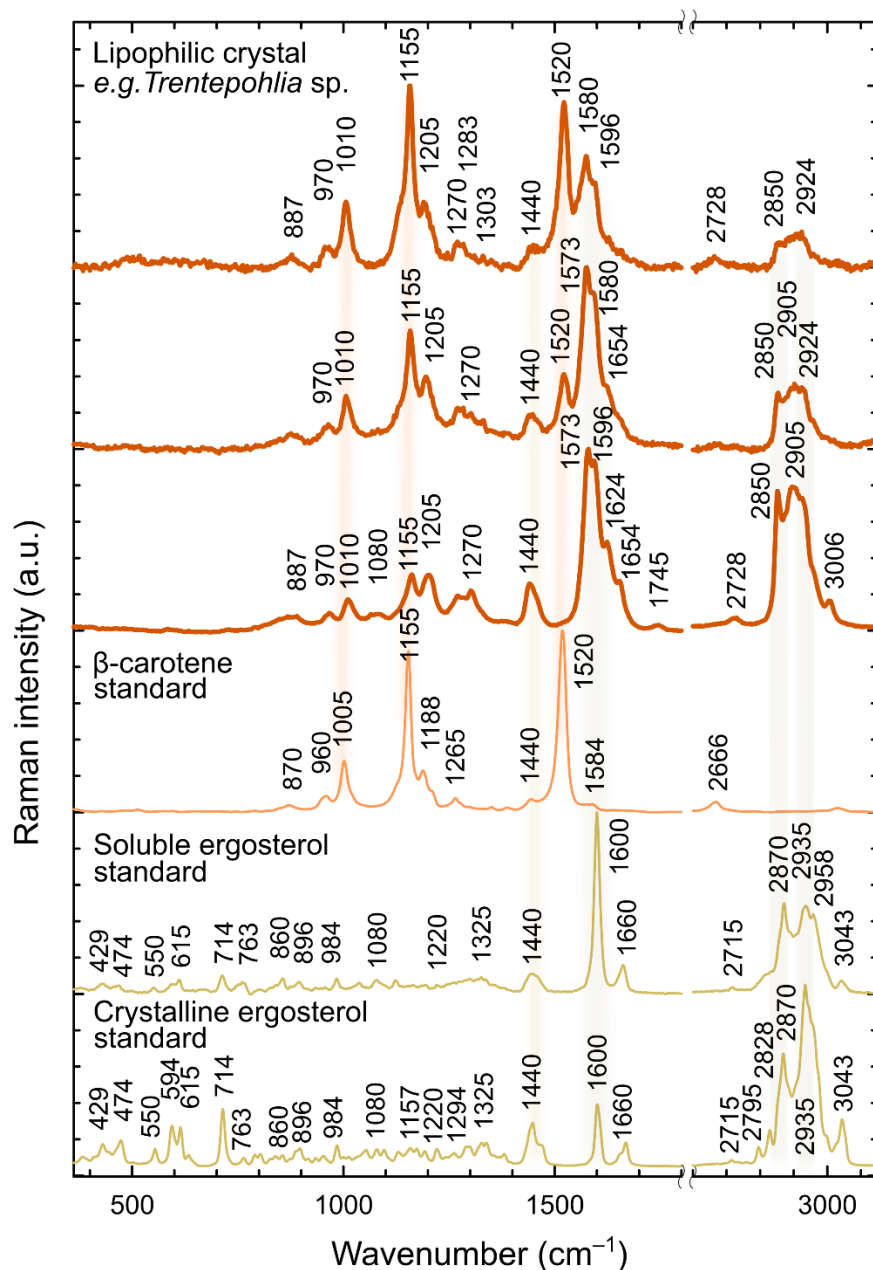
Fig. S6.

Representative Raman spectra of organic crystals polarizing light observed in inspected species followed by respective standards of pure chemical substances: lipophilic crystalline mixtures of carotenoids and sterols found in ulvophytes *Trentepohlia* sp. and *Scotinosphaera giberosa*, rhodophyte *Asterocytis ramonsa* and cyanobacteria *Oscillatoria* sp. Raman measurements using a high-intensity laser beam lead to photo-degradation of carotenoids present in the structure, thus their Raman signal decreases over time and allows observation of other admixtures in greater detail. We failed to find a precisely matching standard for sterols forming these lipophilic crystals; the biogenic crystals may contain a complex mixture of various chemical species.
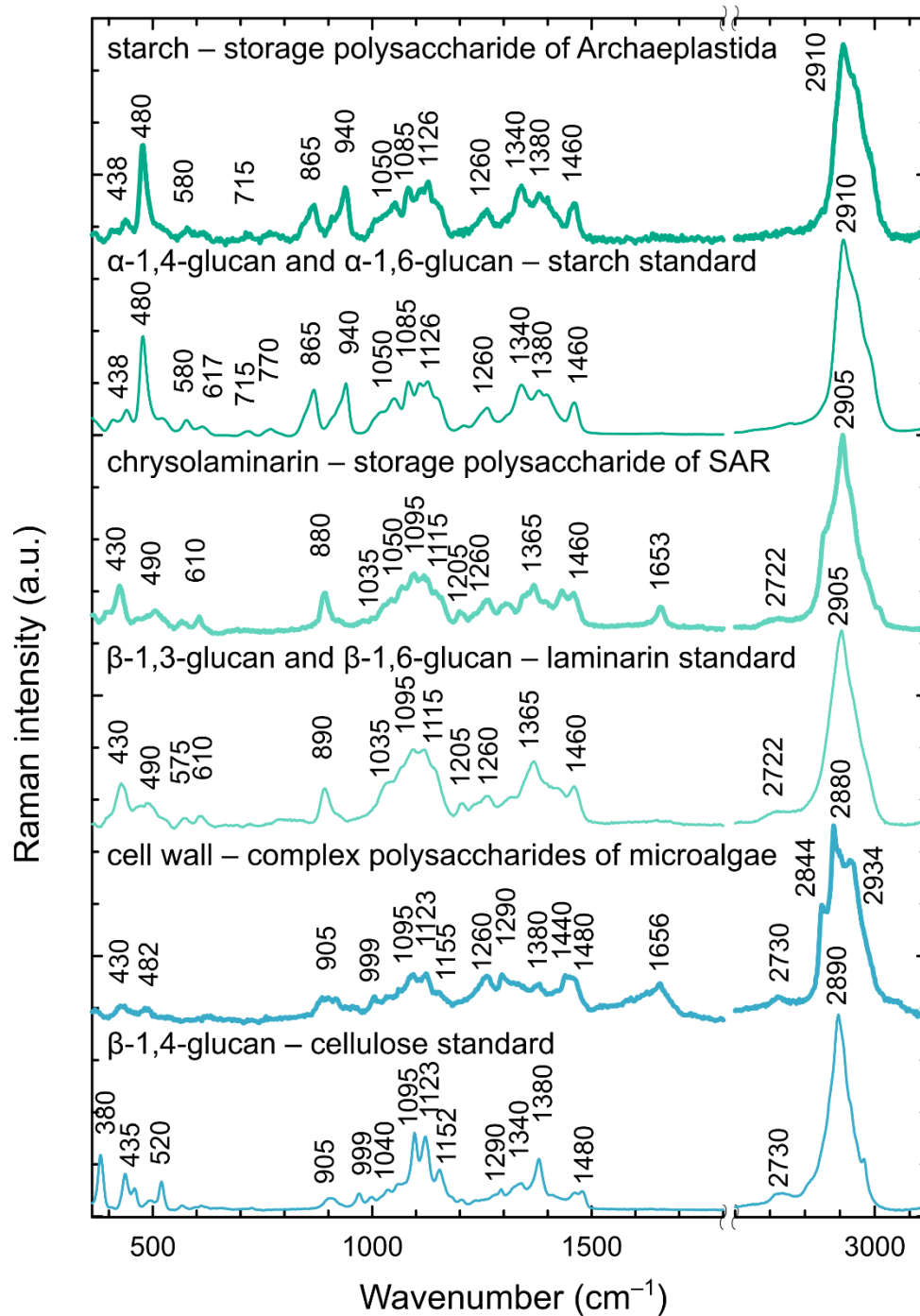
Fig. S7.

Representative Raman spectra of light polarizing polysaccharides in inspected species with respective standards of pure chemical substances: starch – storage polysaccharide of α-1,4-glucan and α-1,6-glucan found in Archaeplastida, chrysolaminarin – storage polysaccharide of β-1,3-glucan and β-1,6-glucan found in SAR, cellulose – structure polysaccharide of β-1,4-glucan forming cell walls of various microalgae (both Archaeplastida and SAR).
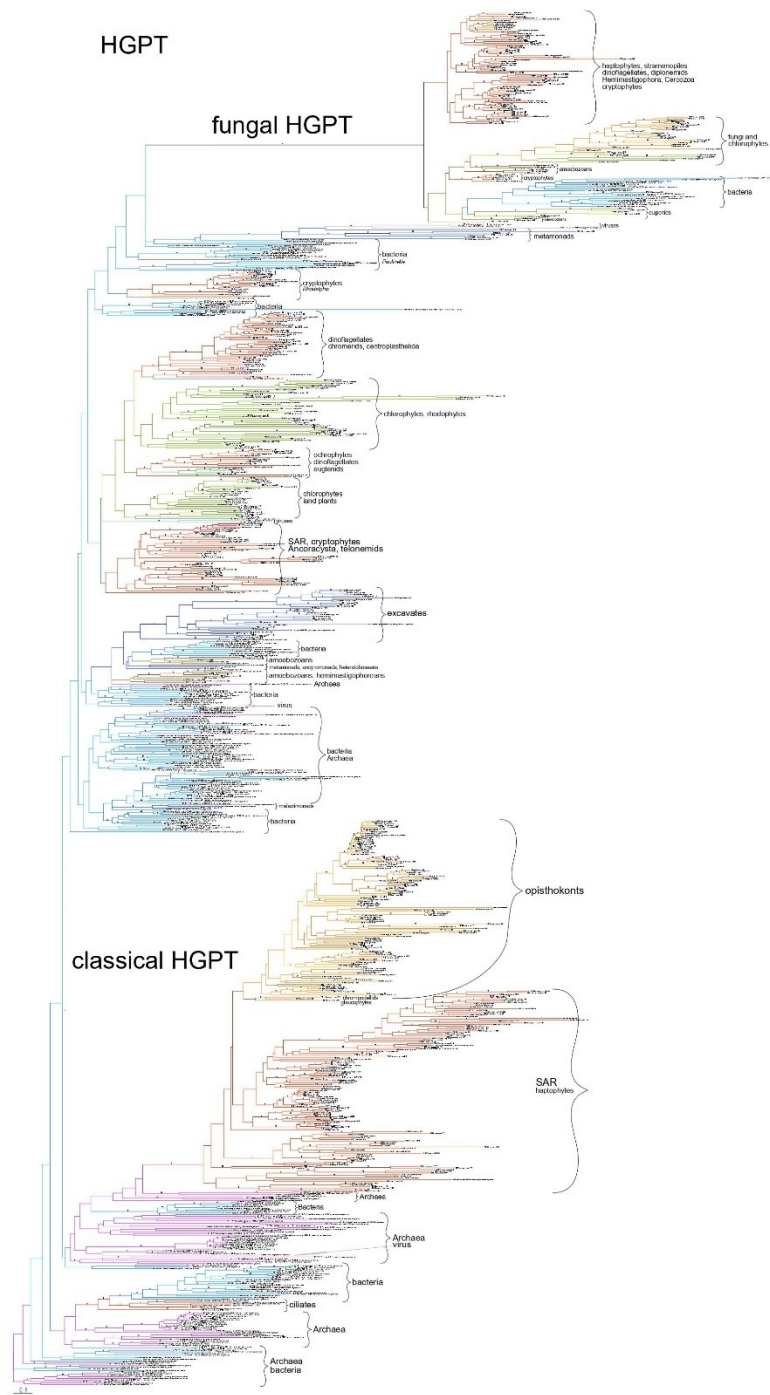
Fig. S8.

Maximum likelihood tree of hypoxanthine-guanine phosphoribosyl transferase (HGPT) as inferred from amino acid sequences (171 aa). Numbers above branches indicate bootstrap support (200 replicates).

23
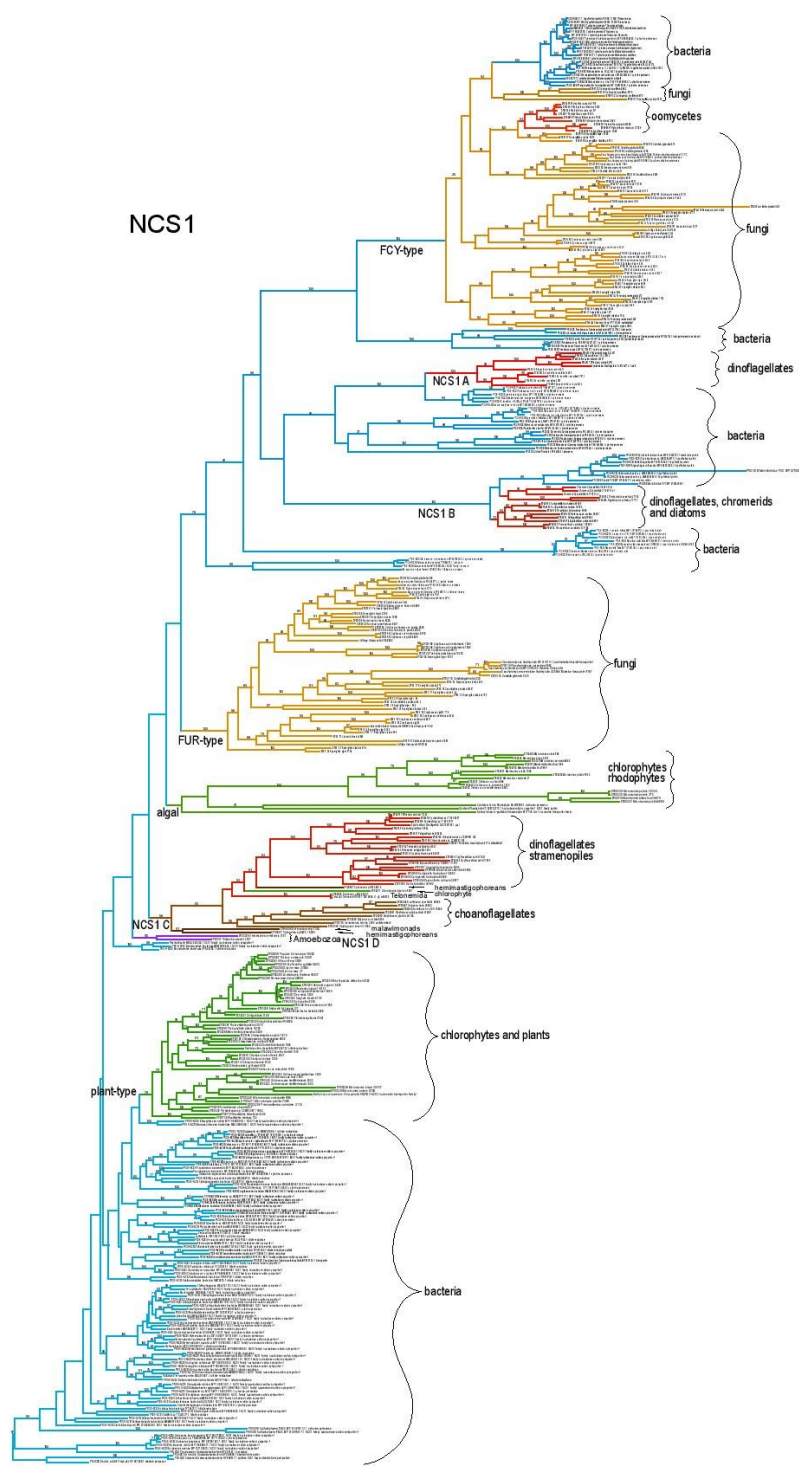
Fig. S9.
Maximum likelihood tree of nucleobase-cation symporter 1 (NCS1) as inferred from amino acid sequences (463 aa positions). Numbers above branches indicate bootstrap support (200 replicates).

Fig. S10.

Maximum likelihood tree of nucleobase-ascorbate transporter (NAT) as inferred from amino acid sequences (385 aa). Numbers above branches indicate bootstrap support (200 replicates).
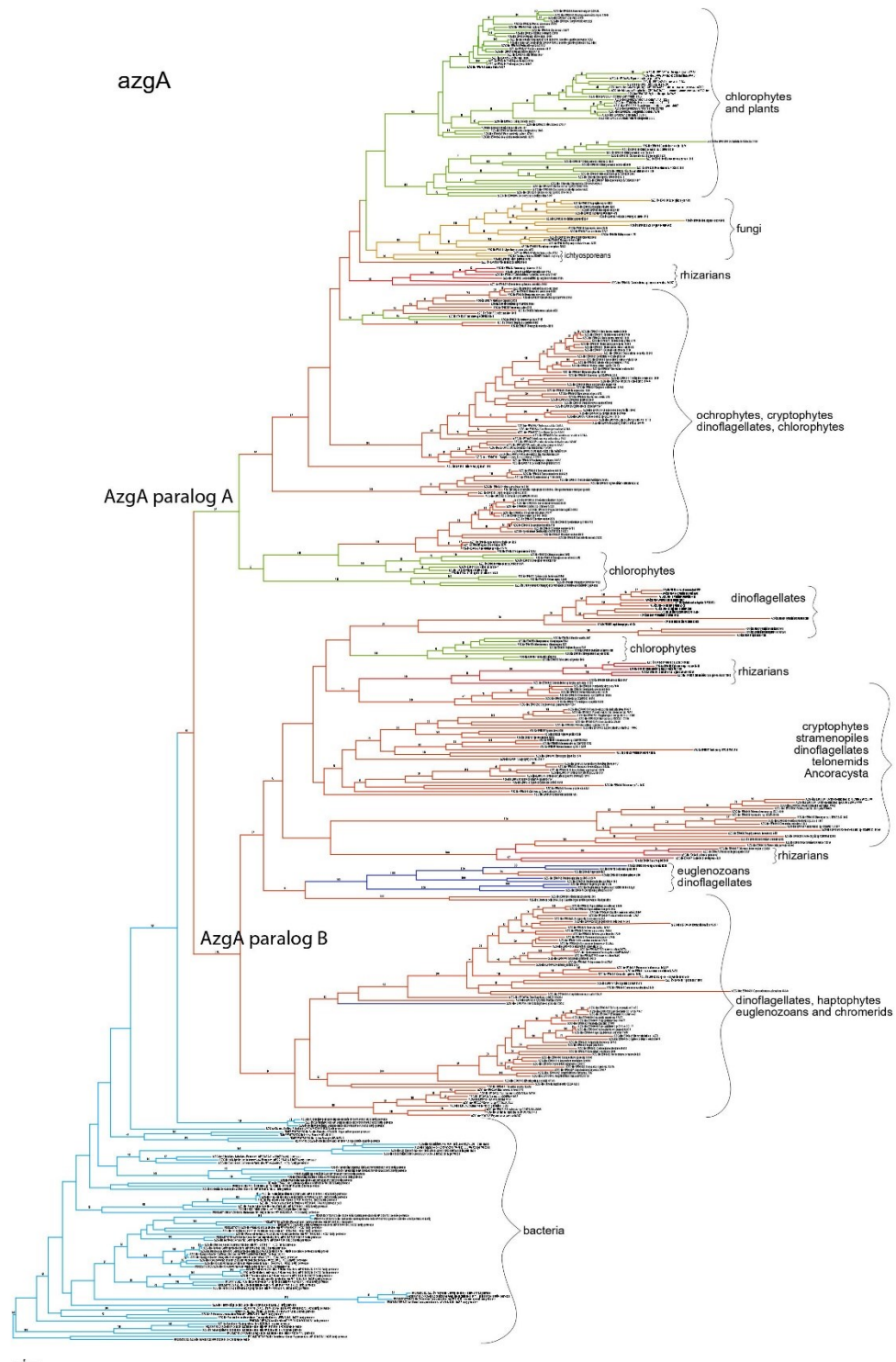
Fig. S11.

Maximum likelihood tree of AzgA as inferred from amino acid sequences (395 aa). Numbers above branches indicate ML bootstrap support (200 replicates).

Table S1. Overview of the cell inclusions present in eukaryotes and cyanobacteria and their identification *via* Raman microscopy and light polarization. Species are listed according to their taxonomic classification and then alphabetically – species positively tested for purine inclusions (in black) and not positively tested for purine inclusions (in grey); capital letters in brackets refer to the phylogeny scheme in Fig. 1; (b) stands for biotechnologically important species and (m) for model organism. **Habitat – trophy:** E – endobiont, F – freshwater, Hp – halophilic, M – marine, S – snow, T – terrestrial; a – autotroph, h – heterotroph, p – parasite. **Culture collections:** ATCC – American Type Culture Collection, Manassas, USA; CAUP – Culture Collection of Algae of Charles University in Prague, Czech Republic; CCALA – Culture collection of Autotrophic Organisms of the Institute of Botany of the AS CR, Třeboň, Czech Republic; CCAP – Culture Collection of Algae and Protozoa, Orban, UK; CCF – Culture collection of Fungi, Praha, Czech Republic; CCMP – Culture Collection of Marine Phytoplankton – part of NCMA: NCMA – National Center for Marine Algae and Microbiota, Bigelow, USA; CRC – Chlamydomonas Resource Center, University of Minnesota, St. Paul, USA; CVCC – China Veterinary Culture Collection Center, National Control Institute of Veterinary Bio-products and Pharmaceutical (NCIVBP), Ministry of Agriculture, Beijing, China; DBM – Department of Biochemistry and Microbiology at University of Chemistry and Technology, Prague, Czech Republic; EUROSCARF – EUROpean Saccharomyces Cerevisiae Archive for Functional analysis, Scientific Research and Development GmbH, Oberursel, Germany; NIES – National Institute for Environmental Studies, Tsukuba, Japan; NCMA – CCMP - National Center for Marine Algae and Microbiota, Culture Collection of Marine Phytoplankton, Bigelow, USA; priv – private collection; RCC – Roscoff Culture Collection, Roscoff, France; SAG – Culture Collection of Algae at Goettingen University, Germany; UTEX – University of Texas at Austin, USA

Cultivation method:
– – no cultivation prior to observations and measurements (in case of environmental samples)
ASW-D – Artificial Sea Water for Diplonemids according to [46], 20 °C
ASW-L – Artificial Sea Water for Labyrinthulomycetes: 3,5% artificial sea water supplied with 1 g of yeast extract and 10 g of glucose, 25 °C
BBM – Basal Bold's Medium according to [47], 20–25 °C, 16:8 h light:dark cycle
BHI – Brain Heart Infusion medium as described in [48]
DY-IV – medium according to [49], 15 °C, 12:12 h light:dark cycle
f/2 – medium according to [50], 20–25 °C, 16:8 h light:dark cycle
f/2B – f/2 medium according to [50] with addition of sterile barley grain, 20–25 °C
Fw – ATCC 802 Sonneborn's Paramecium medium, 20–25 °C
FwAM – Fresh Water Amoeba Medium – ATCC medium 997, 20–25 °C
FwB1 – 25% ATCC 802 Sonneborn's Paramecium medium, with addition of sterile barley grain, 20–25 °C
FwB2 – 25% ATCC 802 Sonneborn's Paramecium medium, with addition of sterile barley grain, 17 °C
HM-V – Halophiles Medium number V according to [51] with addition of sterile barley grain, 20–25 °C
JM – ATCC 1525, 25 °C
LB – 3% Lysogeny Broth medium according to [52], 25 °C
LBM – 3% Lysogeny Broth medium according to [52] in Artificial Sea Water, 25 °C

M7 – medium according to[53], 25 °C
MAM – Marine Amoeba Medium – ATCC medium 994, 25 °C
MEA – Malt Extract Agar according to [54], 25 °C
MS-1 – Murashige and Skoog liquid medium according to [55], 25 °C, 16:8 h light:dark cycle
MS-2 – Murashige and Skoog solid medium according to [55], 25 °C, 16:8 h light:dark cycle
Neff – medium of Neff and Neff according to [56], 25 °C
OG – oat grain on cellulose paper kept in 100% humidity, 25 °C
PDA – Potato Dextrose Agar according to [57], 25 °C
PYGC – Proteose peptone – Yeast extract – Glucose–Cysteine medium according to [58], 25 °C
TYI – ATCC 2695 Keister's Modified TYI-S-33 medium, 37 °C
TYM – medium modified according to [59] by an overlay of inactivated horse serum, 25 °C
YPAD – ATCC 1069 medium, 37 °C
† – fixed cells
* – supplementary guanine added (approximately 30 µM final concentration), sterilized by 0.22µm filtration
# – same species has been measured previously for publication in [3]

Cult. coll.	Code	Species	Habitat -trophy	Taxonomic classification	Raman identity	Cult. method
priv		*Eimeria maxima* **(A)** (m)	E h p	SAR – Alveolata – **Apicomplexa** – Coccidia	Guanine	†
priv		*Psychodiella sergenti*	E h p	SAR – Alveolata – **Apicomplexa** – Gregarinasina	Guanine	–
NCMA	CCMP3155	*Vitrella brassicaformis*	M a	SAR – Alveolata – **Chrompodellids** – Vitrellaceae	Guanine	–
ns		*Coleps* sp.	F h	SAR – Alveolata – **Ciliophora** – Prostomatea	Starch	–
ns		*Cyclidium* sp.	F h	SAR – Alveolata – **Ciliophora** – Oligohymenophorea	Guanine	–
ns		*Euplotes* sp.	F h	SAR – Alveolata – **Ciliophora** – Spirotrichea	Guanine	–
ns		*Euplotes* sp.	M h	SAR – Alveolata – **Ciliophora** – Spirotrichea	Guanine	–
ns		*Halteria* sp.	F h	SAR – Alveolata – **Ciliophora** – Spirotrichea	Guanine	–
ns		*Glaucoma* sp.	F h	SAR – Alveolata – **Ciliophora** – Oligohymenophorea	Guanine	–
ns		Hypotrichia gen. sp.	M h	SAR – Alveolata – **Ciliophora** – Spirotrichea	Guanine	–
ns		*Lembadion* sp.	M h	SAR – Alveolata – **Ciliophora** – Oligohymenophorea	Guanine	–
ns		*Oxytricha* gen. sp.	F h	SAR – Alveolata – **Ciliophora** – Spirotrichea	Guanine	–
ns		*Paramecium* sp. **(C)** (m)	F h	SAR – Alveolata – **Ciliophora** – Oligohymenophorea	Guanine	†
ns		Scuticulociliatia gen. sp.	M h	SAR – Alveolata – **Ciliophora** – Oligohymenophorea	Guanine	–
ns		*Vorticella* sp.	F h	SAR – Alveolata – **Ciliophora** – Oligohymenophorea	–	–
priv		*Borghiella* sp.	F a	SAR – Alveolata – **Dinoflagellata** – Suessiales	Guanine	–
NCMA	CCMP449	*Heterocapsa triquetra*	M a	SAR – Alveolata – **Dinoflagellata** – Peridiniales	Guanine	f/2
priv		*Glenodinium foliaceum* **(B)**	M a	SAR – Alveolata – **Dinoflagellata** – Peridiniales	Guanine	–
ns		*Gymnodinium* sp.	F a	SAR – Alveolata – **Dinoflagellata** – Gymnodiniales	Guanine	–
ns		*Peridinium* sp.	F a	SAR – Alveolata – **Dinoflagellata** – Peridiniales	Guanine	–
priv		*Sphaerodinium* sp.	F a	SAR – Alveolata – **Dinoflagellata** – Suessiales	Guanine	–
priv	370	*Symbiodinium microadriaticum* (m)	M a	SAR – Alveolata – **Dinoflagellata** – Suessiales	Guanine	f/2
NCMA	CCMP829	*Symbiodinium tridacnidorum*	M a	SAR – Alveolata – **Dinoflagellata** – Suessiales	Guanine	f/2
ns		*Symbiodinium* sp. isolated from *Capnella imbricata*	M a	SAR – Alveolata – **Dinoflagellata** – Suessiales	Guanine	f/2
CAUP	J95	*Achnanthidium* sp.	F a	SAR – Stramenopiles – **Ochrophyta** – **Bacillariophyceae**	Calcite	–
ns		*Asterionella formosa*	F a	SAR – Stramenopiles – **Ochrophyta** – **Bacillariophyceae**	–	–
ns		*Aulacoseira* sp.	F a	SAR – Stramenopiles – **Ochrophyta** – **Bacillariophyceae**	–	–
ns		*Encyonema* sp.	F a	SAR – Stramenopiles – **Ochrophyta** – **Bacillariophyceae**	Uric acid	–
ns		*Entomoneis ornata*	M a	SAR – Stramenopiles – **Ochrophyta** – **Bacillariophyceae**	–	–
ns		*Fragilaria* sp.	F a	SAR – Stramenopiles – **Ochrophyta** – **Bacillariophyceae**	Uric acid	–
ns		*Frustulia* sp.	F a	SAR – Stramenopiles – **Ochrophyta** – **Bacillariophyceae**	–	–
ns		*Gomphonema truncatum*	F a	SAR – Stramenopiles – **Ochrophyta** – **Bacillariophyceae**	–	–

Cult. coll.	Code	Species	Habitat -trophy	Taxonomic classification	Raman identity	Cult. method
ns		*Licmophora* sp.	M a	SAR – Stramenopiles – **Ochrophyta** – **Bacillariophyceae**	Calcite	–
ns		*Melosira* sp.	F a	SAR – Stramenopiles – **Ochrophyta** – **Bacillariophyceae**	–	–
ns		*Navicula cryptocephala*	F a	SAR – Stramenopiles – **Ochrophyta** – **Bacillariophyceae**	Uric acid	–
ns		*Navicula* sp.	F a	SAR – Stramenopiles – **Ochrophyta** – **Bacillariophyceae**	Uric acid Xanthine	–
ns		Naviculaceae gen. sp., *Seminavis*-like	M a	SAR – Stramenopiles – **Ochrophyta** – **Bacillariophyceae**	Guanine	–
ns		*Paralia sulcata*	M a	SAR – Stramenopiles – **Ochrophyta** – **Bacillariophyceae**	Calcite	–
CCAP	1052/1B	*Phaeodactylum tricornutum* (m)	M a	SAR – Stramenopiles – **Ochrophyta** – **Bacillariophyceae**	Calcite	f/2
ns		*Pinnularia viridis*	F a	SAR – Stramenopiles – **Ochrophyta** – **Bacillariophyceae**	–	–
ns		*Pleurosigma* sp.	M a	SAR – Stramenopiles – **Ochrophyta** – **Bacillariophyceae**	Uric acid	–
ns		*Stauroneis phoenicenteron*	F a	SAR – Stramenopiles – **Ochrophyta** – **Bacillariophyceae**	–	–
NCMA	CCMP1335	*Thalassiosira pseudonana* (m)	M a	SAR – Stramenopiles – **Ochrophyta** – **Bacillariophyceae**	–	f/2
ns		*Spumella* sp.	F a	SAR – Stramenopiles – **Ochrophyta** – **Synurophyceae**	Guanine	–
CAUP	B710	*Synura hibernica*	F a	SAR – Stramenopiles – **Ochrophyta** – **Synurophyceae**	Guanine	–
CAUP	H4302	*Eustigmatos polyphem* (b)	T a	SAR – Stramenopiles – **Ochrophyta** – **Eustigmatophyceae**	Guanine	BBM
NIES	2146	*Nannochloropsis oculata* **(K)** (b) (m)	M a	SAR – Stramenopiles – **Ochrophyta** – **Eustigmatophyceae**	Guanine	f/2
NIES	2860	*Vacuoliviride crystalliferum*#	Un a	SAR – Stramenopiles – **Ochrophyta** – **Eustigmatophyceae**	Guanine Chrysolaminarin	BBM
ns		*Cystoseira* sp.	M a	SAR – Stramenopiles – **Ochrophyta** – **Phaeophyceae**	Calcite	–
ns		*Dictyota dichotoma*	M a	SAR – Stramenopiles – **Ochrophyta** – **Phaeophyceae**	Calcite	–
ns		*Padina pavonica*	M a	SAR – Stramenopiles – **Ochrophyta** – **Phaeophyceae**	Calcite	–
ns		*Actinophrys* sp.	F a	SAR – Stramenopiles – **Ochrophyta** – **Actinophryidae**	Guanine	–
ns		*Gonyostomum* sp.	F a	SAR – Stramenopiles – **Ochrophyta** – **Raphidophyceae**	Guanine	–
CAUP	D301	*Botrydiopsis intercedens*	F a	SAR – Stramenopiles – **Ochrophyta** – **Xanthophyceae**	Guanine	BBM
UTEX	B 2999	*Heterococcus* sp.	F a	SAR – Stramenopiles – **Ochrophyta** – **Xanthophyceae**	–	BBM
ns		*Ophiocytium* sp.	F a	SAR – Stramenopiles – **Ochrophyta** – **Xanthophyceae**	Guanine	–
CCALA	517	*Tribonema aequale* **(F)** (m)	F a	SAR – Stramenopiles – **Ochrophyta** – **Xanthophyceae**	Guanine	BBM
ns		*Xanthonema* sp.	F a	SAR – Stramenopiles – **Ochrophyta** – **Xanthophyceae**	Guanine	–
DBM	CO3I	*Schizochytrium* sp. (b) (m)	M h	SAR – Stramenopiles – **Labyrinthulomycota**	Guanine	ASW-L
priv		*Cafeteria roenbergensis*	M h	SAR – Stramenopiles – **Bicosoecida**	–	f/2*
priv		*Cafileria marina*	M h	SAR – Stramenopiles – **Bicosoecida**	Guanine	f/2*
CCF	3762	*Phytophthora cactorum*	E h	SAR – Stramenopiles – **Oomycota**	–	PDA

Cult. coll.	Code	Species	Habitat-trophy	Taxonomic classification	Raman identity	Cult. method
CCF	4738	*Phytophthora rosacearum*-like	E h	SAR – Stramenopiles – **Oomycota**	–	PDA
priv	Ther	*Blastocystis* sp. isolated from *Testudo hermanni*	E h	SAR – Stramenopiles – **Opalinata** – Blastocystae	–	TYM
NCMA	CCMP2755	*Bigelowiella natans* **(L)** (m)	M a	SAR – Rhizaria – **Cercozoa** – **Chlorarachnea**	Guanine	f/2
priv	LITO	Cercomonadida gen. sp.	F h	SAR – Rhizaria – **Cercozoa** – **Cercomonadida**	Guanine	Fw
ns		*Viridiraptor invadens*	F h	SAR – Rhizaria – **Cercozoa** – **Viridiraptoridae**	Guanine	–
ns		*Euglypha* sp.	F h	SAR – Rhizaria – **Cercozoa** – **Euglyphida**	Guanine	–
ns		*Trinema* sp.	F h	SAR – Rhizaria – **Cercozoa** – **Euglyphida**	Guanine	–
ns		*Marinomyxa marina*	M h	SAR – Rhizaria – Endomyxa – **Phytomyxea**	–	–
ns		Acantharea gen. sp.	M h	SAR – Rhizaria – **Retaria** – Acantharea	Celestite	†
ns		Globigerinidae gen. sp.	M h	SAR – Rhizaria – **Retaria** – Foramanifera	–	†
ns		Globorotaliidae gen. sp.	M h	SAR – Rhizaria – **Retaria** – Foramanifera	Calcite	†
priv	LIS-Tel	*Telonema* sp.	M h	**Telonemida**	Guanine	f/2B*
NCMA	CCMP371	*Emiliania huxleyi* (m)	M a	Haptista – **Haptophyta**	Guanine	f/2*
RCC	RCC1350	*Isochrysis* sp. **(M)** (b)	M a	Haptista – **Haptophyta**	Xanthine Uric acid	f/2*
ns		*Raphidiophrys* sp.	F h	Haptista – **Centroplasthelida**	Guanine	–
CAUP	F105	*Cryptomonas* sp. (O)	F a	Cryptista – **Cryptophyta**	Uric acid	BBM
ns		*Chroomonas* sp.	F a	Cryptista – **Cryptophyta**	Uric acid Guanine monohydrate	–
CAUP	O101	*Glaucocystis nostochinearum*	F a	Archaeplastida – **Glaucophyta**	Xanthine	BBM
ns		*Asparagopsis taxiformis*	M a	Archaeplastida – **Rhodophyta** – **Florideophyceae**	Calcite	–
CAUP	L201	*Asterocytis ramosa*	M a	Archaeplastida – **Rhodophyta** – **Bangiophyceae**	Carotenoids, lipids	f/2
CCALA	971	*Audouinella* sp.	M a	Archaeplastida – **Rhodophyta** – **Florideophyceae**	–	f/2
ns		*Ceramium* sp.	M a	Archaeplastida – **Rhodophyta** – **Florideophyceae**	Calcite	–
ns		*Hildebrandia rivularis*	M a	Archaeplastida – **Rhodophyta** – **Florideophyceae**	–	–
CCALA	416	*Porphyridium purpureum* (b)	M a	Archaeplastida – **Rhodophyta** – **Porphyridiophyceae**	–	f/2
CCALA	925	*Rhodella violacea*	M a	Archaeplastida – **Rhodophyta** – **Rhodellophyceae**	Lipids	f/2
ns		*Asterococcus* sp.	F a	Archaeplastida – Viridiplantae – Chlorophyta – **Chlorophyceae**	Guanine	–
ns		*Bulbochaete* sp.	F a	Archaeplastida – Viridiplantae – Chlorophyta – **Chlorophyceae**	Guanine	–
CRC	CC-1690	*Chlamydomonas reinhardtii*# (m)	F a	Archaeplastida – Viridiplantae – Chlorophyta – **Chlorophyceae**	Guanine	BBM
CAUP	G224	*Chlamydomonas geitleri*	F a	Archaeplastida – Viridiplantae – Chlorophyta – **Chlorophyceae**	Guanine	BBM

Cult. coll.	Code	Species	Habitat -trophy	Taxonomic classification	Raman identity	Cult. method
ns		*Chlamydomonas* sp.	F a	Archaeplastida – Viridiplantae – Chlorophyta – **Chlorophyceae**	Guanine	–
priv	AMAZONIE	*Chlamydomonadales* gen. sp.	F h	Archaeplastida – Viridiplantae – Chlorophyta – **Chlorophyceae**	Guanine	Fw
priv	KBEL1C	*Polytoma* sp.	F h	Archaeplastida – Viridiplantae – Chlorophyta – **Chlorophyceae**	Guanine	Fw
CAUP	H 6902	*Chlorochytrium lemnae*	E – F a	Archaeplastida – Viridiplantae – Chlorophyta – **Chlorophyceae**	Guanine	BBM
priv		*Chloromonas arctica*	S a	Archaeplastida – Viridiplantae – Chlorophyta – **Chlorophyceae**	Guanine	BBM
ns		*Desmodesmus quadricauda* (m)	F a	Archaeplastida – Viridiplantae – Chlorophyta – **Chlorophyceae**	Guanine	–
ns		*Desmodesmus* sp.	F a	Archaeplastida – Viridiplantae – Chlorophyta – **Chlorophyceae**	Guanine	–
ns		*Eudorina* sp.	F a	Archaeplastida – Viridiplantae – Chlorophyta – **Chlorophyceae**	Guanine	–
ns		*Gleocystis* sp.	F a	Archaeplastida – Viridiplantae – Chlorophyta – **Chlorophyceae**	Guanine	–
ns		*Microspora* sp.	F a	Archaeplastida – Viridiplantae – Chlorophyta – **Chlorophyceae**	Guanine	–
ns		*Monactinus simplex*	F a	Archaeplastida – Viridiplantae – Chlorophyta – **Chlorophyceae**	Guanine	–
CAUP	H2908	*Monoraphidium contortum* (b)	F a	Archaeplastida – Viridiplantae – Chlorophyta – **Chlorophyceae**	Guanine	BBM
ns		*Oedogonium* sp.	F a	Archaeplastida – Viridiplantae – Chlorophyta – **Chlorophyceae**	Guanine	–
ns		*Pediastrum boryanum*	F a	Archaeplastida – Viridiplantae – Chlorophyta – **Chlorophyceae**	Guanine	–
CAUP	H2308	*Pediastrum duplex* **(I)**	F a	Archaeplastida – Viridiplantae – Chlorophyta – **Chlorophyceae**	Guanine	BBM
ns		*Tetraedron* sp.	F a	Archaeplastida – Viridiplantae – Chlorophyta – **Chlorophyceae**	Guanine	–
ns		*Tetraspora* sp.	F a	Archaeplastida – Viridiplantae – Chlorophyta – **Chlorophyceae**	Guanine	–
CAUP	H 1917	*Chlorella vulgaris* **(N)** (b) (m)	F a	Archaeplastida – Viridiplantae – Chlorophyta – **Trebouxiophyceae**	Xanthine	BBM*
CAUP	H 5107	*Coccomyxa elongata*	T a	Archaeplastida – Viridiplantae – Chlorophyta – **Trebouxiophyceae**	Guanine	BBM
ns		*Dictyosphaerium* sp. (b)	F a	Archaeplastida – Viridiplantae – Chlorophyta – **Trebouxiophyceae**	Uric acid	–
ns		*Keratococcus* sp.	F a	Archaeplastida – Viridiplantae – Chlorophyta – **Trebouxiophyceae**	Guanine	–
ns		*Micractinium* sp.	F a	Archaeplastida – Viridiplantae – Chlorophyta – **Trebouxiophyceae**	Guanine	–
CAUP	H8801	*Phyllosiphon arisari*	F a p	Archaeplastida – Viridiplantae – Chlorophyta – **Trebouxiophyceae**	Lipids	BBM
CAUP	H8605	*Symbiochloris tschermakiae*	E/T a	Archaeplastida – Viridiplantae – Chlorophyta – **Trebouxiophyceae**	Lipids	BBM
ns		*Anadyomene* sp.	M a	Archaeplastida – Viridiplantae – Chlorophyta – **Ulvophyceae**	Calcite	–
ns		*Cladophora* sp.	F a	Archaeplastida – Viridiplantae – Chlorophyta – **Ulvophyceae**	Guanine	–
ns		*Cladophora* sp.	M a	Archaeplastida – Viridiplantae – Chlorophyta – **Ulvophyceae**	Calcite	–
ns		*Enteromorpha* sp.	M a	Archaeplastida – Viridiplantae – Chlorophyta – **Ulvophyceae**	Calcite	–
CAUP	H5301	*Scotinosphaera gibberosa*	F/T a	Archaeplastida – Viridiplantae – Chlorophyta – **Ulvophyceae**	Carotenoids, lipids	BBM
CAUP	J1601	*Trentepohlia* sp.	T a	Archaeplastida – Viridiplantae – Chlorophyta – **Ulvophyceae**	Carotenoids, lipids	BBM

Cult. coll.	Code	Species	Habitat -trophy	Taxonomic classification	Raman identity	Cult. method
CAUP	M101	*Prasinocladus ascus*	M a	Archaeplastida – Viridiplantae – Chlorophyta – **Chlorodendrophyceae**	Guanine monohydrate Uric acid	–
CAUP	M201	*Tetraselmis subcordiformis* **(H)** (b)	M a	Archaeplastida – Viridiplantae – Chlorophyta – **Chlorodendrophyceae**	Guanine monohydrate Uric acid	f/2
RCC	RCC745	*Ostreococcus tauri* (m)	M a	Archaeplastida – Viridiplantae – Chlorophyta – **Mamiellophyceae**	–	f/2
ns		*Nephroselmis* sp.	M a	Archaeplastida – Viridiplantae – Chlorophyta – **Nephrophyceae**	Guanine	–
ns		*Pyramimonas* sp.	M a	Archaeplastida – Viridiplantae – Chlorophyta – **Pyramimonadophyceae**	Guanine	–
NIES	995	*Mesostigma viride*	F a	Archaeplastida – Viridiplantae – Streptophyta – **Mesostigmatophyta**	–	–
CAUP	H7601	*Chlorokybus atmophyticus*	T a	Archaeplastida – Viridiplantae – Streptophyta – **Chlorokybophyceae**	Guanine	BBM
NIES	2285	*Klebsormidium flaccidum*# **(P)**	T a	Archaeplastida – Viridiplantae – Streptophyta – **Klebsormidiophyceae**	Uric acid	BBM
ns		*Coleochaete* sp.	F a	Archaeplastida – Viridiplantae – Streptophyta – **Coleochaetophyceae**	Calcium oxalate	–
NIES	1604	*Chara braunii*	F a	Archaeplastida – Viridiplantae – Streptophyta – **Charophyceae**	–	–
CAUP	K 801	*Actinotaenium* sp.	F a	Archaeplastida – Viridiplantae – Streptophyta – **Zygnematophyceae**	Uric acid	BBM
NIES	67	*Closterium peracerosum-strigosum-littorale* complex (m)	F a	Archaeplastida – Viridiplantae – Streptophyta – **Zygnematophyceae**	Baryte Starch	BBM
ns		*Cosmarium* sp.	F a	Archaeplastida – Viridiplantae – Streptophyta – **Zygnematophyceae**	Uric acid Baryte	–
ns		*Cylindrocystis* sp.	T a	Archaeplastida – Viridiplantae – Streptophyta – **Zygnematophyceae**	Calcium oxalate	–
ns		*Euastrum humerosum*	F a	Archaeplastida – Viridiplantae – Streptophyta – **Zygnematophyceae**	Uric acid	–
CAUP	K101	*Mesotaenium caldariorum*	F a	Archaeplastida – Viridiplantae – Streptophyta – **Zygnematophyceae**	Uric acid Guanine monohydrate	BBM*
ns		*Mougeotia* sp.	F a	Archaeplastida – Viridiplantae – Streptophyta – **Zygnematophyceae**	Uric acid	–
ns		*Netrium* sp.	F a	Archaeplastida – Viridiplantae – Streptophyta – **Zygnematophyceae**	Uric acid	–
NIES	303	*Penium margaritaceum* **(Q)**	F a	Archaeplastida – Viridiplantae – Streptophyta – **Zygnematophyceae**	Uric acid	BBM
ns		*Spirogyra* sp.	F a	Archaeplastida – Viridiplantae – Streptophyta – **Zygnematophyceae**	Baryte	–
ns		*Staurastrum* sp.	F a	Archaeplastida – Viridiplantae – Streptophyta – **Zygnematophyceae**	Uric acid	–
ns		*Tetmemorus* sp.	F a	Archaeplastida – Viridiplantae – Streptophyta – **Zygnematophyceae**	Uric acid	–
ns		*Xanthidium* sp.	F a	Archaeplastida – Viridiplantae – Streptophyta – **Zygnematophyceae**	Uric acid	–
ns		*Halophila stipulacea*	M a	Archaeplastida – Viridiplantae – Streptophyta – **Embryophyta**	Calcium oxalate monohydrate, dihydrate	–

Cult. coll.	Code	Species	Habitat -trophy	Taxonomic classification	Raman identity	Cult. method
priv	BY-2	*Nicotiana tabacum*	T a	Archaeplastida – Viridiplantae – Streptophyta – **Embryophyta**	Calcium oxalate monohydrate	MS-1
priv		*Physcomitrela patens*	T a	Archaeplastida – Viridiplantae – Streptophyta – **Embryophyta**	Calcium oxalate monohydrate	MS-2
priv	BW2	*Hemimastix kukwesjijk*	F h	**Hemimastigophora**	Guanine	FwB2*
ns		*Entosiphon* sp.	F a	Excavata – Discoba – **Euglenozoa – Euglenida**	Guanine	–
ns		*Euglena* sp. (m)	F a	Excavata – Discoba – **Euglenozoa – Euglenida**	Guanine	–
NCMA	CCMP1594	*Eutreptiela gymnastica* **(D)** (m)	M a	Excavata – Discoba – **Euglenozoa – Euglenida**	Guanine	f/2
ns		*Lepocynclis oxyuris*	F a	Excavata – Discoba – **Euglenozoa – Euglenida**	Guanine	–
ns		*Monomorphina pyrum*	F a	Excavata – Discoba – **Euglenozoa – Euglenida**	Guanine	–
ns		*Phacus* sp.	F a	Excavata – Discoba – **Euglenozoa – Euglenida**	Guanine	–
priv	SVATBA	*Rhabdomonas* sp.	F h	Excavata – Discoba – **Euglenozoa – Euglenida**	Guanine	Fw
ns		*Trachelomonas* sp.	F a	Excavata – Discoba – **Euglenozoa – Euglenida**	Guanine	–
priv	RIOZ	Free-living Kinetoplastea gen. sp.	F h	Excavata – Discoba – **Euglenozoa – Kinetoplastea**	Guanine	Fw
ns		*Bodo* sp.	F h	Excavata – Discoba – **Euglenozoa – Kinetoplastea**	Guanine	–
priv	M09	*'jaculum'* gen. sp.	E h p	Excavata – Discoba – **Euglenozoa – Kinetoplastea**	–	BHI
priv		*Trypanosoma mega*	E h p	Excavata – Discoba – **Euglenozoa – Kinetoplastea**	–	BHI
priv	YPF 1621	*Namystynia karyoxenos*	M h	Excavata – Discoba – **Euglenozoa – Diplonemea**	Guanine	ASW-D
priv	1.7 clone	*Rhynchopus* sp.	M h	Excavata – Discoba – **Euglenozoa – Diplonemea**	Guanine	ASW-D
priv	DT1610	*Flectonema* sp.	M h	Excavata – Discoba – **Euglenozoa – Diplonemea**	Guanine monohydrate	ASW-D
priv	RUM4AN	*Psalteriomonas lanterna*	F h	Excavata – Discoba – **Heterolobosea**	Guanine	Fw
priv	NEG-M	*Naegleria gruberi* **(E)** (m)	F h	Excavata – Discoba – **Heterolobosea**	Guanine	M7*
priv	BUSSPRAND	*Velundella trypanoides*	M h	Excavata – Discoba – **Jakobida**	–	JM
priv	AND	*Stygiella agilis*	M h	Excavata – Discoba – **Jakobida**	–	JM
priv	SPINDL2	*Gyromonas ambulans*	F h	Excavata – **Metamonada** – Fornicata	Guanine	Fw*
priv	TUN2	*Hexamita* sp.	F h	Excavata – **Metamonada** – Fornicata	Guanine	Fw*
priv	LITO	*Trepomonas rotans*	F h	Excavata – **Metamonada** – Fornicata	Guanine	Fw*
priv	BREZ2C	*Trepomonas* sp.	F h	Excavata – **Metamonada** – Fornicata	Guanine	Fw*
priv	CONGO	*Trepomonas steinii*	F h	Excavata – **Metamonada** – Fornicata	Guanine	LB
priv	Ncub	*Macrotrichomonoides* sp. isolated from *Neotermes cubanus*	E h	Excavata – **Metamonada** – Parabasalia	Guanine	–
priv	249	*Gefionella okellyi* **(J)**	F h	**Malawimonadida**	Guanine	f/2B*
ATCC	HM-1:IMSS	*Entamoeba histolytica*	E h	Amoebozoa – Evosea – **Archamoebae**	Lipids	TYI*

Cult. coll.	Code	Species	Habitat-trophy	Taxonomic classification	Raman identity	Cult. method
ATCC	30984	*Mastigamoeba balamuthi*	F h	Amoebozoa – Evosea – **Archamoebae**	Xanthine Lipids	PYGC*
priv	GO7	*Mastigella eilhardi*	F h	Amoebozoa – Evosea – **Archamoebae**	Guanine	Fw*
ns		*Fuligo septica*	T h	Amoebozoa – Evosea – **Eumycetozoa**	Guanine	–
priv		*Physarum polycephalum*	T h	Amoebozoa – Evosea – **Eumycetozoa**	Xanthine	OG *
priv	Neff	*Acanthamoeba castellanii*	F h	Amoebozoa – **Discosea** – Centramoebia	Xanthine Lipids	Neff*
ns		*Mayorella* sp.	F h	Amoebozoa – **Discosea** – Flabellinia	Xanthine	–
ns		*Mayorella* sp.	M h	Amoebozoa – **Discosea** – Flabellinia	Xanthine	–
priv	WFP252	*Neoparamoeba* sp.	M h	Amoebozoa – **Discosea** – Flabellinia	–	MAM
ns		*Thecamoeba* sp.	F h	Amoebozoa – **Discosea** – Flabellinia	Guanine	–
ns		*Vannella* sp.	F h	Amoebozoa – **Discosea** – Flabellinia	Guanine	–
ns		*Difflugia* sp.	F h	Amoebozoa – **Tubulinea** – Arcellinida	Guanine	–
ns		*Rhizamoeba* sp.	F h	Amoebozoa – **Tubulinea** – Leptomyxida	–	–
ns		*Saccamoeba* sp.	F h	Amoebozoa – **Tubulinea** – Hartmannellidae	Unidentified	–
priv	MSEDG	*Saccamoeba* sp.	F h	Amoebozoa – **Tubulinea** – Hartmannellidae	Unidentified	FwAM*
priv	4391/I	*Vermamoeba vermiformis*	F h	Amoebozoa – **Tubulinea** – Echinamoebida	–	FwAM*
priv	LIS-Man	*Mantamonas* sp.	M h	CRuMs – **Mantamonadida**	–	f/2B*
priv	FB10	*Subulatomonas* sp.	M h	Obazoa – **Breviatea**	–	LBM
priv	C3C	Choanoflagellata gen. sp.	Hp h	Obazoa – Opisthokonta – **Choanoflagellata**	–	HM-V*
ns		Chaetonotidae gen. sp.	F h	Obazoa – Opisthokonta – **Metazoa** – Gastrotricha	Guanine	–
ns		Nematoda gen. sp.	F/T h	Obazoa – Opisthokonta – **Metazoa** – Nematoda	Uric acid	–
ns		*Oncorhynchus mykiss* (scale)	F h	Obazoa – Opisthokonta – **Metazoa** – Chordata	Guanine	–
CCF	2912	*Aspergillus nidulans*	F/T h	Obazoa – Opisthokonta – **Fungi** – Ascomycota – Eurotiales	–	MEA
ATCC	SC5314	*Candida albicans*	F/T h	Obazoa – Opisthokonta – **Fungi** – Ascomycota – Saccharomycetales	Guanine	MEA
EUROS CARF	BY4741	*Saccharomyces cerevisiae*	T h	Obazoa – Opisthokonta – **Fungi** – Ascomycota – Saccharomycetales	–	YPAD
CCF	3485	*Neurospora sitophila*	F/T h	Obazoa – Opisthokonta – **Fungi** – Ascomycota – Sordariales	–	MEA
CCVC	CQ1	*Nosema bombycis*	E h p	Obazoa – Opisthokonta – **Opisthosporidia** – **Microsporidia**	–	–
ns		*Woronichinia naegeliana*	F a	Eubacteria – Cyanobacteria	Aerotopes	–
ns		*Oscillatoria* sp.	F a	Eubacteria – Cyanobacteria	Carotenoids, lipids	–
priv		*Bacillus subtilis*	T h	Eubacteria – Firmicutes	–	

Table S2. Overview of the Concentrative nucleoside transporter (CNT) distribution among eukaryotes based on HMM search in the database of 57 eukaryotic genomes.

Taxonomic rank	Presence of CNT
Amoebozoa	yes
Holomycota	yes
Chrompodellids	yes
Streptophyta	no
Rhizaria	yes
Stramenopiles	no
Holozoa	yes
Chlorophyta	no
Haptophyta	yes
Cryptophyceae	yes
Apicomplexa	no
Rhodophyta	no
Euglenozoa	no
Metamonada	no
Ciliophora	no
Heterolobosea	no
Perkinsidae	no
Apusomonadida	no

Table S3. Overview of the Equilibrative nucleoside transporter (ENT) distribution among eukaryotes based on HMM search in the database of 57 eukaryotic genomes.

Taxonomic rank	Presence of ENT
Amoebozoa	yes
Holomycota	yes
Chrompodellids	yes
Streptophyta	yes
Rhizaria	yes
Stramenopiles	yes
Holozoa	yes
Chlorophyta	yes
Haptophyta	yes
Cryptophyceae	yes
Apicomplexa	yes
Rhodophyta	yes
Euglenozoa	yes
Metamonada	yes
Ciliophora	yes
Heterolobosea	yes
Perkinsidae	yes
Apusomonadida	yes

1. **Movie S1.**

2. Polarized light microscopy of crystalline inclusions in SAR.

3. https://youtu.be/cMkMJthq5KQ

4. **Movie S2.**

5. Polarized light microscopy of crystalline inclusions in Haptista, Cryptista and Telonemia.

6. https://youtu.be/Z30CDbWqOhc

7. **Movie S3.**

8. Polarized light microscopy of crystalline inclusions in Archaeplastida.

9. https://youtu.be/2ZXfOdpsJcU

10. **Movie S4.**

11. Polarized light microscopy of crystalline inclusions in Amoebozoa.

12. https://youtu.be/DUbA5e_1_BE

13. **Movie S5.**

14. Polarized light microscopy of crystalline inclusions in Opisthokonta.

15. https://youtu.be/kyEzbo-IbiM

16. **Movie S6.**

17. Polarized light microscopy of crystalline inclusions in Excavata.

18. https://youtu.be/XWzNBLmE01A

19. **Movie S7.**

20. Polarized light microscopy of crystalline inclusions in Hemimastigophora.

21. https://youtu.be/gnUZhZRRfcw

22. **Movie S8.**

23. Polarized light microscopy of crystalline inclusions in Prokaryota – Cyanobacteria.

24. https://youtu.be/8yGo161rdJU

All the supplementary movies are deposited here: doi: 10.6084/m9.figshare.19604575

Massive Accumulation of Strontium and Barium in Diplonemid Protists

Jana Pilátová,[a,b,c] Daria Tashyreva,[a] Jiří Týč,[a] Marie Vancová,[a,d] Syed Nadeem Hussain Bokhari,[e] Radim Skoupý,[f] Mariana Klementová,[g] Hendrik Küpper,[d,e] Peter Mojzeš,[c] Julius Lukeš[a,d]

[a]Institute of Parasitology, Biology Centre, Czech Academy of Sciences, České Budějovice, Czech Republic
[b]Faculty of Science, Charles University, Prague, Czech Republic
[c]Institute of Physics, Faculty of Mathematics and Physics, Charles University, Prague, Czech Republic
[d]Faculty of Sciences, University of South Bohemia, České Budějovice, Czech Republic
[e]Institute of Plant Molecular Biology, Biology Centre, Czech Academy of Sciences, České Budějovice, Czech Republic
[f]Institute of Scientific Instruments, Czech Academy of Sciences, Brno, Czech Republic
[g]Institute of Physics, Czech Academy of Sciences, Prague, Czech Republic

Jana Pilátová and Daria Tashyreva contributed equally.

ABSTRACT Barium and strontium are often used as proxies of marine productivity in palaeoceanographic reconstructions of global climate. However, long-searched biological drivers for such correlations remain unknown. Here, we report that taxa within one of the most abundant groups of marine planktonic protists, diplonemids (Euglenozoa), are potent accumulators of intracellular barite ($BaSO_4$), celestite ($SrSO_4$), and strontiobarite ($(Ba,Sr)SO_4$). In culture, *Namystinia karyoxenos* accumulates Ba^{2+} and Sr^{2+} 42,000 and 10,000 times higher than the surrounding medium, forming barite and celestite representing 90% of the dry weight, the greatest concentration in biomass known to date. As heterotrophs, diplonemids are not restricted to the photic zone, and they are widespread in the oceans in astonishing abundance and diversity, as their distribution correlates with environmental particulate barite and celestite, prevailing in the mesopelagic zone. We found diplonemid predators, the filter-feeding zooplankton that produces fecal pellets containing the undigested celestite from diplonemids, facilitating its deposition on the seafloor. To the best of our knowledge, evidence for diplonemid biomineralization presents the strongest explanation for the occurrence of particulate barite and celestite in the marine environment. Both structures of the crystals and their variable chemical compositions found in diplonemids fit the properties of environmentally sampled particulate barite and celestite. Finally, we propose that diplonemids, which emerged during the Neoproterozoic era, qualify as impactful players in Ba^{2+}/Sr^{2+} cycling in the ocean that has possibly contributed to sedimentary rock formation over long geological periods.

IMPORTANCE We have identified that diplonemids, an abundant group of marine planktonic protists, accumulate conspicuous amounts of Sr^{2+} and Ba^{2+} in the form of intracellular barite and celestite crystals, in concentrations that greatly exceed those of the most efficient Ba/Sr-accumulating organisms known to date. We propose that diplonemids are potential players in Ba^{2+}/Sr^{2+} cycling in the ocean and have possibly contributed to sedimentary rock formation over long geological periods. These organisms emerged during the Neoproterozoic era (590 to 900 million years ago), prior to known coccolithophore carbonate biomineralization (~200 million years ago). Based on reported data, the distribution of diplonemids in the oceans is correlated with the occurrence of particulate barite and celestite. Finally, diplonemids may provide new insights into the long-questioned biogenic origin of particulate barite and celestite and bring more understanding of the observed

spatial-temporal correlation of the minerals with marine productivity used in reconstructions of past global climate.

Although in most environments strontium (Sr) and barium (Ba) are present in trace amounts, they can be accumulated in substantial quantities by some organisms (1, 2). Depending on their environmental availability, these elements are mostly taken up nonselectively together with Ca^{2+} (3, 4). The soluble form of Ba^{2+} is typically toxic for animals (e.g., use of rodenticides) due to its capacity to block K^+ channels, while insoluble $BaSO_4$ acts as a common contrast agent in medical radio-imaging (5). In contrast, soluble Sr^{2+} is not harmful, with the exception of the radioactive isotope $^{90}Sr^{2+}$ occurring as a nuclear contaminant that accumulates in marine biota and sediments (6). Indeed, in some algae, Sr^{2+} can almost fully replace Ca^{2+} without any discernible deleterious effects (7). In humans, Sr^{2+} treatment of osteoporosis is used to prevent fractures (8). Moreover, predictions concerning climate change stress the increased relevance of higher environmental mobilization of Sr^{2+} and Ba^{2+} due to enhanced solubility upon marine acidification (9). Apart from chemical precipitation treatments of radioactive $^{90}Sr^{2+}$ and toxic Ba^{2+}, there have been new attempts for bioremediation using cyanobacteria, algae, and fungi (1, 2, 6, 10).

In marine environments, microorganisms accumulate more Sr^{2+} than Ba^{2+}, possibly due to higher solubility and availability, i.e., the concentration of Sr^{2+} is around 88 μM compared to 40 to 150 nM Ba^{2+} (11, 12). In protists, Sr^{2+} is mostly present in the form of celestite (also referred to as celestine; $SrSO_4$) and strontianite ($SrCO_3$), while Ba^{2+} forms barite ($BaSO_4$) or witherite ($BaCO_3$) (13, 14). Moreover, Ba^{2+} and Sr^{2+} commonly substitute for each other in various ratios to form strontiobarite and baritocelestite $(Ba,Sr)SO_4$ (15). Celestite with traces of Ba^{2+} is well known for forming the complex skeletons of acanthareans (16). Intracellular barite crystals form statoliths of some freshwater charophyte algae and statocysts of marine ciliates, in which they likely play a role in graviperception (13, 17, 18). Haptophytes and foraminiferans form intracellular barite crystals with trace amounts of Sr^{2+} (19, 20), while strontianite and witherite occur in microalga *Tetraselmis* (21) and coccolithophorids (14, 22). The exact role of these crystalline inclusions remains unknown.

Marine Ba^{2+} and Sr^{2+} are frequently correlated with particulate organic carbon in the water column and sediments on the sea floor, indicating that microorganisms are capable of accumulating these elements (11, 23, 24), yet the celestite-rich skeletons of acanthareans dissolve during sedimentation (25). Ba^{2+} and Sr^{2+} carbonates and phosphates known from coccolithophorids and bacteria, respectively, contribute to the cycling of these elements with possible conversion to sulfates in the process of diagenesis (10, 14, 22, 26). In addition, barite, strontiobarite and celestite crystals are frequently found associated with fecal pellets, which contribute to the sedimentation of particulate Ba^{2+} and Sr^{2+} to the sea floor (24). However, until now, abundant planktonic organisms capable of selective intracellular accumulation of both Ba^{2+} and Sr^{2+} sulfates have not been identified (12, 13). The substantial work of Dehairs et al. (24) presents a series of evidence pointing to the biogenic origin of barite/celestite microcrystals, including micrographs of environmental microcrystals covered by desiccated cellular organic matter. Variable composition of marine suspended microcrystalline sulfates are commonly ascribed to barite with minor admixtures of Sr^{2+} alongside 10 to 30% of crystals dominated by celestite (24). Such variability is most plausibly explained by active biological catalysis (24). Despite the well-documented evidence-based predictions of the biogenic origins of barite and celestite minerals in the oceans (24, 27), the lack of organisms responsible for their production led to the gradual focus on microenvironment-mediated precipitation, stepping away from consideration of their biological origin (28).

Here, we show that diplonemids (Diplonemea, Euglenozoa), a group of biflagellated heterotrophic protists (29–31), are capable of massive intracellular accumulation of Sr^{2+} and Ba^{2+}. Specifically, three cultivable diplonemids accumulate celestite and sometimes barite crystals in intracellular concentrations of Sr^{2+} much greater than in
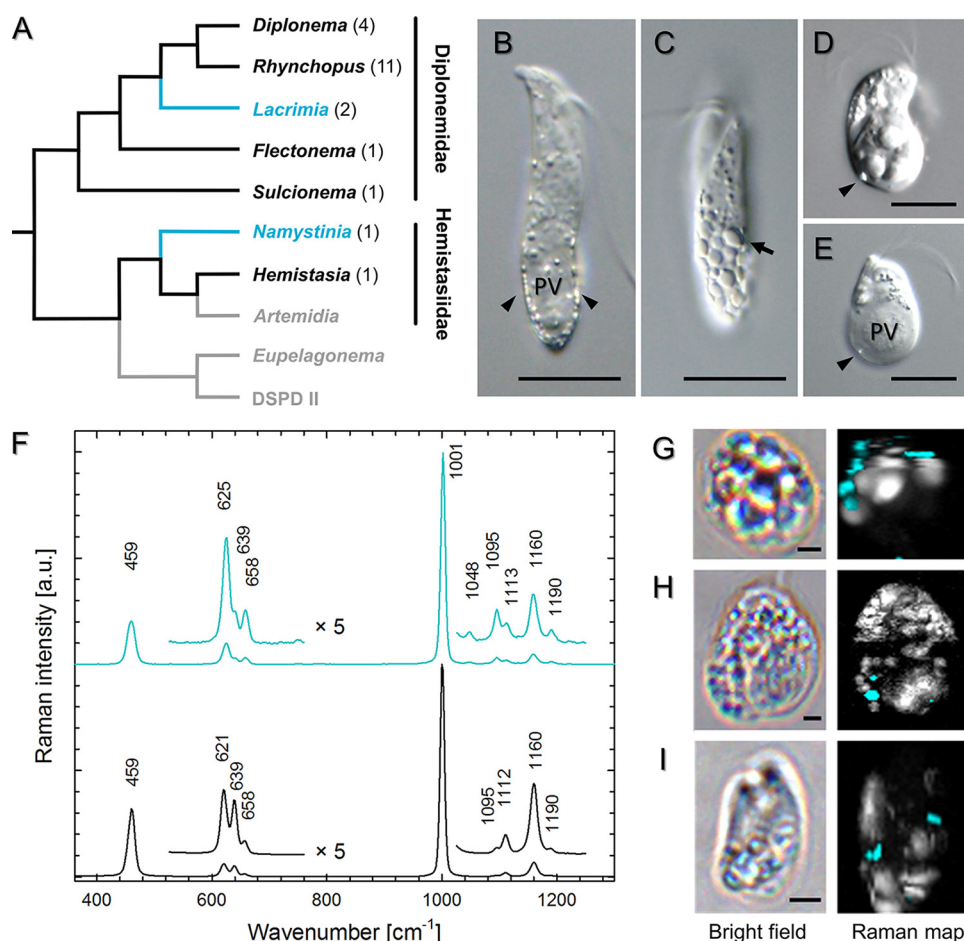
FIG 1 Distribution of celestite in diplonemids, based on Raman microscopy analysis. (A) Phylogenetic tree of diplonemids based on 29 with genera containing celestite (blue), other screened genera (black), and unexamined clades (gray). (B to E) DIC micrographs of *N. karyoxenos* (B and C), *Lacrimia* sp. YPF1808 (D), and *L. lanifica* (E) with celestite crystals marked by arrowheads; arrow points to a large polygonal crystal. Scale bar, 10 μm. (F) Raman spectra of biogenic celestite crystals found in diplonemid cells (blue) and celestite mineral (black). (G to I) Raman chemical maps of *N. karyoxenos* (G), *Lacrimia* sp. YPF1808 (H), and *L. lanifica* JW1601 (I) with celestite in blue and other cytoplasmic contents in white. Scale bar, 2 μm.

other organisms (10, 19). In the world's oceans, diplonemids have only recently been recognized as omnipresent and one of the most diverse and abundant groups of microeukaryotes (comparable to microalgae), with a prevalence within the mesopelagic protist community (32–34). Although relatively rare, they are present in freshwater bodies as well (35). We analyzed their crystalline inclusions by a range of complementary approaches and discuss here their possible biological functions and role in biogeochemical cycles.

RESULTS

Light microscopy and analysis of crystals by Raman microscopy. To determine the chemical composition of biogenic crystals directly within intact cells, Raman microscopy, a vibrational spectroscopic method sensitive to molecular composition, was used. Out of 21 strains belonging to 15 diplonemid species, three members of the distantly related genera *Lacrimia* and *Namystinia*, represented by *Lacrimia* sp. YPF1808, *Lacrima lanifica*, and *Namystinia karyoxenos*, were shown to possess celestite crystals (Fig. 1A). Their Raman spectra were congruent with the spectra of mineral celestite and chemically prepared precipitates of $SrSO_4$ (Fig. 1F), matching also Raman spectra of celestite reported elsewhere (36). Due to the countercation sensitivity of the position

of the most intense Raman band at around 1,000 cm^{-1} belonging to the symmetric ν_1 vibrational mode of the SO_4^{2-} tetrahedron, biogenic celestite could be unambiguously identified as $SrSO_4$ and was easily distinguishable from barite, baritocelestite, gypsum ($CaSO_4$), or calcite ($CaCO_3$) (see Fig. S1 in the supplemental material). Small relative-intensity nuances of other Raman bands of biogenic celestite from various cells (Fig. S2) can be explained by differences in crystal structures (lattice defects), trace admixtures of Ba^{2+}, and/or orientations of the crystals, as these are present also in the spectra of mineral reference and chemical precipitates.

When *N. karyoxenos* was examined by light microscopy with differential interference contrast (DIC), the crystalline structures appeared as small birefringent particles moving fast by Brownian motion (Fig. 1B and C; Movie S1). They were most prominent within the enlarged lacunae, which are peripheral membrane-bounded compartments positioned directly beneath the subpellicular microtubular corset (Movie S1), following the addition of 0.1% (wt/vol) formaldehyde. Within a single culture, the size and quantity of crystals inside the cells ranged from a few small particles (Fig. 1B) up to multiple large, tightly packed, polygonal crystals reflecting the shape of orthorhombic prisms (Fig. 1C). The crystalline particles of *Lacrimia* sp. YPF1808 and *L. lanifica* were far less prominent under the light microscope than those of *N. karyoxenos*. However, large crystals were visible around the posterior vacuole with DIC (Fig. 1D and E; Movie S1) and under polarized light (Movie S1).

Morphology, localization, and elemental analysis of intracellular crystals. Examination with light, Raman, transmission electron microscopy (TEM), and serial block-face scanning electron microscopy (SBF-SEM) showed that the crystalline inclusions in two clades of diplonemids differed in their localization and shapes. In semithin resin-embedded sections of *N. karyoxenos*, numerous orthorhombic prismatic and bipyramidal crystals were localized mostly inside the lacunae (Fig. 2A, C, and D), with a preference towards the cell posterior. Occasionally, crystals were found inside the large posterior vacuole (Fig. 2A) and in smaller vacuoles scattered throughout the cytoplasm (Fig. 2A and B). Only small crystals could be seen in semithin sections, while bigger crystals dropped out, leaving empty crystal-shaped holes. Due to frequent rupturing, it was not possible to visualize celestite crystals in semithin epoxy resin sections of *Lacrimia* species. Thus, we used the SBF-SEM approach, which showed that the celestite crystals of *Lacrimia* sp. YPF1808 appeared mostly in small membrane-bounded compartments with electron-transparent matrix (Fig. 2H to L) adjacent to the large posterior vacuole (Fig. 2H, I, and K). Three-dimensional (3D) reconstruction revealed that each of these compartments contained one crystal of variable size (Movie S2). Less frequently, crystals were found inside the posterior vacuole (Fig. 2I) or in compartments localized near the anterior flagellar pocket (Movie S2), while they were absent from the cytoplasm and other organelles. The crystals had a shape of rhombic prisms (Fig. 2J and M) or asymmetric tabular prismatic structures with pyramidal and pedial terminations (Fig. 2K and N). Although in *L. lanifica* the celestite crystals were mostly lost from the TEM sections, the positions of holes and ruptures within them and the analysis by Raman microscopy showed similar localizations and sizes of the crystals as those of *Lacrimia* sp. YPF1808 (Fig. 2D, E, H, and I). Likewise, the membrane-bounded compartments were positioned around the posterior vacuole (Fig. 2F), with small asymmetric flattened crystals preserved only occasionally in TEM sections (Fig. 2G).

The presence of celestite crystals (Fig. 1 and 2) was further confirmed by elemental analysis using energy-dispersive X-ray (EDX) spectroscopy in the cryo-SEM-EDX mode of freeze-fractured *Lacrimia* sp. YPF1808 (Fig. 3A and C; Fig. S3) and *N. karyoxenos* cells (Fig. 3B and C; Fig. S4) and by TEM-EDX of whole air-dried cells of *L. lanifica* (Fig. 3E). Atomic percentages estimated by cryo-SEM-EDX analysis were 7.2% Sr and 7.2% sulfur (S), compared to 1.1% Sr and 1.8% S in *Lacrimia* sp. YPF1808 and *N. karyoxenos*, respectively. The dominance of C, N, and O atoms can be explained by the presence of ice and signals from other cellular contents obtained from deeper and/or surrounding areas.
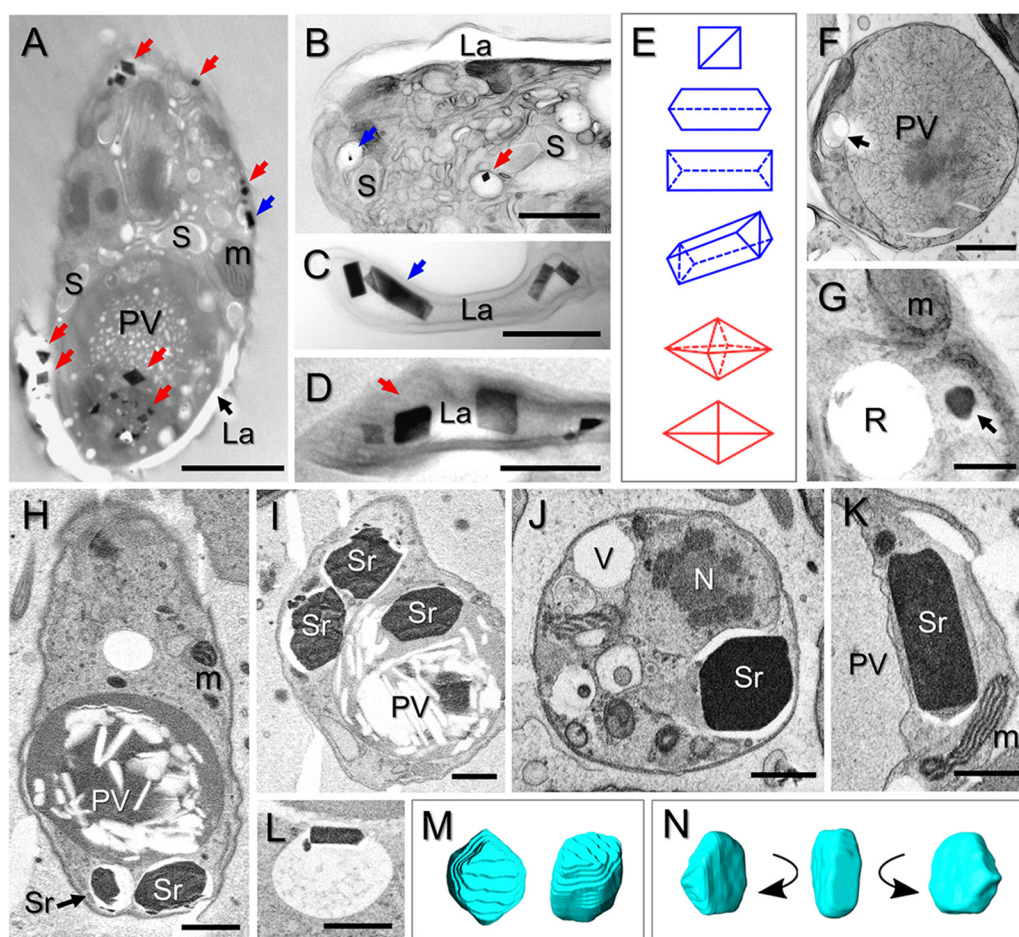
FIG 2 Crystal structures of naturally occurring celestite with possible barite admixtures in diplonemids. (A to E) TEM images of semithin sections of *N. karyoxenos* with longitudinally sectioned cell showing bipyramidal (red arrows) and prismatic (blue arrow) crystals inside peripheral lacunae and posterior vacuole (A); crystals contained within small vacuoles (B); prismatic (C) and bipyramidal (D) crystals inside lacunae; and a schematic representation of prismatic (blue) and bipyramidal (red) crystals (E). (F and G) TEM images of semithin sections of *L. lanifica* JW1601, with cells cross-sectioned through a posterior vacuole. An arrow points to a small membrane-bounded compartment with the hole left after a dropped-out crystal (F), and another arrow indicates a crystal inside a membrane-bounded compartment and the rupture introduced by a crystal during sectioning (G). (H to L) SBF-SEM images of *Lacrimia* sp. YPF1808 showing celestite crystals inside membrane-bounded compartments and the large posterior vacuole (I). (M and N) 3D reconstructions of celestite correspond to the images in panels J and K, respectively, in shape of rhombic prism (M) or asymmetric tabular prismatic crystal with pyramidal and pedial terminations (N). PV, posterior vacuole; M, mitochondrion; S, endosymbiotic bacteria; La, lacuna lumen; R, rupture; Sr, celestite crystal; N, nucleus. Scale bar, 2 μm (A and F), 1 μm (B and H to K), and 500 nm (C, D, and G).

The identities of celestite crystals in *Lacrimia* sp. YPF1808 (1 μm-thick sections from resin blocks used for SBF-SEM) and *N. karyoxenos* (250 nm-thick resin sections examined by TEM) were confirmed by SEM-EDX and TEM-EDX, respectively (Fig. 3D, F, and G; Fig. S5). Additionally, a significant amount of Ba^{2+} was detected in the crystals from *N. karyoxenos*. Crystallographic analysis by electron diffraction showed that the diffraction of measured crystals corresponded to celestite structure (isostructural with $BaSO_4$) with space group Pnma and lattice parameters a = 8.3 Å, b = 5.3 Å, and c = 6.8 Å in *L. lanifica*. Larger lattice parameters (a = 8.7 Å, b = 5.5 Å, c = 7.1 Å) were observed in *N. karyoxenos*, which may be explained by the replacement of Sr^{2+} with larger Ba^{2+} in the structure of celestite.

Quantitative analysis by ICP-MS and SBF-SEM. SBF-SEM-based 3D reconstructions of *Lacrimia* sp. YPF1808 (Movie S2) showed the presence of celestite crystals in all 20 analyzed cells, ranging from 2 to 16 celestite particles per cell (Fig. 4D; Table S2). In total, more than 100 crystals were analyzed, with a volume ranging from 0.017 to
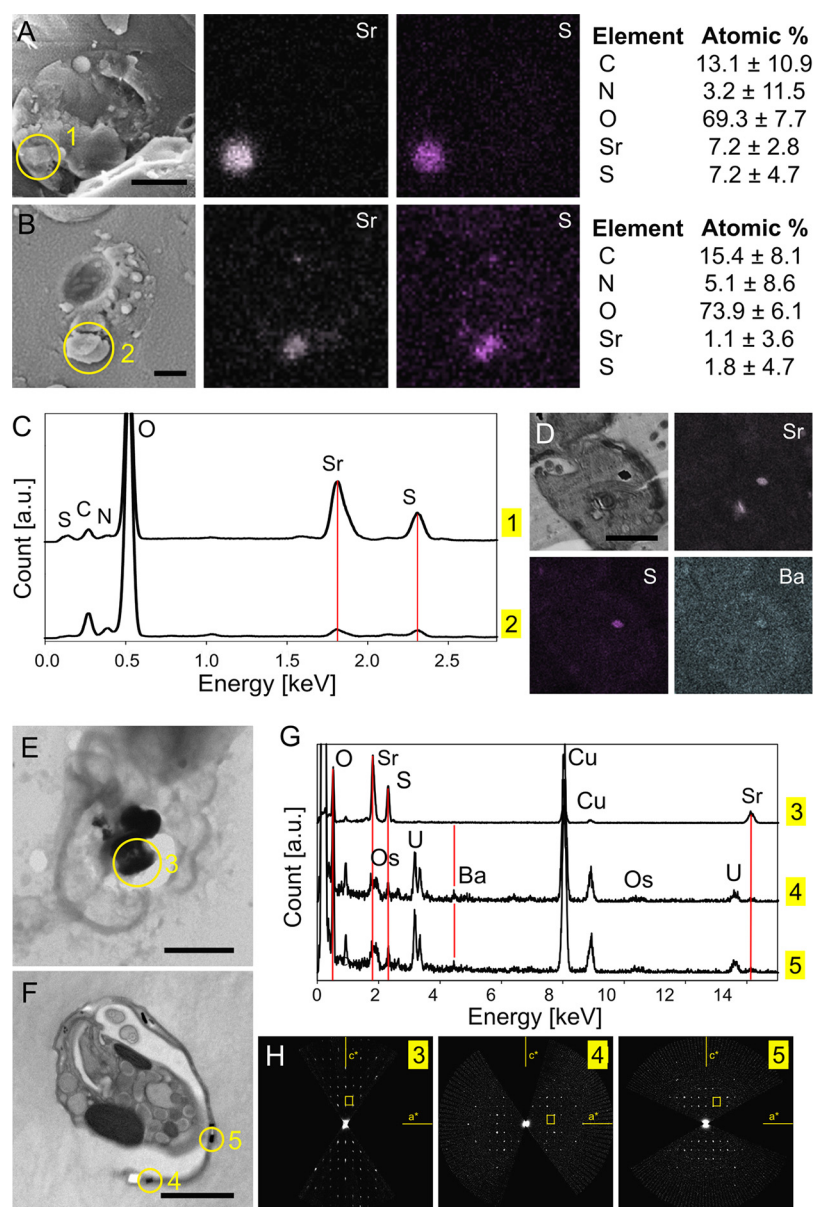
FIG 3 Elemental analysis of diplonemids. (A to C) Cryo-SEM-EDX images of *Lacrimia* sp. YPF1808 (A) and *N. karyoxenos* (B), complemented with EDX elemental spectral analysis (C) obtained from the area marked by circles 1 and 2, respectively. (D) SEM-EDX images of *Lacrimia* sp. YPF1808 showing the presence of S, Sr, and Ba. (E to G) TEM analysis of celestite microcrystals in a micrograph of a dried cell of *L. lanifica* (E), of a semithin section of *N. karyoxenos* (F), or EDX spectra (G) from the corresponding areas marked 3 to 5, with red lines highlighting the positions of O, Sr, Ba, and S. Cu and C originated from the support grid, and Os and U originated from staining compounds. (H) Electron diffraction for h0l-oriented sections through the 3D ED data sets from the corresponding areas shown in panels E and F. The celestite unit cell is displayed as a yellow rectangle. Scale bar, 2 μm.

7 μm³ (Fig. 4C; Table S2). The impacts of the measured celestite contents on the overall cell density ranged from 0.05% to 9%, with an average of 1.3 $\pm$ 0.5% (Fig. 4E; Table S2). The calculations were based on the measured volumes, known density of celestite (3.9 g·cm^{-3}), and common cellular densities of 0.985 to 1.156 g·cm^{-3} reported elsewhere (37).

The lack of celestite crystals in other analyzed species (*Diplonema japonicum*, *Paradiplonema papillatum*, and *Rhynchopus* sp. YZ270) was consistent with the minute ^{88}Sr content measured by ICP-MS. The high values of ^{88}Sr in *N. karyoxenos*, *Lacrimia* sp. YPF1808, and *L. lanifica* corresponded to the abundance of intracellular crystals
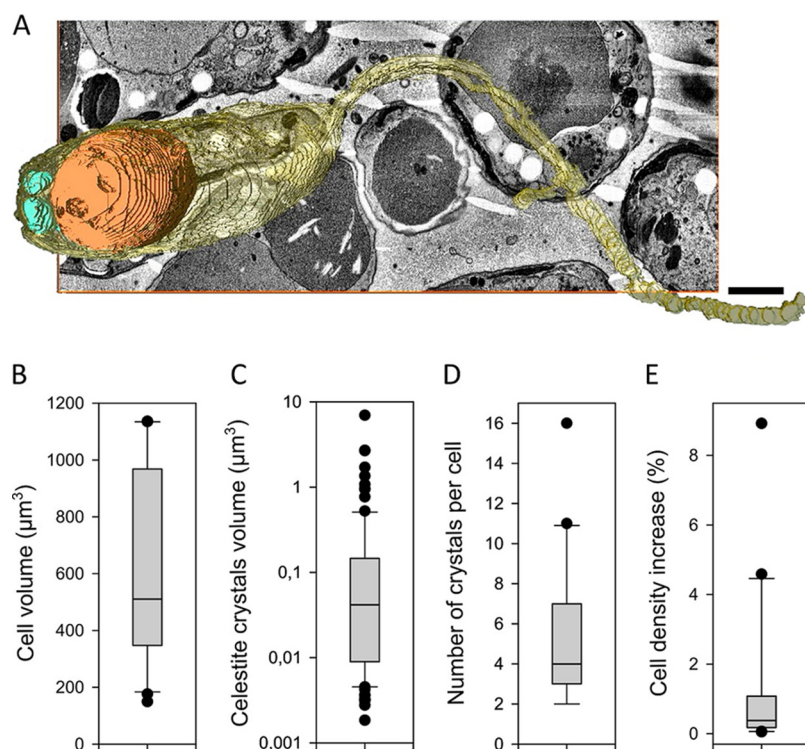
FIG 4 SBF-SEM images of celestite crystals in *Lacrimia* sp. YPF1808. (A) 3D reconstruction of a cell. Cytoplasm is shown in yellow, large posterior vacuole is in orange, and celestine crystals are in cyan. Scale bar, 1 μm. Descriptive analysis of measured data is for cells ($n = 20$) and crystals ($n = 106$). (B) Distribution of cell volumes. (C) Distribution of celestite crystal volumes on a log scale. (D) Number of celestite crystals per cell. (E) Impacts of celestite crystals on cell density; boxplots show medians and quartiles, and whiskers show the range from minimum to maximum values excluding outliers, represented by single data points.

detected by Raman microscopy, TEM, and SBF-SEM. Since direct measurement of the dry mass was impossible due to the inevitable presence of salts from the medium, the elemental composition analysis by ICP-MS was calculated in atoms per cell or femtomoles per cell. To calculate Sr and Ba content per dry mass, the latter was subsequently estimated by quantitative phase imaging using holographic microscopy (Table 1). The ^{88}Sr amounts ranged from 0.01 fmol·cell^{-1} in *P. papillatum* to 5,500 $\pm$ 570 fmol·cell^{-1} (mean $\pm$ standard deviation) in *N. karyoxenos*, corresponding to 340 $\pm$ 38 mg·g^{-1}. *Lacrimia* sp. YPF1808 and *L. lanifica* were also potent ^{88}Sr accumulators, with 370 $\pm$ 58 fmol·cell^{-1} (130 $\pm$ 25 mg·g^{-1}) and 54 $\pm$ 8 fmol·cell^{-1} (64 $\pm$ 13 mg·g^{-1}), respectively. Depending on the species, the intracellular concentration of ^{88}Sr was 1,200 to almost 10,000 times higher than in the surrounding medium (Tables 1 and S2).

Compared to the massive accumulation of ^{88}Sr in diplonemids, the naturally co-occurring Ba was present in much lower amounts (Table 1 and S2), slightly above the detection limit of TEM-EDX analysis (Fig. 3G), possibly reflecting a 12.5 times lower Ba^{2+} concentration in the seawater growth medium (Table S1). Nevertheless, the cells concentrated Ba^{2+} on average 1,000 to over 42,000 times above the level in the growth medium (Table S1), reaching 1,200 $\pm$ 130 fmol·cell^{-1} (120 $\pm$ 14 mg·g^{-1}) in *N. karyoxenos*, with lower values in *Lacrimia* sp. YPF1808 (65 $\pm$ 10 fmol·cell^{-1}, or 36 $\pm$ 7 mg·g^{-1}) and *L. lanifica* (2 $\pm$ 1 fmol·cell^{-1}, or 4 $\pm$ 1 mg·g^{-1}). Altogether, (Ba,Sr)SO$_4$ accumulation reached 91%, 33%, and 14% of dry weight in *N. karyoxenos*, *Lacrimia* sp. YPF1808, and *L. lanifica*, respectively. All strains showed significantly different levels of accumulated Sr or Ba contents (Table 1). Although the concentration of Ba^{2+} in our experiment was 30 to 45 times higher than in nature, the stoichiometry per cell was 5 orders of magnitude lower than in the oceans (Table 1).

Table 1 ICP-MS quantification of ^{88}Sr and Ba in diplonemids[a]

Species	*D. japonicum*	*P. papillatum*	*Rhynchopus* sp. YZ270	*L. lanifica* JW1601	*Lacrimia* sp. YPF1808	*N. karyoxenos*
Number of cells per ml in culture	$2.1 \cdot 10^5 \pm 9.2 \cdot 10^3$	$2.2 \cdot 10^6 \pm 2.1 \cdot 10^5$	$8.1 \cdot 10^5 \pm 2.6 \cdot 10^4$	$7.6 \cdot 10^5 \pm 2.5 \cdot 10^4$	$3.7 \cdot 10^6 \pm 1.7 \cdot 10^5$	$1.33 \cdot 10^6 \pm 5.9 \cdot 10^4$
Dry weight of cell (pg)	109 ± 2.9	68.0 ± 2.0	74.2 ± 2.7	74.1 ± 3.5	248.1 ± 8.2	$1,421 \pm 11$
Sr (fmol·cell^{-1})	0.22 ± 0.01	0.013 ± 0.001	0.08 ± 0.02	54.4 ± 8.4	366 ± 58	$5,530 \pm 570$
Sr (mg·g^{-1})	0.17 ± 0.10	0.02 ± 0.01	0.10 ± 0.07	64 ± 13	129 ± 25	340 ± 38
p	a	b	a	c	d	e
SrSO$_4$ (mg·g^{-1})	n/a	n/a	n/a	135	271	715
Concentration of Sr (folds)*[b]	n/a	n/a	n/a	$1,520 \pm 680$	$1,240 \pm 550$	$10,000 \pm 3,300$
Ba (fmol·cell^{-1})	n/a	n/a	n/a	2.0 ± 0.5	65 ± 10	$1,200 \pm 130$
Ba (mg·g^{-1})	n/a	n/a	n/a	3.7 ± 1.1	35.8 ± 6.8	116 ± 14
p	n/a	n/a	n/a	a	b	c
BaSO$_4$ (mg·g^{-1})	n/a	n/a	n/a	6.3	61	198
Concentration of Ba (folds)*[b]	n/a	n/a	n/a	$1,130 \pm 660$	$4,300 \pm 1,900$	$42,000 \pm 14,000$
Total Ba,Sr(SO$_4$) (mg·g^{-1})	n/a	n/a	n/a	141	332	913

[a]The dry weight was measured by quantitative phase imaging (n = 150 cells). Results of ICP-MS are displayed as mean values of biological triplicates with standard error of the mean. All figures are rounded to two significant numbers. The amounts of ^{88}Sr and Ba per dry mass (mg·g^{-1}) was logarithmically transformed and statistically analyzed by one-way ANOVA $p < 0.001$ (F = 1747.8 and F = 88.6; total degree of freedom: df = 17 and df = 8, respectively), with Tukey's post-hoc test significant differences on the level $p < 0.05$ in column p.

[b]*, calculated as atoms·cell^{-1} based on analyzed cell pellets relative to the theoretical value in atoms·cell^{-1} originating from the culture medium alone (8 mg·l^{-1} Sr^{2+} and 0.64 mg·l^{-1} Ba^{2+} – as listed in SI Appendix Table S1); in *N. karyoxenos*, the amount of accumulated Ba exceeds total Ba available per volume of culture medium due to repeated passages of pelleted cells into fresh medium. n/a, not analyzed.

Ba^{2+} loading experiments and elimination of Sr^{2+} and Ba^{2+} from the medium. Under our cultivation conditions, Ba^{2+} was 20 times less abundant than Sr^{2+} (Table S1), which resulted in formation of celestite with Ba^{2+} admixtures in the examined species. In oceans, the proportion is even 30 times lower (11, 12). Here, we tested whether increases in Ba^{2+} content would impact the biomineralization process by cultivation in artificial seawater loaded with equimolar amounts of Ba^{2+} and Sr^{2+} to 88 μM. To prevent spontaneous precipitation of barite, we supplemented sulfates with NaCl to maintain the osmolarity of the medium. This resulted in the formation of all mineral combinations: pure barite (Raman marker at 988 cm^{-1}), celestite (1,000 cm^{-1}), and mixed forms of (Ba,Sr)SO$_4$ (991 cm^{-1}; strontiobarite or baritocelestite) (Fig. 5), revealing that diplonemids do not show a strong preference toward the accumulation of either element.

Both *L. lafinica* and *Lacrimia* sp. YPF1808 contained mostly mixed crystals of (Ba,Sr)SO$_4$. In *N. karyoxenos*, pure celestite prevailed in the central part of crystals (999 cm^{-1}) while barite dominated at the periphery (988 cm^{-1}), and they gradually overlapped each other (Fig. 5C to F). Additionally, after several passages in the artificial medium without Ba^{2+} and Sr^{2+} (Table S1), barite and celestite were no longer detectable by Raman microscopy. The lack of Ba^{2+} and Sr^{2+} did not result in altered morphology or growth impairment. We did not observe any Ca^{2+}- or Mg^{2+}-containing crystals despite high concentrations of both elements in the medium.

Feeding experiments. Fecal pellets are an important agent mediating sedimentation of biogenically accumulated minerals to the sea floor: large aggregates of crystals held together by undigested fecal organic matter enable their fast sinking, thus preventing dissolution of micrometer-sized crystals in the water column, which is undersaturated for barite and celestite (15, 24). To experimentally address whether zooplankton feeds on diplonemids and whether their celestite crystals are carried into fecal pellets, we incubated *N. karyoxenos* and *Lacrimia* sp. YPF1808 with freshly captured filter-feeding marine copepods *Centropages typicus*, *Temora longicornis*, and *Acartia* sp., starved for 12 h prior to the experiment. After 5-day cocultivation, we determined by Raman microscopy that the fecal pellets contained copious amounts of celestite derived from diplonemids (Fig. 6B). In the control system of the same population of copepods fed with freshly collected marine plankton, the
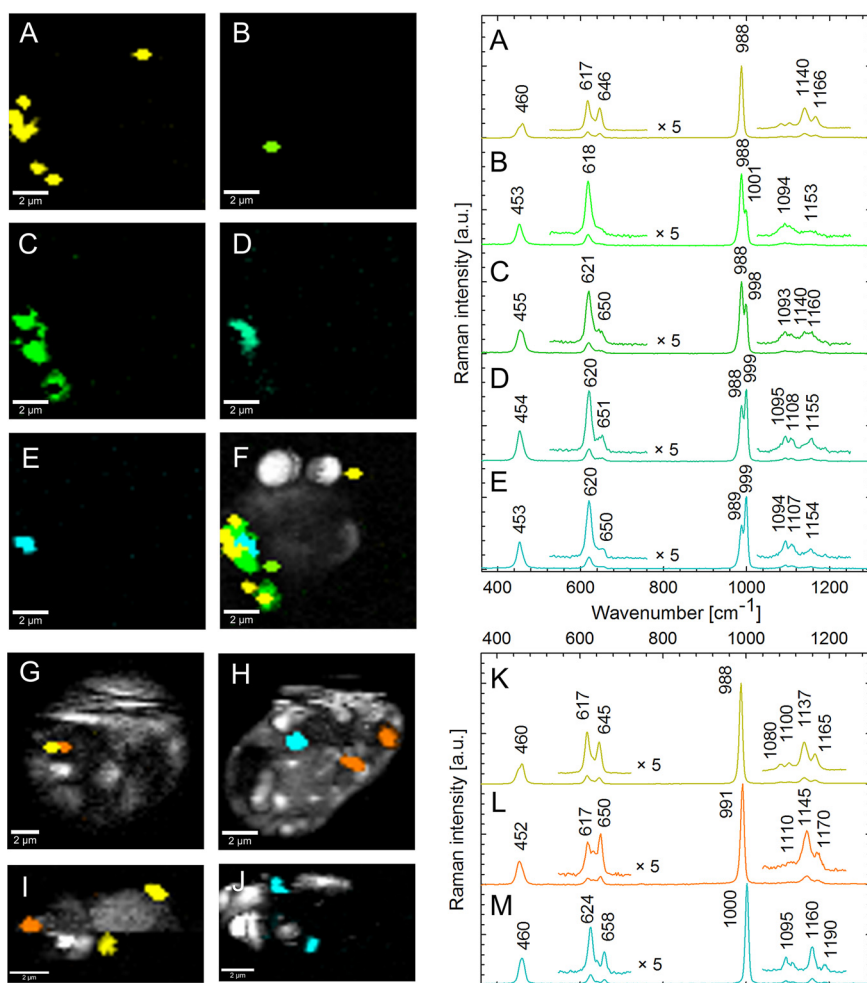
FIG 5 Raman maps and spectra of barite and celestite crystals in diplonemids cultivated with equimolar amounts of Sr^{2+} and Ba^{2+} in the medium. (A to F) A single cell of *N. karyoxenos* containing cocrystallized fractions dominated by celestite in the central part (E; cyan) with gradually overlapping barite (B to D; shades of green) toward the periphery of its pure fraction (A; yellow), and the merged Raman map of of panels A to E (F). The limited spatial resolution of Raman microscopy did not allow distinguishing conglomerates of pure-species microcrystals from a single crystal with a variable elemental composition. (G to M) Two cells of *Lacrimia* sp. YPF1808 (G and H) and two cells *L. lanifica* (I and J) contained pure barite (K; yellow) and celestite (M; blue) and homogenously mixed crystals of $(Ba,Sr)SO_4$ (L; orange).

fecal pellets contained undigested chlorophyll, carotenoids with remnants of lipids, calcite particles, and contaminating polystyrene microplastic particles, but lacked celestite crystals (Fig. 6B).

DISCUSSION

The most studied biominerals in protists are extracellular calcite scales of haptophytes and silicate frustules of diatoms, while studies on intracellular mineral crystals are far less common (38). After more than a century since the skeletons of marine acanthareans and freshwater streptophytes were found to contain celestite (16) and barite (39), respectively, we have identified potent accumulators of Ba^{2+} and Sr^{2+} in an unexpected group of eukaryotes, the diplonemids.

The heterotrophic diplonemids are widespread in the oceans and, as recently described, in astonishing abundance and diversity (31, 33). Despite their abundance and extreme diversity, diplonemid flagellates remain a poorly known group of protists (34) that are abundant from the surface to the deep sea, with a wide peak in the
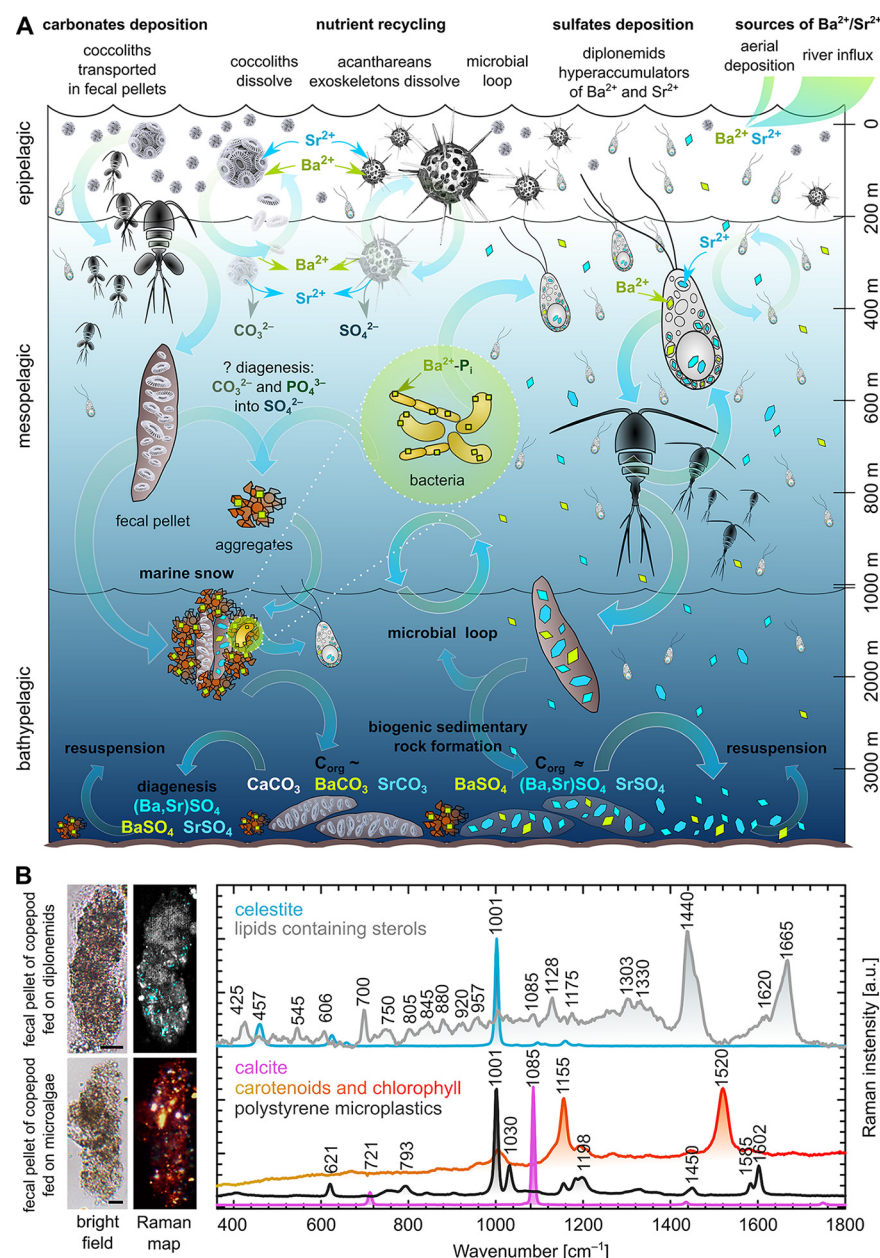
FIG 6 Schematic representation of the biological impact on Ba^{2+} and Sr^{2+} cycling in the oceans. (A) Hypothetical scenario of trace elements inlet, plankton uptake, recycling, and sedimentary deposition. The major source of trace elements is driven by river influx and less prominently by aerial deposition (9) and is mostly balanced by the same amount of total deposition in sediments, correlated with the total marine productivity and particulate organic matter deposition (24). A great proportion of these trace elements is being recycled by living organisms after release from dead cells. Acantharea (image adapted from referene 69) take up a substantial portion of Sr^{2+} and Ba^{2+}, which are further recycled in upper 400 m (25). Coccolithophorids build their scales from calcium carbonate with minor amounts of Ba^{2+} and Sr^{2+} that are proportional to the seawater contents (22), being partially recycled upon dissolution or transported to the marine sediments in fecal pellets (24). The Ba^{2+} accumulated by bacteria sediments in the aggregates of marine snow (26) or is recycled. We highlighted diplonemids as potential players in the marine cycle of both elements and drivers of biogenic formation of celestite and barite crystals found in suspended matter everywhere in the world oceans (24), and they can also feed on bacteria or particulate organic matter or scavenge the dead bodies of zooplankton as major heterotrophic protists in the mesopelagic zone. (B) Raman microscopy analysis of fecal pellets produced by copepods experimentally fed with diplonemids, which contained celestite crystals (cyan) and undigested lipids, including sterols (gray). In the control samples of copepods fed with microalgae, fecal pellets contained undigested carotenoids, chlorophyll (yellow-orange-red), and calcite particles (pink), with unexpected particles of polystyrene microplastics (measured as a single spectrum [not shown on the Raman map]). Scale bars, 20 μm.

mesopelagic zone (32, 33, 40, 41). The high capacity of intracellular Sr^{2+} and Ba^{2+} accumulation in some diplonemids outperforms that of any other reported organisms (10, 13, 21, 42–44). Indeed, while the intracellular concentration of Sr^{2+} in the most efficient accumulators known thus far (yeasts, desmids, and cyanobacteria) reaches a maximum of 220 mg·g^{-1} per dry weight (1, 10, 43), *N. karyoxenos* contains as much as 340 mg·g^{-1} Sr^{2+} together with 120 mg·g^{-1} Ba^{2+}, which in the form of sulfate represents 90% of the cellular dry mass, pointing to the unique Sr^{2+} and Ba^{2+} accumulation capacity of this diplonemid, while both *Lacrimia* species are slightly less potent in this respect (Table 1).

Interestingly, when both trace elements are provided in equimolar concentrations, diplonemids form pure celestite and barite and/or mixed forms of $(Ba,Sr)SO_4$, apparently not discriminating one element over the other. Hence, we explain the higher content of Sr^{2+} over Ba^{2+} inside the crystals by the higher availability of the former element in seawater. Although the mechanisms behind intracellular accumulation of Sr^{2+} and Ba^{2+} are largely unknown, it has been suggested that mineral crystals typically occur in membrane-bounded compartments or vacuoles, in which they are formed from supersaturated solutions via precisely regulated nucleation (13). The Sr^{2+} uptake and transportation within eukaryotic cells have been shown to occur via commonly present transporters of divalent cations, i.e., the Ca^{2+} uniporter and H^+/Ca^{2+} antiporter (45, 46). The diplonemid nuclear genome is not yet available, but these transporters have been documented in the related kinetoplastid *Trypanosoma brucei* (47). Although the reported affinity to Ca^{2+} and Sr^{2+} is usually comparable (45, 46), some organisms including diplonemids clearly favor Ba^{2+} and Sr^{2+} over Ca^{2+} (10). When such vacuoles contain sulfate solutions, they may function as a "sulfate trap" for those cations that precipitate easily in the presence of sulfates (2). At the same time, we did not observe $CaSO_4$ or any of its forms (gypsum, bassanite, anhydride, etc.), even though the concentration of Ca^{2+} in the cultivation medium or in the environment is several orders of magnitude higher than that of Sr^{2+} and Ba^{2+}.

Densities of celestite and barite of 3.9 g·cm^{-3} and 4.5 g·cm^{-3}, respectively, have been repeatedly reported as statoliths in ciliates or charophytic algae (13, 17, 18). In comparison to the seawater density of 1.03 g·cm^{-3} and typical cell density range between 0.985 and 1.156 g·cm^{-3}, the heavy crystals may help maintain appropriate buoyancy by counterbalancing light lipid droplets (0.86 g·cm^{-3}) (37, 48). Indeed, the impact of celestite crystals is substantial, since they may increase the overall density of *Lacrimia* sp. YPF1808 and *N. karyoxenos* by up to 9% and 27%, respectively (Table S2). According to Stokes' law for small particles of low Reynolds numbers, the barite/celestite ballasting can significantly increase the sedimentary velocity for up to 50 to 200 m per month or 0.5 to 2 km per year (Table S2). Hence, while the function of biomineralization in diplonemids remains unknown, we speculate that they may benefit from gravitropic sensing, which would allow directed movement and/or enable passive sedimentation. Another intriguing impact of barite and celestite is associated with their propensity to strong absorption of UV and blue light (49). Hence, in surface waters, these minerals may contribute to UV protection. It is reasonable to assume that by forming celestite, protists adjust their inner osmolarity, the principle analogical to the formation of other cell inclusions, such as oxalate, calcite, or polyphosphate, that are either dissolved and osmotically active or crystallized or polymerized and osmotically inactive inside a vacuole (13, 50).

Celestite-forming acanthareans are considered key players in the upper 400 m of the ocean, yet do not contribute to the sedimentary rock formation, as their skeletons dissolve upon decay of their cells (25). Coccolithophorids and bacteria produce carbonates (44) and/or phosphates (26) of Ba^{2+}/Sr^{2+}, which can also be converted to sulfates either on the bacterial extracellular polymeric substances or in the microenvironment of decaying matter of marine snow aggregates in the process of diagenesis (26). In the chemical continuum between pure barite and celestite, the latter represents 10 to 30%

(24), gradually decreasing, depending on the depth (11, 12). The majority of biogenic particulate barite and celestite is recycled by simple dissolution (25), microbial loop (26), or resuspension of sediments (24). However, the overall influx into the system is balanced by sedimentary deposition (9, 24), which might have a biological driver. Seminal work of Dehairs et al. (24) scrutinized all potential sources of particulate barite and celestite, and they did not find experimental support for either Ba^{2+} incorporation in siliceous plankton or precipitations on decaying organic matter in sulfate-enriched microenvironments. Hence, they ultimately favored the biogenic origin of particulate barite/celestite being hypothetically formed by microorganisms inhabiting the high-productivity mesopelagic zone (24) only to remain unknown since then. These predictions nicely correlate with our measurements in diplonemids, indicating that micron-sized celestite and sometimes barite crystals of variable Ba-Sr ratios (Fig. 2 to 5) are scattered throughout the water column of the world's oceans, with the highest prevalence in the mesopelagic zone (32). Moreover, particulate barite/celestite is often found in fecal pellets and aggregates of marine snow, and finally, in the sediments (24, 27, 32). By providing celestite-containing diplonemids to filter-feeding copepods, we found undigested celestite in their fecal pellets (Fig. 6), the main transport system of micrometric biominerals into the sediments, although the majority is recycled (24). Thus, diplonemids may be involved in Ba^{2+}/Sr^{2+} cycling and/or in sedimentary deposition of celestite or barite. Since these protists likely emerged during the Neoproterozoic era (590 to 900 million years ago [MYA]), overlapping with the Ediacaran period (51), their impact on biogenic marine sediments may cover several geological eras. The coccolithophores appeared around the same time as diplonemids, yet the onset of carbonate biomineralization has been timed to ~200 MYA (52).

As another ecological addition to the big picture of Ba^{2+}/Sr^{2+} cycling, diplonemids have been shown to ingest bacteria as one of their sources of nutrition (30); if bacteria were loaded with Ba^{2+}/Sr^{2+} in the form of (poly)phosphates, as reported elsewhere (26), diplonemids may further transform it into barite upon digestion. Additionally, diplonemids are likely to feed on the organic matter of marine snow providing preconcentrated Ba^{2+}, in which case they may accumulate more Ba^{2+} than Sr^{2+}. In principle, we experimentally supported such a scenario upon doping the cells with equimolar Ba^{2+} and Sr^{2+} concentrations (Fig. 5). Finally, we do not exclude that some species of diplonemids to be described in future would prefer Ba^{2+} over Sr^{2+} or that there are other as-yet-unknown microbial bioaccumulators of these trace elements.

Based on the ability of some diplonemids to store massive amounts of celestite and to lesser extent barite, we speculate that more as-yet-unknown diplonemid species may qualify as impactful players of Ba^{2+}/Sr^{2+} flow through the food web, eventually influencing the sedimentary records.

MATERIALS AND METHODS

Cell cultures, cultivation, and light microscopy. For all experiments, axenic cultures were grown in seawater-based Hemi medium (see Table S1 in the supplemental material) supplemented with 1% horse serum and 0.025 g/liter LB broth powder (53). An artificial seawater medium lacking Sr^{2+}, Ba^{2+}, and sulfates was prepared from 288 mM NaCl, 8 mM KCl, 718 mM KBr, 100 mM $MgCl_2$, 12 mM $CaCl_2$, 40 mM HBO_3, and 60 mM NaF, supplemented with 1% (vol/vol) heat-inactivated horse serum (Sigma-Aldrich) and 25 mg LB broth powder (Amresco). The medium was used as rinsing solution for preparation of ICP-MS samples and cell microcrystal depletion to be measured via quantitative phase imaging (QPI) (see below). For Ba^{2+} loading experiments, $BaCl_2$ was added in equimolar amounts with respect to naturally occurring (88 μM) Sr^{2+} (12).

Axenic clonal cultures of 17 species of diplonemids were grown either at 27°C (*Paradiplonema papillatum* ATCC 50162), 22°C (*Namystinia karyoxenos* YPF1621), or 13°C (of *D. aggregatum* YPF1605, *D. japonicum* YPF1604, *Flectonema* sp. DT1601, *Hemistasia phaeocysticola*, *Lacrimia lanifica* JW1601, *Lacrimia* sp. YPF1808, *Rhynchopus* sp. YZ270 cl. 10.3, *Rhynchopus* sp. YZ270 cl. 9, *Rhynchopus* sp. DT0301, *Rhynchopus humris* YPF1505, *R. euleeides* ATCC 50226, *R. serpens* YPF1515, and *Sulcionema specki* YPF1618). *P. papillatum* and *R. euleeides* were isolated from coastal surface waters (United States) in 1985 and 1986, respectively. The remaining species originated either from coastal seawater around Japan or from Enoshima Aquarium (Kanagawa, Japan) and were continuously maintained in culture for 1 to 7 years prior to the analyses. The identity of not-yet-formally described species was established based on the 18S rRNA sequences as described previously (54). Dense cultures of trophic cells (55) were harvested by centrifugation at 3,000 × *g* for all subsequent analyses.

Light microscopy images and videos were taken with an Olympus BX53 microscope equipped with a DP72 microscope digital camera using CellSens software v. 1.11 (Olympus) and processed with GIMP v. 2.10.14, Irfan View v. 4.54, and Image J v. 1.51 software. Polarized microscopy was performed using crossed polarizers installed to a Raman microscope (as specified below).

Environmental sampling. Zooplankton was collected in the Bay of Villefranche sur Mer, France (43°40′N, 7°19′E) with a 10-min haul from 10 m to the surface, using a 20-μm-mesh-size plankton net. Captured copepods were transferred into 0.5 liters of freshly filtered natural seawater and starved for 12 h. *Centropages typicus*, *Temora longicornis*, and *Acartia* sp. were then picked under a dissection microscope. All experiments were carried out at cultivation temperature of the prey species of diplonemids (13°C for *Lacrimia* sp. YPF1808, room temperature for *N. karyoxenos*). Ten copepods were kept in 20 mL of diplonemid culture (10^5 cells mL^{-1}) for 5 days, after which their fecal pellets were collected under a dissection microscope and immediately analyzed by Raman microscopy (as specified below).

Raman microscopy. For the *in situ* determination of the chemical composition of intracellular structures, a confocal Raman microscope (alpha300 RSA; WITec, Germany) was used as previously described (56–60). To immobilize the fast-moving flagellates on the quartz slide, 5 μL of the cell pellet was mixed with 5 μL of 1% (wt/vol) solution of low-melting-point agarose (catalog number 6351.5; Carl Roth, Germany), immediately spread as a single-cell layer between a quartz slide and coverslip, and sealed with CoverGrip sealant (Biotium, USA). Two-dimensional Raman maps were obtained with laser excitation at 532 nm (20 mW power at the focal plane) and oil-immersion objective UPlanFLN 100×, numerical aperture (NA) 1.30, or water-immersion objective UPlanSApo 60×, NA 1.20 (Olympus, Japan). A scanning step size of 200 nm in both directions and an integration time of 100 ms per voxel were used. A minimum of 30 cells were measured for each strain. Raman chemical maps were constructed by multivariate decomposition of the baseline-corrected spectra into the spectra of pure chemical components by using Project Plus 5.1 software (WITec, Germany).

TEM, TEM-ED, and TEM-EDX. The protocol for the basic sample preparation of all kinds of electron microscopy approaches listed here is described in detail elsewhere (61). We used it with minor modifications, as stated below. Cell pellets were transferred to specimen carriers and immediately frozen in the presence of 20% (wt/vol) bovine serum albumin solution using a high-pressure freezer (Leica EM ICE, Leica Microsystems, Austria). Freeze substitution was performed in the presence of 2% osmium tetroxide diluted in 100% acetone at −90°C. After 96 h, specimens were warmed to −20°C at a step of 5°C/h. After another 24 h, the temperature was increased to 3°C (3°C/h). At room temperature, samples were washed in acetone and infiltrated with 25%, 50%, and 75% acetone/resin mixture for 1 h at each step. Finally, samples were infiltrated in 100% resin and polymerized at 60°C for 48 h. Semithin (250 nm) and ultrathin (70 nm) sections were cut using a diamond knife, placed on copper grids, and stained with uranyl acetate and lead citrate. TEM micrographs were taken with a Mega View III camera (SIS) using a JEOL 1010 TEM operating at an accelerating voltage of 80 kV.

For TEM-EDX, 10 μL of pelleted *L. lanifica* cells was spread over a holey carbon-coated copper grid, washed twice with 10 μL of distilled water in order to reduce the sea salts from the culture medium, and allowed to dry by evaporation at ambient temperature. Semithin sections of resin-infiltrated blocks of *N. karyoxenos* were prepared as stated above. For the identification of the crystalline phase, sections were studied by TEM on an FEI Tecnai 20 system (LaB6, 120 kV) equipped with an Olympus SIS charge-coupled-device camera Veleta (2,048 by 2,048 pixels) and an EDAX windowless EDX detector Apollo XLTW for elemental analysis. The diffraction data were collected by means of 3D electron diffraction (ED) (62). The data processing was carried out using PETS software (63). Structure solution and refinement were performed in the computing system Jana2006 (64).

Cryo-scanning electron microscopy with EDX. Cells pellets were high-pressure frozen as described above and transferred into a Leica ACE 600 preparation chamber (Leica Microsystems, Austria) precooled at −135°C, fractured with a scalpel, freeze-etched at −100°C for 1 min, and sputter-coated with 2.5 nm of gold-palladium at −125°C. Specimens were transferred under vacuum using transfer system VCT100 (Leica Microsystems, Austria) and observed with a Magellan 400L SEM (FEI, Czech Republic and USA) precooled at −125°C (cryo-SEM). Topographical images and EDX measurements were obtained using an EDT detector and EDAX detector (Octane Elect Super; EDAX, USA), respectively, either at 5 keV/0.1 NA or 10 keV/0.8 NA. The taken spectra were analyzed with EDAX TEAM software and quantified by the eZAF method.

Serial block-face SEM. The sample preparation of *Lacrimia* sp. YPF1808 by the high-pressure freezing technique followed the protocol for TEM sample preparation. After freeze-substitution, the samples were subsequently stained with 1% thiocarbohydrazide in 100% acetone for 1.5 h, 2% OsO$_4$ in 100% acetone for 2 h at room temperature, and 1% uranyl acetate in 100% acetone overnight at 4°C. After every staining step, the samples were washed 3 times with 100% acetone for 15 min. Samples were then infiltrated with 25%, 50%, or 75% acetone-resin mixture for 2 h at each step, and finally infiltrated in 100% Hard Resin Plus 812 (EMS) overnight and polymerized at 62°C for 48 h. Resin-embedded blocks were trimmed and imaged using an Apreo SEM equipped with a VolumeScope (Thermo Fisher Scientific, Germany). Serial images were acquired at 3.5 keV, 50 pA, 40 Pa with a resolution of 6 nm, 100-nm slice thickness, and dwell time per pixel of 4 μs. Image data were processed in Microscopy Image Browser v2.702 (65) and Amira v2020.2. The resin-embedded blocks were also collected in the form of 1-μm-thick sections on a silicon wafer and analyzed by SEM-EDX (Magellan 400L system, as described above).

Based on volumetric data, we calculated the percentage of increase in cell density based on measured volumes of crystals compared to the theoretical crystal-free cells of the same volume and reported average theoretical density of 1.07 g·cm^{-3} (37).

ICP-MS. For analysis of Ba and ^{88}Sr concentrations, cultures were grown in triplicates, counted, and washed three times with 1 M sorbitol solution (for *P. papillatum*, *D. japonicum*, and *Rhynchopus* YZ270 cl. 10) or Sr- and Ba-free artificial seawater rinsing solution (see above) (for *L. lanifica* JW1601, *Lacrimia* sp. 1808, and *N. karyoxenos*) to remove Ba^{2+} and Sr^{2+} present in the cultivation medium. Cultivated cells were harvested by centrifugation and rinsed twice with 50 mL and once with 2 mL of the rinsing solution, and the resulting pellets were freeze-dried. A 0.5-mL digestion acid mix (425 μL of 70% $HClO_4$ and 75 μL of 69% HNO_3) prepared as described elsewhere (66) was added directly to the dried biomass. The digestion was done using a Fuji PXG4 Thermoblock (AHF Analysentechnik AG, Germany). After evaporation of the acid mix, 0.5 mL of 5% HCl was added to each test tube to redissolve the salts. The glass tubes were heated to 90°C for 1 h to obtain clear solutions. The final volume of 1.5 mL was adjusted with double-distilled H_2O. Appropriate dilutions were made with 0.2% HNO_3. Indium was added as an internal standard at 1 ng/mL to each test solution. The ICP multielement standard solution VI (Merck, Germany) was used to prepare standard curves. Analyses were done using an inductively coupled plasma sector-field mass spectrometer (ICP sfMS) Element XR-2 with jet interface (Thermo Fisher Scientific, Germany) following a described protocol (67). Medium resolution of 4,000 was used in Ba and ^{88}Sr measurements in triplicate of each technical replicate, with the highest precision and lowest relative standard deviation. Additionally, the elemental composition of samples of standard growth medium and artificial seawater medium without sulfates, Ba^{2+}, or Sr^{2+} were analyzed.

Holographic microscopy and QPI. Samples for holographic microscopy were immobilized prior to measurement as described above for Raman microscopy. Imaging was performed at the Q-Phase microscope (Tescan Orsay Holding, Czech Republic). The holographic Q-Phase microscope is equipped with halogen lamp illumination through an interference filter ($\lambda[\frac{1}{4}]$ 650 nm, 10 nm full-width, half-maximal) and microscope objective (Nikon Plan Fluor oil immersion, 60×, numerical aperture 1.4, providing lateral resolution of 0.57 μm). The numerical reconstruction of acquired data was performed using Q-Phase software (Tescan Orsay Holding, Czech Republic). The technique enables automated cell segmentation and quantitative analysis of cellular mass based on the specific proportions of thickness and refractive indices of measured cells in comparison to the reference (68). Due to the high variability of cell contents and sizes, at least 150 cells were analyzed for each strain. Because crystalline inclusions caused artifacts during capturing due to the big difference in refractive indices, we analyzed crystal-free cells cultivated in the artificial seawater medium lacking Sr^{2+}, Ba^{2+}, and sulfates (as specified above). We calculated the total dry mass of the cells as the sum of crystal-free cells, measured by holographic microscopy, and $SrSO_4$ and $BaSO_4$ amounts measured via ICP-MS. The dry weight ratios of trace elements measured via ICP-MS were calculated based on the total dry weight of corresponding strains.

Statistical data analysis. Statistical analysis was conducted using SigmaPlot v. 12.5 and SPSS v. 23.0. Logarithmically normalized data were subjected to statistical tests (one-way analysis of variance [ANOVA] and Tukey's *post hoc*) on an alpha level of 0.05. Calculations of standard errors of the means based on independent methods (i.e., ICP-MS quantification and QPI dry mass quantification) with different levels of variability were done according to mathematical conversion using Taylor expansion.

Data availability. All data generated or analyzed during this study are included in the published article and its supplemental material files.

SUPPLEMENTAL MATERIAL

Supplemental material is available online only.

MOVIE S1, MOV file, 12.6 MB.
MOVIE S2, MOV file, 12.9 MB.
FIG S1, PDF file, 0.2 MB.
FIG S2, PDF file, 0.1 MB.
FIG S3, PDF file, 0.1 MB.
FIG S4, PDF file, 0.1 MB.
FIG S5, PDF file, 0.1 MB.
TABLE S1, PDF file, 0.04 MB.
TABLE S2, PDF file, 1.8 MB.

REFERENCES

1. Avery SV, Smith SL, Ghazi AM, Hoptroff MJ. 1999. Stimulation of strontium accumulation in linoleate-enriched *Saccharomyces cerevisiae* is a result of reduced Sr^{2+} efflux. Appl Environ Microbiol 65:1191–1197. https://doi.org/10.1128/AEM.65.3.1191-1197.1999.

2. Krejci MR, Wasserman B, Finney L, McNulty I, Legnini D, Vogt S, Joester D. 2011. Selectivity in biomineralization of barium and strontium. J Struct Biol 176:192–202. https://doi.org/10.1016/j.jsb.2011.08.006.

3. Bowen HJM, Dymond JA. 1955. Strontium and barium in plants and soils. Proc R Soc Lindon B Biol Sci 144:355–368.

4. Pors Nielsen S. 2004. The biological role of strontium. Bone 35:583–588. https://doi.org/10.1016/j.bone.2004.04.026.

5. Bhoelan BS, Stevering CH, van der Boog ATJ, van der Heyden MAG. 2014. Barium toxicity and the role of the potassium inward rectifier current. Clin Toxicol 52:584–593. https://doi.org/10.3109/15563650.2014.923903.

6. Fukuda SY, Iwamoto K, Atsumi M, Yokoyama A, Nakayama T, Ishida K-I, Inouye I, Shiraiwa Y. 2014. Global searches for microalgae and aquatic plants that can eliminate radioactive cesium, iodine and strontium from the radio-polluted aquatic environment: a bioremediation strategy. J Plant Res 127:79–89. https://doi.org/10.1007/s10265-013-0596-9.

7. Walker JB. 1953. Inorganic micronutrient requirements of *Chlorella*. I. Requirements for calcium (or strontium), copper, and molybdenum. Arch Biochem Biophys 46:1–11. https://doi.org/10.1016/0003-9861(53)90163-5.

8. Bolland MJ, Grey A. 2016. Ten years too long: strontium ranelate, cardiac events, and the European Medicines Agency. Br Med J 354:i5109. https://doi.org/10.1136/bmj.i5109.

9. Moore JW. 1991. Inorganic contaminants of surface water: research and monitoring priorities, 1st ed. Springer US, New York, NY.

10. Cam N, Benzerara K, Georgelin T, Jaber M, Lambert JF, Poinsot M, Skouri-Panet F, Cordier L. 2016. Selective uptake of alkaline earth metals by cyanobacteria forming intracellular carbonates. Environ Sci Technol 50:11654–11662. https://doi.org/10.1021/acs.est.6b02872.

11. Paytan A, Griffith EM. 2007. Marine barite: recorder of variations in ocean export productivity. Deep Sea Res II 54:687–705. https://doi.org/10.1016/j.dsr2.2007.01.007.

12. Griffith EM, Paytan A. 2012. Barite in the ocean: occurrence, geochemistry and palaeoceanographic applications. Sedimentology 59:1817–1835. https://doi.org/10.1111/j.1365-3091.2012.01327.x.

13. Raven JA, Knoll AH. 2010. Non-skeletal biomineralization by eukaryotes: matters of moment and gravity. Geomicrobiol J 27:572–584. https://doi.org/10.1080/01490451003702990.

14. Langer G, Nehrke G, Thoms S, Stoll H. 2009. Barium partitioning in coccoliths of *Emiliania huxleyi*. Geochim Cosmochim Acta 73:2899–2906. https://doi.org/10.1016/j.gca.2009.02.025.

15. Monnin C, Cividini D. 2006. The saturation state of the world's ocean with respect to $(Ba,Sr)SO_4$ solid solutions. Geochim Cosmochim Acta 70:3290–3298. https://doi.org/10.1016/j.gca.2006.04.002.

16. Bütschli O. 1906. Über die chemische Natur der Skelettsubstanz der Acantharia. Zool Anz 30:784–789.

17. Hemmersbach R, Krause M, Bräucker R, Ivanova K. 2005. Graviperception in ciliates: steps in the transduction chain. Adv Space Res 35:296–299. https://doi.org/10.1016/j.asr.2005.03.024.

18. Brook AJ, Fotheringham A, Bradly J, Jenkins A. 1980. Barium accumulation by desmids of the genus *Closterium* (Zygnemaphyceae). Br Phycol J 15:261–264. https://doi.org/10.1080/00071618000650251.

19. Gooday AJ, Nott JA. 1982. Intracellular barite crystals in two Xenophyophores, *Aschemonella ramuliformis* and *Galatheammina* sp. (Protozoa: Rhizopoda) with comments on the taxonomy of *A. ramuliformis*. J Mar Biol Ass 62:595–605. https://doi.org/10.1017/S0025315400019779.

20. Fresnel J, Galle P, Gayral P. 1979. Résultats de la microanalyse des cristaux vacuolaires chez deux Chromophytes unicellulaires marines: *Exanthemachrysis gayraliae*, *Pavlova* sp. (Prymnesiophycéées, Pavlovacées). C R Hebd Seances Ser D Sci Nat 288:823–825.

21. Martignier A, Filella M, Pollok K, Melkonian M, Bensimon M, Barja F, Langenhorst F, Jaquet JM, Ariztegui D. 2018. Marine and freshwater micropearls: biomineralization producing strontium-rich amorphous calcium carbonate inclusions is widespread in the genus *Tetraselmis* (Chlorophyta). Biogeosciences 15:6591–6605. https://doi.org/10.5194/bg-15-6591-2018.

22. Stoll HM, Rosenthal Y, Falkowski P. 2002. Climate proxies from Sr/Ca of coccolith calcite: Calibrations from continuous culture of *Emiliania huxleyi*. Geochim Cosmochim Acta 66:927–936. https://doi.org/10.1016/S0016-7037(01)00836-5.

23. Dymond J, Collier R. 1996. Particulate barium fluxes and their relationships to biological productivity. Deep Res Part II Top Stud Oceanogr 43:1283–1308. https://doi.org/10.1016/0967-0645(96)00011-2.

24. Dehairs F, Chesselet R, Jedwab J. 1980. Discrete suspended particles of barite and the barium cycle in the open ocean. Earth Planet Sci Lett 49:528–550. https://doi.org/10.1016/0012-821X(80)90094-1.

25. De Deckker P. 2004. On the celestite-secreting Acantharia and their effect on seawater strontium to calcium ratios. Hydrobiologia 517:1–13. https://doi.org/10.1023/B:HYDR.0000027333.02017.50.

26. Martinez-Ruiz F, Jroundi F, Paytan A, Guerra-Tschuschke I, Abad MDM, González-Muñoz MT. 2018. Barium bioaccumulation by bacterial biofilms and implications for Ba cycling and use of Ba proxies. Nat Commun 9:1619. https://doi.org/10.1038/s41467-018-04069-z.

27. Bishop JKB. 1988. The barite-opal-organic carbon association in oceanic particulate matter. Nature 332:341–343. https://doi.org/10.1038/332341a0.

28. Horner TJ, Pryer HV, Nielsen SG, Crockford PW, Gauglitz JM, Wing BA, Ricketts RD. 2017. Pelagic barite precipitation at micromolar ambient sulfate. Nat Commun 8:1342. https://doi.org/10.1038/s41467-017-01229-5.

29. Kostygov AY, Karnkowska A, Votýpka J, Tashyreva D, Maciszewski K, Yurchenko V, Lukeš J. 2021. Euglenozoa: taxonomy, diversity and ecology, symbioses and viruses. Open Biol 11:200407. https://doi.org/10.1098/rsob.200407.

30. Prokopchuk G, Korytář T, Juricová V, Majstorović J, Horák A, Šimek K, Lukeš J. 2022. Trophic flexibility of marine diplonemids: switching from osmotrophy to bacterivory. ISME J 16:1409–1419. https://doi.org/10.1038/s41396-022-01192-0.

31. Tashyreva D, Simpson AGB, Prokopchuk G, Škodová-Sveráková I, Butenko A, Hammond M, George EE, Flegontova O, Záhonová K, Faktorová D, Yabuki A, Horák A, Keeling PJ, Lukeš J. 2022. Diplonemids: a review on "new" flagellates on the oceanic block. Protist 173:125868. https://doi.org/10.1016/j.protis.2022.125868.

32. Flegontova O, Flegontov P, Malviya S, Audic S, Wincker P, de Vargas C, Bowler C, Lukeš J, Horák A. 2016. Extreme diversity of diplonemid eukaryotes in the Ocean. Curr Biol 26:3060–3065. https://doi.org/10.1016/j.cub.2016.09.031.

33. Flegontova O, Flegontov P, Londoño Castañeda AP, Walczowski W, Šantić D, Edgcomb VP, Lukeš J, Horák A. 2020. Environmental determinants of the distribution of planktonic diplonemids and kinetoplastids in the oceans. Environ Microbiol 22:4014–4031. https://doi.org/10.1111/1462-2920.15190.

34. de Vargas C, Audic S, Henry N, Decelle J, Mahé F, Logares R, Lara E, Berney C, Le Bescot N, Probert I, Carmichael M, Poulain J, Romac S, Colin S, Aury J-M, Bittner L, Chaffron S, Dunthorn M, Engelen S, Flegontova O, Guidi L, Horák A, Jaillon O, Lima-Mendez G, Lukeš J, Malviya S, Morard R, Mulot M, Scalco E, Siano R, Vincent F, Zingone A, Dimier C, Picheral M, Searson S, Kandels-Lewis S, Tara Oceans Coordinators, Acinas SG, Bork P, Bowler C, Gorsky G, Grimsley N, Hingamp P, Iudicone D, Not F, Ogata H, Pesant S, Raes J, Sieracki ME, Speich S, et al. 2015. Eukaryotic plankton diversity in the sunlit ocean. Science 348:1261605. https://doi.org/10.1126/science.1261605.

35. Mukherjee I, Salcher MM, Andrei AŞ, Kavagutti VS, Shabarova T, Grujčić V, Haber M, Layoun P, Hodoki Y, Nakano SI, Šimek K, Ghai R. 2020. A freshwater radiation of diplonemids. Environ Microbiol 22:4658–4668. https://doi.org/10.1111/1462-2920.15209.

36. Zhou L, Mernagh TP, Mo B, Wang L, Zhang S, Wang C. 2020. Raman study of barite and celestine at various temperatures. Minerals 10:260. https://doi.org/10.3390/min10030260.

37. Walsby AE, Reynolds CS. 1980. Sinking and floating, p 371–412. *In* Morris I (ed), The physiological ecology of the phytoplankton. Blackwell Science, Oxford, United Kingdom.

38. Knoll AH. 2003. Biomineralization and evolutionary history. Rev Mineral Geochem 54:329–356. https://doi.org/10.2113/0540329.

39. Kreger DR, Boeré H. 1969. Some observations on barium sulphate in *Spirogyra*. Acta Bot Neerl 18:143–151. https://doi.org/10.1111/j.1438-8677.1969.tb00579.x.

40. Gawryluk RMR, Del Campo J, Okamoto N, Strassert JFH, Lukeš J, Richards TA, Worden AZ, Santoro AE, Keeling PJ. 2016. Morphological identification and single-cell genomics of marine diplonemids morphological identification. Curr Biol 26:3053–3059. https://doi.org/10.1016/j.cub.2016.09.013.

41. Cavan EL, Laurenceau-Cornec EC, Bressac M, Boyd PW. 2019. Exploring the ecology of the mesopelagic biological pump. Prog Oceanogr 176:102125. https://doi.org/10.1016/j.pocean.2019.102125.

42. Fisher NS, Guillard RRL, Bankston DC. 1991. The accumulation of barium by marine phytoplankton grown in culture. J Mar Res 49:339–354. https://doi.org/10.1357/002224091784995882.

43. Brook AJ, Grime GW, Watt F. 1988. A study of barium accumulation in desmids using the Oxford scanning proton microprobe (SPM). Nucl Instruments Methods Phys Res 30:372–377. https://doi.org/10.1016/0168-583X(88)90027-4.

44. Sun S, Liu M, Nie X, Dong F, Hu W, Tan D, Huo T. 2018. A synergetic biomineralization strategy for immobilizing strontium during calcification of the coccolithophore *Emiliania huxleyi*. Environ Sci Pollut Res Int 25:22446–22454. https://doi.org/10.1007/s11356-018-1271-4.

45. Kirichok Y, Krapivinsky G, Clapham DE. 2004. The mitochondrial calcium uniporter is a highly selective ion channel. Nature 427:360–364. https://doi.org/10.1038/nature02246.

46. Schumaker KS, Sze H. 1986. Calcium transport into the vacuole of oat roots. Characterization of H^+/Ca^{2+} exchange activity. J Biol Chem 261:12172–12178. https://doi.org/10.1016/S0021-9258(18)67219-9.

47. Docampo R, Lukeš J. 2012. Trypanosomes and the solution of a fifty years-mitochondrial calcium mystery. Trends Parasitol 28:31–37. https://doi.org/10.1016/j.pt.2011.10.007.

48. Veronis G. 1972. On properties of seawater, defined by temperature, salinity and pressure. J Mar Res 30:227–255.

49. Gaft ML, Bershov LV, Krasnaya AR, Yaskolko VY. 1985. Luminescence centers in anhydrite, barite, celestine and their synthesized analogs. Phys Chem Minerals 11:255–260. https://doi.org/10.1007/BF00307403.

50. Raven JA. 1985. Regulation of pH and generation of osmolarity in vascular plants: a cost-benefit analysis in relation to efficiency of use of energy, nitrogen and water. New Phytol 101:25–77. https://doi.org/10.1111/j.1469-8137.1985.tb02816.x.

51. Butenko A, Hammond M, Field MC, Ginger ML, Yurchenko V, Lukeš J. 2021. Reductionist pathways for parasitism in Euglenozoans? Expanded datasets provide new insights. Trends Parasitol 37:100–116. https://doi.org/10.1016/j.pt.2020.10.001.

52. De Vargas C, Aubry M-P, Probert I, Young J. 2007. Origin and evolution of coccolithophores: from coastal hunters to oceanic farmers, p 251–285. Evolution of primary producers in the sea. Elsevier, Amsterdam, Netherlands.

53. Tashyreva D, Prokopchuk G, Yabuki A, Kaur B, Faktorová D, Votýpka J, Kusaka C, Fujikura K, Shiratori T, Ishida K-I, Horák A, Lukeš J. 2018. Phylogeny and morphology of new diplonemids from Japan. Protist 169:158–179. https://doi.org/10.1016/j.protis.2018.02.001.

54. Prokopchuk G, Tashyreva D, Yabuki A, Horák A, Masařová P, Lukeš J. 2019. Morphological, ultrastructural, motility and evolutionary characterization of two new Hemistasiidae species. Protist 170:259–282. https://doi.org/10.1016/j.protis.2019.04.001.

55. Tashyreva D, Prokopchuk G, Votýpka J, Yabuki A, Horák A, Lukeš J. 2018. Life cycle, ultrastructure, and phylogeny of new diplonemids. mBio 9:e02447-17. https://doi.org/10.1128/mBio.02447-17.

56. Moudříková Š, Sadowsky A, Metzger S, Nedbal L, Mettler-Altmann T, Mojzeš P. 2017. Quantification of polyphosphate in microalgae by Raman microscopy and by a reference enzymatic assay. Anal Chem 89:12006–12013. https://doi.org/10.1021/acs.analchem.7b02393.

57. Moudříková Š, Mojzeš P, Zachleder V, Pfaff C, Behrendt D, Nedbal L. 2016. Raman and fluorescence microscopy sensing energy-transducing and energy-storing structures in microalgae. Algal Res 16:224–232. https://doi.org/10.1016/j.algal.2016.03.016.

58. Moudříková Š, Nedbal L, Solovchenko A, Mojzeš P. 2017. Raman microscopy shows that nitrogen-rich cellular inclusions in microalgae are microcrystalline guanine. Algal Res 23:216–222. https://doi.org/10.1016/j.algal.2017.02.009.

59. Barcytė D, Pilátová J, Mojzeš P, Nedbalová L. 2020. The arctic *Cylindrocystis* (Zygnematophyceae, Streptophyta) green algae are genetically and morphologically diverse and exhibit effective accumulation of polyphosphate. J Phycol 56:217–232. https://doi.org/10.1111/jpy.12931.

60. Pilátová J, Pánek T, Oborník M, Čepička I, Mojzeš P. 2022. Revisiting biocrystallization: purine crystalline inclusions are widespread in eukaryotes. ISME J 16:2290–2294. https://doi.org/10.1038/s41396-022-01264-1.

61. Yurchenko V, Votýpka J, Tesařová M, Klepetková H, Kraeva N, Jirků M, Lukeš J. 2014. Ultrastructure and molecular phylogeny of four new species of monoxenous trypanosomatids from flies (Diptera: Brachycera) with redefinition of the genus *Wallaceina*. Folia Parasitol 61:97–112. https://doi.org/10.14411/fp.2014.023.

62. Gemmi M, Mugnaioli E, Gorelik TE, Kolb U, Palatinus L, Boullay P, Hovmöller S, Abrahams JP. 2019. 3D electron diffraction: The nanocrystallography revolution. ACS Cent Sci 5:1315–1329. https://doi.org/10.1021/acscentsci.9b00394.

63. Palatinus L, Brázda P, Jelínek M, Hrdá J, Steciuk G, Klementová M. 2019. Specifics of the data processing of precession electron diffraction tomography data and their implementation in the program PETS2.0. Acta Crystallogr B Struct Sci Cryst Eng Mater 75:512–522. https://doi.org/10.1107/S2052520619007534.

64. Petříček V, Dušek M, Palatinus L. 2014. Crystallographic computing system JANA2006: general features. Z Krist 229:345–352. https://doi.org/10.1515/zkri-2014-1737.

65. Belevich I, Joensuu M, Kumar D, Vihinen H, Jokitalo E. 2016. Microscopy Image Browser: a platform for segmentation and analysis of multidimensional datasets. PLoS Biol 14:e1002340. https://doi.org/10.1371/journal.pbio.1002340.

66. Zhao F, McGrath SP, Crosland AR. 1994. Comparison of three wet digestion methods for the determination of plant sulphur by inductively coupled plasma atomic emission spectroscopy (ICP-AES). Commun Soil Sci Plant Anal 25:407–418. https://doi.org/10.1080/00103629409369047.

67. Andresen E, Lyubenova L, Hubáček T, Bokhari SNH, Matoušková Š, Mijovilovich A, Rohovec J, Küpper H. 2020. Chronic exposure of soybean plants to nanomolar cadmium reveals specific additional high-affinity targets of cadmium toxicity. J Exp Bot 71:1628–1644. https://doi.org/10.1093/jxb/erz530.

68. Strbkova L, Carson BB, Vincent T, Vesely P, Chmelik R. 2020. Automated interpretation of time-lapse quantitative phase image by machine learning to study cellular dynamics during epithelial–mesenchymal transition. J Biomed Opt 25:e086502.

69. Decelle J, Not F. 2015. Acantharia. John Wiley & Sons, Hoboken, NJ.

16
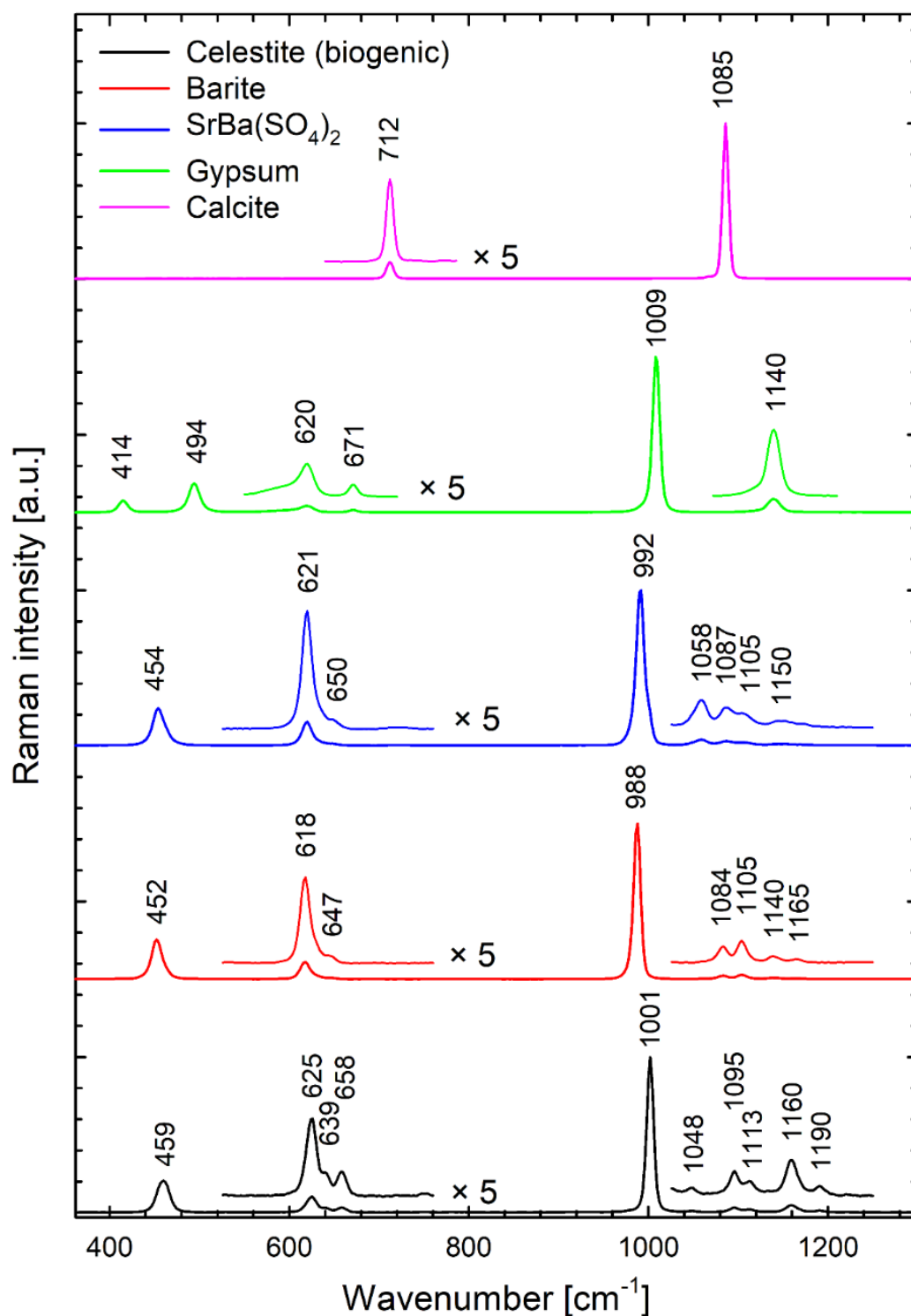
FIG S1. Typical Raman spectrum of biogenic celestite crystals compared with the spectra of chemically prepared barite, the equimolar precipitate of SrSO₄ and BaSO₄, gypsum (CaSO₄) and calcite (CaCO₃). Each complex of SO_4^{2-} with Sr^{2+}, Ba^{2+} or Ca^{2+} can be unambiguously identified by the position of the most intense Raman band at around 1000 cm^{-1} belonging to the symmetric ν_1 vibrational mode of oxygen atoms within SO_4^{2-} tetrahedron.
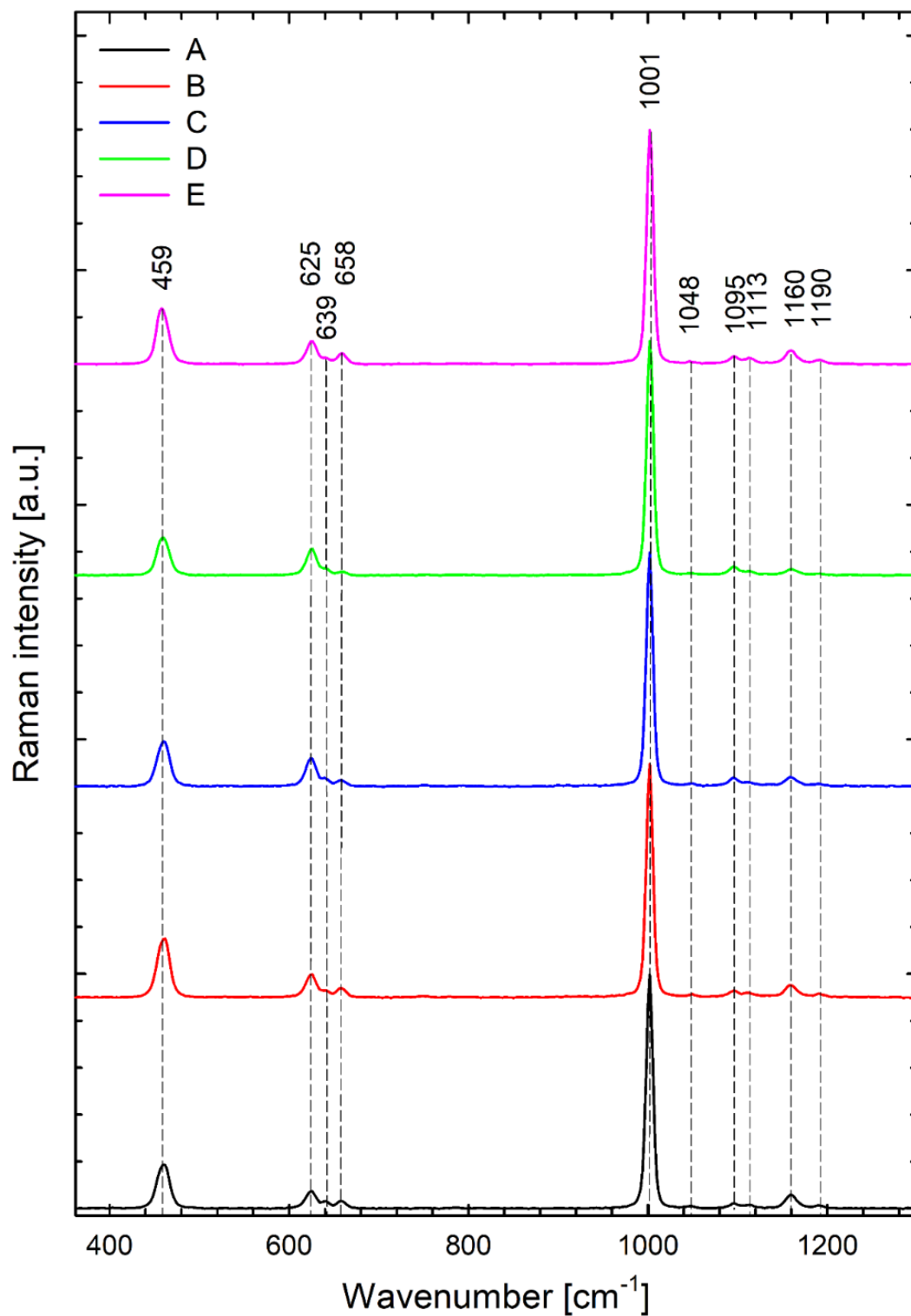
FIG S2. Typical Raman spectra (A–E) of biogenic celestite crystals found in various *Diplonema* cells. As concerns Raman frequencies, the spectra are virtually identical, however minor spectral variability in the relative intensities of Raman bands can be observed. Similar variability was also observed for mineral celestite and chemically prepared $SrSO_4$ precipitates.
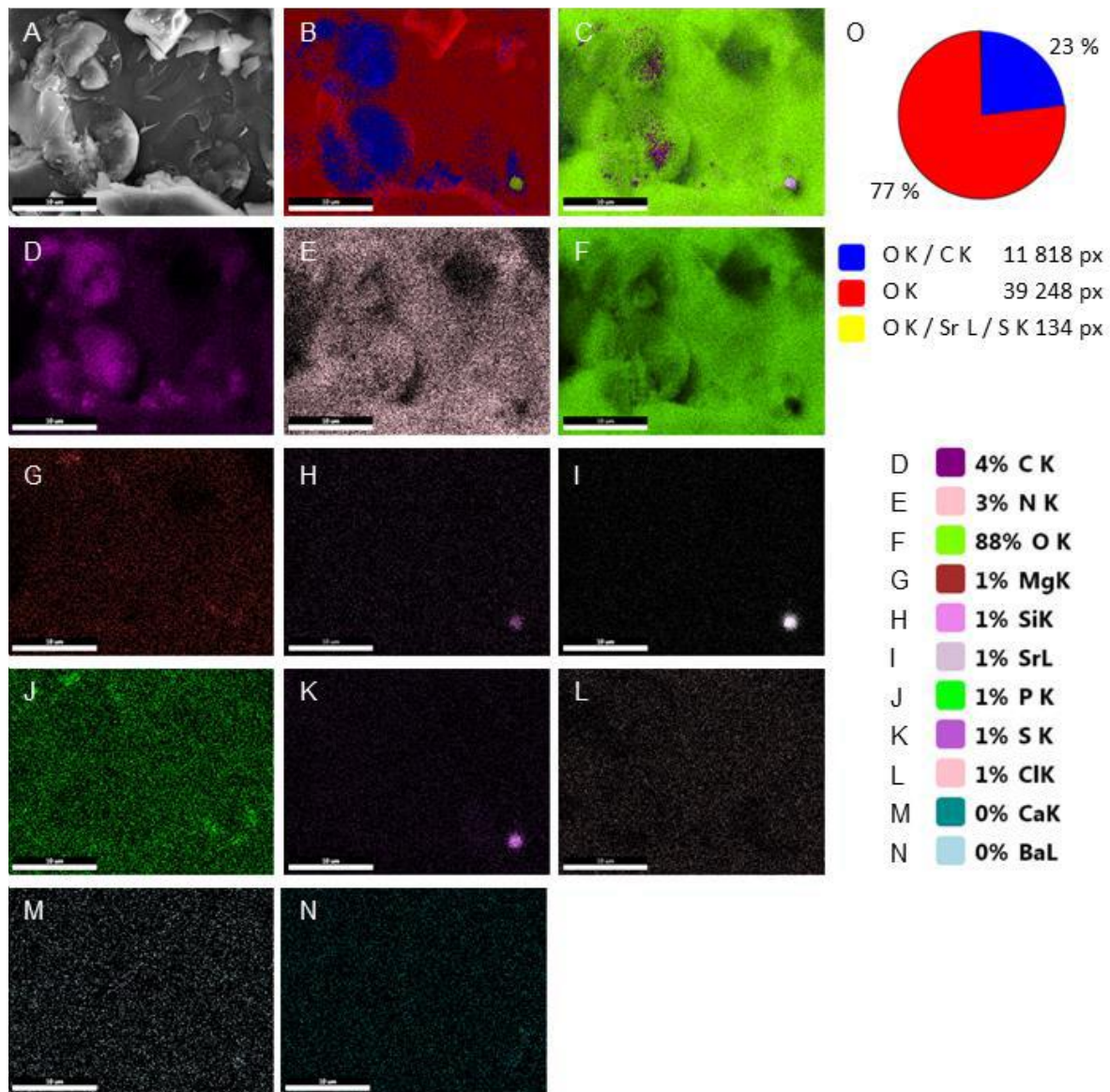
FIG S3. Cryo-SEM-EDX analysis of *Lacrimia* sp. YPF1808 shows the elemental analysis of freeze-fractured samples. (A) SEM micrograph, (B) merged image of the most common elements, (C) merged image of all elements present, (D) map of carbon K line, (E) map of nitrogen K line, (F) map of oxygen K line, (G) map of magnesium K line, (H) map of silicon K line, (I) map of strontium L line, (J) map of phosphorus K line, (K) map of sulfur K line, (L) map of chlorine K lines, (M) map of calcium K line, (N) map of barium L line, (O) pie chart of the most common elements detected in the area with particular pixel counts as depicted in (B): oxygen and carbon K lines (blue), oxygen K line (red), oxygen K line, strontium L line, sulfur K line (yellow), scale bar 10 μm.

FIG S4. Cryo-SEM-EDX analysis of *N. karyoxenos* shows freeze-fractured samples' elemental analysis. (A) SEM micrograph, (B) merged image of the most common elements, (C) merged image of all elements present, (D) map of carbon K line, (E) map of nitrogen K line, (F) map of magnesium K line, (G) map of silicon K line, (H) map of strontium L line, (I) map of phosphorus K line, (J) map of sulfur K line, (K) map of chlorine K lines, (L) map of calcium K line, (M) pie chart of the most common elements detected in the area with particular pixel counts as depicted in (B): oxygen and carbon K lines (blue), oxygen K line (dark red), oxygen and carbon K lines (yellow), scale bar 10 µm.

FIG S5. SEM-EDX analysis of *Lacrimia* sp. YPF1808 showing the elemental composition of samples used for 3D reconstruction by SBF-SEM. (A) electron-micrograph, (B) merged image of the most common elements, (C) merged image of all elements present, (D) map of carbon K line, (E) map of oxygen K line, (F) map of strontium L line, (G) map of calcium L line, (H) map of barium M line, (I) map of osmium M line, (J) map of nitrogen K line, (K) map of sodium K line, (L) map of sulfur K lines, (M) pie chart of the most common elements detected in the area with particular pixel counts as depicted in (B): * represents oxygen K line / calcium L line, ** represents oxygen K line/ calcium L line / nitrogen K line, *** represents oxygen K line / calcium L line / nitrogen K line / strontium L line / osmium M line, scale bar 2 μm.

TABLE S1. ICP-MS analysis of seawater growth medium and artificial medium without the addition of sulfates, Ba^{2+} and Sr^{2+} sources. The latter was used for culturing cells in Ba^{2+}-loading experiments and as a rinsing solution for the preparation of ICP-MS samples. Mean of three technical replicates (±SD of the mean).

Element	unit	Standard seawater growth medium		Artificial seawater medium without the addition of sulfates, Ba and Sr	
		mean	SD	mean	SD
Mg	ppb	1 710 000	69 000	3 190 000	120 000
	nM	71 200 000	2 900 000	132 900 000	4 900 000
K	ppb	1 360 000	190 000	1 291 000	52 000
	nM	34 800 000	4 900 000	33 100 000	1 300 000
Ca	ppb	513 000	34 000	545 000	18 000
	nM	11 650 000	770 000	12 390 000	420 000
S	ppb	165 000	12 000	2 570	120
	nM	1 870 000	140 000	29 200	1 300
^{56}Fe	ppb	500	240	1 170	140
	nM	9 000	4 400	20 800	2 400
P	ppb	1 100	1 300	630	630
	nM	35 000	42 000	20 000	20 000
Zn	ppb	320	70	303	27
	nM	4 900	1 100	4 600	400
^{88}Sr	ppb	7 870	440	246	16
	nM	89 400	5 000	2 800	180
Ba	ppb	638	21	291	17
	nM	4 590	150	2 100	120
Ni	ppb	101	4	95	4
	nM	1 680	73	1 585	61
Mn	ppb	46	2	79	8
	nM	832	31	1 430	140
Cr	ppb	50	3	49	4
	nM	956	66	948	76
Cu	ppb	88	58	55	10
	nM	1 390	930	870	160

TABLE S2. ICP-MS data and calculations with Sr and Ba amounts in 6 diplonemid species (Table S2A), calculations of concentration of Ba and Sr inside the cells relative to the concentration in the surrounding medium (Table S2B), volumetric measurements of diplonemid *Lacrimia* sp. YPF1808 is based on SBF-SEM 3D reconstruction with the calculation of theoretical cell density based on literature, calculations of cell and crystal densities and theoretical sedimentation rates assumed based on Stokes' law (Table S2C).

Table S2A. ICP-MS data and calculations - page 1/2

Sr amounts in 6 species

Species	Strain	Sample	Cell dry weight pg/cell	Sr atoms/cell	Sr fmol/cell	Sr pg/cell	SrSO₄ pg/cell	Sr mg/g DW	SrSO₄ mg/g DW	Legend
Namystinia karyoxenos	YPF1621	x1	1421,1	2,88E+12	4790,15	419,713	879,855	295,35	619,14	"atoms/cell" = atoms Sr/Ba in sample/N of cells in sample
Namystinia karyoxenos	YPF1621	x2	1421,1	4,00E+12	6646,40	582,358	1220,811	409,80	859,07	"fmol/cell" = (atoms/cell / NA 6.022E23)*1E15
Namystinia karyoxenos	YPF1621	x3	1421,1	3,11E+12	5162,02	452,296	948,159	318,28	667,21	"pg/cell" = fmol/cell*Aw/1E3
Lacrimia sp.	YPF1808	x1	248,1	2,71E+11	450,28	39,454	82,708	159,01	333,33	"mg/g DW" = "pg/cell"/pg DW of 1 cell by holographic microscopy
Lacrimia sp.	YPF1808	x2	248,1	2,36E+11	391,45	34,299	71,901	138,23	289,78	"SrSO4 mg/g DW" = 1:1 stoichiometry of Sr:SO4
Lacrimia sp.	YPF1808	x3	248,1	1,54E+11	255,63	22,398	46,954	90,27	189,23	"BaSO4 mg/g DW" = 1:1 stoichiometry of Ba:SO4
Lacrimia lanifica	JW1601	x1	74,1	4,05E+10	67,24	5,891	12,350	79,50	166,66	"(Ba,Sr)SO4 mg/g DW" is a sum of BaSO4 and SrSO4
Lacrimia lanifica	JW1601	x2	74,1	3,45E+10	57,32	5,023	10,529	67,78	142,09	
Lacrimia lanifica	JW1601	x3	74,1	2,32E+10	38,60	3,382	7,090	45,64	95,68	**constants**
Rhynchopus sp. YZ270	cl. 10.3	x1	104,0	1,36E+07	0,02	0,002	0,004	0,02	0,04	NA - Avogadro's constant = 6.022E23
Rhynchopus sp. YZ270	cl. 10.3	x2	104,0	1,52E+07	0,03	0,002	0,005	0,02	0,04	Aw(Sr) = 87.62
Rhynchopus sp. YZ270	cl. 10.3	x3	104,0	1,29E+07	0,02	0,002	0,004	0,02	0,04	Aw(Ba) = 137.3
Diplonema japonicum	YPF1604	x1	109,7	1,18E+08	0,20	0,017	0,036	0,16	0,33	Mw(SO4) = 96.1
Diplonema japonicum	YPF1604	x2	109,7	1,35E+08	0,22	0,020	0,041	0,18	0,37	
Diplonema japonicum	YPF1604	x3	109,7	1,40E+08	0,23	0,020	0,043	0,19	0,39	
Diplonema papillatum	ATCC 50162	x1	68,0	7,55E+06	0,01	0,001	0,002	0,02	0,03	
Diplonema papillatum	ATCC 50162	x2	68,0	7,61E+06	0,01	0,001	0,002	0,02	0,03	
Diplonema papillatum	ATCC 50162	x3	68,0	8,48E+06	0,01	0,001	0,003	0,02	0,04	

Ba amounts in 6 species

Species	Strain	Sample	Cell dry weight pg/cell	Ba atoms/cell	Ba fmol/cell	Ba pg/cell	BaSO₄ pg/cell	Ba mg/g DW	BaSO₄ mg/g DW	(Ba,Sr)SO₄ mg/g DW
Namystinia karyoxenos	YPF1621	x1	1421,1	6,26E+11	1039,36	142,73	242,574	100,44	170,70	789,84
Namystinia karyoxenos	YPF1621	x2	1421,1	8,80E+11	1460,48	200,56	340,857	141,13	239,86	1098,93
Namystinia karyoxenos	YPF1621	x3	1421,1	6,67E+11	1108,37	152,21	258,678	107,11	182,03	849,24
Lacrimia sp.	YPF1808	x1	248,1	4,74E+10	78,76	10,82	18,381	43,59	74,08	407,41
Lacrimia sp.	YPF1808	x2	248,1	4,24E+10	70,44	9,67	16,441	38,99	66,26	356,04
Lacrimia sp.	YPF1808	x3	248,1	2,72E+10	45,09	6,19	10,523	24,95	42,41	231,64
Lacrimia lanifica	JW1601	x1	74,1	1,21E+09	2,01	0,28	0,468	3,72	6,32	172,98
Lacrimia lanifica	JW1601	x2	74,1	1,72E+09	2,86	0,39	0,667	5,30	9,00	151,09
Lacrimia lanifica	JW1601	x3	74,1	7,08E+08	1,18	0,16	0,274	2,18	3,70	99,38
Rhynchopus sp. YZ270	cl. 10.3	x1	104,0	N/A	N/A	N/A	N/A	N/A	N/A	N/A
Rhynchopus sp. YZ270	cl. 10.3	x2	104,0	N/A	N/A	N/A	N/A	N/A	N/A	N/A
Rhynchopus sp. YZ270	cl. 10.3	x3	104,0	N/A	N/A	N/A	N/A	N/A	N/A	N/A
Diplonema japonicum	YPF1604	x1	109,7	N/A	N/A	N/A	N/A	N/A	N/A	N/A
Diplonema japonicum	YPF1604	x2	109,7	N/A	N/A	N/A	N/A	N/A	N/A	N/A
Diplonema japonicum	YPF1604	x3	109,7	N/A	N/A	N/A	N/A	N/A	N/A	N/A
Diplonema papillatum	ATCC 50162	x1	68,0	N/A	N/A	N/A	N/A	N/A	N/A	N/A
Diplonema papillatum	ATCC 50162	x2	68,0	N/A	N/A	N/A	N/A	N/A	N/A	N/A
Diplonema papillatum	ATCC 50162	x3	68,0	N/A	N/A	N/A	N/A	N/A	N/A	N/A

Table S2A. ICP-MS data and calculations - page 2/2

Sorbitol as rinsing solution

Strain	Replicate	Cells/ml	Culture volume	Total cells
Rhynchopus YZ270 cl. 10.3*	x1	9,09E+05	45	4,09E+07
Rhynchopus YZ270 cl. 10.3*	x2	9,13E+05	45	4,11E+07
Rhynchopus YZ270 cl. 10.3*	x3	1,02E+06	45	4,57E+07
Diplonema japonicum YPF1604*	x1	1,93E+05	220	4,25E+07
Diplonema japonicum YPF1604*	x2	2,09E+05	225	4,70E+07
Diplonema japonicum YPF1604*	x3	2,25E+05	185	4,16E+07
Diplonema papillatum ATCC 501	x1	2,64E+06	50	1,32E+08
Diplonema papillatum ATCC 501	x2	2,03E+06	50	1,02E+08
Diplonema papillatum ATCC 501	x3	1,99E+06	50	9,95E+07

Sr- and Ba-free artificial seawater as rinsing solution

Strain	Replicate	Cells/ml	Sample volume	Total cells	Initial volume of culture, ml
Lacrimia sp. YPF1808*	x1	3,59E+06	3,95	1,42E+07	250
Lacrimia sp. YPF1808*	x2	3,49E+06	4,15	1,45E+07	250
Lacrimia sp. YPF1808*	x3	4,03E+06	3,95	1,59E+07	250
Lacrimia lanifica JW1601**	x1	7,35E+05	247	1,82E+08	247
Lacrimia lanifica JW1601**	x2	8,05E+05	245	1,97E+08	245
Lacrimia lanifica JW1601**	x3	7,25E+05	244	1,77E+08	244
Namystinia karyoxenos YPF1621	x1	1,37E+06	2,6	3,56E+06	100
Namystinia karyoxenos YPF1621	x2	1,21E+06	2,2	2,66E+06	100
Namystinia karyoxenos YPF1621	x3	1,40E+06	3,22	4,51E+06	100

*Counted after 2 round of centrifugation

**Counted directly from cultures, before centrifugation

Table S2B. Concentration of Ba and Sr inside the cells relative to the concentration in the surrounding medium - page 1/2

Species	Strain	Replicate	Ba			Sr		
			Atoms/cell measured by ICP-MS	Atoms/cell calculated* theoretical value	Measured/theoretical, factor	Atoms/cell measured by ICP-MS	Atoms/cell calculated* theoretical value	Measured/theoretical, factor
Namystinia karyoxenos	YPF1621	x1	6,26E+11	2,10E+07	29864,21	2,88E+12	4,10E+08	7037,41
Namystinia karyoxenos	YPF1621	x2	8,80E+11	2,21E+07	39715,41	4,00E+12	4,33E+08	9241,21
Namystinia karyoxenos	YPF1621	x3	6,67E+11	1,17E+07	57055,80	3,11E+12	2,29E+08	13586,74
Average			**7,24E+11**	**1,83E+07**	**42211,81**	**3,33E+12**	**3,57E+08**	**9955,12**
Lacrimia sp.	YPF1808	x1	4,74E+10	8,01E+06	5918,10	2,71E+11	1,57E+08	1729,98
Lacrimia sp.	YPF1808	x2	4,24E+10	8,96E+06	4734,67	2,36E+11	1,75E+08	1345,24
Lacrimia sp.	YPF1808	x3	2,72E+10	1,21E+07	2242,96	1,54E+11	2,37E+08	650,22
Average			**3,90E+10**	**9,69E+06**	**4298,58**	**2,20E+11**	**1,90E+08**	**1241,81**
Lacrimia lanifica	JW1601	x1	1,21E+09	1,02E+06	1179,25	4,05E+10	2,00E+07	2019,98
Lacrimia lanifica	JW1601	x2	1,72E+09	9,81E+05	1755,04	3,45E+10	1,92E+07	1800,01
Lacrimia lanifica	JW1601	x3	7,08E+08	1,58E+06	448,64	2,32E+10	3,09E+07	753,29
Average			**1,21E+09**	**1,19E+06**	**1127,64**	**3,28E+10**	**2,34E+07**	**1524,43**

* - an estimation on how many atoms a cell would contain if it was in equilibrium with the surrounding medium, calculated as shown below (column H)

Species	Strain	Replicate	Atoms/1 mg of Hemi medium	Weight of pellet, mg	Atoms per theoretical pellet	N of cells in actual pellet	Atoms per theoretical cell	
Namystinia karyoxenos	YPF1621	x1	2,80E+12	26,67	7,47E+13	3,56E+06	**2,10E+07**	
Namystinia karyoxenos	YPF1621	x2	2,80E+12	21,06	5,90E+13	2,66E+06	**2,21E+07**	
Namystinia karyoxenos	YPF1621	x3	2,80E+12	18,84	5,27E+13	4,51E+06	**1,17E+07**	
Lacrimia sp.	YPF1808	x1	2,80E+12	40,6	1,14E+14	1,42E+07	**8,01E+06**	**Ba**
Lacrimia sp.	YPF1808	x2	2,80E+12	46,36	1,30E+14	1,45E+07	**8,96E+06**	
Lacrimia sp.	YPF1808	x3	2,80E+12	68,84	1,93E+14	1,59E+07	**1,21E+07**	
Lacrimia lanifica	JW1601	x1	2,80E+12	66,47	1,86E+14	1,82E+08	**1,02E+06**	
Lacrimia lanifica	JW1601	x2	2,80E+12	69,09	1,93E+14	1,97E+08	**9,81E+05**	
Lacrimia lanifica	JW1601	x3	2,80E+12	99,71	2,79E+14	1,77E+08	**1,58E+06**	
Namystinia karyoxenos	YPF1621	x1	5,47E+13	26,67	1,46E+15	3,56E+06	**4,10E+08**	
Namystinia karyoxenos	YPF1621	x2	5,47E+13	21,06	1,15E+15	2,66E+06	**4,33E+08**	
Namystinia karyoxenos	YPF1621	x3	5,47E+13	18,84	1,03E+15	4,51E+06	**2,29E+08**	
Lacrimia sp.	YPF1808	x1	5,47E+13	40,6	2,22E+15	1,42E+07	**1,57E+08**	
Lacrimia sp.	YPF1808	x2	5,47E+13	46,36	2,54E+15	1,45E+07	**1,75E+08**	**Sr**
Lacrimia sp.	YPF1808	x3	5,47E+13	68,84	3,77E+15	1,59E+07	**2,37E+08**	
Lacrimia lanifica	JW1601	x1	5,47E+13	66,47	3,64E+15	1,82E+08	**2,00E+07**	
Lacrimia lanifica	JW1601	x2	5,47E+13	69,09	3,78E+15	1,97E+08	**1,92E+07**	
Lacrimia lanifica	JW1601	x3	5,47E+13	99,71	5,46E+15	1,77E+08	**3,09E+07**	

Table S2B. Concentration of Ba and Sr inside the cells relative to the concentration in the surrounding medium - page 2/2

Legend

Column	Meaning
"D"	Number of atoms in 1 µl of Hemi medium based on ICP-MS measurements of the medium (calculated below)
"E"	Wet weight of cell pellets (rinsed with Ba/Sr-free medium), which was provided for ICP-MS measurements
"F"	D*E - total number of atoms that each pellet would contain if cells were in equilibrium with the medium and did not concentrate Ba/Sr
"G"	Number of cells in pellets provided for the ICP-MS measurements
"H"	E/F - number of atoms a cell would contain if it was in equilibrium with the medium and did not concentrate Ba/Sr

Calculation of number of atoms are in 1 ul of Hemi medium based on ICP-MS measurements of the medium

	MW	Concentration*	Concentration	Concentration	Atoms/µl or mg of Hemi medium**
	g/mol	g/l	mol/l	atoms/l	
Sr	88	0,008	9,09E-05	5,47E+19	5,47E+13
Ba	137,33	0,00064	4,65E-06	2,80E+18	2,80E+12

* - resuts of ICP-MS measurement
** - not considering difference in density (1.03g/ml)

Table S2C. Volumetric measurements of diplonemid Lacrimia sp. YPF1808 based on SBF-SEM 3D reconstruction - page 1/3

Volumetric measurements of diplonemid *Lacrimia* sp. YPF1808 based on SBF-

Cell	Vol. cryst 1 (µm³)	Vol. cryst 2 (µm³)	Vol. cryst 3 (µm³)	Vol. cryst 4 (µm³)	Vol. cryst 5 (µm³)	Vol. cryst 6 (µm³)	Vol. cryst 7 (µm³)	Vol. cryst 8 (µm³)	Vol. cryst 9 (µm³)	Vol. cryst 10 (µm³)	Vol. cryst 11 (µm³)	Vol. Cryst 12 (µm³)	Vol. cryst 13 (µm³)	Vol. cryst 14 (µm³)	Vol. cryst 15 (µm³)	Vol. cryst 16 (µm³)
1	2,704	0,942	-	-	-	-	-	-	-	-	-	-	-	-	-	-
2	0,769	0,214	0,052	-	-	-	-	-	-	-	-	-	-	-	-	-
3	1,708	0,523	0,500	-	-	-	-	-	-	-	-	-	-	-	-	-
4	0,962	0,027	0,011	0,009	-	-	-	-	-	-	-	-	-	-	-	-
5	0,037	0,017	-	-	-	-	-	-	-	-	-	-	-	-	-	-
6	0,170	0,130	0,124	0,116	0,061	0,054	0,026	0,015	-	-	-	-	-	-	-	-
7	0,208	0,013	0,009	0,009	0,008	0,007	0,007	0,007	0,007	0,007	0,005	0,005	0,005	0,005	0,003	0,002
8	0,115	0,101	0,029	0,009	-	-	-	-	-	-	-	-	-	-	-	-
9	0,150	0,010	-	-	-	-	-	-	-	-	-	-	-	-	-	-
10	0,211	0,195	0,004	-	-	-	-	-	-	-	-	-	-	-	-	-
11	0,433	0,323	0,109	-	-	-	-	-	-	-	-	-	-	-	-	-
12	0,383	0,067	0,056	0,030	0,028	0,027	0,014	0,013	0,012	0,010	0,009	-	-	-	-	-
13	0,274	0,192	0,012	0,011	0,008	0,004	-	-	-	-	-	-	-	-	-	-
14	0,089	0,053	0,038	-	-	-	-	-	-	-	-	-	-	-	-	-
15	1,080	0,264	0,072	0,034	0,012	0,007	0,003	-	-	-	-	-	-	-	-	-
16	1,353	0,503	0,436	0,106	0,014	-	-	-	-	-	-	-	-	-	-	-
17	2,664	0,045	-	-	-	-	-	-	-	-	-	-	-	-	-	-
18	0,140	0,125	0,119	0,100	0,072	0,023	0,008	0,006	0,005	0,003	-	-	-	-	-	-
19	0,084	0,056	0,016	0,003	-	-	-	-	-	-	-	-	-	-	-	-
20	0,171	0,124	0,089	0,087	0,013	0,004	0,003	-	-	-	-	-	-	-	-	-
21	6,968	-	-	-	-	-	-	-	-	-	-	-	-	-	-	-

Cell	Number of crystals	Total volume of crystals (µm³)	Average size of 1 crystal (µm³)	Volume of the cell (µm³)	Ratio of cell volume / crystal	Ratio of crystal volume / cell	Volumetric percentage of crystal (%)
1	2	**3,646**	1,823	148,930	40,849	0,024	2,448
2	3	**1,036**	0,345	175,930	169,885	0,006	0,589
3	3	**2,732**	0,911	251,160	91,937	0,011	1,088
4	4	**1,008**	0,252	315,810	313,191	0,003	0,319
5	2	**0,054**	0,027	328,390	6092,262	0,000	0,016
6	8	**0,696**	0,087	404,150	580,337	0,002	0,172
7	16	**0,306**	0,019	411,010	1345,180	0,001	0,074
8	4	**0,254**	0,064	470,300	1848,341	0,001	0,054
9	2	**0,160**	0,080	489,070	3059,479	0,000	0,033
10	3	**0,410**	0,137	502,410	1226,509	0,001	0,082
11	3	**0,864**	0,288	518,000	599,631	0,002	0,167
12	11	**0,649**	0,059	626,010	965,266	0,001	0,104
13	6	**0,500**	0,083	660,190	1319,325	0,001	0,076
14	3	**0,180**	0,060	789,630	4390,609	0,000	0,023
15	7	**1,473**	0,210	947,900	643,551	0,002	0,155
16	5	**2,412**	0,482	975,460	404,414	0,002	0,247
17	2	**2,710**	1,355	987,680	364,503	0,003	0,274
18	10	**0,601**	0,060	1131,700	1884,546	0,001	0,053
19	4	**0,160**	0,040	1134,900	7114,807	0,000	0,014
20	7	**0,491**	0,070	1136,000	2315,494	0,000	0,043
21	1	**6,968**	6,968	620,200	89,002	0,011	1,124

Table S2C. Volumetric measurements of diplonemid Lacrimia sp. YPF1808 based on SBF-SEM 3D reconstruction - page 2/3

Theoretical cell density based on literature

Density	value	unit	
ρ (cell min)	0,985	g/cm^3	REFERENCE: Cellular density range based on the reference: Walsby, A. E.
ρ (cell max)	1,156	g/cm^3	& Reynolds, C. S. Sinking and floating. in The Physiological Ecology of the
ρ (cell mean)	1,0705	g/cm^3	Phytoplankton. (ed. Morris, I.) 371–412 (Blackwell Science, 1980).
ρ (SrSO$_4$)	3,9	g/cm^3	

Calculations of cell and crystal densities

Cell	Volume of cell	Volume of crystals (cumulative)	Density of cells with crystals	Increase in cell density	Legend
	μm^3	μm^3	g/cm^3	%	
1	148,93	3,65	1,14	6,32	
2	175,93	1,04	1,09	1,55	Based on measured cell and crystal volumes via SBF-SEM and the
3	251,16	2,73	1,10	2,84	average theoretical cell density 1,0705 g/cm^3 and celestite density 3,9
4	315,81	1,01	1,08	0,84	g/cm^3, the increase in the overall cell density with crystals was counted
5	328,39	0,05	1,07	0,04	* crystal volumes are less than 1 % of cell volume, therefore we
6	404,15	0,70	1,08	0,45	neglected their volumes in the overall cellular volume
7	411,01	0,31	1,07	0,20	
8	470,3	0,25	1,07	0,14	
9	489,07	0,16	1,07	0,09	
10	502,41	0,41	1,07	0,22	
11	518	0,86	1,08	0,44	
12	626,01	0,65	1,07	0,27	
13	660,19	0,50	1,07	0,20	
14	789,63	0,18	1,07	0,06	
15	947,9	1,47	1,07	0,41	
16	975,46	2,41	1,08	0,65	
17	987,68	2,71	1,08	0,72	
18	1131,7	0,60	1,07	0,14	
19	1134,9	0,16	1,07	0,04	
20	1136	0,49	1,07	0,11	
21	620,2	6,97	1,10	2,94	
Mean	620,23	1,30	1,08	0,89	
SEM	70,36	0,36	0,00	0,33	

Table S2C. Volumetric measurements of diplonemid Lacrimia sp. YPF1808 based on SBF-SEM 3D reconstruction - page 3/3

Theoretical sedimentation rates assumed based on Stokes' law:

Physical property	value	unit	Legend
g	9,81	m/s^2	* Negative buyoncy
R	0,00001	m	
ρ_p 1*	900	kg/m^3	** Values that could be reached in case of
ρ_p 2	1050	kg/m^3	Lacrimia sp. YPF 1808 based on 3D
ρ_p 3**	1100	kg/m^3	reconstructions of SBF-SEM
ρ_p 4	1200	kg/m^3	
ρ_p 5***	1300	kg/m^3	*** Predicted values for Namystinia
ρ_f	1030	kg/m^3	karyoxenos based on extrapolation of ICP MS
μ	0,00089	kg/m/s	quantifications on 3D reconstructions in Lacrimia sp. YPF1808

$$v = \frac{2}{9}\frac{(\rho_p - \rho_f)}{\mu}\, g\, R^2$$

(vertically downwards if $\rho_p > \rho_f$, upwards if $\rho_p < \rho_f$), where:

- g is the gravitational field strength (m/s^2)
- R is the radius of the spherical particle (m)
- ρ_p is the mass density of the particle (kg/m^3)
- ρ_f is the mass density of the fluid (kg/m^3)
- μ is the dynamic viscosity (kg/(m*s)).

Potential particle/cell densities		Velocity	value	unit	value	unit	value	unit	value	unit	value	unit
ρ_p 1 *	900 kg/m^3	v1	-3,18E-05	m/s	-31,84	µm/s	-2,75	m/day	-83	m/month	-990	m/year
ρ_p 2	1050 kg/m^3	v2	4,9E-06	m/s	4,90	µm/s	0,42	m/day	13	m/month	152	m/year
ρ_p 3 **	1100 kg/m^3	v3	1,71E-05	m/s	17,15	µm/s	1,48	m/day	44	m/month	533	m/year
ρ_p 4	1200 kg/m^3	v4	4,16E-05	m/s	41,64	um/s	3,60	m/day	108	m/month	1295	m/year
ρ_p 5 ***	1300 kg/m^3	v5	6,61E-05	m/s	66,13	µm/s	5,71	m/day	171	m/month	2057	m/year

Movie legends

Movie 1. *N. karyoxenos* and *Lacrimia* sp. YPF1808 under bright field DIC microscopy showing fast moving celestite crystals in lacunae marked by arrows. *N. karyoxenos* and *Lacrimia* sp. YPF1808 under bright field polarization microscopy showing light-polarizing celestite crystals marked by arrows.

Movie 2. Visualization of serial sections through the celestite-containing cell of *Lacrimia* sp. YPF1808 taken by SBF-SEM with celestite crystals marked by arrows. PV – posterior vacuole, N – nucleus, FP – flagellar pocket. 3D reconstruction of a single cell *via* SBF-SEM: cytoplasm in yellow, large posterior vacuole in orange and celestine crystals in cyan.

All the supplementary movies are deposited here: 10.6084/m9.figshare.21647135

PROOFS

Unravelling the hidden complexity in diversity and pigment composition of a colonial flagellate *Synura sphagnicola* (Chrysophyceae, Stramenopiles)

Pavel Škaloud[1*], Magda Škaloudová[1], Iva Jadrná[1], Jana Pilátová[2,3], Woonnghi Shin[4] & Jiří Kopecký[5]

[1] *Charles University, Faculty of Science, Department of Botany, 12800 Praha 2, Czech Republic; *Corresponding author e–mail: skaloud@natur.cuni.cz*

[2] *Charles University, Faculty of Science, Department of Experimental Plant Biology, 12800 Praha 2, Czech Republic*

[3] *Charles University, Faculty of Mathematics and Physics, Institute of Physics, Division of Biomolecular Physics, 12000 Praha 2, Czech Republic*

[4] *Chungnam National University, Department of Biology, 34141 Daejeon, Korea*

[5] *Laboratory of Algal Biotechnology – Centre ALGATECH, Institute of Microbiology of the Czech Academy of Sciences, Opatovický mlýn, 379 81 Třeboň, Czech Republic*

Abstract: In this study, we aim to taxonomically evaluate a unique example of cryptic diversity in a freshwater protist species *Synura sphagnicola*, occurring at two evolutionary levels. First, we characterize two species, *S. sphagnicola* and *S. rubra* sp. nov., that diverged from one another approx. 14 Mya. These species are morphologically well differentiated by the morphology of silica scales. Second, we propose seven evolutionary young, but ecologically and geographically well differentiated lineages as separate sub–species, *sphagnicola*, *agilis*, *borealis* (within *S. sphagnicola*), *rubra*, *ampla*, *bella* and *caelica* (within *S. rubra*). In addition, we examine the autofluorescence and pigment composition of two selected strains, identifying fucoxanthin as a predominant carotenoid. We further show that the red droplets in the cytoplasm, a prominent feature of both species, are formed by a previously unknown pigment. Finally, we identify chlorophyll–c_2 in *S. sphagnicola*. Since the lack of this pigment represents a major distinguishing character to discriminate between classes Synurophyceae and Chrysophyceae, we formally synonymize these taxa.

Key words: cryptic diversity, evolution, molecular phylogeny, morphology, pigments, Synura, Synurophyceae, taxonomy

INTRODUCTION

Synura sphagnicola (Korshikov) Korshikov (Chrysophyceae, Synurales) is a colonial, cosmopolitan, silica–scaled flagellate originally described from peat bogs near Zvenigorod, Moscow district, Russia as *Skadovskiella sphagnicola* Korshikov, including figures of its scales (Korshikov 1927). Two years later, Korshikov clarified his observations and transferred *Skadovskiella sphagnicola* to the genus *Synura* Ehrenberg (Korshikov 1929). Later on, the detailed information on scale and cell ultrastructure of *Synura sphagnicola* based on electron microscopic (EM) examination was published by Petersen & Hansen (1958) and Hibberd (1978). The expanding availability of EM to phycologists initiated a plethora of floristic and ecological studies which often found *S. sphagnicola* dominant in slightly to very acidic

waters (Siver 1989; Kristiansen & Preisig 2007). More recently, with the continuing development of molecular methods, *S. sphagnicola* was inferred to represent a distinct, genetically quite separate lineage within the section Curtispinae of *Synura* (Jo et al. 2016). Pusztai et al. (2016) showed *Synura synuroidea* (Prowse) Pusztai, Čertnerová, Škaloudová et Škaloud, formerly described as *Chrysodidymus* Prowse, to be a sister clade of *Synura sphagnicola*.

Recently, a detailed investigation of *S. sphagnicola* diversity was published by Škaloud et al. (2019), based on the collection of 71 strains isolated from various water bodies from Europe, Newfoundland and Korea. According to the multilocus phylogenetic analysis, *S. sphagnicola* was shown to split into two distinct lineages referred to as sp1 and sp2, approximately 15.4 million years ago. In addition, Škaloud et al. (2019) reported a rapid diversification of both lineages into several geographically

and ecologically diverse incipient species that occurred during the late Pleistocene.

Both *S. sphagnicola* lineages and *S. synuroidea* are remarkable by a permanent presence of red droplets in the cytoplasm (Korshikov 1927; Conrad 1939; Harris & Bradley 1958; Graham et al. 1993; Pusztai et al. 2016). These droplets, occasionally observed also in related species *S. curtispina* (Petersen et Hansen) Asmund (Andersen 2010), and *S. spinosa* Korshikov (our observations), are situated mainly at the anterior end of the cell. Though red droplets represent a prominent feature present in these above–mentioned taxa, their nature is still not known. In the old literature these droplets are referred to as an accumulation of haematochrome (Korshikov 1927; Conrad 1939), which is however an obsolete term for a mixture of carotenoid pigments and their derivates.

The major aim of this study was to taxonomically evaluate the uncovered diversity within the *S. sphagnicola* morphotype. We recognized the lineages sp1 and sp2 as two separate species, and further described several evolutionary young, incipient species as sub–species taxa. In addition, we used fluorescence microscopy and high–performance liquid chromatography (HPLC) analyses to examine the pigment composition of both *S. sphagnicola* lineages in order to characterize the nature of their enigmatic red droplets.

MATERIAL AND METHODS

Investigated strains. The origin and sampling details of *Synura* strains used in this study are described in Škaloud et al. (2019). In addition, we further investigated four newly obtained strains: NIES 695, Hudong11291J2, K35 and M44 strains (for origin see Supplementary Table 1). All strains were cultured in 50 ml Erlenmeyer flasks filled with the MES buffered DY IV liquid medium (pH ≈ 6; Andersen et al. 2005), at 15 °C, under constant illumination of 40 μmol.m^{-2}.s^{-1} (TLD 18W/33 fluorescent lamps, Philips, Amsterdam, the Netherlands).

Sequencing and phylogenetic analysis. A total of seven molecular loci were sequenced for newly obtained strains: nuclear (nu) ITS rDNA, 18S rDNA, 26S rDNA, plastid (pt) 23S rDNA, rbcL, psaA, and mitochondrial (mt) coxI. DNA isolation and amplification was performed as described in Škaloud et al. (2020). Multiple alignments of above–mentioned loci sequences were constructed using MAFFT v6, applying the Q–INS–i strategy (Katoh et al. 2002). The positions with deletions prevailing in a majority of sequences were removed from the alignment. Two phylogenetic analyses were performed as follows.

First, a concatenated nu–18S rDNA, nu–26S rDNA, pt–23S rDNA, pt–rbcL and pt–psaA was prepared to infer the phylogeny of the genus *Synura*, using *Neotessella* as an outgroup (Supplementary Table 1). Prior to performing the concatenated phylogenetic analysis, maximum likelihood (ML) analyses were performed separately for each locus to verify there are no obvious topological incongruencies among the loci. The ML analyses were performed using RAxML 8.1.20, using the default GTR+Γ evolutionary model. Bootstrap analyses

were performed with the rapid bootstrapping procedure, using 100 pseudoreplicates. The analyses were shown to be highly congruent in statistically supported lineages (bootstraps >70). Accordingly, the concatenated analysis was performed on the partitioned alignment, separating all loci as well as three codon positions in protein–coding pt–rbcL and pt–psaA genes. Statistical significance of inferred phylogeny was further evaluated by maximum parsimony (MP) analysis and Bayesian inference (BI). The MP bootstrapping was performed using PAUP v.4.0b10 (Swofford 2003) by heuristic searches with 1000 random sequence addition replicates and random addition of sequences. The bootstrap support values were obtained from 100 pseudoreplicates, respectively. BI was performed using MrBayes v.3.2.6 (Ronquist et al. 2012), carried out on partitioned datasets applying the substitution models described in Škaloud et al. (2020). Two parallel MCMC runs were carried out for eight million generations, each with one cold and three heated chains. Convergence of the two cold chains was assessed during the run by calculating the average standard deviation of split frequencies (SDSF). The SDSF value between simultaneous runs was 0.0016.

Second, the species tree analysis was performed on *S. sphagnicola* nu–ITS rDNA, pt–psaA, and mt–coxI sequences, using the StarBEAST template in BEAST2 v.2.4.7 (Bouckaert et al. 2014). Eight haplotypes were defined in taxon set, including haplotypes sp1A, sp1B, sp1C, sp1D, sp2A, sp2B, sp2C described in Škaloud et al. (2019), and a newly recovered haplotype sp1E representing the strain NIES 695. MCMC analyses were run for 100 million generations, using the setting as described in Škaloud et al. (2019). To infer node divergence times, the clock rates for ITS rDNA (9.569×10^{-3}), psaA (2.571×10^{-3}) and coxI (4.962×10^{-2}) loci were specified based on fossil data estimations published by Škaloud et al. (2019).

The trees were analysed in DensiTree (Bouckaert 2010) and the trees showing the most likely tree topology were drawn, along with the consensus tree.

Morphological analyses of silica scales. The morphological analyses were based on seventeen cultures selected in both the lineage sp1 (nine cultures) and sp2 (ten cultures), respectively. The cultures were inoculated into fresh media, and after 4–5 weeks of cultivation they were examined with a JEOL 1011 transmission electron microscope. For each of these cultures, the five characters were measured in at least 30 randomly selected scales, as follows: (1) scale length, (2) scale width, (3) spine length, (4) spine width near its base, and (5) rim width. At the lower–most portion of the scale. The same characters were measured in figures illustrating the iconotypes of scales of *S. sphagnicola* and *S. bioretii* Huber–Pestalozzi in the papers of Korshikov (1927) and Huber–Pestalozzi (1941). Statistical analyses were performed in R 4.2.0 (R Core Team 2021). First, a Principal Component Analysis (PCA) was performed on 926 morphologically characterized scales, analysing all five measured morphological traits. Second, the PCA was performed on the same dataset of 926 scales supplemented by ten iconotypes of *S. sphagnicola* and *S. bioretii*. Since it was impossible to measure the exact dimensions of iconotype scales due to the absence of scale bars and rather illustrative nature of drawings, we analysed the three relative values only, as follows: (1) scale length to width ratio, (2) scale length to spine length ratio, (3) scale width to spine length ratio. The PCA ordinations were plotted using the vegan (Oksanen et al. 2020) and labdsv (Roberts 2019) packages in R. In addition, we performed a Linear Discriminant Analysis (LDA) using the MASS package

(VENABLES & RIPLEY 2002). All five measured morphological traits were analysed. The LDA scores were visualized using the ggplot2 (WICKHAM 2016) and ggridges (WILKE 2021) packages. The confusion matrix was then calculated to measure the performance of the model. This matrix reports the number of cases correctly and incorrectly assigned to each of the groups based on the discriminant analysis.

Ecological analyses. To test for ecological differentiation of particular sp1 and sp2 haplotypes, we obtained climatic data for 51 *S. sphagnicola* strains with known geographic origins and genotype affiliations (Supplementary Table 2). Altitude and 19 bioclimatic variables were obtained from the WorldClim database (HIJMANS et al. 2005) at resolution of 2.5 arc minutes to characterize the general climatic conditions. Seven physical and chemical soil properties (pH in water, cation exchange capacity, clay, silt and sand content, and organic carbon stock and content were obtained from the SoilGrids database (soilgrids. org) to characterize bedrock properties. Prior to the analysis, forward selection by redundancy analysis was used to reduce the number of predictors, using the ordiR2step function in vegan package in R. Finally, we performed the LDA analysis as described above, based on standardized variables.

Morphological and fluorescence analyses of cells. Cells of strains Hudong11291J2 (sp1) and M44 (sp2) were observed regularly under the Olympus BX51 light microscope equipped by Canon EOS 700D camera. The strains grown for three weeks were also observed for their fluorescent properties, using Olympus Provis AX70 microscope equipped by mercury lamp, an appropriate fluorescent block (U–MWU), and Nikon D3100 DSLR camera. Fluorescent micrographs contrasting was adjusted in Photoshop CS5. For better resolved emission spectra, we used an alpha300 RSA laser scanning confocal microscope (WITec, Germany) equipped with a 442 nm laser set to 10 µW power, Olympus UPlanFL N Oil 100x NA = 1.3 and spectrometer UHTS300S VIS with grating 600 g.mm⁻¹ set for spectral in situ stitching of emission spectra in the range of 445 to 800 nm averaging five measurements of 0.7 ms integration time. Data were analysed using WITec Project FIVE Plus v5.1 software.

Pigment extraction. Organic solvents for pigment extraction and HPLC analyses were obtained from Analytika (Czech Republic). All solutions were prepared using reverse–osmosis deionized water (Ultrapur, Watrex, Prague, Czech Republic). For the pigment analyses the *Synura* cells were removed from culture medium by centrifugation for 10 min at 4.500×g. The sediment was homogenized with glass beads in vortex and extracted twice at room temperature with 100% acetone for 15 min. The combined extracts were clarified using 0.2 µm nylon filters (Micro–spin centrifuge filter, Alltech, Deerfield, IL, USA). All other chemicals used were of analytical grade and were purchased from Sigma–Aldrich.

HPLC/DAD/MS. The extracts were analysed on a Dionex UltiMate 3000 UHPLC (Thermo Scientific, Sunnyvale, CA, USA) equipped with a diode array detector (DAD) and Impact HD high resolution mass spectrometer (Bruker, Billerica, Massachusetts, USA) with electrospray ionization source (ESI). The following settings of MS were used: drying temperature 250 ˚C; drying gas flow 12 l.min⁻¹; nebulizer gas pressure 4 bar; capillary voltage 4000 V; endplate offset 500 V. The spectra were collected in the range 20–2200 m.z⁻¹ with spectra rate of 3 Hz. Collision energy was 35 eV. Mass spectrometer was calibrated with sodium formate clusters and LockMass. Tuning Mix (622 Da) was used as the lockmass calibrant at the beginning of each analysis. The formulas of obtained molecular peaks and fragments were calculated using Smart Formula in Bruker Compass DataAnalysis software (version 4.2).

Pigments were separated using a modified method of VAN HEUKELEM & THOMAS (2001) on the Luna C8(2) 100 Å column (100 × 4.6 mm, 3 µm, Phenomenex) thermostated to 30 °C, with binary solvent system (0 min 100% A, 20 min 100% B, 25 min 100% B, 27 min 100% A, 30 min 100% A, where A is 80% methanol and B is 100% methanol). The solvent flow rate was 0.8 ml.min⁻¹. Injection volume was 20 µl. The identification of the carotenoids was performed, considering the combination of the following parameters: elution order on the reverse phase column, UV–vis spectrum features (maximum absorption wavelength (λ_{max}), spectral fine structure (%III/II) and peak cis intensity (%Ab/AII)), MS and MS/MS spectra characteristics and data available in the literature.

RESULTS

Phylogenetic analyses

Congruently with the analysis published by ŠKALOUD et al. (2019), *S. sphagnicola* strains were inferred to form two distinct, well–resolved sister clades, referred to as sp1 and sp2 (Fig. 1A). The split of these clades was estimated to 14.0 [5.6–29.8] Mya, which is similar to the estimate of 15.4 [8–25] Mya given by ŠKALOUD et al. (2019). The clades were separated by a long branch from the remaining *Synura* species of the section Curtispinae (*S. synuroidea*, *S. spinosa*, *S. curtispina*, and *S. longitubularis* Jo, Shin, Kim et Siver). The coalescence species tree analysis recovered the existence of eight haplotypes, five within the clade s1 and the remaining three within the clade s2 (Fig. 1B). The coalescence analysis was consistent with that published by ŠKALOUD et al. (2019) with the exception of recovering a novel haplotype sp1E representing the strain NIES 695 (Supplementary Table 1). The haplotypes were inferred to be evolutionary very young, with their age spanning from 20,000 to 80,000 years.

Morphological analyses of silica scales

The principal component analysis (PCA) of silica scales characteristics based on measurement of 17 strains clearly separated the sp1 and sp2 lineages (Fig. 2A). The lineages were morphologically well differentiated by most of the measured characters, namely scale length and width, rim width and spine length, which were correlated with the PC1 axis (Figs 2B–D). The linear discriminant analysis (LDA) also showed a clear separation of sp1 and sp2 lineages along the first LD axis (Fig. 2E). The accuracy of the model was 0.92, meaning that 92% of the scales were correctly assigned to the appropriate clade based on the morphological traits only.

To determine which of the two inferred lineages indeed represent *S. sphagnicola*, we further performed the PCA supplemented by *S. sphagnicola* scales
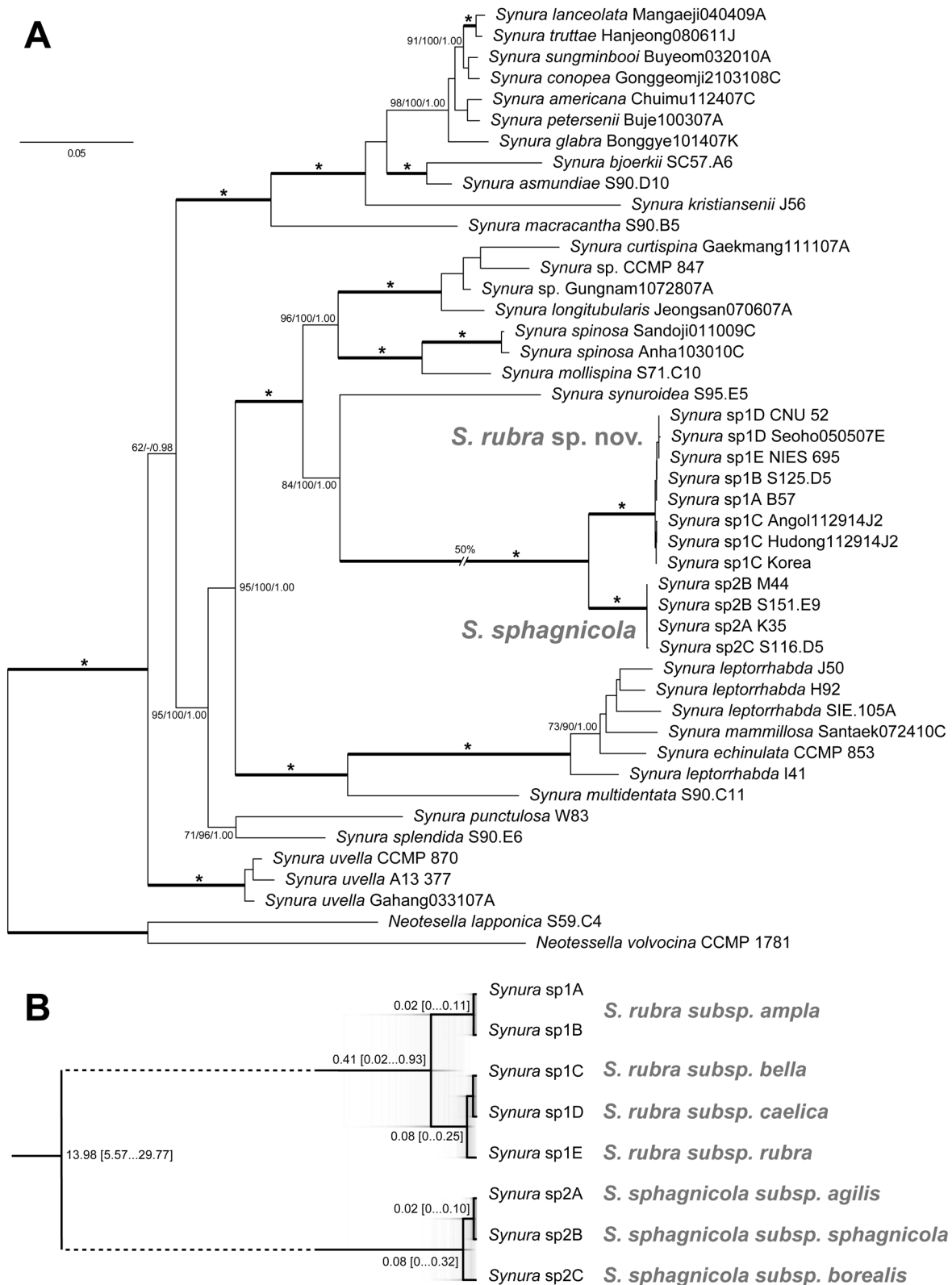
Fig. 1. Phylogenetic position and relationships of *S. sphagnicola* strains. (A) Phylogeny of the genus *Synura* based on concatenated nuclear 18S rDNA, 26S rDNA, and plastid 23S rDNA, rbcL, and psaA sequences; values at the nodes indicate statistical support estimated by three methods; MrBayes posterior node probability (left), maximum likelihood bootstrap (middle) and weighted maximum parsimony bootstrap (right); thick branches with asterisks highlight nodes receiving the highest statistical supports (1.00/100/100); scale bar represents the expected number of substitutions per site; (B) time–calibrated coalescence species tree with visualization of the consensus topology, based on ITS rDNA, psaA and coxI sequences; mean divergence times are given for selected nodes, along with 95% highest posterior density (HPD) values in square brackets.
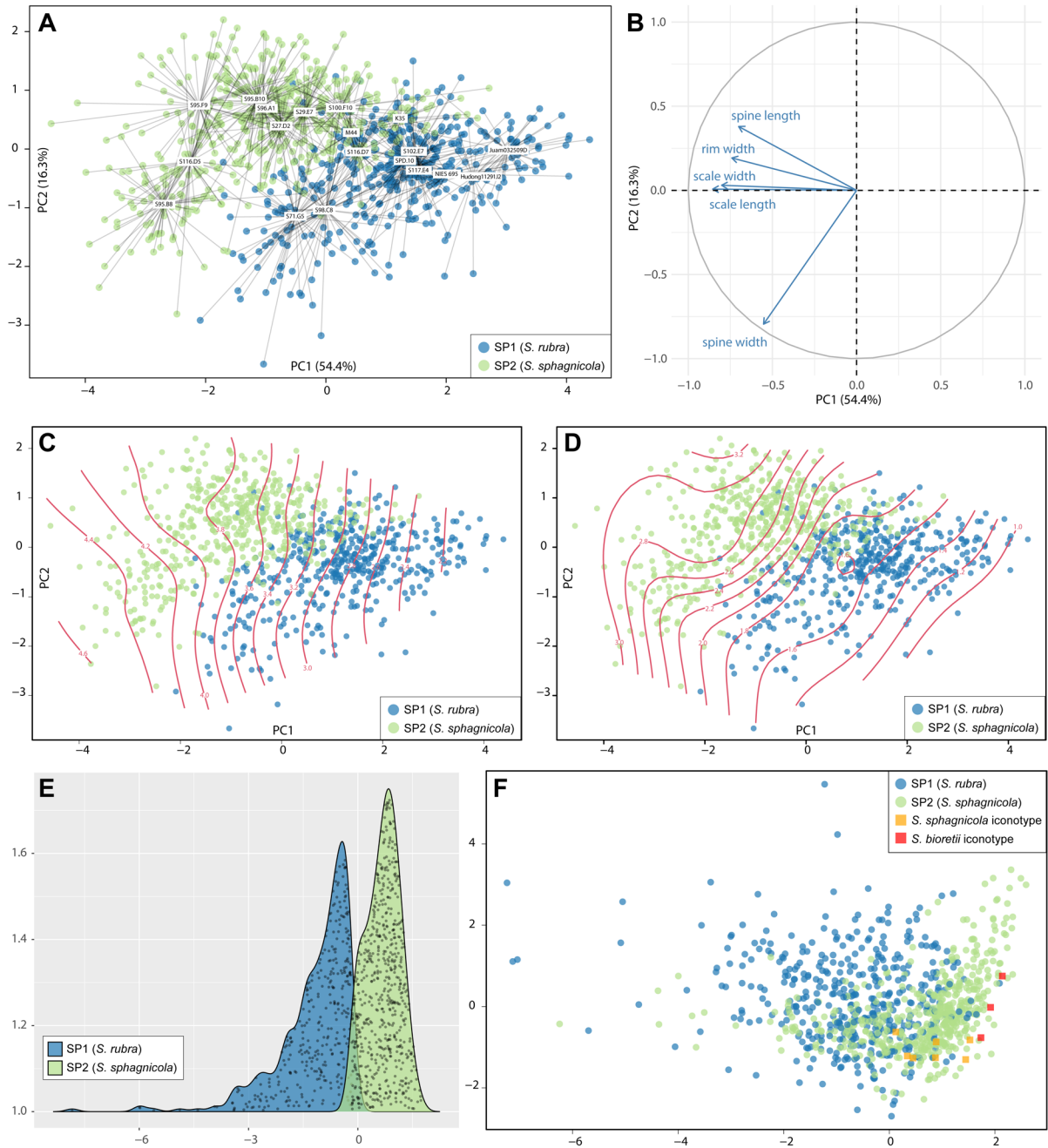
Fig. 2. Morphological analyses of silica scales. (A) principal component analysis (PCA) based on five morphological traits measured on 926 scales, showing differentiation of sp1 (*S. rubra*, sp. nov.) and sp2 (*S. sphagnicola*) lineages; the scales are clustered based on their affiliation to 17 investigated strains; (B) correlation of morphological variables with PCA axes; (C, D) contour plots showing the relationships between PCA scores and scale (C) and spine lengths (D); (E) linear discriminant analysis (LDA) showing morphological differentiation of lineages; (F) PCA analysis based on three morphological traits measured on 926 scales and ten iconotypes of *S. sphagnicola* and *S. bioretii*.

illustrated by Korshikov (1927) and representing the species iconotype. In addition, we included the originally illustrated scales of morphologically similar species *S. bioretii* (Huber–Pestalozzi 1941). The scales of both species were inferred to morphologically correspond to the lineage sp2 (Fig. 2F). Indeed, a classification matrix computed by LDA assigned all ten iconotype scales to the lineage sp2. The posterior probabilities for the lineage sp2 ranged 0.63–0.86 and 0.87–0.88 for *S. sphagnicola* and *S. bioretii*, respectively.

Ecological differentiation of haplotypes.

Most of the haplotypes within the sp1 and sp2 lineages were morphologically indistinguishable. However, with the exception of haplotypes sp1A and sp1B they clearly differ by climatic and bedrock preferences. Within the lineage sp1, mean diurnal range, maximum temperature of warmest month, annual precipitation, precipitation of wettest month and warmest quarter, altitude, and pH were identified as major drivers of haplotype differentiation (Fig. 3A). The accuracy of the LDA model was 0.83,
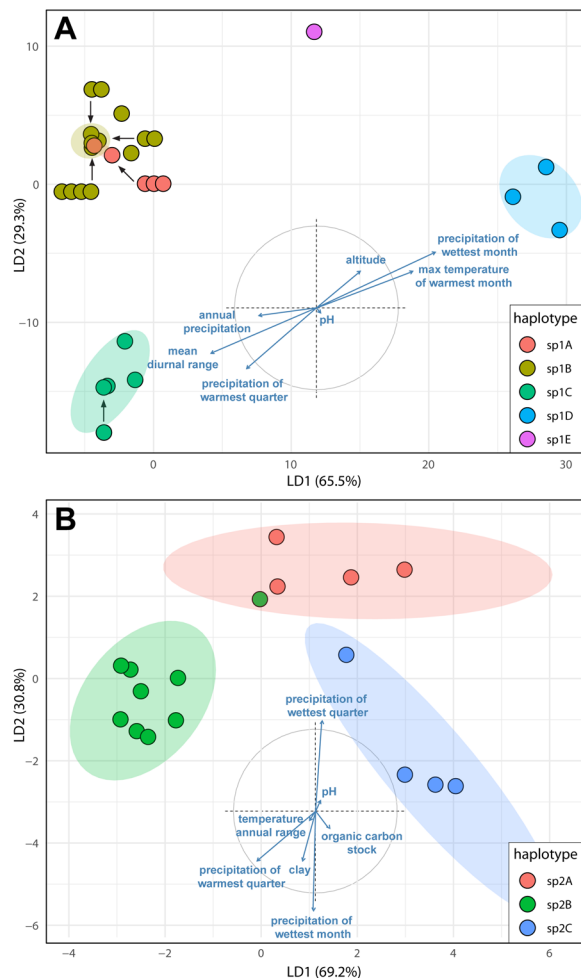
Fig. 3. Ecological differentiation of haplotypes. (A) LDA analysis of sp1 (*S. rubra*, sp. nov.) haplotypes based on seven ecological parameters selected by forward selection; (B) LDA analysis of sp2 (*S. sphagnicola*) haplotypes based on seven ecological parameters selected by forward selection; correlations of environmental variables with the first and second PCA axes are shown within the plots.

meaning that 83% of the strains were correctly assigned to the appropriate haplotype based on the climatic data. However, when treating the sp1A and sp1B as a single haplotype (sp1AB), the accuracy of the model increases to 1.00. Accordingly, all four haplotypes are well differentiated based on their ecology. Whereas the haplotype sp1AB occurs in dry environments, haplotype sp1E prefers much humid climate (Fig. 4A). The haplotypes sp1AB and sp1E also prefer more acidic localities (Fig. 4B). The haplotype 1C can be well differentiated by occurring in those environments showing high diurnal range (high differences between day and night temperatures; Fig. 4C). Similarly, the sp2 haplotypes clearly differentiated by their ecology. Temperature annual range, precipitation of wettest quarter, warmest month and wettest month, as well as pH, clay content and organic carbon stock were identified as major drivers of haplotype differentiation (Fig. 3B). The haplotype sp2B prefers those environments showing high temperature annual range (high differences between the hottest and the coldest months; Fig. 4D), as

well as habitats with lower organic carbon stock (Fig. 4E). The sp2C haplotype occurs in areas with lower temperature and higher precipitation in wettest months (Fig. 4F). The accuracy of the LDA model was 0.91.

Light microscopy

The colonies and cells of both sp1 and sp2 lineages shared a very similar morphology. Colonies of sp1 lineage were 29–34 μm in diameter, mostly composed of 8–16 cells (Fig. 5A). Cells were rounded, distinctly spiny, with rather small, pale green chloroplasts filling less than a half of the cell content. The storage products (probably chrysolaminaran (=chrysolaminarin, leucosin), HIBBERD 1978) were deposited in droplets in the posterior part of the cell. In the old cells, storage products could fill a high portion of the cell volume (Fig. 5B). Colonies of sp2 lineage were 32–40 μm in diameter, mostly composed of 8–16 cells (Fig. 5C). Cells were rounded, distinctly spiny, with pale green to brownish chloroplasts filling at least half of the cell content. Similar to sp1 lineage, the storage products were first deposited in droplets, filling a high portion of the cell volume (Fig. 5D). Cells of both lineages had two flagella of almost equal length, one of them having a distinct undulating appearance (Figs 5E, G). The most prominent feature of both lineages was the presence of distinct red or red–violet droplets, first occurring at the apical part of the cell (Fig. 5F), later on produced beneath the entire cell membrane (Fig. 5H).

Fluorescence of *Synura* cells

Under fluorescence microscope using UV excitation, we detected (i) blue autofluorescence of some enigmatic droplets and/or diffusively present in the cytoplasm, (ii) green autofluorescence of the flagellum, (iii) red autofluorescence of plastids and (iv) rather inconspicuous dark red autofluorescence of red droplets, that changed over the course of observation towards orange–yellow (Figs 5I–L). To address the spectral properties of autofluorescence in *Synura*, their emission spectra were measured by a laser scanning confocal microscope with 442 nm laser excitation in situ that limited the observation of the blue autofluorescence (Figs 5M, N). The spectra of sp1 and sp2 lineages were highly congruent. First, green autofluorescence of the narrow, not undulating flagellum was observed in both lineages and in both cases with the prominent flagellar swelling supposedly acting in photoreception and phototaxis. The relatively less intense green fluorescence of flagella peaked between 490 and 500 nm. Second, in both lineages, the strongest fluorescence emission was detected between 660 and 720 nm corresponding to chlorophyll. Third, the dark red fluorescence appearing in red droplets was caused by its low intensity rather than an emission wavelength clearly distinguishable from the plastids, showing wide emission spectra ranging from 580 to 710 nm (expressed as the full width at half–maximum) with a peak in 640 nm.

Table 1. Identification of major pigments present in *Synura* strains.

t_R [min.]	Pigment	Absorption maxima [nm]	$[M+H]^+$	Fragments
			967	653, 339
5.0	**unknown pigment**	292, **494-500**	983	669, 355
			999	685, 371
6.7	Chlorophyll–c$_2$	**449**, 582, 635	**609,2718**	591.2624, 549.1838
9.4	Fucoxantin	**450**	**659,4349**	641.4265, 623.4127, 581.4021, 563.3923
10.6	Neoxanthin	416, **440**, 468	**601,4189**	583.4588, 565.4195, 509.3618
11.7	cis-Fucoxantin	**334**, **442**	**659,4352**	641.4246, 623.4130, 581.4018, 563.3967
12.7	Unknown carotenoid	422, 446, 472	601,4277	–
14.5	Zeaxantin	**452**, 476	**569,4344**	551.5106, 489.3749, 477.3748, 416.4050
20.4	Chlorophyll–a	**432**, **666**	**893,5469**	614.2410, 583.2214, 555.2273, 481.1904
22.2	Phaeophytin–a	**410**, 508, 538, 608, **666**	**871,5767**	593.2787, 533.2575
23.3	β-Carotene	**450**, 474	**537,4481**	457.3897, 413.3222

Pigment composition

The lineages sp1 and sp2 showed highly congruent elution profiles of the pigments, though their relative abundances significantly differed (Fig. 6). Identification of the individual pigments is given in the Table 1. Fucoxanthin with retention time (Rt) = 9.4 min represented the dominant pigment of the lineage sp1. Interestingly, in the lineage sp2 fucoxanthin was overrepresented by so far unknown pigment with Rt = 5.0 min. This pigment was detected in the lineage sp1, as well, however, in a much lower abundance. Other pigments detected include chlorophyll–c$_2$ (Rt = 6.7 min), neoxanthin (Rt = 10.6 min.), cis–fucoxanthin (Rt = 11.7 min), zeaxanthin (Rt = 14.5 min), chlorophyll–a (Rt = 20.4 min), and β–carotene (Rt = 23.3 min).

DISCUSSION

Taxonomic consequences

Synura sphagnicola represents a unique example of cryptic diversity in protists, occurring at two evolutionary levels. First, two evolutionary older lineages, here referred to as sp1 and sp2, evolved approximately 14 million years ago. Here, we pointed out that these lineages can be morphologically differentiated by detailed analyses of silica scales, in particular by scale dimensions and spine length (Figs 2B, D). Second, several very young genotypes were detected in both lineages, diverging 20,000 to 80,000 years ago. Since all but one genotypes clearly differ ecologically (Figs 3, 4) and in their distribution pattern (ŠKALOUD et al 2019), we hypothesise they represent very young, incipient species–level lineages. Contrary to evolutionary older cryptic species of microalgae, reports on much recent species divergences are extremely scarce (LOGARES et al. 2007; ANNENKOVA et al. 2015), apparently due to the absence of any distinguishing morphological traits. Nevertheless, in the case of ecologically differentiated *S. sphagnicola* genotypes, the above data lead us to believe that these are young but already fully differentiated species that arose during the last glaciation period due to adaptation to various climatic oscillations (HEWITT 2000) or due to differences in their geographical distribution. To distinguish between these two evolutionary levels of speciation, we propose here to describe evolutionary older lineages as two separate species, while more recently evolved, ecologically distinct genotypes as their subspecies. With the exception of ecologically identical genotypes sp1A and sp1B considered here as a single subspecies, the ecological distinction of all other genotypes warrants their recognition as separate subspecies.

Prior to formal description of selected evolutionary older lineage as a new species, it is necessary to i) identify which of two lineages represents *S. sphagnicola*, and ii) check if the second lineage corresponds to any previously described species. A total of five *Synura* species are known to produce red droplets in the cytoplasm: *S. curtispina*, *S. spinosa*, *S. synuroidea*, *S. sphagnicola*, and *S. bioretii*. Only the last species remains to be characterized genetically. Based on the morphometric analyses of species' iconotypes (Fig. 2F), both *S. sphagnicola* and *S. bioretii* morphologically correspond to the lineage sp2. Since *S. bioretii* was described after the description of *S. sphagnicola*, the former represents a junior synonym of the latter. The
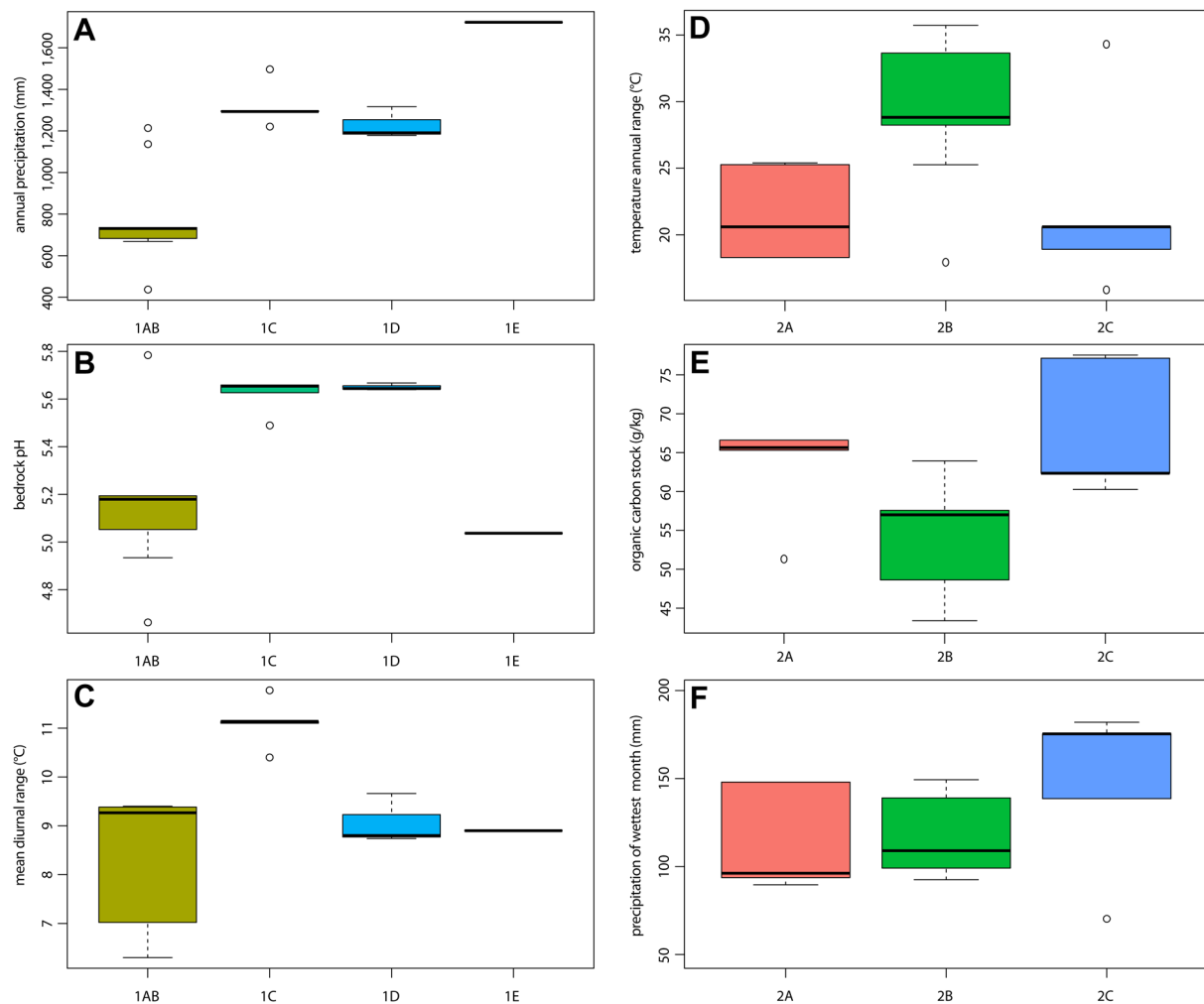
Fig. 4. Ecological preferences of *Synura* haplotypes. (A–C) Differences in the distribution of four sp1 (*S. rubra* sp. nov.) haplotypes along the gradients of (A) annual precipitation (BIO12), (B) bedrock pH, and (C) mean diurnal range (BIO2); (D–F) differences in the distribution of four sp2 (*S. sphagnicola*) haplotypes along the gradients of (D) temperature annual range (BIO7), (E) organic carbon stock, and (F) precipitation of wettest month (BIO13).

sp1 lineage then represents a new, undescribed species, proposed here as *Synura rubra* sp. nov. (see Taxonomic revisions and diagnoses below).

Autofluorescence in *Synura* cells

The enigmatic blue autofluorescence may correspond to multiple cellular compartments and/or substrates, and its exact composition is therefore difficult to address. Based on the literature, blue autofluorescence is a distinct feature of compounds possessing conjugated systems of double bounds or aromatic rings in their structures under UV excitation, i.e., pyridine nucleotides (e.g., nicotine–amide–adenine–dinucleotide (phosphate)), pterins, phenolics (e.g., flavones, coumarins etc.), alkaloids, tyrosine oxidation products, amyloid and non–amyloid protein aggregates etc. (Huang et al. 2002; Roschina 2012; Fricano et al. 2019; Donaldson 2020).

Green autofluorescence of the short (posterior) flagellum is a common feature in brown and golden algae and has been previously well documented in *Synura*

petersenii and *S. synuroidea* (= *Chrysodidymus synuroideus*; Kawai 1988; Graham et al. 1993). Maximum intensity of autofluorescence is concentrated on the base of the flagellum. Here is a swelling that is considered to be a photoreceptive site for phototaxis (Kreimer 1994). The fluorescent flagellar substance was attributed to flavin(s) in the flavoprotein (Fujita et al. 2005). We observed autofluorescence throughout the flagellum (Figs 5J, L), however, our repetitive examination of several *S. sphagnicola* strains revealed its fluctuating character. In some cells, and especially in these from old cultures, the green autofluorescence was weak or even absent. We recognized that its absence relates to the formation of palmelloid stages where cells lose their flagella.

Fluorescence pattern of plastids containing the complex mixture of photosynthetic pigments of chlorophyll–a and c together with carotenoids correspond to emission spectra reported elsewhere (Silkina et al. 2009).
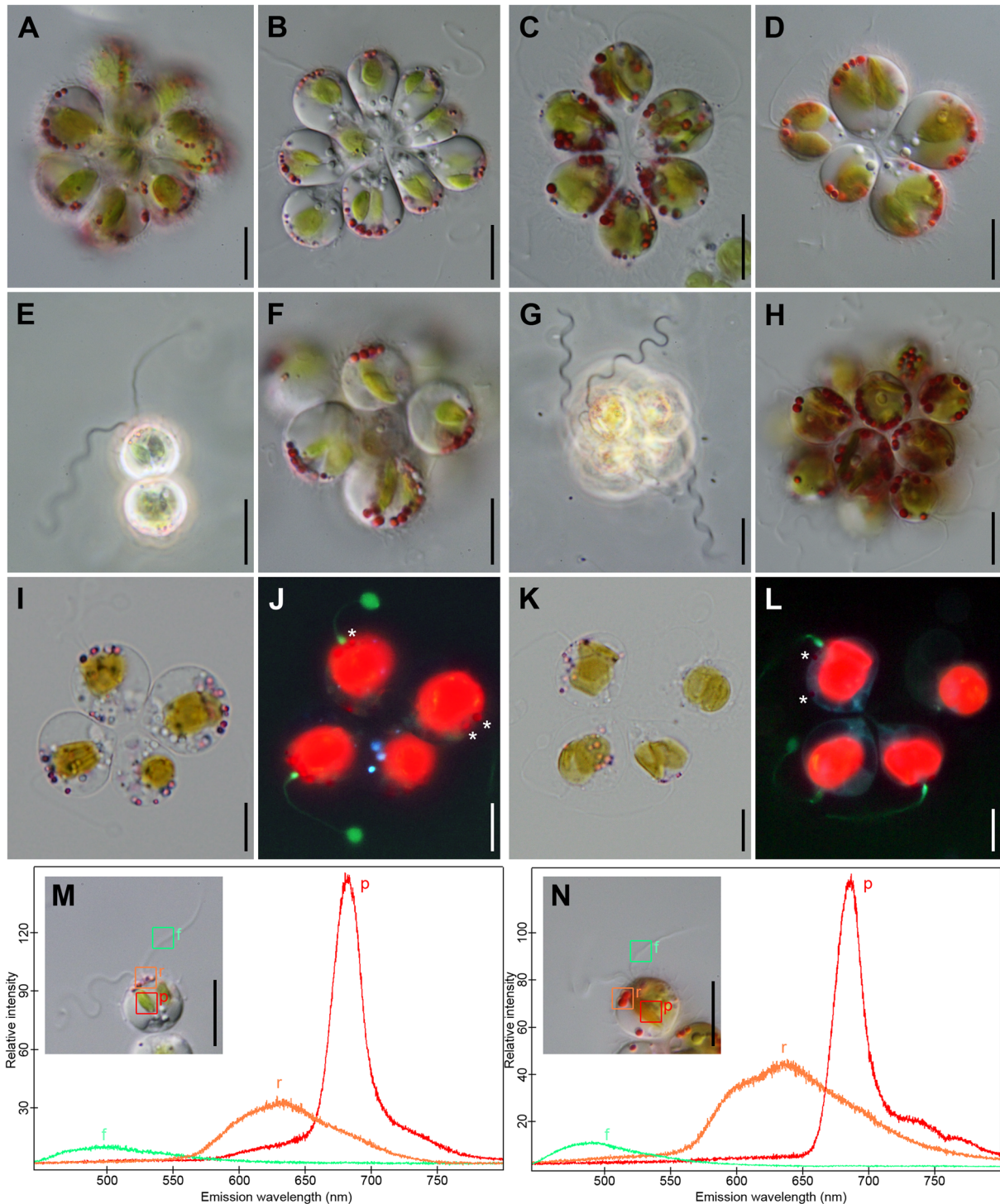
Fig. 5. Light microscopy and autofluorescence. (A–H) Morphology of colonies (A, B, E, F – sp1: *S. rubra*, sp. nov., C, D, G, H – sp2: *S. sphagnicola*); note typical Stramenopile flagella in E, G visualized by phase contrast; (I–L) light and autofluorescence pictures of four–celled colonies (I, J – sp1: *S. rubra*, sp. nov., K, L – sp2: *S. sphagnicola*); (M–N) autofluorescence emission spectra of plastids (in red), red droplets (in orange) and flagella (in green); investigated cells are shown in insets, showing the measured areas by squares of corresponding colours (M – sp1: *S. rubra*, sp. nov., N – sp2: *S. sphagnicola*). Scale bars represent 10 μm.

Pigment composition

The carotenoid composition found in *Synura sphagnicola* and *S. rubra* sp. nov. was typical of chrysophytes: fucoxanthin as the predominant carotenoid, and neoxanthin, zeaxanthin and b–carotene as minor carotenoids (WHITERS et al. 1981). Surprisingly, chlorophyll –c_1 was not detectable both in *Synura sphagnicola* and *S. rubra* sp. nov., and chlorophyll–c_2 was identified in *S. sphagnicola*. According to ANDERSEN & MULKEY (1983) chlorophyll–c_2 is missing in the genera *Synura* and *Mallomonas* Perty, where it is replaced by chlorophyll– c_1. Indeed, the lack of chlorophyll–c_2 was mentioned among major distinguishing
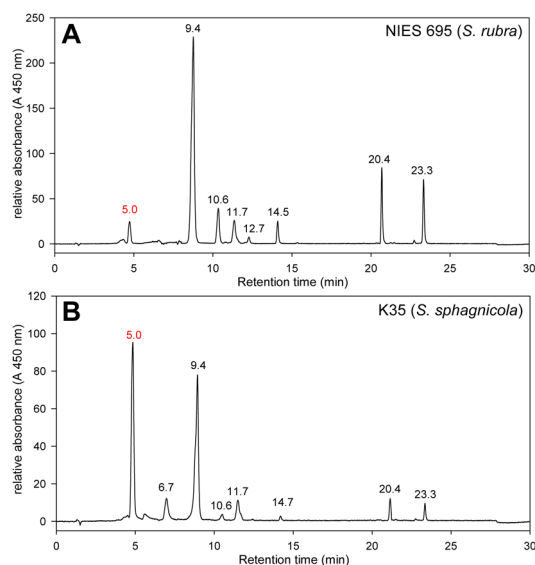
Fig. 6. Elution profiles of pigments extracted from cells of (A) sp1 (*S. rubra*, sp. nov.) and (B) sp2 (*S. sphagnicola*) lineages. Individual pigments are labelled by retention times (Rt). An unknown pigment with Rt = 5.0 is given in red colour.

characters to discriminate between classes Synurophyceae and Chrysophyceae (ANDERSEN 1987; 2010). However, FAWLEY (1989) found a new chlorophyll–c_2–like pigment in one culture of *S. petersenii.* Later on, with the development of more sensitive HPLC methods a new chlorophyll–c diversity was found in several groups of algae, including three chrysophyte species (ZAPATA et al. 2006). Interestingly, these authors already reported the presence of chlorophyll–c_2 in *S. sphagnicola*, in addition to a novel chlorophyll–c_2–like pigment of *Pavlova gyrans* type (ZAPATA et al. 2006). Finally, BOENIGK et al. (2023) recently reported the presence of chlorophyll– c_2 in five *Mallomonas* and four *Synura* taxa investigated. Accordingly, the pigment composition can no longer be used to define Synurophyceae. In addition, several recently published phylogenies show Synurophyceae to be nested within Chrysophyceae and referred to as the order Synurales Andersen (e.g., DEL CAMPO & MASSANA 2011; YANG et al. 2012; ŠKALOUD et al. 2013; SCOBLE & CAVALIER–SMITH 2014; KRISTIANSEN & ŠKALOUD 2017). Since there is no justification to recognize Synurales as a separate class Synurophyceae, we formally synonymize it with Chrysophyceae (see Taxonomic revisions and diagnoses below).

One of the most interesting results of pigment composition analysis is the discovery of the unknown pigment with Rt = 5.0 min. Since this pigment was dominant in the strain K35 characterized by a significant production of red droplets, we propose that the red droplets are formed from this newly recognized pigment. Various algae are known to produce red–coloured pigments (GRUNG & LIAAEN–JENSEN 1993; FRASSANITO 2006; LEMOINE & SCHOEFS 2010; LIU et al. 2014) including the industrially relevant species *Haematococcus pluvialis* used for

aquaculture and cosmetics industries (BUBRICK 1991; LORENZ & CYSEWSKI 2000; TOMINAGA et al. 2012). In all above mentioned cases this pigment is astaxanthin, a pigment that belongs to the family of the xanthophylls, the oxygenated derivatives of carotenoids. However, we did not detect astaxanthin in either of the investigated strains. Astaxanthin is reported to have a peak emission at ~675 nm (OTA et al. 2018), which is not in the range of the red droplets emission spectra we documented (630–640 nm; Fig. 5). Further characterization of this compound using other methods is still underway.

TAXONOMIC REVISIONS AND DIAGNOSES

Chrysophyceae Pascher
Synonym: Synurophyceae ANDERSEN 1987; Am. J. Bot. 74(3): 338.
**Description**: Unicellular or colonial organisms with cells naked or surrounded by an envelope (cell wall, lorica, silica scales). Swarmers with two unequal flagella and contractile vacuoles. Longer flagellum hairy, shorter smooth. Cells can contain chloroplast derived from a red alga, with chlorophylls a, c_1 and/or c_2, but lacking chlorophyll–b. Fucoxanthin is the most important accessory pigment. Storage product β–1,3–glucan (chrysolaminaran). Known to form endogenous silicified cysts (statospores, stomatocysts) which are common in many geological deposits.

Synura rubra Škaloud, Škaloudová et Jadrná sp. nov.
Description: Colonies are spherical, 29–34 μm in diameter, mostly composed of 8–16 cells. Cells are rounded, posteriorly tapering into the tail, 6–15(–17) μm in diameter. They possess pale green chloroplasts filling less than a half of the cell content, translucent droplets, and distinct red or red–violet droplets produced beneath the cell membrane. Each cell is surrounded by a distinct layer of spiny siliceous scales. Body scales are 2.5–5.3 μm long (mean 3.4 μm) and 1.7–3.3 μm wide (mean 2.4 μm), consisting of a basal plate with a spine. The basal plate is perforated by numerous pores and possess a posterior thickened rim encircling half to two–thirds of the scale perimeter, 0.1–0.4 μm in width. Spine is 0.8–2.6 μm long (mean 1.6 μm) and 0.1–0.5 μm wide (mean 0.3 μm), with distal end rounded or bearing two small teeth on the tip. Tubular scales are linear or slightly bent, up to 6.2 μm in length.

Etymology: The name refers to the reddish colour of the cells caused by the production of red pigment.
Holotype (here designated): Portion of a single gathering of cells on TEM grid NIES 695, deposited at the Culture Collection of Algae of Charles University in Prague, Czech Republic (CAUP). Fig. 7A is a representative scale from the specimen.
Strain information: The live culture of the holotype is deposited as NIES 695 at the Microbial Culture

Collection at the National Institute for Environmental Studies, Tsukuba, Japan.
Type locality: Miyatoko Mire, Fukushima, Japan (37°15'2.1" N, 139°33'56.3" E).

Synura rubra subsp. *rubra* (genotype sp1E, Figs 7A, B)
Description: Colonies are spherical, composed of rounded cells posteriorly tapering into the tail. Cells surrounded by a distinct layer of spiny siliceous scales. Body scales are 2.0–2.8 μm long and 1.5–2.5 μm wide, consisting of a basal plate with a spine. A basal perforated plate strengthened by a posterior rim, 0.1–0.4 μm in width. Spine is 0.5–1.9 μm long and 0.2–0.4 μm wide.

Distribution: So far known only from Japan.
Ecology: Prefers humid climate (annual precipitation ~ 1.700 mm.year⁻¹) and more acidic habitats (pH ~ 5.0).

Synura rubra subsp. *ampla* **Škaloud, Škaloudová et Jadrná subsp. nov. (genotype sp1AB, Figs 7C, D)**
Description: Colonies are spherical, composed of rounded cells posteriorly tapering into the tail. Cells surrounded by a distinct layer of spiny siliceous scales. Body scales are 2.5–5.3 μm long and 1.9–3.3 μm wide, consisting of a basal plate with a spine. A basal perforated plate strengthened by a posterior rim, 0.1–0.3 μm in width. Spine is 0.8–2.4 μm long and 0.1–0.5 μm wide.

Etymology: The name "ampla" (Latin), meaning wide or common, is used as an adjective in reference to the common occurrence of this subspecies.
Holotype (here designated): Portion of a single gathering of cells on TEM grid S71.G5, deposited at the Culture Collection of Algae of Charles University in Prague, Czech Republic (CAUP). Fig. 7C is a representative scale from the specimen.
Type locality: Borkovická blata, Czech Republic (49°14'8" N, 14°37'25.2" E).
Distribution: Restricted to Europe (Czech Republic, Sweden, United Kingdom, Ireland).
Ecology: Prefers drier climate (annual precipitation ~ 700–900(–1300) mm.year⁻¹) and more acidic habitats (pH ~ 5.0–5.2).

Synura rubra subsp. *bella* **Škaloud, Škaloudová et Jadrná subsp. nov. (genotype sp1C, Figs 7E, F)**
Description: Colonies are spherical, composed of rounded cells posteriorly tapering into the tail. Cells surrounded by a distinct layer of spiny siliceous scales. Body scales are 2.0–3.0 μm long and 1.3–2.0 μm wide, consisting of a basal plate with a spine. A basal perforated plate strengthened by a posterior rim, 0.1–0.3 μm in width. Spine is 0.9–2.3 μm long and 0.2–0.3 μm wide.

Etymology: The name "bella" (Latin), meaning pretty or lovely, is used as an adjective in reference to the beautiful coloration of this subspecies.
Holotype (here designated): Portion of a single gathering

of cells on TEM grid Juam032509D, deposited at the Culture Collection of Algae of Charles University in Prague, Czech Republic (CAUP Fig. 7E is a representative scale from the specimen.
Type locality: Dam Juam, Juam–myeon, Korea (34°59'21.5" N, 127°13'43.1" E).
Distribution: So far known only from South Korea.
Ecology: Prefers less acidic habitats (pH ~ 5.6) and environments showing high differences between day and night temperatures (mean diurnal range ~ 11 °C).

Synura rubra subsp. *caelica* **Škaloud, Škaloudová et Jadrná subsp. nov. (genotype sp1D, Figs 7G, H)**
Description: Colonies are spherical, composed of rounded cells posteriorly tapering into the tail. Cells surrounded by a distinct layer of spiny siliceous scales. Body scales are 2.2–3.0 μm long and 1.7–2.4 μm wide, consisting of a basal plate with a spine. A basal perforated plate strengthened by a posterior rim, 0.1–0.3 μm in width. Spine is 0.7–2.3 μm long and 0.2–0.4 μm wide.

Etymology: The name "caelica" (Latin), meaning heavenly or magnificent, is used as an adjective in reference to the splendid appearance of this subspecies.
Holotype (here designated): Portion of a single gathering of cells on TEM grid CNU52, deposited at the Culture Collection of Algae of Charles University in Prague, Czech Republic (CAUP). Fig. 7G is a representative scale from the specimen.
Type locality: Beseokje, Gochang–gun, Korea (35°21'20.7" N, 126°33'27.4" E).
Distribution: So far known only from South Korea.
Ecology: Prefers less acidic habitats (pH ~ 5.6) and environments showing smaller differences between day and night temperatures (mean diurnal range ~ 7–9 °C).

Synura sphagnicola (Korshikov) Korshikov
Synonym: *Synura bioretii* HUBER–PESTALOZZI 1941; Das Phytoplankton des Susswassers. 2,1: 141, Fig. 197 (as '*bioreti*').
Description: Colonies are spherical, 32–40 μm in diameter, mostly composed of 8–16 cells. Cells are rounded, posteriorly tapering into the tail, 10–17(–18) μm in diameter. They possess pale green to brownish chloroplasts filling at least half of the cell content, translucent droplets, and distinct red or red–violet droplets produced beneath the cell membrane. Each cell is surrounded by a distinct layer of spiny siliceous scales. Body scales are 2.4–4.8 μm long (mean 3.8 μm) and 1.9–4.0 μm wide (mean 2.8 μm), consisting of a basal plate with a spine. The basal plate is perforated by numerous pores and possess a posterior thickened rim encircling half to two–thirds of the scale perimeter, 0.1–0.6 μm in width. Spine is 0.8–4.1 μm long (mean 2.6 μm) and 0.1–0.6 μm wide (mean 0.3 μm), with a blunt distal end bearing 2–3, rarely 4 small teeth. Tubular scales present.

Type locality: Peat bogs near Zvenigorod, Russia (~ 55°41'56" N, 36°43'23" E).
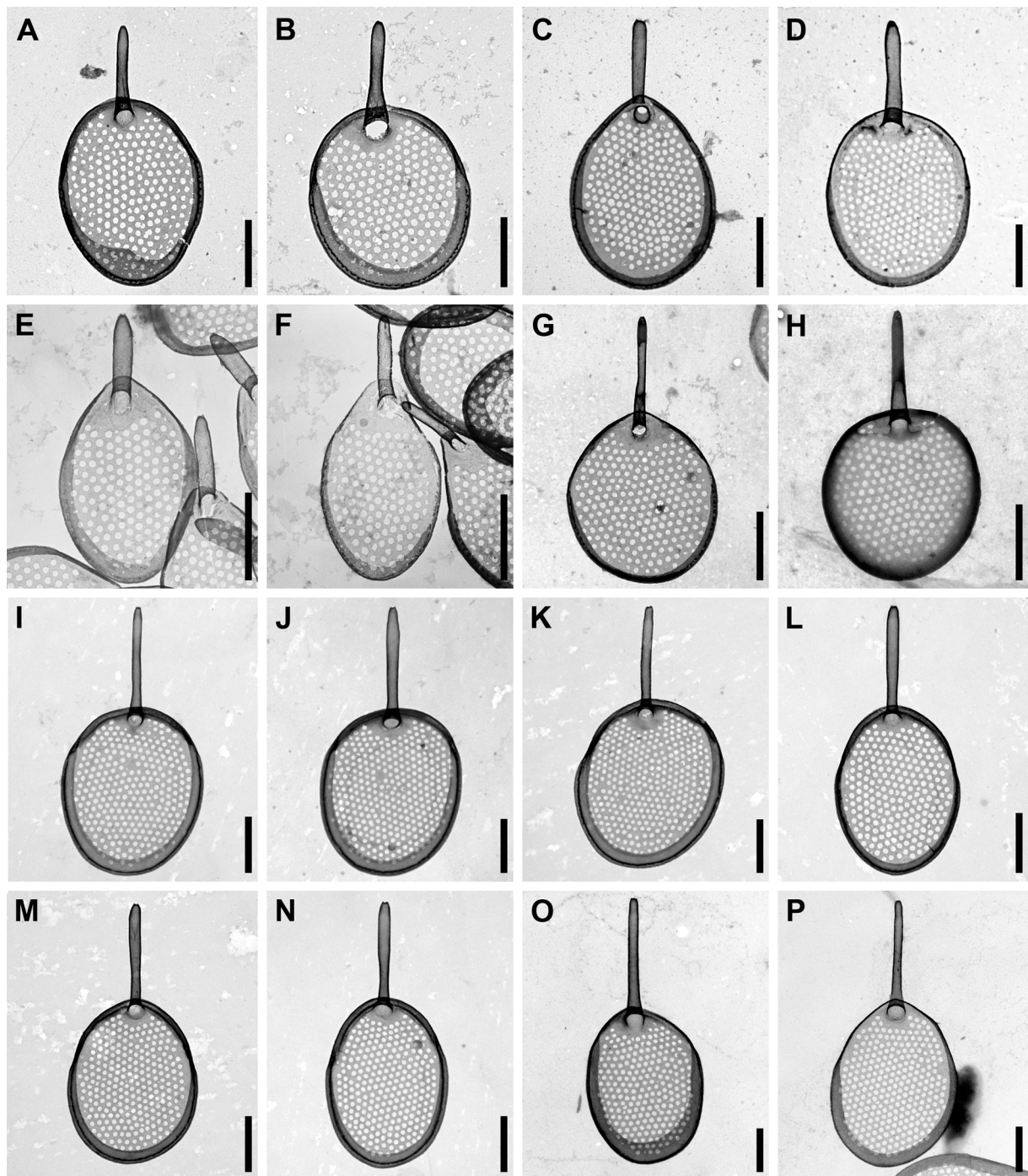
Fig. 7. Morphology of silica scales. (A–H) sp1: *S. rubra*, sp. nov.; (I–P) sp2: *S. sphagnicola*. (A–B) *S. rubra* subsp. *rubra* (strain NIES 695); (C–D) *Synura rubra* subsp. *ampla* (strains S71.G5 and S117.E4); (E–F) *Synura rubra* subsp. *bella* (strain Juam032509D); (G–H) *Synura rubra* subsp. *caelica* (strain CNU52); (I–K) *Synura sphagnicola* subsp. *sphagnicola* (strain M44); (L–N) *Synura sphagnicola* subsp. *agilis* (strain K35); (O–P) *Synura sphagnicola* subsp. *borealis* (strain S95.F9). Scale bars represent 1 μm.

Synura sphagnicola subsp. *sphagnicola* (genotype sp2B, Figs 7I–K)

Description: Colonies are spherical, composed of rounded cells posteriorly tapering into the tail. Cells surrounded by a distinct layer of spiny siliceous scales. Body scales are 2.8–3.4 μm long and 2.1–2.8 μm wide, consisting of a basal plate with a spine. A basal perforated plate strengthened by a posterior rim, 0.2–0.4 μm in width. Spine is 1.5–2.4 μm long and 0.2–0.3 μm wide.

Distribution: Czech Republic, Norway, Canada, Russia.
Ecology: Prefers environments showing high differences between the hottest and the coldest months (temperature annual range ~ 28–35 °C) and habitats with low organic carbon stock (~ 50–58 g.kg⁻¹).

***Synura sphagnicola* subsp. *agilis* Škaloud, Škaloudová et Jadrná subsp. nov. (genotype sp2A, Figs 7L–N)**
Description: Colonies are spherical, composed of rounded cells posteriorly tapering into the tail. Cells surrounded by a distinct layer of spiny siliceous scales. Body scales are 2.6–4.8 µm long and 1.9–4.0 µm wide, consisting of a basal plate with a spine. A basal perforated plate strengthened by a posterior rim, 0.1–0.6 µm in width. Spine is 1.3–2.9 µm long and 0.2–0.5 µm wide.

Etymology: The name "agilis" (Latin), meaning agile or moving, is used as an adjective in reference to its swimming motion.
Holotype (here designated): Portion of a single gathering of cells on TEM grid K35, deposited at the Culture Collection of Algae of Charles University in Prague, Czech Republic (CAUP). Fig. 7L is a representative scale from the specimen.
Type locality: Jizerské hory, Czech Republic (50°50'14.2" N, 15°14'45.8" E).
Distribution: Czech Republic, United Kingdom.
Ecology: Occurred in moderately humid climate (annual precipitation ~ 800–1,200 mm, precipitation of wettest month ~ 100–150 mm.year^{-1}) and habitats with high organic carbon stock (~ 65 g.kg^{-1}).

***Synura sphagnicola* subsp. *borealis* Škaloud, Škaloudová et Jadrná subsp. nov. (genotype sp2C, Figs 7O, P)**
Description: Colonies are spherical, composed of rounded cells posteriorly tapering into the tail. Cells surrounded by a distinct layer of spiny siliceous scales. Body scales are 3.4–4.8 µm long and 2.1–3.8 µm wide, consisting of a basal plate with a spine. A basal perforated plate strengthened by a posterior rim, 0.2–0.6 µm in width. Spine is 1.7–4.1 µm long and 0.2–0.6 µm wide.

Etymology: The name "borealis" (Latin), meaning northern, is used as an adjective in reference to the presence of this subspecies in Northern Europe.
Holotype (here designated): Portion of a single gathering of cells on TEM grid S95.F9, deposited at the Culture Collection of Algae of Charles University in Prague, Czech Republic (CAUP). Fig. 7O is a representative scale from the specimen.
Type locality: Loch Carrie, Scotland, United Kingdom (57°21'32.6" N, 4°52'46.3" W).
Distribution: Sweden, Norway, United Kingdom.
Ecology: Prefers more humid climate (annual precipitation ~ 1,200–1,500 mm, precipitation of wettest month ~ 150–180 mm.year^{-1}) and habitats with high organic carbon stock (~ 60–80 g/kg).

References
Andersen, R.A. (1987): Synurophyceae classis nov., a new class of algae. – American Journal of Botany 74: 337–353.
Andersen, R.A. (2010): Chapter 11. Chrysophyta. – In: Algae: Source to Treatment. AWWA Manual M57. – pp. 249–270, American Water Works Association, Denver.
Andersen, R.A.; Berges, J.; Harirson, P. & Watanabe, M. (2005): Appendix A – recipes for freshwater and seawater media. – In: Andersen, R. A. (ed.) Algal Culturing Techniques, – pp. 429–538, Elsevier, Amsterdam, the Netherlands.
Andersen, R.A. & Mulkey, T.J. (1983): The occurrence of chlorophylls c₁ and c₂ in the Chrysophyceae. – Journal of Phycology 19: 289–294.
Annenkova, N.V.; Hansen, G.; Moestrup, Ø. & Rengefors, K. (2015): Recent radiation in a marine and freshwater dinoflagellate species flock. – ISME Journal 9: 1821–1834.
Boenigk, J., Beisser, D., Franke, L., Klar, L., Ilić, M. & Fink, P. (2023): Differences in pigment composition and concentration between phototrophic, mixotrophic and heterotrophic Chrysophyceae. – Fottea (this issue). DOI: 10.5507/fot.2023.001
Bouckaert, R.R. (2010): DensiTree making sense of sets of phylogenetic trees. – Bioinformatics 26 (10): 1372–1373.
Bouckaert, R.; Heled, J.; Kühnert, D; Vaughan, T.; Wu, C.H.; Xie, D.; Suchard, M.A.; Rambaut, A. & Drummond, A.J. (2014): BEAST 2: A Software Platform for Bayesian Evolutionary Analysis. – PLOS Computational Biology 10(4): e1003537.
Bubrick, P. (1991): Production of astaxanthin from *Haematococcus*. – Bioresource Technology 38: 237–239.
del Campo, J. & Massana, R. (2011): Emerging diversity within chrysophytes, choanoflagellates and bicosoecids based on molecular surveys. – Protist 162(3): 435–48.
Conrad, W. (1939): Notes Protistologiques. VIII. *Synura sphagnicola* Korsch. en Belgique. – Bull. Inst. r. Sci. nat. Belq. 15(4): 1–4.
Donaldson, L. (2020): Autofluorescence in plants. – Molecules 25(10): 1–20.
Fawley, M.W. (1989): A new form of chlorophyll c involved in light–harvesting. – Plant Physiology 91: 727–732.
Frassanito, R.; Flaim, G.; Mancini, I. & Guella, G. (2006): High production of unexpected carotenoids in Dinophyceae. Astaxanthin esters from the freshwater dinoflagellate *Tovellia sanguinea*. – Biochemical Systematics and Ecology 34: 843–853.
Fricano, A.; Librizzi, F.; Rao, E.; Alfano, C. & Vetri, V. (2019): Blue autofluorescence in protein aggregates "lighted on" by UV induced oxidation. – Biochimica et Biophysica Acta (BBA) – Proteins and Proteomics 1867(11): 1–10.
Fujita, S.; Iseki, M.; Yoshikawa, S.; Makino, Y.; Watanabe, M.; Motomura, T.; Kawai, H. & Murakami, A. (2005): Identificationand characterization of a fluorescent flagellar protein from the brown alga *Scytosiphon lomentaria* (Scytosiphonales, Phaeophyceae): A flavoprotein homologous to Old Yellow Enzyme. – European Journal of Phycology 40: 159–167.
Graham, L.E.; Graham, J.M. & Wujek, D.E. (1993): Ultrastructure of *Chrysodidymus synuroideus* (Synurophyceae). – Journal of Phycology 29: 330–341.
Grung, M. & Liaaen–Jensen, S. (1993): Algal carotenoids 52*; secondary carotenoids of algae 3; carotenoids in a natural bloom of *Euglena sanguinea*. – Biochemical

Systematics and Ecology 21(8):757–763.

HARRIS, K. & BRADLEY, D.E. (1958): Some unusual Chrysophyceae studied in the electron microscope. – Journal of General Microbiology 18: 71–83.

HEWITT, G. (2000): The genetic legacy of the quaternary ice ages. – Nature 405: 907–913.

HIBBERD, D.J. (1978): The fine structure of *Synura sphagnicola* (Korsh.) Korsh. (Chrysophyceae). – British Phycological Journal 13: 403–412.

HIJMANS, R.J.; CAMERON, S.E.; PARRA, J.L.; JONES, P.G. & JARVIS, A. (2005): Very high resolution interpolated climate surfaces for global land areas. – International Journal of Climatology 25: 1965–1978.

HUANG, S.; HEIKAL, A.A. & WEBB, W.W. (2002): Two–photon fluorescence spectroscopy and microscopy of NAD(P)H and flavoprotein. – Biophysical Journal 82: 2811–2825.

HUBER–PESTALOZZI, G. (1941): Das Phytoplankton des Susswassers. 2,1. Chrysophyceen, farblose Flagellaten, Heterokonten. – IN: THIENEMANN, A. (ed.): Die Binnengewasser XVI, 2, 1. – 365 pp., Schweizerbartsche Verlagsbuchbehandlung, Stuttgart.

JO, B.Y.; KIM, J.I.; SKALOUD, P.; SIVER, P.A. & SHIN, W. (2016): Multigene phylogeny of *Synura* (Synurophyceae) and descriptions of four new species based on morphological and DNA evidence. – European Journal of Phycology 51: 413–30.

KATOH, K.; MISAWA, K.; KUMA, K. & MIYATA, T. (2002): MAFFT: a novel method for rapid multiple sequence alignment based on fast Fourier transform. – Nucleic Acid Research 30: 3059–3066.

KAWAI, H. (1988): A flavin–like autofluorescent substance in the posterior flagellum of golden and brown algae. – Journal of Phycology 24: 114–117.

KORSHIKOV, A.A. (1927): *Skadovskiella sphagnicola*, a new colonial Chrysomonad. – Archiv für Protistenkunde 58: 450–455.

KORSHIKOV, A.A. (1929): Studies on the Chrysomonads. I. – Archiv für Protistenkunde 67: 253–290.

KREIMER, G. (1994): Cell biology of phototaxis in flagellate algae. – International Review of Cytology: 229–310.

KRISTIANSEN, J. & PREISIG, H.R. (2007): Chrysophyte and Haptophyte Algae, 2nd part. Synurophyceae. In: BÜDEL, B., GÄRTNER, G., KRIENITZ, L., PREISIG, H.R. & SCHAGERL, M. (eds.) Süsswasserflora von Mitteleuropa 1/2. Springer–Verlag, Berlin, 252 pp.

KRISTIANSEN, J. & SKALOUD, P. (2017): Chrysophyta. – IN: ARCHIBALD, J. M.; SIMPSON, A.G.B. & SLAMOVITS, C.H. (eds): Handbook of the Protists: Second Edition. – pp. 331–366, Springer International Publishing, Cham, Switzerland.

LEMOINE, Y. & SCHOEFS, B. (2010): Secondary ketocarotenoid astaxanthin biosynthesis in algae: a multifunctional response to stress. – Photosynthesis Research 106: 155–177.

LIU, J., Z. SUN, H. GERKEN, Z. LIU, Y. JIANG, AND F. CHEN (2014): *Chlorella zofingiensis* as an alternative micro-algal producer of astaxanthin: Biology and industrial potential. – Marine Drugs 12: 3487–3515.

LOGARES, R.; RENGEFORS, K.; KREMP, A.; SHALCHIAN–TABRIZI, K.; BOLTOVSKOY, A.; TENGS, T.; SHURTLEFF, A. & KLAVENESS, D. (2007): Phenotypically different micro-algal morphospecies with identical ribosomal DNA: a case of rapid adaptive evolution? – Microbial Ecology 53(4): 549–561.

LORENZ, R.T. & CYSEWSKI, G.R. (2000): Commercial potential for *Haematococcus* microalgae as a natural source of astaxanthin. – Trends in Biotechnology 18:160–167.

OKSANEN, J.; BLANCHET, F.G.; FRIENDLY, M.; KINDT, R.; LEGENDRE, P.; MCGLINN, D.; MINCHIN, P.R.;. O'HARA, R.B.; SIMPSON, G.L.; SOLYMOS, P.; STEVENS, M.H.H.; SZOECS, E. & WAGNER, H. (2020): vegan: Community Ecology Package. R package version 2.5–7, from https://CRAN.R–project.org/package=vegan.

OTA, S.; MORITA, A.; OHNUKI, S.; HIRATA, A.; SEKIDA, S.; OKUDA, K.; OHYA, Y. & KAWANO, S.J. (2018): Carotenoid dynamics and lipid droplet containing astaxanthin in response to light in the green alga *Haematococcus pluvialis*. – Scientific Reports 8: 5617.

PETERSEN, J.B. & HANSEN, J.B. (1958). On the scales of some *Synura* species, II. – Biologiske Meddelelser, Kongelige Danske. Videnskabernes Selskab 23(7): 1–13.

PUSZTAI, M.; CERTNEROVA, D.; SKALOUDOVA, M. & SKALOUD, P. (2016): Elucidating the phylogeny and taxonomic position of the genus *Chrysodidymus* Prowse (Chrysophyceae, Synurales). – Cryptogamie Algologie 37: 297–307.

R CORE TEAM (2021): R: A language and environment for statistical computing. R Foundation for Statistical Computing, Vienna, Austria. Available at: https://www.R–project.org/.

ROBERTS, D.W. (2019): labdsv: Ordination and Multivariate Analysis for Ecology. R package version 2.0–1. from https://CRAN.R–project.org/package=labdsv.

ROSHCHINA, V.V. (2012): Vital autofluorescence: application to the study of plant living cells. –International Journal of Spectroscopy: 1–14.

RONQUIST, F.; TESLENKO, M.; VAN DER MARK, P.; AYRES, D.L.; DARLING, A.; HÖHNA, S.; LARGET, B.; LIU, L.; SUCHARD, M.A. & HUELSENBECK, J.P. (2012): MrBayes 3.2: efficient Bayesian phylogenetic inference and model choice across a large model space. – Systematic Biology 61(3): 539–542.

SCOBLE, J. M. & CAVALIER–SMITH, T. (2014): Scale evolution in paraphysomonadida (Chrysophyceae): Sequence phy-logeny and revised taxonomy of *Paraphysomonas*, new genus *Clathromonas*, and 25 new species. – European Journal of Protistology 50(5): 551–592.

SILKINA, A.; BAZES, A.; VOUVÉ, F.; LE TILLY, V.; DOUZENEL, P.; MOUGET, J. L. & BOURGOUGNON, N. (2009): Antifouling activity of macroalgal extracts on *Fragilaria pinnata* (Bacillariophyceae): A comparison with Diuron. – Aquatic Toxicology 94(4): 245–254.

SIVER, P.A. (1989): The distribution of scaled chrysophytes along a pH gradient. – Canadian Journal of Botany 67: 2120–2130.

SWOFFORD, D.L. (2003): PAUP. Phylogenetic analysis using parsimony (and other methods). Version 4. Sinauer Associates, Sunderland.

ŠKALOUD, P.; KRISTIANSEN, J. & ŠKALOUDOVÁ, M. (2013): Developments in the taxonomy of silica–scaled chrysophytes – from morphological and ultrastructural to molecular approaches. – Nordic Journal of Botany 31: 385–402.

ŠKALOUD, P.; ŠKALOUDOVÁ, M.; DOSKOČILOVÁ, P.; KIM, J.I.; SHIN, W. & DVOŘÁK, P. (2019): Speciation in protists: Spatial and ecological divergence processes cause rapid species diversification in a freshwater chrysophyte. – Molecular Ecology 28: 1084–1095.

ŠKALOUD, P.; ŠKALOUDOVÁ, M.; JADRNÁ, I.; BESTOVÁ, H.; PUSZTAI, M.; KAPUSTIN, D. & SIVER, P.A. (2020): Comparing morphological and molecular estimates

of species diversity in the freshwater genus *Synura* (Stramenopiles): A model for understanding diversity of eukaryotic microorganisms. – Journal of Phycology 56: 574–591.

Tominaga, K.; Hongo, N.; Karato, M. & Yamashita, E. (2012): Cosmetic benefits of astaxanthin on humans subjects. – Acta Biochimica Polonica 59: 43–47.

Van Heukelem, L. & Thomas, C.S. (2001): Computer–assisted high–performance liquid chromatography method development with applications to the isolation and analysis of phytoplankton pigments. – Journal of Chromatography A, 910(1): 31–49.

Venables, W.N. & Ripley, B.D. (2002): Modern Applied Statistics with S. Fourth Edition. Springer, New York.

Wickham, H. (2016): ggplot2: Elegant Graphics for Data Analysis. Springer–Verlag New York.

Wilke, C.O. (2021): ggridges: Ridgeline Plots in ‚ggplot2'. R package version 0.5.3. from https://CRAN.R–project.org/package=ggridges.

Withers, N.W.; Fiksdahl, A.; Tuttle, R.C. & Liaaen–Jensen, S. (1981): Carotenoids of the Chrysophyceae. – Comparative Biochemistry and Physiology 68B: 345–349.

Yang, E.C.; Boo, G.H.; Kim, H.J.; Cho, S.M.; Boo, S. M.; Andersen, R.A. & Yoon, H.S. (2012): Supermatrix data highlight the phylogenetic relationships of photosynthetic Stramenopiles. – Protist 163: 217–231.

Zapata, M.; Garrido, J.L. & Jeffrey, S.W. (2006): Chapter 3. Chlorophyll c Pigments: Current Status. – In: Grimm, B.; Porra, R.J.; Rüdiger, W. & Scheer, H. (eds): Chlorophylls and Bacteriochlorophylls. Advances in Photosynthesis and Respiration, vol 25. – pp. 39–53, Springer, Dordrecht.

Table S1. List of taxa, sampling details and GenBank accession numbers for sequences analysed for Figure 1A.

	Taxon	Strain number	18S nu SSU rDNA	28S nu LSU rDNA	23S pt LSU	pt *rbc* L	pt psaA	nu ITS rDNA	mt coxI	Origin - locality name	Origin - coordinates
1	*Neotessella lapponica*	S59.C4	HF549063	KM590690	-	HF549074	-			Helgassjön, Sweden	56.956234, 14.716519
2	*Neotessella volvocina*	CCMP1781	EF165119	KM590691	KM590765	EF165199	KM590834			Freshwater reservoir, Mount Macedon, Victoria, Australia	-37.476944, 144.560000
3	*Synura americana*	Chimu112407C	KM590551	KM590617	KM590692	KM590838	KM590769			Chimu, Daesan-myeon, Haman-gun, Gyeongsangnam-do, Korea	35.339167, 128.429722
4	*Synura conopea*	Gonggeomji4031909C	KM590555	KM590621	KM590697	KM590842	KM590773			Gonggeom, Yangseong-ri, Gonggeom-myeon, Sangju-si, Gyeongsangbuk-do, Korea	36.495000, 128.124722
5	*Synura glabra*	Bonggye101407K	KM590564	KM590630	KM590706	KM590851	KM590782			Bonggye, Bonggye-ri, Dudong-myeon, Ulju-gun, Ulsan, Korea	35.681944, 129.211944
6	*Synura lanceolata*	Mangaeji040409A	KM590577	KM590643	KM590720	KM590864	KM590796			Mangae, Bibong-myeon, Cheongyang-gun, Chungcheongnam-do, Korea	36.559722, 126.761667
7	*Synura petersenii*	Buje100307A	KM590586	KM590657	KM590732	KM590873	KM590804			Buje, Gapje-dong, Gyeongsan-si, Gyeongsangbuk-do, Korea	35.831667, 128.770556
8	*Synura sungminbooi*	Buyeom032010A	KM590604	KM590675	KM590751	KM590891	KM590822			Buyeon, Buyeon-ri, Bugi-myeon, Cheongwon-gun, Chungcheongbuk-do, Korea	36.736667, 127.571667
9	*Synura truttae*	Hanjeong080611J	KM590609	KM590680	KM590756	KM590896	KM590827			Hanjeong, Girin-ri, Soseong-myeon, Jeongeup-si, Jeollabuk-do, Korea	35.565278, 126.775000
10	*Synura asmundiae*	S90D10	KM590553	KM590619	KM590695	KM590840	-			Rutajärvi, Finland	61.913889, 26.081111
11	*Synura bjoerkii*	SC57.A6	HF549070			HF549080				a small canal, Store Mosse, Sweden	57.30640, 14.01257
12	*Synura kristiansenii*	J56	MN782170	MN782229	MN782234	MN783126	MN783151			Rattling Brook (K70), Newfoundland, Canada	48.806944, -55.531944
13	*Synura macracantha*	S90B5	HF549064	KM590648	KM590725	HF549075	MW149257			Tehriselkä, Finland	61.756409, 26.486514
14	*Synura curtispina*	Gaekmang111107A	KM590559	KM590625	KM590701	KM590846	KM590777			Gaekmang, Udeok-ri, Deokcheon-myeon, Jeongeup-si, Jeollabuk-do, Korea	35.626111, 126.844722
15	*Synura sp.*	CCMP847	EF165128	-	-	EF165196	-			Winter's Creek, Keeweenaw County, MI, USA	47.291667, -88.071944
16	*Synura sp.*	Gungnam1072807A	KM590616	KM590689	KM590763	KM590903	KM590832			Gungnamji, Buyeo-eup, Buyeo-gun, Chungcheongnam-do, Korea	36.270000, 126.912778
17	*Synura longitubularis*	Jeongsan070607A	KM590580	KM590646	KM590723	KM590867	KM590799			Jeongsan, Jeongsan-myeon, Cheongyang-gun, Chungcheongnam-do, Korea	36.420278, 126.937778
18	*Synura spinosa*	Anha103010C	KM590599	KM590670	KM590746	KM590886	KM590818			Anha, Jisa-myeon, Imsil-gun Jeollabuk-do, Korea	35.581111, 127.353611
19	*Synura spinosa*	Sandoji011109C	KM590602	KM590673	KM590749	KM590889	KM590821			Sandoji, Hwangsan-dong, Gimje-si, Jeollabuk-do, Korea	35.772500, 126.931667
20	*Synura mollispina*	S71C10	HF549067	KM590655	KM590731	HF549077	MW149259			Podhradská pool, Czech Republic	50.461111, 14.911667
21	*Synura synuroidea*	S95E5	KX815882	KX815883	MW148518	KX815884	MW149262			Cairngorns NP, Scotland	57.225833, -3.722500
22	*Synura rubra A*	B57	MK322768			MK322927	MK322865	MK322808	MK322910	pond Vizír, Czech Republic	48.964622, 14.888456
23	*Synura rubra B*	S125.D5	MK322770			MK322929	MK322880	MK322824	MK322924	Lettererafroe Lough, Ireland	53.37457, -9.41682
24	*Synura rubra C*	Angol1129J2	KT364487	KT364489	KT364491	KT364495	KT364493			Angol, Jeongsan-myeon, Korea	36.420226, 126.937713
25	*Synura rubra C*	Hudong121209D	KT364488	KT364490	KT364492	KT364496	MK322883			Hudongje, Jeongsan-myeon, Chungcheongnam-do, Korea	36.425080, 126.940727
26	*Synura rubra C*	Hudong11291J2	*new*	*new*	*new*	*new*	*new*	*new*	*new*	Hudongje, Jeongsan-myeon, Chungcheongnam-do, Korea	36.425080, 126.940727
27	*Synura rubra D*	CNU52	GU325516			GU325417	MK322886	GU338152	GU295459	Beseokje, Gochang-gun, Korea	35.355757, 126.557604
28	*Synura rubra D*	Seoho050507E	MK322769			MK322928.1	MK322884			Seoho Lake, Suwon-si, Gyeonggi-do, Korea	37.277866, 126.988486
29	*Synura rubra E*	NIES 695	*new*	*new*	*new*	*new*	*new*	*new*	*new*	Miyatoko Mire, Fukushima, Japan	37.250571, 139.565626
30	*Synura sphagnicola A*	K35	*new*	*new*	*new*	*new*	*new*	*new*	*new*	Klečové louky NR, Jizerské hory, Czech Republic	50.8372739, 15.2460517
31	*Synura sphagnicola B*	S151.E9	MK322771	-	-	MK322930	MK322851			Conne River Pond, Canada	48.17876, -55.48391
32	*Synura sphagnicola B*	M44	*new*	*new*	*new*	*new*	*new*	*new*	*new*	Conne River Pond, Canada	48.17876, -55.48391
33	*Synura sphagnicola C*	S116.D5	*new*				MK322859	MK322802	MK322904	Pernilsavatnet, Norway	68.508933, 15.882923
34	*Synura mammillosa*	Santaek072410C	KM590583	KM590649	KM590727	KM590870	KM590801			Santaek, Santaek-ri, Yonggung-myeon, Yecheon-gun, Gyeongsangbuk-do, Korea	36.608889, 128.298611
35	*Synura echinulata*	CCMP853	KM590563	KM590629	KM590705	KM590850	KM590781			Bog near calumet, MT, USA	47.243889, -88.520000
36	*Synura leptorrhabda*	SIE105A	HF549065	KM590654	MN782236	HF549076	-			Caha lakes, Beara, Ireland	51.721667, -9.660278
37	*Synura leptorrhabda*	H92	MN782173	MN782231	MN782237	MN783129	MN783153			First pond (K30), Newfoundland, Canada	47.457778, -52.729444
38	*Synura leptorrhabda*	I41	MN782174	MN782232	MN782238	MN783130	MN783154			First pond (K30), Newfoundland, Canada	47.457778, -52.729444
39	*Synura leptorrhabda*	J50	MN782175	MN782233	-	MN783131				unnamed lake (K69), Newfoundland, Canada	48.843611, -55.503611
40	*Synura multidentata*	S90C11	HF549068	KM590656	-	HF549078	MW149260			Heinäjärvi, Finland	62.881111, 25.497222
41	*Synura punctulosa*	W83	MW148519	MW148516	MW148517	MW149255	MW149261			Большая Речка, flooded valley, Siberia, Russia	60.948056, 68.340833
42	*Synura splendida*	S90E6	KM590603	KM590674	KM590750	KM590890	-			Rutajärvi, Finland	61.913889, 26.081389
43	*Synura uvella*	A13.377	KM590614	KM590685	-	KM590901	-			Lake of the Clouds, Ontonagon, MI, USA	46.802500, -89.752222
44	*Synura uvella*	CCMP870	KM590615	KM590686	-	AF015586	-			Volo Bog Nature Preserve, McHenry County, IL, USA	42.351389, -88.184444
45	*Synura uvella*	Gahang033107A	KM590611	KM590682	KM590759	KM590898	KM590829			Gahang, Gahang-ri, Yueo-myeon, Changnyeong-gun, Gyeongsangnam-do, Korea	35.524167, 128.408056

Table S2. List of taxa, sampling details and GenBank accession numbers for sequences analysed for Figure 1B.

Strain	Lineage	Haplotype	Locality	Lat	Lon	Date	pH	Cond	Morphology	ITS rDNA	*psa*A	*cox*I
S62.E3	sp2	2A	peat bog Jizerka, Czech Republic	50,852077	15,342411	05.11.2011	3,8	30	-	MK322785	MK322842	MK322887
S95.B8	sp2	2A	Loch a' Chuilinn, Scotland, UK	57,610947	-4,85459	19.09.2012	6,3	37	yes	MK322786	MK322843	MK322888
S95.B10	sp2	2A	Loch a' Chuilinn, Scotland, UK	57,610947	-4,85459	19.09.2012	6,3	37	yes	MK322787	MK322844	MK322889
S130.G9	sp2	2A	unnamed pool, New Forest, England, UK	50,89875	-1,64163	19.03.2017	6,8	45	-	MK322788	MK322845	MK322890
K35	sp2	2A	CZE, Jizerské hory	50,8372739	15,2460517	07.06.2017	3,9	51	yes	**NEW**	**NEW**	**NEW**
S103.D2	sp2	2B	a pool near Smědava, Czech Republic	50,846056	15,236734	14.10.2012	5	40	-	MK322789	MK322846	MK322891
S100.F10	sp2	2B	Matresvatnet, Norway	60,887267	5,581748	21.10.2012	4,5	20	yes	MK322790	MK322847	MK322892
S147.G4	sp2	2B	Gallows Cove Pond, Canada	47,67992	-52,72789	25.05.2017	7,7	235	-	MK322791	MK322848	MK322893
S150.D10	sp2	2B	Rattling Brook, Canada	48,80686	-55,53192	28.05.2017	7,5	32	-	MK322792	MK322849	MK322894
S150.E11	sp2	2B	Rattling Brook, Canada	48,80686	-55,53192	28.05.2017	7,5	32	-	MK322793	MK322850	MK322895
S151.E9	sp2	2B	Conne River Pond, Canada	48,17876	-55,48391	28.05.2017	6,6	28	-	MK322794	MK322851	MK322896
S152.E5	sp2	2B	unnamed lake, Canada	48,94364	-55,82331	29.05.2017	7,4	39	-	MK322795	MK322852	MK322897
S154.C7	sp2	2B	a small sandpit near Cep, Czech Republic	48,9231269	14,8397844	01.08.2017	6,2	31	-	MK322796	MK322853	MK322898
S154.D7	sp2	2B	Borkovická blata, Czech Republic	49,2342722	14,6264719	01.08.2017	6,4	91	-	MK322797	MK322854	MK322899
S154.E7	sp2	2B	peat bog Pelé, Czech Republic	48,9591742	14,9653167	01.08.2017	5,3	93	-	MK322798	MK322855	MK322900
M44	sp2	2B	Canada, K78, Conne River Pond	48,17876	-55,48391	28.05.2017	6,6	28	yes	**NEW**	**NEW**	**NEW**
S93.B8	sp2	2C	Storträsket, Sweden	63,556324	19,774063	03.06.2012	5,6	27	-	MK322799	MK322856	MK322901
S95.F9	sp2	2C	Loch Carrie, Scotland, UK	57,359047	-4,879537	19.09.2012	6,1	37	yes	MK322800	MK322857	MK322902
S116.D4	sp2	2C	Pernilsavatnet, Norway	68,508933	15,882923	17.06.2013	6,5	30	-	MK322801	MK322858	MK322903
S116.D5	sp2	2C	Pernilsavatnet, Norway	68,508933	15,882923	17.06.2013	6,5	30	yes	MK322802	MK322859	MK322904
S124.B2	sp2	2C	Shannagrena, Ireland	53,46669	-9,5493	03.02.2017	6,4	67	-	MK322803	MK322860	MK322905
S71.G8	sp1	1A	Borkovická blata, Czech Republic	49,235555	14,623654	10.11.2011	6,4	91	-	MK322804	MK322861	MK322906
S71.G6	sp1	1A	Borkovická blata, Czech Republic	49,235555	14,623654	10.11.2011	6,4	91	-	MK322805	MK322862	MK322907
S71.G5	sp1	1A	Borkovická blata, Czech Republic	49,235555	14,623654	10.11.2011	6,4	91	yes	MK322806	MK322863	MK322908
S71.G2	sp1	1A	Borkovická blata, Czech Republic	49,235555	14,623654	10.11.2011	6,4	91	-	MK322807	MK322864	MK322909
B57	sp1	1A	pond Vizír, Czech Republic	48,964622	14,888456	09.10.2016	6,6	89	-	MK322808	MK322865	MK322910
B82	sp1	1A	Cep I., Czech Republic	48,917259	14,883842	09.10.2016	7,5	185	-	MK322809	-	MK322911
B83	sp1	1A	Cep I., Czech Republic	48,917259	14,883842	09.10.2016	7,5	185	-	MK322810	MK322866	MK322912
B84	sp1	1A	Cep I., Czech Republic	48,917259	14,883842	09.10.2016	7,5	185	-	MK322811	MK322867	MK322913
S57.F11	sp1	1B	Fräjen, Sweden	57,13794	14,60973	22.04.2011	5,4	83	-	MK322812	MK322868	MK322914

Strain	Lineage	Haplotype	Locality	Lat	Lon	Date	pH	Cond	Morphology	ITS rDNA	*psa* A	*cox* I
S96.B4	sp1	1B	Loch Craggie, Scotland, UK	58,009328	-4,842658	19.09.2012	6	118	-	MK322813	MK322869	MK322915
S102.E6	sp1	1B	a small sandpit near Cep, Czech Republic	48,923523	14,839122	14.11.2012	6,2	31	-	MK322814	MK322870	MK322916
S102.E7	sp1	1B	a small sandpit near Cep, Czech Republic	48,923523	14,839122	14.11.2012	6,2	31	yes	MK322815	MK322871	MK322917
S102.E11	sp1	1B	a small sandpit near Cep, Czech Republic	48,923523	14,839122	14.11.2012	6,2	31	-	MK322816	MK322872	MK322918
S117.E2	sp1	1B	unnamed lake, Sweden	68,34812	18,963588	17.06.2013	4,7	17	-	MK322817	MK322873	MK322919
S117.E3	sp1	1B	unnamed lake, Sweden	68,34812	18,963588	17.06.2013	4,7	17	-	MK322818	MK322874	MK322920
S117.E4	sp1	1B	unnamed lake, Sweden	68,34812	18,963588	17.06.2013	4,7	17	yes	MK322819	MK322875	MK322921
C14	sp1	1B	Cep I., Czech Republic	48,917259	14,883842	11.10.2016	7,5	185	-	MK322820	MK322876	-
S125.D7	sp1	1B	Lettererafroe Lough, Ireland	53,37457	-9,41682	04.02.2017	6,3	78	-	MK322821	MK322877	-
S125.D9	sp1	1B	Lettererafroe Lough, Ireland	53,37457	-9,41682	04.02.2017	6,3	78	-	MK322822	MK322878	MK322922
S125.D10	sp1	1B	Lettererafroe Lough, Ireland	53,37457	-9,41682	04.02.2017	6,3	78	-	MK322823	MK322879	MK322923
S125.D5	sp1	1B	Lettererafroe Lough, Ireland	53,37457	-9,41682	04.02.2017	6,3	78	-	MK322824	MK322880	MK322924
Mutgol031909C	sp1	1C	Chungcheongbuk-do Mutgolje, Boeun-gun, Korea	36,468762	127,754987	19.03.2009	-	-	-	MK322825	MK322881	-
Juam032509D	sp1	1C	Dam Juam, Juam-myeon, Korea	34,989305	127,228638	25.03.2009	8,2	70	yes	MK322826	MK322882	-
Angol112914J2	sp1	1C	Angol, Jeongsan-myeon, Korea	36,420226	126,937713		-	-	-	KT364497	KT364493	MK322925
Hudong121209D	sp1	1C	Hudongje, Jeongsan-myeon, Korea	36,42508	126,940727	12.12.2009	7,9	128	-	MK322827	MK322883	MK322926
Hudong11291J2	sp1	1C	Hudongje, Jeongsan-myeon, Korea	36,42508	126,940727	Korea	7,9	128	yes	**NEW**	**NEW**	**NEW**
Seoho050507E	sp1	1D	Seoho Lake, Suwon-si, Korea	37,277866	126,988486	05.05.2007	7,3	613	-	MK322828	MK322884	-
Muryeong120807A	sp1	1D	Muryeongje, Yeonggwang-gun, Korea	35,286058	126,51279	12.08.2007	-	-	-	MK322829	MK322885	-
CNU52	sp1	1D	Beseokje, Gochang-gun, Korea	35,355757	126,557604	12.08.2007	-	-	-	GU338152	MK322886	GU295459
NIES695	sp1	1E	Miyatoko Mire, Fukushima, Japan	37,250571	139,565626	27.04.1992	-	-	yes	**NEW**	**NEW**	**NEW**

Contributor ISME J

Behind the paper Under the microscope

Revisiting biocrystallization: Purine biocrystals are widespread in eukaryotes

Paradigm shift in eukaryotic biocrystallization: purine biocrystals are likely an ancestral type of cellular inclusions in eukaryotes. Cell inclusions in the spotlight of Raman microspectroscopy.

Published Jun 14, 2022

Jana Pilatova
researcher, Charles University

[Follow]

Each of us produces biocrystals – in our bones and teeth. Some can be malignant, such as those causing urolithiases in our kidneys, bile stones, or atheromatous plaques. Different types of crystals are present in reptiles, fish and insects, having brilliant optical properties enabling the beautiful color changes of chameleons and iridescent fish scales; they also form mirror-like layers in the backs of the eyes of nocturnal insects, mollusks and deep-sea fish to improve their vision under low light.

Unicellular microorganisms – protists and algae – represent 70 % of estimated diversity of living organisms on earth and many of them also possess biocrystals that have been observed since the very beginning of microscopy. They have been mentioned even by pioneers of biology – Charles Darwin and Ernst Haeckel, and repeatedly admired by laymen (see Fig. 1, http://y2u.be/H purine crystals are widespread in eukaryotes bwV-EzP67Q). But since then still (!), the chemical nature of intracellular crystals has remained unclear, with traditionally repeated myths about calcites or oxalates. According to our systematical revision, this is not the case (https://y2u.be/UtygkzDmz8U).
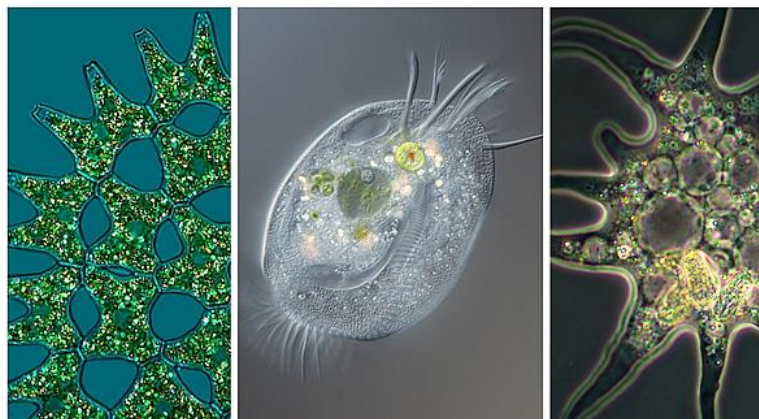
Figure 1. Birefringent crystalline inclusions polarize light and appear as shining particles inside the micro-eukaryotic cells under polarizing microscopy – admired and captured by both scientists and laymen, despite their as-yet-unknown composition which was revealed to be formed by purines in our recent work; from left to right: microalga (*Pediastrum duplex*) by Jacek; ciliate (*Euplotes* sp.) by Waldo Nell, amoeba by pitschuni.

Fortunately, nowadays we have the powerful method of Raman microscopy – enabling measurements of vibrational spectra reflecting the chemical composition *in vivo* and *in*

situ. Our initial serendipitous discovery of guanine crystals in microalgae led me to a bold guess that it might not be limited to algae, as it is not connected to chloroplasts. Not to mention, algae emerged many times independently, so they are as closely related to each other as, for example, we are to amoebae. Since I tested more than 200 species from model and biotechnologically exploited species, medically important parasites, and environmental samples from a broad variety of habitats – ranging from toxic algal bloom freshwater species to the anaerobes of termite guts and slime molds, I eventually found that my bold guess was correct – purine crystals are universally present in microscopic eukaryotes. So, I proposed a paradigm shift in the concept of eukaryotic biocrystallization, originally assuming the presence of previously found calcite or oxalates in microorganisms. I have also found other minor types of crystalline inclusions: calcium oxalate, strontianite, calcite, baryte, celestite, lipophilic crystals of sterols, fatty acids, and carotenoids.

Figure 2: Eukaryotic tree of life with clades positively screened for purine crystals of four types: anhydrous guanine (cyan), guanine monohydrate (blue), uric acid (yellow) and xanthine (orange). The full caption is in the original publication.

Moreover, purine crystals may have occurred in the last eukaryotic common ancestor and be the oldest form of biocrystallization. Hence, we outlined an evolutionary scenario for purine crystal formation inside cells due to highly conserved purine transporters. Purines are surprisingly versatile molecules: building blocks of DNA and RNA, sources of chemical energy (ATP, GTP), and messengers in cellular signaling (cAMP, cGMP). Caffeine is another type of purine that is our favorite and luckily more soluble than those forming biocrystals. We found a new function of purines in the cells. They act as high-capacity nitrogen storage that is reusable once cells are deprived of nitrogen sources (https://www.pnas.org/doi/10.1073/pnas.2005460117). A single cell can store up to 150 pg guanine per cell that can cover up to 3 consecutive cell divisions solely supplied from internal sources of nitrogen after inoculation to nitrogen depleted medium. Thus, they may serve a great competitive advantage in the environment with fluctuating supplies of nitrogen. They are key to the understanding of the global nitrogen cycle, which in turn, is tightly interconnected with the carbon cycle and global climate change. The extra nitrogen load might be further used in green biofertilizers, which are increasing in popularity. However, purine crystals in algal-based food supplements may potentially cause hyperuricemia and its complications, such as gouty arthritis or nephropathy, if consumed regularly.

Simultaneously, purine crystals exhibit exquisite optical properties enabling cells to modulate light – that might be mostly prominent in photosynthetic algae – either increasing light intensity in respect to plastids, or shielding them from excessive light irradiation that may be deleterious to photosystems (https://www.sciencedirect.com/science/article/abs/pii/S1047847719300759). The high reflectivity of crystalline purine inclusions (e.g., photonic mirrors) may be exploited in the field of optics and cosmetic beauty products due to the magnetic tunable reflectivity of guanine biocrystals.

Final statistics: so far, there have been published a million research articles on microbial eukaryotes, half a million on purine metabolism and tens of thousands dedicated to biomineralization, nitrogen cycle, and microbial biotechnologies according to PubMed. All that without the basic awareness that crystalline purines are the most common crystalline inclusion of microscopic eukaryotes. We dare to believe that our findings have similar inspiring potential as the discovery of the biological role of inorganic polyphosphates by the Nobel Prize winner Arthur Kornberg eighty years ago, who initiated extensive research of that mysterious substance, considered to be just a molecular fossil, and thus contributed to the discovery of a multitude of their biological functions.

For full details, check our new paper at: https://www.nature.com/articles/s41396-022-01264-1

Twitter: @Jana Pilátová

Article is available online:

https://microbiologycommunity.nature.com/posts/revisiting-biocrystallization-purine-biocrystals-are-widespread-in-eukaryotes

Video:

https://microbiologycommunity.nature.com/videos/revisiting-biocrystallization-purine-biocrystals-are-widespread-in-eukaryotes